Politecnico di Milano

SCUOLA DI INGEGNERIA INDUSTRIALE E DELL'INFORMAZIONE
Doctoral programme in Information Technology - Telecommunications

Interference Mitigation Techniques in Hybrid Wired-Wireless Communications Systems for Cloud Radio Access Networks with Analog Fronthauling

Doctoral Dissertation of:
Andrea Matera

Supervisor:
Prof. Umberto Spagnolini

Tutor:
Prof. Andrea Virgilio Monti Guarnieri

Supervisor of the Doctoral Program:
Prof. Andrea Bonarini

Cycle XXXI, 2015-2018

"There are things you know about, and things you don't,
the known and the unknown, and in between are the
doors—that's us."

Ray Manzarek

Ringraziamenti

Questi tre anni di dottorato sono stati lunghi, faticosi, frenetici, ma al tempo stesso pieni di soddisfazioni. E se così è stato, è anche grazie al supporto di tutte le persone che mi sono state vicine, e che per questo ci tengo a ringraziare.

Il primo di questi "grazie" va al Prof. Spagnolini che è stato la mia guida in questi tre anni, riponendo sempre grande fiducia in me (anche quando io stesso ne avevo poca) e affidandomi responsabilità che mi hanno aiutato a crescere sia professionalmente che personalmente. Grazie per il suo spirito critico, per le discussioni tecniche, per i confronti e, soprattutto, per le opportunità che mi ha dato.

Thank you to Prof. Moonen and Prof. Calvanese-Strinati for having spent their time in reviewing my PhD thesis and for their valuable comments.

Un grazie alla Prof.ssa Nicoli e al Prof. Rampa, e agli altri colleghi del WisyLab Stefano, Sanaz e Mattia. Grazie ai compagni di ufficio Naqvi, Ali, Maria e Gloria che mi hanno sopportato in questi ultimi tre anni. Parlo tanto, lo so.

Un grazie particolare a Lollo che è stato un vero e proprio compagno di avventure in questo dottorato (e non solo) e con il quale sono cresciuto fianco a fianco.

Grazie a Sanvitz, Dario, Bomber, Omran, Andreoletz, Rodolfo e a tutti gli amici del Politecnico con i quali ho condiviso questo percorso.

Grazie a tutti gli amici di sempre di Verbania, agli amici di Milano e a tutti quelli che sono lontani ma, nonostante ciò, hanno saputo starmi vicino.

Un grazie speciale ai miei genitori Letizia e Mingus e a mio fratello Carlo che mi hanno sempre ascoltato e sostenuto... che pazienza! Grazie a mia nonna Franca che per la Laurea Magistrale mi ha regalato un vestito talmente bello che non solo mi ha accompagnato a tutte le conferenze e presentazioni degli ultimi tre anni, ma che indosserò anche il giorno della presentazione della tesi di dottorato!

Un ultimo grazie, ma non per importanza, va alla mia ragazza Elena, con la quale ho vissuto per tutta la durata del dottorato e con la quale ho condiviso tutti i momenti, più belli e più brutti. Grazie per questi tre anni a Milano e grazie per la nostra nuova vita a Madrid, insieme.

Grazie.

Andrea

Contents

Abstract

Centralized Radio Access Network (C-RAN) is an attractive solution to handle the huge number of user devices and antennas that are expected to populate next generation (5G and beyond) communication networks. C-RAN is already adopted in current (4G) mobile networks, in which BaseBand Units (BBUs) and Remote Antenna Units (RAUs) exchange In-phase and Quadrature (I/Q) digitized signals over the so-called FrontHaul (FH) link. However, the expected increase in radio frequency bandwidth calls into question the effectiveness of digital I/Q stream.

Among the numerous FH functional splits that have been proposed over the last years, mostly based on digital FH, C-RAN based on analog fronthauling is considered a low-cost and bandwidth efficient solution. In analog C-RAN, the RAUs directly relay the radio signals to/from the BBU, thus bypassing any bandwidth expansion due to digitization, reducing latency, and providing synchronization among multiple RAUs. In particular, C-RAN with analog FH based on copper cables, namely Analog Radio-over-Copper (A-RoC), is a suitable solution to enhance indoor wireless coverage into buildings and enterprises.

In this thesis, A-RoC is considered for multiple-antennas RAUs and multiple twisted-pairs copper cables, e.g., Local Area Networks (LAN) cables, thus leading to the Analog MIMO RoC paradigm. In the proposed A-MIMO-RoC architecture, radio signals from multiple-antennas are opportunely mapped over the copper cables multiplexed both in space dimension, given by the multiple twisted-pairs, and in frequency dimension, given by the bandwidth of each twisted pair. Such all-analog radio-cable resource mapping enables the full exploitation of the transport bandwidth capability of copper cables.

The A-MIMO-RoC system design requires the optimization over the cascade of two different MIMO channels, i.e., the radio and cable channels, each of which with different characteristics and constraints. As a first step, signal processing techniques have been investigated for these two channels, separately. In particular, on the one hand, the focus was on non-linear precoding techniques for next generation xDSL systems, namely G.fast; on the other hand, interference mitigation techniques have been designed for wireless systems with focus on multi-operator scenarios, and for optical wireless systems, i.e., Visible Light Communications (VLC). Merging the knowledge acquired from this preliminary step, the core of the thesis discusses the design and optimization of the Analog-MIMO-RoC architecture, which is complicated by the mutual interaction between the wireless and wired communication

channels. This thesis provides extensive numerical analysis showing the benefits of the proposed A-MIMO-RoC architecture for 5G indoor networks. As a conclusive step, the real world implementation of the proposed architecture has been demonstrated by developing a first A-MIMO-RoC prototype, which was able to prove experimentally and for the first time the potentials of the proposed analog C-RAN architecture for FH indoor applications.

1. Introduction

INTERFERENCE is at the center of this thesis. To be more precise, the focus here is on interference in the context of a peculiar communication scenario, herein denoted as hybrid wired-wireless communication system. However, after a quick look at the thesis title, the following questions naturally arise: What do we mean by hybrid wired-wireless communication systems? What is the role that hybrid wired-wireless systems will play in next generation networks? Why are they so important?

The scope of these first few paragraphs is to clarify these points by providing a brief introduction to the concepts and motivations lying behind the research activity that I carried out during my PhD. Although this thesis is about interference mitigation techniques for hybrid wired-wireless systems, in order to convince the reader about the importance of this task in next generation communication networks, a first fundamental step is to introduce the network architecture which inspired the overall work: the so-called Analog Radio-over-Copper (A-RoC) architecture.

Toward this end, we will mandatorily need to go through four main pillars ideas, namely *i)* indoor coverage, *ii)* Cloud Radio Access Network (C-RAN), *iii)* analog fronthauling, and, finally, *iv)* the RoC paradigm. These concepts, which will continually recur in the remainder of the thesis, are now introduced one-by-one by answering four simple questions.

i) Why Indoor?

According to [1], even today, 80% of mobile traffic is consumed indoor, and this is expected to grow more than ever in the very next years. By 2020, when 5G networks will become a reality, 96% of wireless data traffic will originate or terminate within a building, raising the indoor wireless market value up to $16.71 billion [2]. However, only 2% of the 30 billion square meters of indoor commercial real estate have dedicated in-building wireless cellular systems [3]. In other words, nowadays, the large majority of *indoor* areas are served by networks that have been originally designed for *outdoor* scenarios. This is the reason why providing bandwidth-efficient, ultra-low latency and low-cost solutions for enhanced indoor coverage is the main task that both industries and academia will have to face in investigating, developing, and deploying next generation 5G networks.

ii) Why Centralizing 5G Radio Access Networks?

By 2020, 5G is expected to meet very strict requirements in terms of minimum guaranteed data-rate, service reliability, latency, coverage, and number of interconnected devices. Just to give some numbers, 5G will have to pursue a 1000-fold rate increment with respect to today's networks, lower the end-to-end latency down to 1 ms, and guarantee 99.999% aggregate service reliability. In order to meet these requirements, upcoming 5G networks will mandatorily need to support advanced physical layer technologies and network deployment strategies, such as massive Multiple-Input Multiple-Output (MIMO), mmWaves, and small cell densification. As a consequence, unprecedented complex interference scenarios will raise, thus calling for a proper revolution in the way RAN resources and functions are handled [4].

In this context, C-RAN [5, 6] appears to be an attractive solution to cope with such challenging interference management task. As such, C-RAN architecture, taking benefits from centralized processing and mutual cooperation for interference mitigation, is capable to handle a massive number of antennas/cells/users in the same physical resources, thus substantially increasing the bandwidth per unit area. Key enablers for C-RAN are: *i)* the co-location of BaseBand Units (BBUs) in so-called BBU pools or hotels, that allow for signal processing centralization and provide remarkable benefits in terms of cost reduction; *ii)* the remotization of the Radio-Frequency (RF) equipment, which are hosted in Remote Antenna Units (RAUs). RAUs are densely geographically distributed both indoor and outdoor close to the end-users, and this provides network scalability and improved spectral efficiency. These are the reasons why the C-RAN concept, which is already adopted in current 4G networks, will surely play a fundamental role also in next generation 5G networks, albeit it will need to be substantially redesigned to accommodate the stringent 5G requirements.

iii) Why Analog Fronthauling?

C-RAN is already present in current 4G networks. In particular, the communication between today's RAUs and BBUs takes place over the so-called FrontHaul (FH) link, which is a high-capacity link usually based on fiber optics. As detailed later in Section 1.1, this architecture, known as Digital Radio-over-Fiber (D-RoF), is designed to support the streaming of digitized RF signals in form of In-phase and Quadrature (I/Q) samples, where the process of RF signals digitization and packetization is handled by protocols specifically designed, such as the Common Public Radio Interface (CPRI) [7] or the Open Base Station Architecture Initiative (OBSAI).

In perspective, it is widely agreed that current CPRI-based mobile fronthaul will hardly scale to the increased radio signal bandwidth foreseen by 5G networks, especially for RAUs equipped with massive number of antennas. The reason for

this lies mainly in the Analog-to-Digital Conversion (ADC) operation, that would introduce a bandwidth expansion that can be as severe as 30x, thus exceeding the capacity of current fronthaul links. Another critical aspect is the end-to-end latency that next generation networks will have to guarantee. Recently, several approaches have been proposed to overcome these limitations, such as CPRI compression, able to reduce the bandwidth expansion down to 16-18x [8], or novel RAN functional split options, aimed at redistributing in a flexible way the RAN functionalities between BBU and RAU [9, 10, 11].

A more in depth discussion about the several RAN functional splits options that have been proposed for 5G RAN is covered in Sect. 1.1 and Sect. 1.2. For the purposes of this introductory paragraph, it is enough to say that differently from the aforementioned novel RAN architectures, which are mostly digital, an alternative solution to relax the requirements of mobile fronthaul is simply the overtaking of conventional digital fronthauling in favor of a fully analog transmission of RF signal between RAUs and the BBU pool. This fully analog fronthaul architecture completely by-passes any bandwidth/latency issue due to digitization, reduces hardware costs, improves energy efficiency, and allows for synchronization among multiple decentralized RAUs, thus enabling MIMO joint processing. C-RAN with analog fronthauling can be seen as an extreme RAN functional split option in which even the ADC and the Digital-to-Analog Converters (DAC) are shifted to the BBU, while only the RF functionalities are left to the RAUs, which become extremely low-complexity and cheap devices. In particular, in such all-analog architecture, the RAU functionalities are limited to the relaying of the Intermediate Frequency (IF) signals to/from the BBUs, after these are frequency-converted and scaled in order to comply with the capabilities of the analog fronthaul.

iv) Why Radio-over-Copper?

Over the last, several analog C-RAN architectures based on different fronthaul technologies have been proposed. Among these, an effective example of analog mobile fronthauling is Analog Radio-over-Fiber (A-RoF), which is based o the analog relaying of IF over long-range fiber optic links. A-RoF, which is discussed in more details in section 1.3.1, is very attractive due to its capability to carry several Gbps in terms of equivalent data-rate [12, 13, 14]. Although A-RoF perfectly matches the requirements of outdoor networks in which the mobile fronthaul extends over several kilometers, the deployment and installation of a pervasive optical infrastructure is not always feasible, e.g., in dense urban areas. For these scenarios, a possible solution is to employ high-capacity point-to-point wireless FH links, mainly based on mmWave or THz bands. This architecture, known as Analog Radio-over-Radio (A-RoR) [15], provides several advantages in terms of flexibility, resiliency, hardware complexity and cost.

Indoor is another application scenario where the installation of fiber links may be too expensive to provide satisfactory business cases. In this case, the most

intuitive solution is to extend indoor coverage by relaying the FH signals over the pre-existing Local Area Network (LAN) cabling infrastructure of buildings and enterprises. This solution, known as A-RoC, allows for the remotization of the RF equipment, which are moved closer and closer to the end-users without the need of a new network infrastructure, thus improving indoor wireless coverage over the last 100-200m while containing deployment costs. Furthermore, by leveraging the Power over Ethernet (PoE) technology, A-RoC allows for the powering of the RF equipment over the same copper cables, so that no additional power supplier is needed. A-RoC encompasses both the advantages of analog fronthauling and the economical benefits of reusing the existing copper transport infrastructures, thus becoming the first candidate for extending in-building wireless coverage of next generation 5G networks.

A-RoC technology is at basis of this thesis, whose goal is to extend the A-RoC concept to a more general fronthaul architecture characterized by the cascade of a MIMO wired channel over a MIMO wireless channel. By deeply investigating the resulting hybrid wired-wireless communication system, and by paying particular attention to how to handle in an efficient and flexible way both wireless and wired resources, A-RoC evolves to the Analog MIMO-RoC (A-MIMO-RoC) paradigm, which is proposed in this thesis.

As we will see all along this work, in order to fully exploit the potential of A-MIMO-RoC architecture, several issues need to be faced: first of all, an all-analog and low-complexity design criterion needs to be specified for the RAU, which is the equipment representing the "interface" between wired and wireless channels; then, more importantly, interference mitigation strategies need to be specifically designed in order to cope with the resulting mutually coupled wired and wireless interferences.

Organization

The remainder of this chapter is organized as follows.

Sect. 1.1 provides an overview on the recent evolution of RAN for 5G networks. In this regards, alternative RAN architectures based on different functional split options are presented, starting from today's mobile fronthaul towards the concept of a fully analog C-RAN architecture considered here. In Sect. 1.2, C-RAN with analog fronthauling is placed into the context of existing low-layer RAN functional split options, and compared with these alternative RAN architectures in terms of both latency and bandwidth fronthaul requirements. Sect. 1.3 presents both pros and cons of A-RoC with respect to another well-established analog C-RAN architecture, namely A-RoF, but also with respect to the digital counter-part of A-RoC, denoted here as Digital Radio-over-Copper (D-RoC). Sect. 1.4, after providing an overview of the A-RoC literature and start-of-the A-RoC-based solutions, details

how A-RoC lead to the hybrid wired-wireless A-MIMO-RoC architecture discussed is this thesis, which is introduced together with its peculiarities.

Sect. 1.5 describes the thesis structure by proving a chapter-by-chapter summary outlining the original contributions and the related publications. Finally, Sect. 1.6 provides the full publications lists, while the mathematical notation adopted in the thesis is in Sect. 1.7.

Contribution on International Conferences/Journals

Part of the material presented in this chapter has been published in:

- **A. Matera**, V. Rampa, M. Donati, A. Colamonico, A. F. Cattoni and U. Spagnolini, "Analog MIMO Radio-over-Copper for Enhanced Indoor Coverage: Concepts and Validations" submitted to *IEEE Communications Magazine*.

Acknowledgements

The part of this chapter about 5G RAN functional split options is the result of a fruitful interaction with Nokia and their support is acknowledged.

1.1. 5G RAN Evolution for 5G Systems

C-RAN architecture, as standardized in current LTE networks, is based on the exchange of digital I/Q samples through the CPRI protocol. However, as already pointed out, there is no doubt that this mobile fronthaul architecture, as it stands, cannot be simply extended to meet the requirements of next generation mobile systems. In order to relax such bandwidth and latency requirements, one possible solution is to redistribute the RAN functionalities between the BBU, which performs centralized processing, and the RAU, which performs local processing at the antenna site. In this direction, lots of standardization efforts have been devoted to investigating and testing new functional split options between BBU and RAU [10]. The main RAN functional split options recently proposed for 5G RAN have been shown in Fig. 1.1 and described in the following making a division among high-, medium- and low-layer functional splits [16]. Pros and cons of each solution, including the aforementioned analog fronthauling, have been highlighted focusing mainly on four aspects, considered vital for upcoming 5G networks: *i)* the bandwidth required over the fronthaul link, *ii)* the maximum latency allowed from BBU to RAU, *iii)* the possibility to implement advanced Cooperative MultiPoint (CoMP) schemes such as Joint Reception/Transmission

(JR/JT), centralized scheduling and interference mitigation, and *iv)* the complexity of the RF equipment. The latter is especially critical for indoor deployment, as RAUs are requested to be as simple/cheap as possible.

The goal of this section is two-fold: *i)* clarify in which aspects the several newly proposed RAN functional split options differ among them, and *ii)* contextualize C-RAN with analog fronthauling, denoted in the following as *Split 9 - Analog Split Option,* into the framework of RAN functional split options, and show its benefits if compared with other fronthaul architectures.

The characteristics of the different functional split options are summarized in Table 1.1.

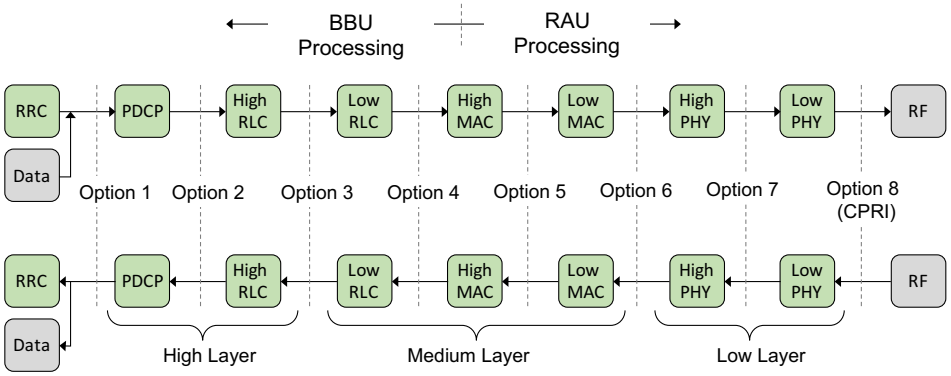

Figure 1.1.: RAN functional split options: downlink (upper), uplink (lower)

1.1.1. High-Layer Functional Splits

High-Layer Functional Splits options are referred to the set of split options in which the high layer functionalities of the RAN stack, such as Radio Resource Control (RRC), are performed centrally at the BBU, while all the other functions are performed locally at the RAU. Three main high-layer functional split options have been proposed:

- Option 1 (RRC-PDCP): Only RRC is centralized at the BBU. All the RAN functions, from the Packet Data Convergence Protocol (PDCP) to the reception of RF signals, are implemented locally at the RAU, which handles the entire user plane;
- Option 2 (PDCP-RLC): RRC and PDCP are performed at the BBU, while Radio Link Control (RLC), Medium Access Control (MAC), PHysical Layer (PHY) and RF functionalities are implemented at the RAU;

- Option 3 (Intra-RLC): also some of the RLC functionalities, such as segmentation and Automatic Repeat reQuest (ARQ), are centralized at the BBU. Option 3 has more stringent latency requirements with respect to previous splits due to the ARQ centralization, that requires timely exchange of control information between BBU and RAU.

Pros

- relatively relaxed latency constraints: if not limited by the end-to-end latency budget required by the specific application (i.e., 1ms for ultra low-latency applications), the required Round Trip Time (RTT) is between 5 and 10 ms depending on the radio settings;
- relaxed bandwidth requirements;

Cons

- increased complexity and costs for installation and maintenance of RAUs, since they are in charge to implement most of the RAN functionalities;
- limited network scalability;
- do not allow for the implementation of advanced radio coordination schemes such as CoMP, which become mandatory to cope with the interference generated by the billions of user devices expected to populate upcoming 5G networks.

1.1.2. Medium-Layer Functional Splits

In medium layer functional split options, all the high-layer and part of the MAC functions are centralized at the BBU. Three medium-layer functional splits options have been proposed:

- Option 4 (RLC-MAC): RRC, PDCP and RLC are in the BBU, while MAC, PHY and RF are in the RAU;
- Option 5 (Intra-MAC): RRC, PDCP, RLC and the higher part of the MAC layer (e.g., high-level centralized scheduling decisions, inter-cell interference coordination) are centralized in the BBU, while RF, PHY and the lower part of the MAC layer (e.g., time critical functions such as HARQ, radio channel and signal measurements from PHY) are in the RAU.
- Option 6 (MAC-PHY): MAC and upper layers are in the BBU, while only PHY and RF are implemented locally at the RAU.

1.1.2.1. Pros

- bandwidth constraints are still relatively relaxed, i.e., only marginally higher w.r.t. those of high-layer split options;
- allows for the implementation of some of the advanced coordination schemes such as centralized radio resource scheduling, inter-cell interference coordination and even (option 6 only) downlink (DL) JT;

1.1.2.2. Cons

- the RAU complexity is still very high since it implements all the PHY processing which is the most computationally demanding;
- most of the advanced CoMP schemes, such as UpLink (UL) JR, cannot be implemented;
- very strict latency requirements due to the centralization of time-critical MAC functions (i.e., from option 6 onwards the fronthaul latency is constrained to $200\mu s$ due to HARQ centralization).

1.1.3. Low-Layer Functional Splits

In the case of low-layer split options, the high-layer, medium-layer, and part (or even all) of the PHY functions are centralized at the BBU. In particular, split Option 8 corresponds to today's CPRI mobile fronthaul, while Option 7 envisages three different intra-PHY sub-splits which are described in the following. Intra-PHY splits are shown in Fig. 1.2, together with the all-analog fronthaul covered here, denoted as split Option 9, even if this split option has not been considered in 5G New Radio (NR) standardization. It is important to remark that the CPRI forum is currently working on the definition of a new transport fronthaul interface based on intra-PHY split options, denoted as enhanced CPRI (eCPRI) [17].

A brief description of the low-layer split options is given in the following, while a more in depth discussion including the computation of latency and bandwidth fronthaul requirements is in Section 1.2.

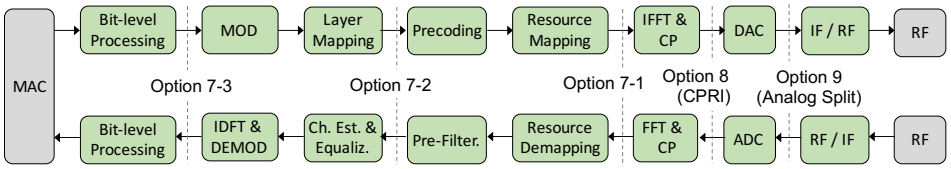

Figure 1.2.: Intra-PHY (eCPRI), RF & Analog split options

1.1.3.1. Option 7-2 & Option 7-3

In Options 7-2 in UL direction, Fast Fourier Transform (FFT), Cyclic Prefix (CP) removal, resource demapping and pre-filtering functions are locally implemented at the RAU, while the rest of PHY functions are centralized at the BBU. Symmetrically, in DL direction, inverse Fast Fourier Transform (iFFT), CP addition, resource mapping and precoding are implemented at the RAU, while the rest of PHY functions are centrally implemented at the BBU.

In Option 7-3 only the encoder is hosted at the BBU, while all the other PHY functionalities reside in the RAU.

Pros

- the capacity requirements are relaxed since they scale only with the number of MIMO layers and the system bandwidth;

Cons

- very strict latency constraints due to HARQ centralization (i.e., $200\mu s$);
- not all the advanced coordination CoMP schemes can be implemented (i.e., precoding/pre-filtering and resource mapping/demapping are locally implemented at the RAU).

1.1.3.2. Option 7-1 & Option 8 (CPRI)

In Option 7-1 in UL direction, only FFT and CP removal reside at the RAU, while all the other PHY functionalities are centralized at the BBU. Symmetrically, in DL direction, iFFT and CP addition functions are implemented at the RAU and the rest of PHY functions are at the BBU. In Option 8, all the PHY functions are centralized, while only the ADC/DAC reside at the RAU. The only difference between Option 7-1 and Option 8 is that the former has slightly more relaxed bandwidth requirements due to the removal of CP and guard subcarriers, since FFT and iFFT are implemented locally at the RAU.

Pros

- allow for the implementation of all the advanced coordination CoMP schemes since all the PHY processing is centralized at the BBU;

Cons

- very strict latency constraints due to HARQ centralization (i.e., 200μs);
- very strict capacity requirements which scale with the number of antenna ports (i.e., usually much higher then the number of streams/users) and the system bandwidth;

1.1.4. Option 9 (Analog Split Option)

Focus of this section is to describe a further functional split option, denoted here as Analog Split Option (Option 9), which is at the basis of the analog C-RAN architecture considered in this thesis. Analog split option is based on the full analog transmission of RF signal over the fronthaul link between RAU and BBU. Option 9 has not been considered in the 5G NR standardization process yet, however, it provides several benefits, as detailed in the following. Contrarily to all the the aforementioned functional split options, in Option 9, even the ADC/DAC are moved to the BBU, while the low-complexity RAU is in charge only of down-converting the radio signal from RF to IF and scaling the signal power to comply with the fronthaul link capabilities, depending on whether the fronthaul link is based on fiber-optics or copper cables.

Pros

- no strict bandwidth constraints, as no digitization is performed at the RAU (i.e., no bandwidth expansion due to ADC)
- allow for the implementation of all the advanced coordination CoMP schemes (i.e., all the PHY processing is centralized at the BBU with remarkable benefits in terms of interference cancellation);
- very simple and low-complexity RAUs (i.e., responsible only for frequency translation and power scaling);
- since no digital signal processing is performed at RAU, as this would vanish most of the benefits of analog fronthaul, the latency budget on the fronthaul is up to signal propagation only;
- in case of copper-based analog fronthaul, thanks to the PoE technology, the RF equipment can be powered over the same cables without the need of further power supply;

Cons

- even if latency is no longer a problem due to the absence of any ADC/DAC at the RAUs, the maximum allowed latency is still contained to 200μs due to HARQ centralization;

- the needed fronthaul bandwidth still scales with the number of antennas ports (eventually, this can be strongly relaxed by the implementation of analog beamforming at the RAU, not covered here).

Table 1.1.: RAN functional split options summary

	Functional Split Option										
Characteristic	1	2	3	4	5	6	7-3	7-2	7-1	8	9
							eCPRI			CPRI	Analog
Bandwidth Requirements	-	Relaxed (scale with MIMO layers)					Tight (scale with antenna ports)				Relaxed (no digitalization)
Data Type	-	Baseband bits					Quant. I/Q (f)			Quant. I/Q(t)	Analog RF signal
HARQ location	RAU						BBU				
Latency Requirements	Relaxed						Tight (200μs)				
Multi-cell/freq. coord.	Multiple Schedulers at RAUs						Centralized Scheduler at BBU				
Full Advanced CoMP	NO								YES		

1.2. Analog Fronthaul and Low-Layer RAN Functional Split Options: Transport Requirements

In this section, we mainly focus on low-layer functional split options, as they provide more meaningful reference schemes to be compared with analog fronthaul discussed here. In fact, even if high- and medium-layer functional split options offer relaxed bandwidth and latency constraints, they do not allow for the implementation of centralized processing techniques (i.e., CoMP, centralized scheduling, JR/JT, centralized interference coordination/mitigation, cooperative precoding/equalization etc.), thus vanishing most of the benefits of C-RAN in handling the complicated interference-limited scenarios foreseen for 5G networks.

In this section, the transport requirements of low-layer functional split options are analyzed for both current (4G) and future (5G) network settings based on [18, 19] and considering a single-user uplink system (downlink would be symmetrical). The parameters employed in the bitrate requirements computation are listed in Table 1.2, and the corresponding bandwidth requirements are shown in Table 1.4. Similarly to [20], the approach followed here for the bitrate computation is to start by the current mobile fronthaul based on the CPRI protocol (split Option 8), and then describe the difference in terms of bandwidth requirements provided by increasingly shifting parts of the BBU functionalities to the RAU. Finally, the bandwidth requirements of analog split option (Option 9) are illustrated.

Concerning the maximum latency allowed over the BBU-RAU fronthaul link, low-layer functional split options have all approximately the same strict requirements, due to the centralization of the HARQ process. The HARQ process allows for

at most 4ms, however, if we consider the delay introduced by PHY processing, scheduling, time for transmission from RAU to User Equipment (UE), etc., the time left for the transmission between BBU and RAU is $\approx 200\mu s$.

Table 1.2.: Parameters for bandwidth requirements computation

Parameter	Symbol	LTE	5G[*]
System bandwidth [*MHz*]	B_w	20	500
Reference bandwidth [*MHz*]	B_{ref}	20	200
Sampling frequency for B_{ref} [*MHz*]	f_s	30.72	245.76
# of subcarriers used in B_{ref}	N_{sc}	1200	3300
Symbol duration [μs]	T_s	66.67	16.67
Subcarrier Spacing [*kHz*]	Δ_f	15	60
Quantization/soft bits per I/Q	N_Q	16	16
RX BS antennas	N_r	8	64
MIMO layers	N_t	1	4
Spectral Efficiency [*bps/Hz*]	S	6	8
Assumed RB utilization [%]	η	50	70

1.2.1. Split Option 8 (CPRI)

The fronthaul rate required by the digital I/Q streaming based on CPRI protocol can be computed as

$$R_{\text{CPRI}} = 2 \cdot N_Q \cdot N_r \cdot f_s \cdot (B_w/B_{20}), \tag{1.1}$$

where N_Q is the bit resolution per I and Q dimensions of the radio samples, factor 2 accounts for the complex nature of the samples, N_r is the total number of BS antenna ports, f_s is the sampling rate for wireless channel bandwidth equal to $B_{20} = 20$ MHz, and B_w is the system bandwidth. In (9.16), to ease the reasoning, we omitted the controlling overhead (which in general is $N_{\text{ovh}} = 16/15$, i.e., one out of the 16 words contained in a basic frame is used for controlling purposes) and the capacity increase due to the encoding employed, which can be either $N_{8\text{B}10\text{B}} = 1.25$ or $N_{64\text{B}63} = 1.016$. According to [11], 5G NR should be able to support channel bandwidths up to $B_w = 1$ GHz and a number of BS antenna ports up to $N_r = 256$, however, it is clear that the bandwidth required by CPRI protocol to support such 5G settings is huge and unpractical. Table 1.3 presents some examples of required CPRI bitrate (Gbps) on a fronthaul transmission link for different settings and assuming $N_Q = 16$ bits in order to show how the CPRI fronthaul bandwidth requirements scale with both the number of antenna ports N_t and the channel bandwidth B_w.

Table 1.3.: Required CPRI bitrate (Gbps) for different system settings

	Frequency System Bandwidth, B_w [MHz]					
# BS antenna ports, N_r	10	20	100	200	500	1000
2	1	2	10	20	50	100
4	2	4	20	40	100	200
8	4	8	40	80	200	400
16	8	16	80	160	400	800
64	32	64	320	640	1600	3200
256	128	256	1280	2560	6400	12800

1.2.2. Split Option 7-1

Since in Split Option 7-1 the FFT is implemented at the RAU, I/Q frequency-domain data are exchanged over the fronthaul link. This allows for the removal of the Cyclic Prefix (CP) and, moreover, for the removal of guard subcarriers prior to the transmission to the BBU, thus reducing the bitrate requirements (e.g., in LTE the number of guard subcarriers is $\approx 40\%$, since 848 subcarriers out of the total 2048 are set to zero). Hence, the bandwidth requirements for split option 7-1 can be computed as

$$R_{7,1} = (B_w/B_{ref}) \cdot N_{sc} \cdot T_s^{-1} \cdot 2 \cdot N_Q \cdot N_r, \tag{1.2}$$

where N_{sc} is the number of subcarriers used in the reference bandwidth B_{ref} and T_s (i.e., corresponding to the inverse of the subcarrier spacing Δ_f) is the symbol duration.

1.2.3. Split Option 7-2

In split Option 7-2, the resource demapping is implemented locally at the RAU, thus allowing for the transmission over the fronthaul link only of those Resource Elements (REs) actually used by the user equipment. Therefore, the bitrate required by option 7-2 is computed as

$$R_{7,2} = R_{7,1} \cdot \eta, \tag{1.3}$$

where η represents the fraction of utilized REs.

1.2.4. Split Option 7-3

In split option 7-3, the RAU is in charge of implementing all the receiver processing, which includes equalization in frequency domain, iFFT, MIMO receive processing and demodulation. During equalization, the signals of multiple-antennas are combined together. Hence, the required bandwidth no longer scales with the number

of receiving Base Station (BS) antennas N_r, but with the number of MIMO layers per UE, denoted as N_t, which is usually $N_t \leq N_r$, thus resulting in a remarkable bitrate reduction w.r.t. the previously discussed functional split options. The bitrate can be thus computed as

$$R_{7,3} = R_{7,2} \cdot N_t/N_r. \tag{1.4}$$

1.2.5. Split Option 6

In split option 6, all the PHY functionalities are implemented at the RAU, including Forward Error Correction (FEC) decoding (block DEC). Therefore, in this option, it is possible to recover at the RAU the data bits from the received symbols with the consequent removal of redundant bits, thus transmitting over the fronthaul link the pure MAC payload at the decoder output. In this case, the bandwidth required is computed as

$$R_6 = N_{sc} \cdot T_s^{-1} \cdot \eta \cdot S \cdot N_t, \tag{1.5}$$

where S [bps/Hz] is the spectral efficiency which depends on the employed Modulation and Coding Scheme (MCS).

1.2.6. Split Option 9 (Analog Split)

In case of fully analog fronthaul transmission over the RAU-BBU link, it is not meaningful to describe the bandwidth requirements in terms of "bitrate", since the digitization of RF signal is shifted to the BBU. Instead, two different metrics are introduced to evaluate the analog fronthaul bandwidth constraints: *i)* the analog bandwidth occupied by the analog RF signal over the fronthaul link, computed as

$$B_9 = N_r \cdot B_w, \tag{1.6}$$

and *ii)* the corresponding equivalent air-link data-rate computed as the one for option 6, i.e,

$$R_9 = R_6. \tag{1.7}$$

Remark 1.1. It is important to notice that if hybrid beamforming (i.e., the conventional beamforming is split in two parts where an analogical beamforming performed at the RAU is then completed by a digital processing at the BBU) is applied, the analog bandwidth required over the BBU-RAU link can reduce up to $B_{hb,9} \approx B_9 \cdot N_t/N_r$.

Concluding, analog fronthauling has been compared with all the other functional split options proposed for 5G NR. In particular, it has been outlined that analog

split option stands out among the low-layer splits, since it allows for the implementation of all the most advanced CoMP techniques (e.g., JT/JR, centralized scheduling, cooperative interference mitigation/coordination, etc.), while allowing for relatively low bandwidth constraints. Furthermore, option 9 guarantees very low propagation delay from the UE to the BBU, as no time-demanding digital processing is performed at the RAU, thus making the $200\mu s$ fronthaul latency constraints due to HARQ centralization not an issue. Finally, the RAUs needed for analog split options are very simple and cheap, since they do not have to perform any complicated digital processing except for signal scaling and frequency conversion.

Beside the A-RoC architecture based on copper fronthaul links discussed here, analog fronthauling can be also based on wireless or fiber links. These two technologies correspond to two different fronthaul architectures, A-RoR and A-RoF, respectively. However, only the latter is of particular interest for the purposes of this thesis.

Table 1.4.: Bandwidth requirements for different functional split options

		Bandwidth Requirments	
Functional Split Option		**LTE**	**5G**
8 (CPRI)		8 Gpbs	1600 Gbps
7-1		4.6 Gbps	1010 Gbps
7-2		1.8 Gbps	710 Gbps
7-3		250 Mbps	45 Gbps
6		200 Mbps	4.5 Gbps
9 (Analog)	Equivalent air-link data-rate	**200 Mbps**	**4.5 Gbps**
	Analog bandwidth	• w/o hybrid-BF: **160 MHz** • w/ hybrid-BF: **20 MHz**	• w/o hybrid-BF: **32 GHz** • w/ hybrid-BF: **2 GHz**

1.3. Trading over Costs, Latency and Bandwidth: Analog Radio-over-Fiber versus Digital Radio-over-Copper

As mentioned, A-RoC architecture is especially suitable for low-latency/high-rate indoor fronthaul deployments, as it combines the economical benefits of leveraging the pre-existing copper cabling infrastructure of buildings with the latency/bandwidth advantages of analog fronthauling. The goal of this section is to detail two alternative fronthaul architectures, i.e., A-RoF and D-RoC, that trade over such economical and latency/bandwidth benefits. In particular, A-RoF architecture provides high bandwidth/low-latency analog fronthaul but implies high

infrastructural costs, whereas in contrast D-RoC, which is the digital counterpart of A-RoC, enables the exploitation of the already deployed copper cables but it suffers from bandwidth/latency limitations due to ADC/DAC operations at the RAU. The characteristics of A-RoF and D-RoC are detailed and compared with A-RoC in the next section, while a summary is in Table 1.5.

1.3.1. Analog Radio-over-Fiber (A-RoF)

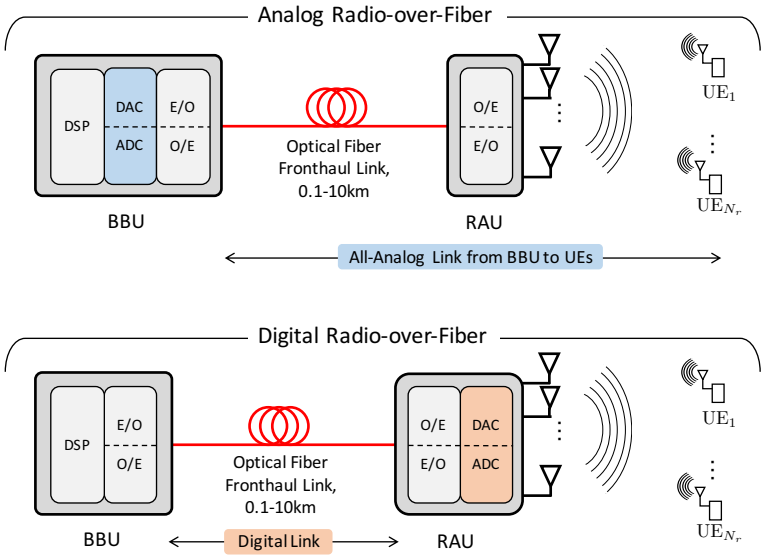

Figure 1.3.: Analog Radio-over-Fiber versus Digital Radio-over-Fiber

A-RoF refers to an analog C-RAN architecture whereby RF signals are exchanged over optical fiber fronthaul links [14, 12]. A schematic block scheme of A-RoF architecture is shown in Fig. 1.3, highlighting the differences with respect to conventional D-RoF architecture (i.e., CPRI - Split Option 8). In particular, in A-RoF, the RF signals directly modulate the laser light signal, and the resulting intensity modulated optical signal is transported over fiber links for several kms. At the other end of the fiber link, the optical signal is demodulated by direct detection. The combination of these transmit/receive strategies, known as Intensity-Modulation with Direct Detection (IM-DD), represents the most common technique of RF signals relaying over fiber due to its low-complexity and costs. Eventually, RF signals can be down-converted to lower IF bands prior to signal relaying over fiber, leading to the so-called IF-over-Fiber (IFoF) architecture. Even if RAUs need to be equipped with up- and down-converters, IFoF allows for a

relatively low-complexity hardware implementation as only low-speed optics and electronics are necessary. This is in contrast with RF-over-Fiber (RFoF), in which wireless signals are optical relayed between RAU and BBU at high frequency, thus requiring expensive high-frequency components at the RAU.

A-RoF has the inherent advantage of allowing for the transmission over several tens of kms with very small, if not negligible, performance degradation. In fact, conventional Single Mode Fibers (SMFs) commercially available suffers from signal attenuation ranging from 0.2 dB/km to 0.5 dB/km depending on the wavelength, which means that is potentially possible to relay RF signals over more than 10 km distance experiencing less than 5 dB signal degradation. On the contrary, the attenuation over copper cables rapidly increases with both frequency and cable length. Copper cable characteristics are further explored in Chapter 6, however, just to make a practical example, consider that the attenuation of a 200m Category-5 LAN cable at 200 MHz is around 50 dB.

Another advantage of fiber optics technology is the enormous bandwidth availability, which, in principle, amounts to more than 50 THz by combining the three main optical windows, i.e., 850 nm, 1310 nm and 1550 nm. In practice, the optical bandwidth that can be exploited by today's optical systems is less than 2 THz, due to the bandwidth limitation of electronic systems. Nevertheless, this is more than enough for fronthaul applications, especially if compared with copper cables, whose bandwidth available for practical applications is up to 1 GHz/per-twisted pair, 4GHz overall if the four twisted-pairs bonded together into the cable are considered.

Furthermore, fiber optic is exempt from any sort of Electro-Magnetic Interference (EMI). Beside the immediate advantage of providing interference-free signal propagation, immunity to EMI directly translates into immunity to eavesdropping, thus making fiber optic a very robust solution from both security and privacy perspectives.

The other side of the coin is that, in most of practical cases, A-RoF requires the deployment and the installation of brand-new, pervasive and costly optical networks, in addition to the fact that the RF equipment hosted at the RAU need to be externally powered. These are the main drawback that makes fiber optic non appropriate for indoor scenarios, thus pushing into the direction of more cost-efficient solutions such as RoC-based architectures.

1.3.2. Digital Radio-over-Copper (D-RoC)

A possible solution addressing the cost issues related to the deployment of RoF-based fronthaul architectures is to reuse the pre-existing copper cable infrastructure of buildings for the last 100-200m. This is the main principle lying behind conventional technologies currently employed to provide fully digital broadband Internet access, such as Digital Subscriber Line (DSL) [21].

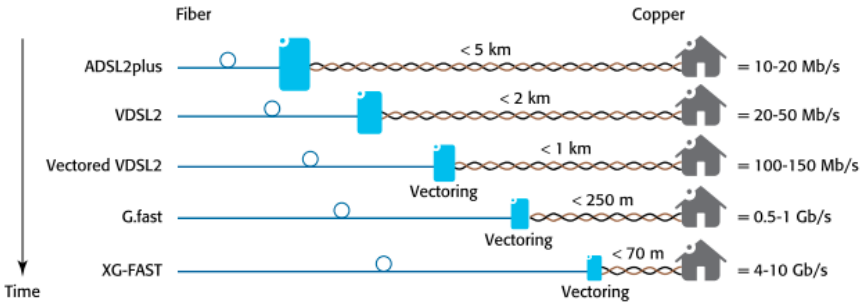

Figure 1.4.: Evolution of the copper-based access network: shorter cables for higher data-rate. Source: Bell Labs Technical Journal [22]

DSL is the main broadband access technology due to its capability to provide very high data-rate connectivity to thousands of users, denoted in DSL jargon as Costumer Promises Equipments (CPEs), by reusing the already existing copper plants. Leveraging these attractive features, DSL technology has been undergoing a rapid evolution over the last two decades. As shown in Fig. 1.4, with the advent of fiber-optics, it has been possible to move the DSL Central Office (CO) closer and closer to the end-users, thus keep shortening copper cable length and, consequently, extending copper cables bandwidth up to several hundreds of MHz [22]. This has been the main driving factor that made it possible to improve DSL data-rate from the initial 56 kb/s, achieved over 3 KHz bandwidth, to today's 1 Gb/s, achieved by the latest DSL standards, namely G.fast, over 106 MHz (to be later extended to 212 MHz) [23]. A 5th generation DSL system, known as XG.fast, has been recently proposed in order to further extend copper cable bandwidth up to 350-500 MHz over 30-70m copper loop length, and able to break the 10 Gbits/s data-rate barrier over a single twisted-pair [24].

One critical aspect in DSL technology, especially for standards employing high cable frequency such as (X)G.fast, is the crosstalk interference among the twisted-pairs that are bonded together into the same cable. In fact, at G.fast bands, crosstalk interference arising at the opposite ends of the cable binder, denoted as Far-End-CrossTalk (FEXT), is the major cause of performance degradation, and mandatorily needs to be specifically taken care of. Over the last 10 years, DSL evolution has been always complemented by more and more powerful, and also complex, FEXT cancellation techniques (or vectoring) [25, 26, 27, 28, 29]. From the simplest form of FEXT cancellation adopted in VDSL2, namely Diagonal Precoding (DP), vectoring has evolved towards non-linear interference mitigation techniques based on successive interference cancellation, such as Tomlinson-Harashima Precoding (THP), thus raising the problem of designing vectoring techniques able to cope with a large number of twisted-pairs mutually coupled by high FEXT, but at the same time with limited complexity, and also latency, of signal processing

algorithms.

In this regards, FEXT cancellation techniques for G.fast are investigated in depth in Part I of this thesis. The conclusion is that, once advanced vectoring solutions have been properly designed, G.fast offers a potential attractive solution for reusing the pre-existing copper cables plants for fronthaul applications. However, the digital nature of DSL technology poses the problem of requiring very high data-rate over the fronthaul link in order to transport the digitized RF signals between RAUs and BBUs, thus requiring some RAN architectural change, such as one of the possible RAN functional split options previously described. Once again, an extreme, but very practical, solution in this sense would be to adopt a fully analog fronthaul based on RoC whereby even the ADC/DAC are shifted to the BBU side, and analog RF signals are directly relayed over the copper cables. Nevertheless, as we will see in Chapter 8, even in the case of analog relaying over copper cables, FEXT among pairs turns out to be still the most limiting factor, so that all the technical knowledge and tools acquired, investigated and developed for digital wireline communications systems (see Part I of this thesis) can be suitably tailored to cope with the impairments of the analog fronthauling in A-RoC architecture.

	Analog Radio-over-Fiber (A-RoF)	Digital Radio-over-Copper (D-RoC)	Analog Radio-over-Copper (A-RoC)
Bandwidth requirements	Relaxed (no bandwidth expansion)	Very Strict	Relaxed (no bandwidth expansion)
Latency over fronthaul	Very low (signal propagation only)	Strict	Very low (signal propagation only)
Bandwidth availability	Very high	up to 4GHz/LAN cable	up to 4GHz/LAN cable
Fronthaul range	Outdoor scenarios, long distances, 1-10km	Indoor deployments, short distances, last 50-200m	Indoor deployments, short distances, last 50-200m
Deployment costs	Very high	Very low (already deployed LAN cabling)	Very low (already deployed LAN cabling)
Components complexity	Low-speed electronics & optics	High-speed electronics	Low-speed electronics
Linearity of components	Mandatory (optical components)	Mandatory (electronic components)	Mandatory (electronic components)
Synchronization	Carrier frequency & symbols	Packet Level	Carrier frequency & symbols
RAU power supply	Extra power supply needed	RAU powered over the same cables (PoE)	RAU powered over the same cables (PoE)

Table 1.5.: Characteristics of Analog Radio-over-Fiber (A-RoF), Digital Radio-over-Copper (D-RoC) and Analog Radio-over-Copper (A-RoC)

1.4. Towards Analog *MIMO* Radio-over-Copper: The Mutual Interaction between Wireless and Wired Channels

Two attractive fronthaul technologies have been introduced in the previous sections. From the one hand, A-RoF provides very low-latency and high-bandwidth fully analog fronthaul link, but it implies very high infrastructural cost due to the

deployment of fiber optics. From the other hand, D-RoC is quite cost-effective as it reuses the pre-existing copper cables, but it presents some serious bandwidth limitation which complicate the transport of digitized RF signals. In this context, A-RoC appears to be a perfect fit for indoor fronthaul applications, as it merges the benefits of both architectures. A-RoC is still based on copper cables, with the resulting economical benefits, and, at the same time, its analog nature allows for very low-latency, bandwidth-efficient communication over the fronthaul, while providing full synchronization between multiple RAUs that can thus cooperate for joint MIMO processing. Moreover, as mentioned, the RF equipment hosted at the RAU do not need external power supply, as they can be powered over the same copper cables by the PoE technology, with several cost and power benefits.

1.4.1. From Analog-RoC to Analog-*MIMO*-RoC

The concept of A-RoC makes its first appearance in Gambini *et al.* [30], where twisted-pairs copper cables were proposed for femto-cell systems to exchange analog RF signals between a remote location hosting all the PHY/MAC functionalities (i.e., BBU) and an in-home device performing only the analog relay of signals (i.e., RAU).

Afterwards, A-RoC gained lots of attention becoming the basis of indoor commercial solutions which exploit the LAN cables already deployed in buildings and allows to extend the indoor coverage over distances longer than 100m [31]. By utilizing all the 4 twisted-pairs bounded together into the cable at low-frequency (characterized by low attention and crosstalk interference), one can serve up to 4 antennas (e.g., 4x4 MIMO) per LAN cable.

Still based on the A-RoC concept, Huang *et al.* [32] proposed an LTE-over-copper architecture based on the colocation of RAU and DSL equipment in the same street cabinets. Authors proved that by employing a single-twisted pair in the 21-24 MHz cable frequency band, which is not used by any DSL service, it is feasible to transport a 3GPP compliant LTE radio signal up to 350m away from the cabinet. Crosstalk mitigation in LTE-over-copper systems is covered in Medeiros *et al.* [33], which shows the precoding gain provided for the case of 6 twisted-pairs interfering each other, still utilizing frequency bands in the 21-24 MHz range.

All the aforementioned works contributed to prove the feasibility of A-RoC as an alternative/complementary technology for the FH. However, none of them attempt to push the usage of cable frequency beyond the first few tens of MHz, thus not making an efficient usage of the bandwidth capabilities of copper cables, which is one of the main point of this thesis.

Inspired by the A-RoC concept, the first stepping-stone for this thesis has been to demonstrate the huge transport capabilities offered by copper cables, whose frequency bandwidth can be exploited for analog applications up to more than 500 MHz per twisted-pairs, thus providing approx. 2 GHz bandwidth overall if

4-pairs LAN cables are considered. It turns out that in order to fully exploit such bandwidth potential for fronthaul applications, it is necessary to define a more flexible mapping between the wireless resources, i.e., the RF signals corresponding to different Radio Access Technologies (RATs) received at the RAU antennas, and the cable resources, i.e., defined by the twisted-pairs bonded together into the cable binder and having up to 500 MHz bandwidth/each. In other words, as shown in Fig. 1.5, the overall fronthaul architecture can be seen as the cascade over two MIMO channels: *i)* the wireless MIMO channel, describing the communications among multiple end-users and the multiple-antenna RAUs, and *ii)* the wired MIMO channel, which in turn represents the fronthaul link between RAUs and BBU. This novel hybrid wireless-wired fronthaul architecture, which has been denoted as Analog MIMO Radio-over-Copper (A-MIMO-RoC) emphasizing the multiple-antenna nature of both channels, is the focus of this thesis.

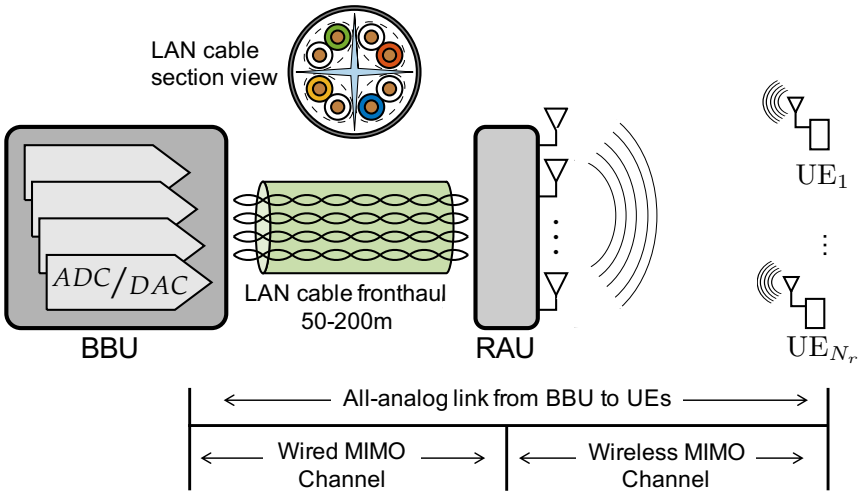

Figure 1.5.: Analog MIMO Radio-over-Copper architecture: MIMO wired channel over MIMO wireless channel

1.4.2. Designing Analog-MIMO-RoC: Explored Research Directions

A-MIMO-RoC is proposed in this thesis, and deeply investigated under different perspectives and scenarios.

At first, a feasibility study has been performed in order to confirm the viability of employing already deployed copper cable (i.e., LAN cables) for fronthaul applications.

Once proofed the A-MIMO-RoC concept, the focus shifted to the optimal design of A-MIMO-RoC architecture. As mentioned, in order to get the most out of the transport capabilities of LAN cables, a novel resource allocation strategy needs to be designed between the signals transmitted over the MIMO wireless channels and those relayed over the MIMO cable channels. In particular, in order to maximize the system performance, the RF signals at the RAU antennas, possibly corresponding to multi-RAT, need to be transmitted to/from the BBU over opportunely selected twisted-pair/frequency cable resource blocks which are minimally impaired by the analog cable fronthaul. It is proved in the thesis that this mapping operation, denoted as Space-Frequency to Space-Frequency (SF2SF) multiplexing recalling the two multiplexing dimensions in both wired and wireless channels, has a strong impact on the performance of the system. In this direction, SF2SF multiplexing techniques have been designed for both uplink and downlink channels of A-MIMO-RoC architecture, and considering both single- and multi-user settings. For the latter case, SF2SF has been jointly designed with multi-user interference mitigation techniques, which have been inspired by vectoring techniques originally proposed for DSL systems.

A further step in the thesis has been to extend the proposed A-MIMO-RoC to heterogeneous 5G architectures, in which different services with different requirements in terms of data-rate, latency, and reliability coexist in the same physical resources.

Finally, in order to validate the overall theoretical discussion and the numerical evaluations, a first A-MIMO-RoC prototype has been developed in order to prove experimentally, and for the first time, the possibility to carry multiple multi-RAT radio signals over a single LAN cable, even at high cable frequency, and thus FEXT impaired, with negligible performance degradation.

One of the main issues faced all along the above research path lies the fact that A-MIMO-RoC performance are primarily determined by the mutual interaction between the wireless and the wired MIMO channels, each of which with different characteristics and constraints. Hence, the overall optimization and, more in details, the design of effective interference mitigation techniques for the A-MIMO-RoC architecture, require a joint optimization over these two channels, whose physical properties need to be fully understood. In this regards, a first preliminary as well as fundamental step for this thesis has been to investigate and design interference mitigation techniques for each of the two channel, separately. Once acquired a full understanding of both MIMO wireless and MIMO wired channels, their joint behavior has been investigated, thus leading to the so-called hybrid wireless-wired system which is at the foundations of A-MIMO-RoC.

1.5. Thesis Outline and Contribution

The thesis is organized in three main parts, which reflect the three different stages of the evolution of my research work, namely the investigation of interference mitigation techniques for wired communication systems (Part I), for wireless communication systems (Part II) and, finally, for hybrid wired-wireless communication systems such as the A-MIMO-RoC architecture (Part III). Each part is structured in chapters, each of which focuses on a particular aspect of the same problem. The organization of the chapters is similar for all of them. In particular, each chapter includes: *i)* a brief introduction illustrating the motivations for the work and contextualizing that specific chapter into the overall thesis, *ii)* a section outlining the chapter novel contributions, *iii)* a section indicating the published paper (or papers) containing part of the material covered in the chapter, and *iv)* concluding remarks summarizing the achievements of the chapter. The overall thesis structure has been thought in order to enable the reader, that may be interested just in some specific aspect of the thesis, to read even a single chapter, while being still able to get the main ideas and concepts, rather than having to go through the whole thesis.

In the following, outline and novel contributions of the thesis are described chapter-by-chapter, together with the related publications.

Part I - Interference Mitigation Techniques for Wired Communication Systems

This first part of the thesis focuses on the design and investigation of both linear and non-linear interference cancellation techniques for wired communication systems *alone*. In particular, the goal is to design FEXT cancellation techniques for next generation DSL standard, i.e., G.fast, aimed at achieving a satisfactory degree of interference cancellation capability while limiting both latency and complexity of signal processing algorithms.

- **Chapter 2:** ***Non-Linear Precoding Techniques for G.fast Downstream:*** This chapter proposes two non-linear FEXT cancellation techniques for the G.fast downstream, namely Tomlinson-Harashima Precoding with Dynamic Ordering (THP-DO) and Lattice-Reduction Aided Zero-Forcing Precoding with Optimal Power Allocation (LR-ZF-OPA). THP-DO is a modified version of conventional THP whereby the order in which interference is successively cancelled user by user is optimized following a user fairness criterion. THP-DO is proved to provide higher minimum user rate with respect to conventional linear and non-linear DSL precoding techniques. However, it has the disadvantage inherent to any THP-based technique to introduce additional signal processing delay and complexity due to the sequential non-linear interference cancellation procedure. In contrast, LR-ZF-OPA, which is a non-linear vectoring technique based on LR concept, allows

for the parallel implementation of the non-linear operations over all the lines, hence limiting both latency and complexity. However, this comes at the price of a lower minimum user rate with respect to THP-DO.

Part of the material presented in this chapter has been published in:

- M. Hekrdla, **A. Matera**, W. Wang, D. Wei, and U. Spagnolini, "Ordered Tomlinson-Harashima Precoding in G.fast Downstream" in *IEEE Global Telecommunications Conference (GLOBECOM)*, 2015, San Diego;
- M. Hekrdla, **A. Matera**, U. Spagnolini, and W. Wang, "Per-Line Power Controlled Lattice-Reduction Aided Zero-Forcing Precoding for G.fast Downstream" in *IEEE Global Telecommunications Conference (GLOBECOM)*, 2016, Washington D.C..

- **Chapter 3:** ***Parallelazing Tomlinson-Harashima Precoding in G.fast Downstream:*** Along the lines of Chapter 2, this chapter proposes a novel distributed vectoring architecture for G.fast in which latency and complexity caused by sequential non-linear interference cancellation in conventional THP are reduced by parallelizing THP over several vectored groups. In particular, linear precoding is used to mitigate interference arising among different vectored groups, while FEXT among lines belonging to the same vectored group is cancelled by conventional THP, which is implemented in parallel at the Vector Processor (VP) of each vectored group. This hybrid linear/non-linear parallel THP architecture, referred to as multi-VP THP, is shown to attain the performance of fully non-linear centralized THP while reducing latency and complexity of signal processing algorithms.

  Part of the material presented in this chapter has been published in:

  - S. H. R. Naqvi, **A. Matera**, E. Wang, A. H. Fazlollahi, and U. Spagnolini, "Multi-Vector Tomlinson-Harashima Precoding in G.fast Downstream System", in *IEEE International Conference on Communication Systems (ICCS)*, 2016, Shenzhen.

Part II - Interference Mitigation Techniques for Wireless Communication Systems

This second part of the thesis covers the investigation and design of interference mitigation techniques for wireless communication systems *alone*. More in details, two particular communication scenarios are investigated, i.e., multi-operator cellular systems and optical wireless communications.

- **Chapter 4:** ***Cooperative Precoding in Multi-Operator Wireless Systems:*** This chapter proposes a novel multi-operator interference cancellation strategy in which multiple operators cooperate in order to combat the resulting mutual inter-operator interference. Key characteristics of the proposed

cooperative mechanism is that operators are not required to exchange any sensitive users' data. In turn, they only exchange each others' interference. The first part of the chapter shows the capability of the proposed strategy not only to successfully mitigate inter-operator interference, but even to turn interference into benefit, thus increasing the overall system performance. To complement the discussion about multi-operator cellular systems, by leveraging tools from information theoretic security, the second part of the chapter formally proves that the proposed cooperative multi-operator scheme based on interference sharing actually provides privacy guarantees for all the operators.

Part of the material presented in this chapter has been published in:

- M. Hekrdla, **A. Matera**, S. H. R. Naqvi, and U. Spagnolini, "Interference-Sharing Multi-Operator Cooperation for Downlink Precoding in Cloud-RAN Architecture" in *IEEE International Conference on Communications (ICC), Workshop on Next Generation Backhaul/Fronthaul Networks (BackNets'2016)*, 2016, Kuala Lumpur;

- **A. Matera**, P.-H. Lin, E. A. Jorswieck, and U. Spagnolini, "Secure 2-user Gaussian Interference Channel with Limited Information Exchange at the Transmitters" in *IEEE Global Telecommunications Conference (GLOBECOM), Workshop on Trusted Communications with Physical Layer Security (TCLPS 2016)*, 2016, Washington D.C..

- **Chapter 5:** ***Non-Linear Precoding for Visible Light Communications In-Flight Systems:*** Motivated by the promising results obtained for wired communication systems, this chapter proposes THP for in-flight Visible Light Communications (VLC) systems in order to face the Multi Light Interference (MLI) arising from the numerous and closely spaced transmitting light sources. For the in-flight VLC scenario considered in this chapter, THP is proved to outperform conventional linear precoding methods, providing a fair performance distribution among all the airplane passengers. Furthermore, THP is shown to guarantee high-rate connectivity even in the challenging scenario of transmitter-receiver misalignment, e.g., caused by a passenger moving its terminal from hand to hand.

  Part of the material presented in this chapter has been published in:

  - D. Tagliaferri, **A. Matera**, C. Capsoni, and U. Spagnolini, "Nonlinear Visible Light Communications Broadcast Channel Precoding: A New Solution for In-flight Systems", 2018, in *IEEE Photonics Journal*, 10(4), 1-14.

Part III - Interference Mitigation Techniques for Hybrid Wired-Wireless Communications Systems: *The Analog MIMO Radio-over-Copper Architecture*

This third and last part of the thesis represents the core of the overall research work. By merging the knowledge acquired by the investigation of wireless and wired channels separately (i.e., Part I, II), here the focus is on interference mitigation techniques for hybrid wired-wireless communication systems. In particular, the Analog MIMO RoC architecture is proposed and deeply investigated from different perspectives and settings.

- **Chapter 6:** ***The Genesis of Analog MIMO Radio-over-Copper: Do LAN Cables Provide Enough Bandwidth for Fronthaul Applications?*** This chapter, which has been the starting point for the overall research work, represents the proof of concept for the proposed Analog MIMO RoC architecture. In particular, the chapter collets several results aimed at demonstrating the potentially huge transport capabilities offered by the pre-existing LAN cabling infrastructure of buildings and enterprises. Numerical simulations show that a single Cat-5 LAN cable 100 m long, which is the reference distance for indoor deployments, is capable to serve up to 60 RAU antennas each carrying a 20-MHz LTE signal. A-MIMO-RoC is thus confirmed to be a very attractive and bandwidth-efficient analog fronthaul solution to handle multiple-antenna RAUs for providing enhanced in-building wireless coverage.

  Part of the material presented in this chapter has been published in:

  – S. H. R. Naqvi, **A. Matera**, L. Combi, and U. Spagnolini, "On the Transport Capability of LAN Cables in All-Analog MIMO-RoC Fronthaul", in *IEEE Wireless Communications and Networking Conference (WCNC)*, 2017, San Francisco.

- **Chapter 7:** ***Analog MIMO RoC Uplink with Space-Frequency to Space-Frequency Multiplexing:*** Focusing on the A-MIMO-RoC uplink channel, this chapter investigates a novel and flexible resource allocation strategy between the radio signals at each RAU antennas, received from the users over the wireless channel, and the twisted-pair/frequency resources over the cable fronthaul link. This wireless-wired resource mapping, referred to as SF2SF multiplexing, is shown in the chapter to have a strong impact on the A-MIMO-RoC performance. In fact, SF2SF multiplexing, if properly designed, allows to fully exploit the LAN cable bandwidth capabilities for fronthaul applications. The analysis in this chapter is limited to a single-user scenario.

  Part of the material presented in this chapter has been published in:

  – **A. Matera**, L. Combi, S. H. R. Naqvi, and U. Spagnolini, "Space-

Frequency to Space-Frequency for MIMO Radio over Copper", in *IEEE International Conference on Communications (ICC)*, 2017, Paris;

- **A. Matera** and U. Spagnolini, "On the Optimal Space-Frequency to Frequency Mapping in Indoor Single-Pair RoC Fronthaul", in *European Conference on Networks and Communications (EuCNC)*, 2017, Oulu, Finland.

- **Chapter 8:** ***Analog MIMO RoC Downlink with Space-Frequency to Space-Frequency Multiplexing:*** In this chapter, the problem of optimally designing SF2SF multiplexing is tackled for the A-MIMO-RoC downlink channel in both single-user and multi-user settings. Differently from the uplink, the downlink SF2SF problem is complicated by the different power constraints that need to be fulfilled both at the cable input and at the RAU antennas. As a first step, the chapter confirms the potential of SF2SF also for the single-user downlink A-MIMO-RoC channel. Furthermore, in multi-user settings, it is shown that the joint optimization of SF2SF multiplexing (performed at the RAU) with digital precoding of the overall wired-plus-wireless channels (performed at the BBU) is able to cope with both multi-user interference and analog fronthaul impairments, thus providing substantial performance gains in terms of minimum rate guaranteed for all the users.

  Part of the material presented in this chapter has been published in:

  - **A. Matera** and U. Spagnolini, "Analog MIMO-RoC Downlink with SF2SF", 2018, in *IEEE Wireless Communications Letters*, pp. 1-1, 2018;

  - **A. Matera** and U. Spagnolini, "Analog MIMO Radio-over-Copper Downlink with Space-Frequency to Space-Frequency Multiplexing for Multi-User 5G Indoor Deployments", submitted to *IEEE Transactions on Wireless Communications.*

- **Chapter 9:** ***Analog MIMO RoC in Heterogeneous 5G Network:*** In this chapter, A-MIMO-RoC architecture is extended to 5G heterogeneous networks, in which multiple services with different requirements in terms of data-rate, latency and reliability share the same physical resources. In particular, the chapter investigates the coexistence between Ultra Reliable Low Latency Communications (URLLC) and enhanced Mobile BroadBand (eMBB) services in the uplink of the proposed A-MIMO-RoC architecture. Both Orthogonal and Non-Orthogonal Multiple Access techniques (OMA and NOMA, respectively) are compared. For the latter, three different decoding strategies have been investigated, namely puncturing, treating interference as noise, and successive interference cancellation. By leveraging information theoretical tools, the chapter provides useful insights into the performance trade-offs between eMBB and URLLC traffic types in the A-MIMO-RoC architecture.

Part of the material presented in this chapter has been published in:

  - **A. Matera**, R. Kassab, O. Simeone and U. Spagnolini, "Non-Orthogonal eMBB-URLLC Radio Access for Cloud Radio Access Networks with Analog Fronthauling", 2018, in *Entropy*, 20, 661.

- **Chapter 10: *A First Experimental Demonstration of Analog MIMO RoC:*** This last chapter, which represents the final point of the thesis, collects experimental results aimed at validating the previous theoretical discussion and numerical results. In particular, a first A-MIMO-RoC prototype has been developed in order to prove experimentally, and for the first time, the capability of A-MIMO-RoC to carry multiple RF signals over a single LAN cable up to 400 MHz cable bandwidth. The experiment shows that this is possible even when these signals are carried over different twisted-pairs but at the same frequency, and thus interfering with each other due to FEXT. Furthermore, the prototype also demonstrates the possibility to simultaneously relay both MIMO LTE signal and MIMO WiFi singles over a single LAN cable with negligible performance degradation, thus going in the direction of full heterogeneity promised by 5G networks.

  Part of the material presented in this chapter has been published in:

  - **A. Matera**, V. Rampa, M. Donati, A. Colamonico, A. F. Cattoni and U. Spagnolini "A First Experimental Evaluation of Analog MIMO Radio-over-Copper", submitted to *IEEE Wireless Communications Letters;*
  - **A. Matera**, V. Rampa, M. Donati, A. Colamonico, A.F. Cattoni and U. Spagnolini, "Dual-RoC: Dual Radio-over-Copper Remotization for C-RAN Architecture in 5G Deployments" presented at *15th International Symposium on Wireless Communication Systems (ISWCS), Workshop on End-to-end Performance Evaluation of Services, Applications and Devices in 5G Networks*, 2018, Lisbon.

1.6. Complete List of Publications

Complete list of publications, including papers that are not covered in the thesis and patents.

Conference Publications

- G. Soatti, M. Nicoli, **A. Matera**, S. Schiaroli, and U. Spagnolini, "Weighted consensus algorithms for distributed localization in cooperative wireless networks" in *11th International Symposium on Wireless Communications Systems (ISWCS)*, 2014, pp. 116–120, Barcelona (Spain);

- M. Hekrdla, **A. Matera**, W. Wang, D. Wei, and U. Spagnolini, "Ordered Tomlinson-Harashima Precoding in G.fast Downstream" in *IEEE Global Telecommunications Conference (GLOBECOM)*, 2015, San Diego;
- M. Hekrdla, **A. Matera**, S. H. R. Naqvi, and U. Spagnolini, "Interference-Sharing Multi-Operator Cooperation for Downlink Precoding in Cloud-RAN Architecture" in *IEEE International Conference on Communications (ICC), Workshop on Next Generation Backhaul/Fronthaul Networks (BackNets'2016)*, 2016, Kuala Lumpur;
- M. Hekrdla, **A. Matera**, U. Spagnolini, and W. Wang, "Per-Line Power Controlled Lattice-Reduction Aided Zero-Forcing Precoding for G.fast Downstream" in *IEEE Global Telecommunications Conference (GLOBECOM)*, 2016, Washington D.C.;
- **A. Matera**, P.-H. Lin, E. A. Jorswieck, and U. Spagnolini, "Secure 2-user Gaussian Interference Channel with Limited Information Exchange at the Transmitters" in *IEEE Global Telecommunications Conference (GLOBECOM), Workshop on Trusted Communications with Physical Layer Security (TCLPS 2016)*, 2016, Washington D.C.;
- S. H. R. Naqvi, **A. Matera**, E. Wang, A. H. Fazlollahi, and U. Spagnolini, "Multi-Vector Tomlinson-Harashima Precoding in G.fast Downstream System", in *IEEE International Conference on Communication Systems (ICCS)*, 2016, Shenzhen;
- S. H. R. Naqvi, **A. Matera**, L. Combi, and U. Spagnolini, "On the Transport Capability of LAN Cables in All-Analog MIMO-RoC Fronthaul", in *IEEE Wireless Communications and Networking Conference (WCNC)*, 2017, San Francisco;
- L. Combi, **A. Matera**, A. Gatto, P. Parolari, P. Boffi, and U. Spagnolini, "Radio-over-Modes for C-RAN Architecture with Smart Optical Resources Assignment", in *IEEE International Conference on Communications (ICC)*, 2017, Paris;
- **A. Matera**, L. Combi, S. H. R. Naqvi, and U. Spagnolini, "Space-Frequency to Space-Frequency for MIMO Radio over Copper", in *IEEE International Conference on Communications (ICC)*, 2017, Paris;
- **A. Matera** and U. Spagnolini, "On the Optimal Space-Frequency to Frequency Mapping in Indoor Single-Pair RoC Fronthaul", in *European Conference on Networks and Communications (EuCNC)*, 2017, Oulu, Finland;
- **A. Matera**, V. Rampa, M. Donati, A. Colamonico, A.F. Cattoni and U. Spagnolini, "Dual-RoC: Dual Radio-over-Copper Remotization for C-RAN Architecture in 5G Deployments" presented at *15th International Symposium on Wireless Communication Systems (ISWCS), Workshop on End-to-end Performance Evaluation of Services, Applications and Devices in 5G Networks*, 2018, Lisbon.

Journal Publications

- **A. Matera** and U. Spagnolini, "Analog MIMO-RoC Downlink with SF2SF", 2018, in *IEEE Wireless Communications Letters*, pp. 1-1, 2018;
- D. Tagliaferri, **A. Matera**, C. Capsoni, and U. Spagnolini, "Nonlinear Visible Light Communications Broadcast Channel Precoding: A New Solution for In-flight Systems", 2018, in *IEEE Photonics Journal*, 10(4), 1-14.;
- **A. Matera**, R. Kassab, O. Simeone and U. Spagnolini, "Non-Orthogonal eMBB-URLLC Radio Access for Cloud Radio Access Networks with Analog Fronthauling", 2018, in *Entropy*, 20, 661;
- **A. Matera**, V. Rampa, M. Donati, A. Colamonico, A. F. Cattoni and U. Spagnolini "A First Experimental Evaluation of Analog MIMO Radio-over-Copper", submitted to *IEEE Wireless Communications Letters;*
- **A. Matera** and U. Spagnolini, "Analog MIMO Radio-over-Copper Downlink with Space-Frequency to Space-Frequency Multiplexing for Multi-User 5G Indoor Deployments", submitted to *IEEE Transactions on Wireless Communications;*
- **A. Matera**, V. Rampa, M. Donati, A. Colamonico, A. F. Cattoni and U. Spagnolini, "Analog MIMO Radio-over-Copper for Enhanced Indoor Coverage: Concepts and Validations" submitted to *IEEE Communications Magazine.*

Patents

- S. H. R. Naqvi, **A. Matera**, U. Spagnolini, E. Wang, and A. H. Fazlollahi, "DSLAM APPARATUS, CODING METHOD AND COMPUTER PROGRAM", published on January 4th, 2016;
- D. Wei, U. Spagnolini, M. Hekrdla and **A. Matera**, "CHANNEL ORDERING FOR MULTI-CARRIER MULTI-CHANNEL COMMUNICATION SYSTEMS", published on October 1st, 2017;
- P. Boffi, L. Combi, A. Gatto, **A. Matera**, P. Parolari and U. Spagnolini, "METHOD AND SYSTEM FOR TRANSPORTING MULTIPLE SIGNALS OVER OPTICAL MODES", published, 2017.

1.7. Notation

This section defines the notation adopted in the overall thesis. Please consider that, while the mathematical notation is the same, the meaning of a specific variable may change chapter by chapter.

- Bold upper- and lower-case letters describe matrices and column vectors.
- The ij-th element of matrix $\mathbf{A}$ is denoted as $[\mathbf{A}]_{ij} = a_{ij}$.
- Letters $\mathbb{Z}, \mathbb{Z}_{\mathrm{j}}, \mathbb{R}, \mathbb{R}_{\geq 0}, \mathbb{C}$ refer to integers, complex integers, real, non-negative real and complex numbers, respectively.
- Real and imaginary part of numbers are represented by $\Re(\star)$ and $\Im(\star)$, while $\lfloor \star \rfloor$ is floor operator.
- Transpose, conjugate transpose, trace and matrix inversion are denoted by $(\star)^T, (\star)^H, \mathrm{tr}(\star), (\star)^{-1}$.
- Symbol $\triangleq$ denotes equality from definition.
- Operator $\mathrm{diag}(\star)$ produces a diagonal matrix with input vector components on the main diagonal, if the input is a vector. In case of matrix input, the main diagonal of the input matrix forms the output diagonal matrix. In case the input is a sequence of matrices, i.e., $\mathrm{diag}(\mathbf{A}_1, \ldots, \mathbf{A}_N)$, it denotes a block-diagonal matrix with matrices $\mathbf{A}_1, \ldots, \mathbf{A}_N$ on the main diagonal.
- Matrix $\mathbf{I}_n$ is an identity matrix of size n and $\mathbf{1}_n$ is a column vector made by n "1s". Pedix n may be omitted, when no confusion arises.
- $E[\star]$ is a statistical average.
- Symbol $\otimes$ denotes the Kronecker operator and $\mathrm{vec}(\cdot)$ is the vectorization operator.
- Notations $\|\mathbf{x}\|_1 = \sum_i |x_i|$ and $\|\mathbf{x}\|_2 = \sqrt{\sum_i |x_i|^2}$ denote the l_1- and l_2- norms of vector $\mathbf{x}$, respectively.
- The Q-function $\mathcal{Q}(\cdot)$ is the complementary cumulative distribution function of the standardized normal random variable, and $\mathcal{Q}^{-1}(\cdot)$ is its inverse.

Part I.

Interference Mitigation Techniques for Wired Communications Systems

2. Non-Linear Precoding Techniques for Next Generation Digital Subscriber Lines (G.fast) Downstream

2.1. Introduction

DIGITAL Subscriber Line (DSL) is the dominant broadband access technology due to its ability to fulfill the demands for reliable high-data-rate connectivity in a cost-effective way by exploiting the existing infrastructure of twisted-pair copper lines. The main limiting factor of DSL technology is the undesired electromagnetic coupling among the twisted-pairs that are bonded together into the same cable binder. This electromagnetic coupling causes crosstalk among pairs, which severely impairs the communication, and needs to be properly handled.

Near-End-Crosstalk (NEXT) is the interference arising across the lines at the same end of the cable binder when UpStream (US) and DownStream (DS) transmissions coexist in the same frequency band at the same time, and it is usually avoided using duplexing techniques such as Frequency Division Duplexing (FDD) or Time Division Duplexing (TDD). On the contrary, Far-End-Crosstalk (FEXT), i.e., the cross-coupling among the lines at opposite ends of the cable binder (see Fig. 2.1), cannot be simply avoided using duplexing. In turn, FEXT needs to be mitigated by spectrum management or multi-user processing techniques carefully designed, which are the focus of this chapter.

FEXT interference mitigation becomes particularly critical for higher cable frequencies, such as those employed by the latest DSL standard, namely G.fast [34], which has been recently approved by the International Telecommunication Union (ITU) [35, 26]. In fact, aiming at fiber-like connection (up to 1 Gbps), G.fast proceeds in the trend of shortening copper lines (up to 250 m) between Central Office (CO) and Consumer Premised Equipments (CPEs). Short lines enable the usage of wider bandwidth (initially up to 106 MHz, later extended to 212 MHz) than the one used by the foregoing Very-high-bit-rate DSL (VDSL2) standard operating up to 30 MHz. However, as a consequence of the higher cable frequencies or, equivalently, the shortest wavelength, the electromagnetic coupling among pairs increases, and thus FEXT.

In DS direction, which is covered in this chapter, FEXT is typically taken care of by suitable transmitter precoding or, if signal coordination is restricted (e.g. multiple non-cooperating providers sharing the same cable bundle), by spectrum coordination techniques, i.e., dynamic spectrum management [36]. The easiest DS FEXT mitigation technique is Diagonal Precoding (DP), which is the linear FEXT cancellation precoding adopted in VDSL2. DP performs at the information theoretical limits in VDSL2 band, where FEXT channel is much weaker than direct lines [25]. However, for higher frequency bands characterized by stronger FEXT, such as the G.fast bands, traditional linear FEXT cancellation techniques fail in providing satisfactory interference mitigation capability, thus pushing to look for novel non-linear precoding strategies [37], which are the focus of this chapter.

2.1.1. Chapter Contribution

The goal of this chapter is the investigation and design of novel non-linear precoding strategies for the G.fast DS, with particular emphasis on two specific non-linear techniques, namely Tomlinson-Harashima Precoding (THP) [38] and Lattice Reduction (LR) [39]. Both techniques are based on the G.fast DS model defined in the following Sect. 2.2. In particular, in Sect. 2.3, the canonical THP vectoring scheme proposed for DSL systems in [38] is modified by optimizing the ordering in which the interference is successively cancelled user by user. The proposed ordered THP, referred to as Dynamic Ordering (DO) THP, is optimized following a user fairness criterion, thus aiming at maximizing the minimum rates among users. However, DO-THP has the inherent disadvantage to introduce additional processing delay due to the successive interference cancellation process. As an alternative to THP-based techniques, Sect. 2.4 focuses on a novel non-linear FEXT cancellation scheme for the DS G.fast channel based on the LR concept, which allows for parallel implementation, and thus avoid any additional processing delay.

2.1.2. Contribution in International Conferences/Journals

Part of the material presented in this chapter has been published in:

- M. Hekrdla, **A. Matera**, W. Wang, D. Wei, and U. Spagnolini, "Ordered Tomlinson-Harashima Precoding in G.fast Downstream" in *2015 IEEE Global Communications Conference (GLOBECOM)*, pp. 1–6, Dec 2015.

- M. Hekrdla, **A. Matera**, U. Spagnolini, and W. Wang, "Per-Line Power Controlled Lattice-Reduction Aided Zero-Forcing Precoding for G.fast Downstream" in *2016 IEEE Global Communications Conference (GLOBECOM)*, pp. 1–6, IEEE, 2016.

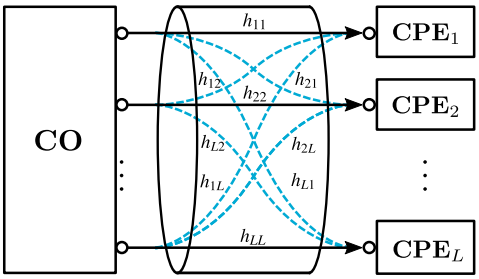

Figure 2.1.: DownStream (DS) Digital Subscriber Line (DSL) channel model.

2.2. System Model: Downstream Channel Model

This section introduces the G.fast DS model utilized in the rest of the chapter. We assume here centralized transmission from the CO to the non-cooperating CPEs in DS, as shown in Fig. 2.1. Discrete Multi-Tone (DMT) modulation is employed to turn the frequency selective channel into a set of frequency flat orthogonal channels [21]. As a consequence, on each tone, the signal received by the L CPEs $\mathbf{y} \in \mathbb{C}^L$ is modeled as

$$\mathbf{y} = \mathbf{H}\mathbf{x} + \mathbf{w}, \tag{2.1}$$

where $\mathbf{x} = [x_1, \ldots, x_L]^T \in \mathbb{C}^L$ denotes the transmitted signal vector and $\mathbf{w} \in \mathbb{C}^L$ is the Additive White Gaussian Noise (AWGN) at the receivers. We assume that the cable bundle contains only the L lines, and we avoid tone indexing to simplify the notation. The main diagonal elements $h_{ii} = [\mathbf{H}]_{ii}$ of the channel matrix $\mathbf{H} \in \mathbb{C}^{L \times L}$ characterize Insertion Loss (IL) of direct lines, and the off-diagonal elements $h_{ij} = [\mathbf{H}]_{ij}$, with $i \neq j$, characterize FEXT. As common in wireline communications, the channel is nearly-static and time-invariant [40], and it is assumed to be known at the transmitter.

2.2.1. Per-Line Per-Carrier Power Constraint

In DSL systems, the transmitted power on each line and each carrier is constrained to a specified limit [35]. These per-line per-carrier power constraints, also known in DSL jargon as Power Spectral Density (PSD) masks, must fulfill the following condition:

$$E\left[|x_i|^2\right] \leq 1, \quad \forall i = 1, ..., L, \tag{2.2}$$

where x_i is the symbol transmitted over the i-th line.

2.2.2. Tested 100m Long 20×20 Paper-Insulated Cable

For the FEXT cancellation algorithms designed in this chapter, we employ a measured 100m long 20×20 paper-insulated G.fast cable. IL and FEXT, depicted in Fig. 2.2, show that, for high cable frequencies, strong FEXT often overcomes IL. In particular, Fig. 2.3 shows the 100m long paper-insulated G.fast channel matrices at 5 MHz and 100 MHz, confirming that at G.fast frequencies the diagonal dominant property of VDSL2 is not present any more. Interestingly, IL appears to change more dynamically as frequency increases. Moreover, with a more detailed analysis, it can be shown that the symmetric FEXT coefficients $|h_{ij}|$ and $|h_{ji}|$ are highly correlated due to symmetrical electromagnetic properties. Moreover, IL between $|h_{2i-1,2i-1}|$ and $|h_{2i,2i}|$ are highly correlated, and FEXT for $|h_{2i-1,2i}|$ is much stronger than the other FEXT components of the same line, i.e.,

$$|h_{2i-1,2i}| \gg |h_{2i-1,j}|\,, \quad \forall j, j \neq 2i. \tag{2.3}$$

Therefore, we expect that the constellation geometry of lines in the bundle is such that always a pair of lines goes strictly together as shown in Fig. 2.4, while different pairs of lines may have very diverse quality even though the lines are approximately of the same length. This last observation helped to understand that performance may substantially change line by line, thus leading to an unfair rate distribution among users. This motivated us to propose a novel ordering technique specifically designed to achieve fairness among user, which is detailed in the next sections.

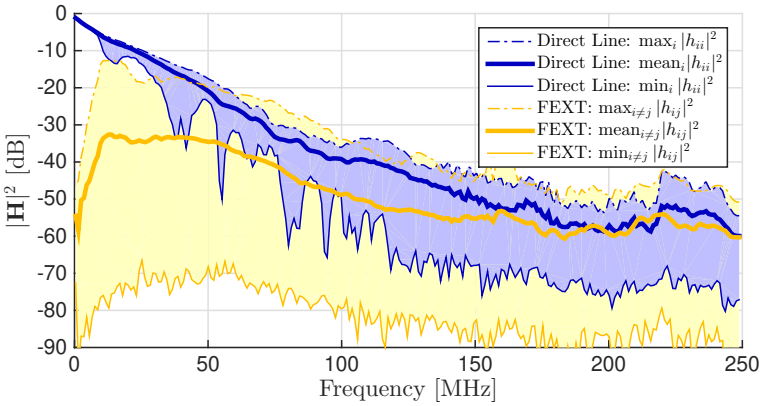

Figure 2.2.: Direct line and crosstalk power characteristics of tested 100 m long paper-insulated cable. Values are smoothed by averaging over 1 MHz bin.

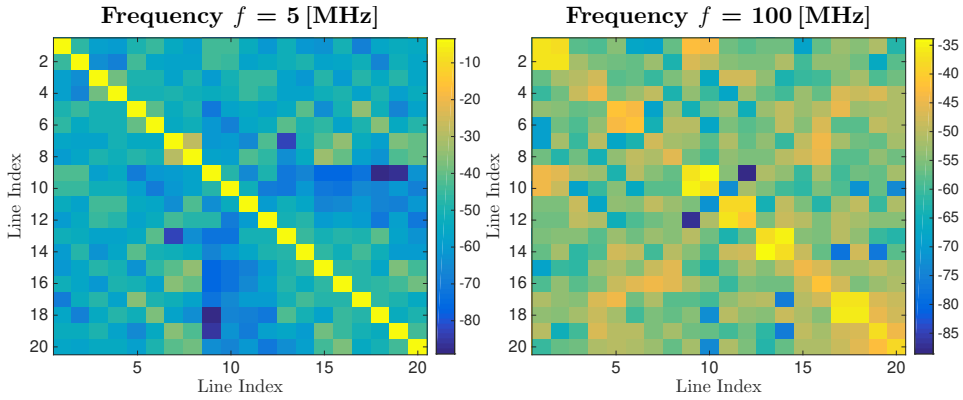

Figure 2.3.: Channel matrix characteristics $|\mathbf{H}|^2$ [dB] at carrier frequency 5 [MHZ] and 100 [MHz]: for higher frequency the twisted-pairs channel is no longer diagonal dominant

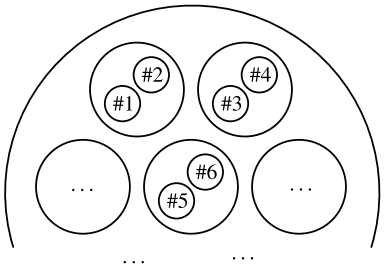

Figure 2.4.: Geometrical constellation similarities between paired lines in the cable bundle.

2.3. Ordered Tomlinson-Harashima Precoding for G.fast Systems

In this first part of the chapter, the canonical vectoring schemed based on THP proposed in [38] is modified by introducing an ordering of successive interference pre-cancellation performed at the CO that is optimized for non-cooperating CPEs. Ordering optimization for THP has been already presented in [41, 42], but for a different THP structure denoted here as Equal-Rate THP (ER-THP), as it provides constant Signal-to-Noise Ratio (SNR) at each line. The THP scheme proposed here can be concatenated with any type of ordering. The ordering which maximizes the minimum rate on a single tone of Discrete Multi-Tone (DMT) modulation is known as V-BLAST (VB) ordering [43], [44]. However, VB does not provide the maximal minimum of aggregated rates when applied on all DMT tones. Motivated by this consideration, we propose a novel Dynamic Ordering (DO) strategy that

takes into account the asymmetry of G.fast channel statistics. The proposed THP scheme aided by DO provides the maximal minimum rate of $\sim 955\,\text{Mbps}$ over the tested 100 m long paper-insulated cable. Unlike the computation of the optimal ordering arbitrary adjusting general user demands, which requires considerable computation power [45], the complexity of our heuristic DO is negligible.

2.3.1. General THP Scheme and Basic Properties

We describe the considered THP schemes in the common framework in Fig. 2.5. The linear block $\mathbf{E}$ represents the ordering operator (or later assumed lattice reduction). The feedback loop, which consists of a non-linear modulo block $\boldsymbol{\Gamma}_{\boldsymbol{\tau}}$ and a linear block given by lower triangular matrix $\mathbf{B}$ with units along the main diagonal, implements the inversion of $\mathbf{B}$ while reducing the transmitted power by modulo $\boldsymbol{\Gamma}_{\boldsymbol{\tau}}$. $\mathbf{F}$ is the feedforward filter which also ensures that the transmitted signal satisfy the power constraints. The diagonal matrix $\mathbf{G}$ describes the linear operations performed by non-cooperating receivers. Finally, the input to the precoding chain is denoted by the vector $\mathbf{a} = [a_1, \ldots, a_L]^T \in \mathbb{C}^L$, which contains the data symbols, and the output is the decision variable vector $\hat{\mathbf{y}} \in \mathbb{C}^L$.

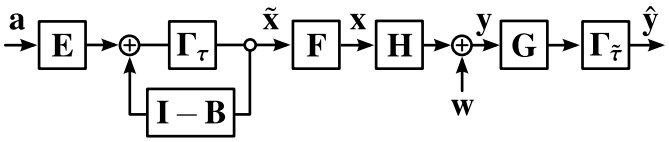

Figure 2.5.: General Tomlinson-Harashima Precoding (THP) scheme.

2.3.1.1. Linearized Scheme

Block $\boldsymbol{\Gamma}_{\boldsymbol{\tau}}$ represents the modulo function over base τ with origin shifted by $\tau/2$. This is applied individually along each dimension of the input $\mathbf{x}$. In particular,

$$\begin{aligned}
&\Gamma_\tau[x] \triangleq (x + \tau/2)_{\text{mod}\,\tau} - \tau/2, \quad x \in \mathbb{R},\\
&\Gamma_\tau[x] \triangleq \Gamma_\tau[\Re\{x\}] + \mathrm{j}\Gamma_\tau[\Im\{x\}], \quad x \in \mathbb{C},\\
&\boldsymbol{\Gamma}_{\boldsymbol{\tau}}[\mathbf{x}] \triangleq [\Gamma_{\tau_1}[x_1], \ldots, \Gamma_{\tau_L}[x_2]]^T, \quad \mathbf{x} \in \mathbb{C}^L.
\end{aligned}$$

Every modulo reminder equals the input minus an integer multiple of base τ such that the reminder is lower than τ. Therefore, the operation performed by $\boldsymbol{\Gamma}_{\boldsymbol{\tau}}$ can be described as $\boldsymbol{\Gamma}_{\boldsymbol{\tau}}[\mathbf{x}] = \mathbf{x} - \mathbf{d}$, where $\mathbf{d}$ is a vector such that $\mathbf{x} - \mathbf{d} \in [-\tau_1/2, \tau_1/2) \times \cdots \times [-\tau_L/2, \tau_L/2)$. The i-th component of $\mathbf{d}$ is $d_i \in \tau_i \mathbb{Z}_\mathrm{j}$, where $\mathbb{Z}_\mathrm{j} \triangleq \mathbb{Z} + \mathrm{j}\mathbb{Z}$ denotes complex integers and $\boldsymbol{\tau} = [\tau_1, \ldots, \tau_L]^T$ is a vector of thresholds. Figure 2.6 shows the linear-equivalent THP scheme, where $\boldsymbol{\Gamma}_{\boldsymbol{\tau}}$ is replaced by the additive term $-\mathbf{d}$.

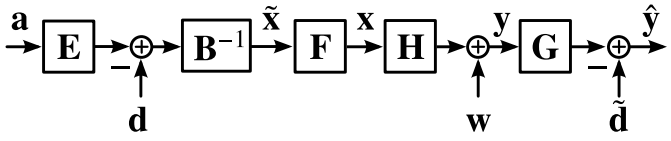

Figure 2.6.: Linearized general THP scheme.

2.3.1.2. Zero-Forcing Condition

Zero-Forcing (ZF) precoding inverts the channel by fully eliminating the crosstalk such that

$$\hat{\mathbf{y}} = \mathbf{GHFB}^{-1}\mathbf{Ea} - \mathbf{GHFB}^{-1}\mathbf{d} + \mathbf{Gw} - \tilde{\mathbf{d}} \tag{2.4}$$

equals the input data $\mathbf{a}$ plus noise. The whole chain of linear blocks in Fig. 2.6 needs to fulfill the ZF condition

$$\mathbf{GHFB}^{-1}\mathbf{E} = \mathbf{I}, \tag{2.5}$$

with $\mathbf{I}$ being the $L \times L$ identity matrix. Condition (2.5) implies that $\mathbf{GHFB}^{-1} = \mathbf{E}^{-1}$, which leads to

$$\hat{\mathbf{y}} = \mathbf{a} - \mathbf{E}^{-1}\mathbf{d} + \mathbf{Gw} - \tilde{\mathbf{d}}. \tag{2.6}$$

It follows from 2.6 that the ZF property, i.e., $\hat{\mathbf{y}} = \mathbf{a} + \mathbf{Gw}$, is obtained when

$$\mathbf{E}^{-1}\mathbf{d} + \tilde{\mathbf{d}} = 0, \tag{2.7}$$

which is realized by properly designing the thresholds $\boldsymbol{\tau}$ and , as detail below.

2.3.1.3. Modulo Threshold τ

Size of τ is chosen to wrap constellations within the $\tau \times \tau$ frame such that the distance from the edge point to the boundary is half of minimal distance $d_{\min}$. Figure 2.7 shows the frame for several constellations considered in this chapter. It is straightforward to verify that square-shaped QAM constellations including odd-bit cardinality variants (black points in Fig. 2.7) have $\tau = \sqrt{M}d_{\min}$. Table 2.1 lists values of τ considered here.

Table 2.1.: Threshold τ and power increase ΔE due to modulo $\boldsymbol{\Gamma}_{\boldsymbol{\tau}}$ for considered unit-mean square-shape M-QAM constellations.

M	$2, 4$	$8, 16$	$32, 64$	$128, 256$	$512, 1024$	$2048, 4096$
τ	2.83	2.53	2.47	2.45	2.45	2.45
ΔE [dB]	1.25	0.28	0.068	0.017	0.0042	0.0011

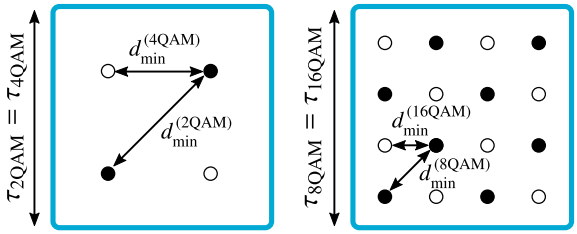

Figure 2.7.: Threshold τ for several considered square-shape QAM constellations.

2.3.1.4. Power Increase by Modulo $\mathbf{\Gamma}_{\tau}$

Paper [38] shows that the statistics of the output of modulo $\mathbf{\Gamma}_{\tau}$ are well approximated by uniform distribution. For unit mean power constellation symbols, i.e., $E\left[|a_i|^2\right] = 1$ ($E[\star]$ denotes the statistical expectation), the power of the symbol $\tilde{x}$ at the output of the modulo operator is slightly higher and can be approximated as

$$\Delta E = E[|\tilde{x}_i|^2] \simeq \frac{M}{M-1}. \tag{2.8}$$

In order to satisfy the power constraints in (2.2), we need to keep in mind and downscale constellations to pre-compensate the power increase ΔE due to modulo $\mathbf{\Gamma}_{\tau}$. The same formula holds for odd-bit cardinalities if twice higher value of M is used, as shown in Table 2.1. For example, notice that ΔE is the same for 2QAM and 4QAM. Odd-bit constellations with a square shape have significantly lower $E[|\tilde{x}_i|^2]$ than popular cross-shaped constellations [37].

2.3.2. Reference THP Scheme and Basic Properties

The proposed ordered THP scheme enhances the scheme described in [38], which is reviewed here. Reference scheme [38] is described by definition of the blocks in Fig. 2.6 as

$$\mathbf{E} = \mathbf{I}, \quad \mathbf{B} = \mathrm{diag}(\mathbf{R})^{-1}\mathbf{R}^H, \quad \mathbf{F} = \mathbf{Q}, \quad \mathbf{G} = \mathrm{diag}(\mathbf{R})^{-1}, \tag{2.9}$$

where $\mathrm{diag}(\mathbf{R})^{-1} = \mathrm{diag}\left(r_{11}^{-1}, \ldots r_{LL}^{-1}\right)$ is a diagonal matrix with diagonal components $r_{ii} = [\mathbf{R}]_{ii}$. Unitary matrix $\mathbf{Q}$ and upper-triangular $\mathbf{R}$ follow from the QR decomposition of transposed channel matrix

$$\mathbf{H}^H = \mathbf{QR}. \tag{2.10}$$

Let us now confirm that this scheme meet the basic properties introduced in Sec. 2.3.1. The reference scheme fulfills ZF condition (2.5), as

$$\mathbf{GHFB}^{-1}\mathbf{E} = \mathrm{diag}(\mathbf{R})^{-1}\mathbf{R}^H\mathbf{Q}^H\mathbf{QR}^{-H}\mathrm{diag}(\mathbf{R})\mathbf{I} = \mathbf{I}. \tag{2.11}$$

It is also easy to show that the transmitted signal meets per-line power constraint 2.2, which is shown by

$$E\left[|x_i|^2\right] = \sum_{j=1}^{L} |q_{ij}|^2 E\left[|\tilde{x}_j|^2\right] = \sum_{j=1}^{L} |q_{ij}|^2 = 1, \tag{2.12}$$

where $q_{ij} = [\mathbf{Q}]_{ij}$. In 2.12 we use the fact that $\mathbf{x}$ is approximately uncorrelated [41] and the power increase due to $\Gamma_{\boldsymbol{\tau}}$ has been pre-compensated $E\left[|\tilde{x}_j|^2\right] = 1$. The last equality follows from that unitary $\mathbf{Q}$ has unit-length rows. The decision variable

$$\hat{\mathbf{y}} = \mathbf{a} + \mathrm{diag}(\mathbf{R})^{-1}\mathbf{w} \tag{2.13}$$

implies that output SNR at the i-th line is

$$\gamma_i = \gamma_{base} \cdot r_{ii}^2, \tag{2.14}$$

where γ_{base} is the baseline input SNR. The main diagonal components $\left\{r_{ii}^2\right\}_{i=1}^{L}$ can attain different values providing different SNR at each line. In this case, different bit-loading per-line is required, as well as different modulo threshold $\tau_i \neq \tau_j$ in $\boldsymbol{\tau} = [\tau_1, \ldots, \tau_L]^T$, see Table 2.1 for actual values. Finally, since $\mathbf{E} = \mathbf{I}$, the selection of $\tilde{\boldsymbol{\tau}} = \boldsymbol{\tau}$ fulfills the modulo condition (2.7).

2.3.3. Ordered Tomlinson-Harashima Precoding

2.3.3.1. Ordered QR Decomposition

The ordered THP scheme proposed here incorporates the ordered QR decomposition of transposed channel

$$\mathbf{H}^H = \mathbf{Q}\mathbf{R}\mathbf{P}^T \tag{2.15}$$

into the reference scheme (Sec. 2.3.2). Permutation matrix $\mathbf{P}$ describes arbitrary permutation $[1, \ldots, L]^T \rightarrow [p_1, \ldots, p_L]^T$ as

$$\mathbf{P}\begin{bmatrix} 1 \\ \vdots \\ L \end{bmatrix} = \begin{bmatrix} p_1 \\ \vdots \\ p_L \end{bmatrix}, \quad \text{where} \quad \mathbf{P} = \begin{bmatrix} \mathbf{e}_{p_1} \\ \vdots \\ \mathbf{e}_{p_L} \end{bmatrix} \tag{2.16}$$

and $\mathbf{e}_i$ denotes a row vector with 1 in the i-th position and 0 elsewhere. Note that $\mathbf{PX}$ denotes permutation of rows of $\mathbf{X}$, while $\mathbf{X}\mathbf{P}^T$ permutation of columns since $\mathbf{X}\mathbf{P}^T = \left(\mathbf{P}\mathbf{X}^T\right)^T$.

2.3.3.2. Proposed THP Scheme and Basic Properties

The ordered THP scheme is given by the following matrices

$$\mathbf{E} = \mathbf{P}^T, \mathbf{B} = \mathrm{diag}(\mathbf{R})^{-1}\mathbf{R}^H, \mathbf{F} = \mathbf{Q}, \mathbf{G} = \mathbf{P}\,\mathrm{diag}(\mathbf{R})^{-1}\mathbf{P}^T. \tag{2.17}$$

Key observation is that if the receiver diagonal matrix $\mathbf{G}$ has permuted rows and columns by the same permutation (as $\mathbf{G}$ in (2.17)), then it remains diagonal and can be performed by non-cooperating receivers. Now, we show that ZF condition (2.5) is satisfied:

$$\mathbf{GHFB}^{-1}\mathbf{E} = \mathbf{P}\mathrm{diag}(\mathbf{R})^{-1}\mathbf{P}^T\mathbf{P}\mathbf{R}^H\mathbf{Q}^H\mathbf{Q}\mathbf{R}^{-H}\mathrm{diag}(\mathbf{R})\mathbf{P}^T = \mathbf{I},$$

since $\mathbf{P}^T$ describes inverse permutation and thus $\mathbf{P}\mathbf{P}^T = \mathbf{I}$. As in the reference scheme in Sec. 2.3.2, feedforward matrix $\mathbf{F}$ is unitary and therefore transmitted signal meets per-line power constraint (2.2). The decision variable $\hat{\mathbf{y}} = \mathbf{a} + \mathbf{P}\,\mathrm{diag}(\mathbf{R})^{-1}\mathbf{P}^T\mathbf{w}$ implies the output SNR at the i-th line to be

$$\gamma_i = \gamma_{base} \cdot r^2_{p_i p_i}, \tag{2.18}$$

where γ_{base} denotes baseline SNR and p_i is the i-th element of permutation output (2.16). Similarly to the reference THP, different values of main diagonal components $\left\{r^2_{p_i p_i}\right\}_{i=1}^{L}$ require different bit-loading with thresholds $\boldsymbol{\tau} = [\tau_1, \ldots, \tau_L]^T$ where generally $\tau_i \neq \tau_j$. Vector of thresholds $\tilde{\boldsymbol{\tau}}$ needs to be chosen to fulfill condition (2.7) which means $\tilde{\boldsymbol{\tau}} = \mathbf{P}\boldsymbol{\tau} = [\tau_{p_1}, \ldots, \tau_{p_L}]^T$.

Remark 2.1. Any type of ordering $\mathbf{P}$ can be concatenated with the proposed ordered THP and it is a degree of freedom to be exploited. The reference scheme is obtained for the ordering $\mathbf{P} = \mathbf{I}$, which means that optimized ordering can only improve the performance of the reference scheme.

2.3.4. Optimized Ordering of THP in G.fast Downstream

A rich number of possible orderings (see [46] and references therein) can be concatenated with the scheme proposed here. Generally, different orderings lead to different SNR at each line (2.18). The optimal selection is a multi-objective optimization problem where utility target considering fairness has significant impact on the result. We mainly focus on max-min fairness by maximizing the minimum rate, and thus providing the same quality of service to each CPE, although also sum-rate maximization and the simple combination of both are discussed.

2.3.4.1. V-BLAST (VB) Ordering

The ordering strategy introduced in [43] is the optimal max-min fair ordering maximizing the minimum SNR. The algorithm requires multiple calculations of

channel matrix pseudo-inverse, and so its complexity is much higher than the complexity of closely-related semi-optimal algorithms, such as the one [44]. Instead of [43], we pragmatically use [44] since it performs close to the optimum, but avoiding the computational burdens.

VB ordering [44] is based on Gram-Schmidt (GS) QR decomposition of the transposed channel $\mathbf{H}^H = \tilde{\mathbf{H}} = \mathbf{QR}$. In the i-th iteration, the algorithm choses the column vector $\tilde{\mathbf{h}}_i$ of $\tilde{\mathbf{H}} = \left[\tilde{\mathbf{h}}_1, \ldots, \tilde{\mathbf{h}}_L\right]$ which minimizes the diagonal element $r_{ii} = [\mathbf{R}]_{ii}$ given as

$$r_{ii} = \left\| \tilde{\mathbf{h}}_i - \sum_{j=1}^{i-1} \left\langle \tilde{\mathbf{h}}_i, \mathbf{q}_j \right\rangle \mathbf{q}_j \right\|, \tag{2.19}$$

where $\langle \mathbf{h}, \mathbf{q} \rangle = \mathbf{q}^H \mathbf{h}$ denotes an inner product. The order in which $\tilde{\mathbf{h}}$ are chosen forms permutation matrix $\mathbf{P}$ in (2.15). This strategy, referred to as "weakest first", leads to the ordering which maximizes the minimum of $\left\{r_{ii}^2\right\}_{i=1}^{L}$ elements and so the SNR of the weakest line (2.18).

2.3.4.2. Inverse V-BLAST (IVB) Ordering

Inverse VB (IVB) ordering follows the opposite principle of VB. In each GS iteration, it is chosen the column vector $\tilde{\mathbf{h}}_i$ whose corresponding diagonal element r_{ii}in (2.19) is maximal. This is a greedy maximization approach which maximizes the sum-rate. We freely interchange sum-rate and mean-rate being the difference just a scaling factor. The IVB ordering, also referred to as "strongest first", is also known in the mathematical literature as QR decomposition with pivoting [47].

2.3.4.3. Dynamic Ordering (DO)

Although VB is the optimal max-min fair ordering, it does not lead to equal user rates when those are aggregated over multiple DMT tones, (see Fig. 2.12). Hence, if on a single tone, we selected instead of VB ordering a different ordering in favor of the line with the minimal aggregated rate, we would obtain a higher minimum rate. In other words, VB ordering is optimal on a single tone, but it does not reach the global optimum if applied independently on each tones. The reason behind is that G.fast channel does not have the same statistical properties on each line, as discussed in Sect. 2.2.2. Some lines are more often the weakest lines (i.e., being selected first by VB) due to asymmetric physical arrangement of twisted-copper pairs within the cable bundle as confirmed by numerical evaluation in Fig. 2.8. Based on these considerations, we propose a novel ordering strategy, referred to as Dynamic Ordering (DO), which takes into account this statistical asymmetry in providing the highest minimum aggregated rate. DO ordering is inspired by VB approach which states that being taken first into GS is an advantage. Instead

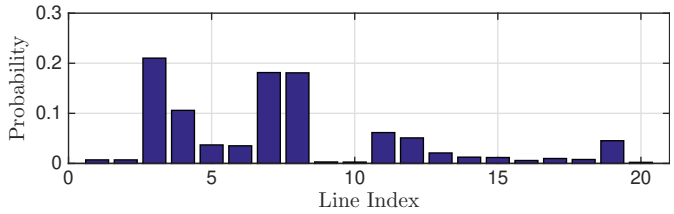

Figure 2.8.: Empirical probability density function for a line to be the weakest (i.e., being selected as the first to enter the GS procedure in V-BLAST ordering).

of VB "weakest first" approach applied independently on each tone, we propose to take first the line with so far minimum aggregated rate ("aggregated minimum first"). DO is ordering with memory deciding the order inductively in sequence. If the ordering on tone index 1 to $i-1$ has been already chosen, then DO orders the lines on the i-th tone as the order of aggregated bit-loading over the tones from 1 to $i-1$. Figure 2.9 shows an illustrative example explaining why DO provides higher aggregated minimum than VB. Complexity of DO is negligible, since the order is

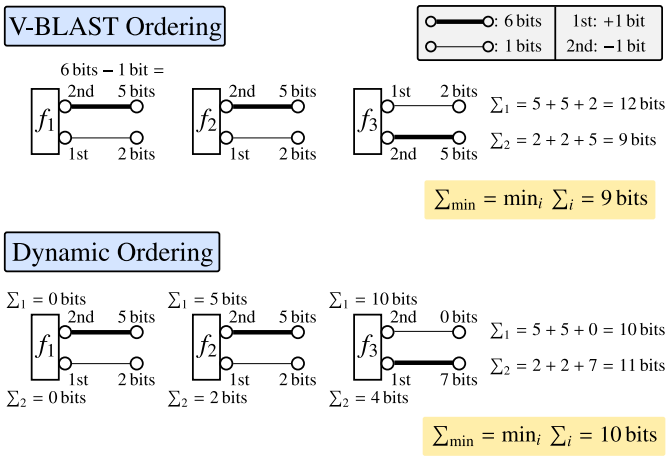

Figure 2.9.: Toy example of Dynamic Ordering (DO). Let us assume a DMT system with 2 lines and 3 tones $\{f_i\}_{i=1}^{3}$. Strong lines with throughput of 6 bits are denoted by a thick line, weak lines with throughput of 1 bit are denoted with a thin line. Entering the GS procedure first is an advantage increasing the throughput by +1 bit, while being second decreases the throughput by −1 bit. The minimum aggregated rate $\sum_{\min}$ of V-BLAST ("weakest first") is lower than DO ("aggregated minimum first"). Symbol $\sum_i$ denotes aggregated rate at the i-th line. We assume that the initial order at f_1 of DO is given by VB.

given by cumulative summation performed once at the beginning of transmission. The order is computed outside of QR algorithm and can be connected to whatever

type of QR implementation, not only the one based on GS as in [44].

2.3.4.4. Frequency-Sharing Between DO and IVB

IVB ordering maximizes sum-rate on a single tone as well as when applied independently on multiple tones, unlike in the case of max-min VB and DO ordering. We propose a simple frequency-sharing between the two extreme types of ordering, i.e., IVB and DO, in order to adjust the fairness among CPEs. By frequency-sharing, we mean similar concept as time-sharing, but in the frequency domain. We propose to divide the overall bandwidth into lower and upper parts where we expect different behavior (e.g., diagonal dominant property is present only on lower frequencies as shown in Fig. 2.3). DO ordering can be thus enforced to lower frequencies or to higher frequencies. As shown in Fig. 2.10, in the former case the strategy is denoted as DO-IVB, while in the latter it is IVB-DO. Numerical evaluation in Fig. 2.11 shows that DO-IVB sharing achieves superior performance, regardless of the portion of bandwidth allocated to DO (denoted in Fig. 2.10 as B_{DO})

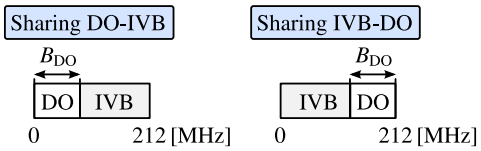

Figure 2.10.: Frequency sharing between two extreme types of orderings: DO (maximizing minimum) and IVB (maximizing sum-rate). Parameter B_{DO} describes the bandwidth assigned to DO.

2.3.5. Comparison with Ordered Equal Rate THP (ER-THP)

Ordering optimization has been introduced in [41], [42] for the THP structure denoted here as ER-THP (term centralized THP is also used [48]). Label 'equal rate' corresponds to the feature that ER-THP provides constant SNR over all lines. The proposed THP scheme and ER-THP have essentially different structure.

2.3.5.1. Ordered ER-THP Scheme and Basic Properties

Ordered ER-THP is defined by the following matrices

$$\mathbf{E} = \mathbf{P}^T, \mathbf{B} = \mathbf{R}^H \mathrm{diag}(\mathbf{R})^{-1}, \mathbf{F} = \frac{1}{g}\,\mathbf{Q}\,\mathrm{diag}(\mathbf{R})^{-1},\ \mathbf{G} = g\mathbf{I}, \tag{2.20}$$

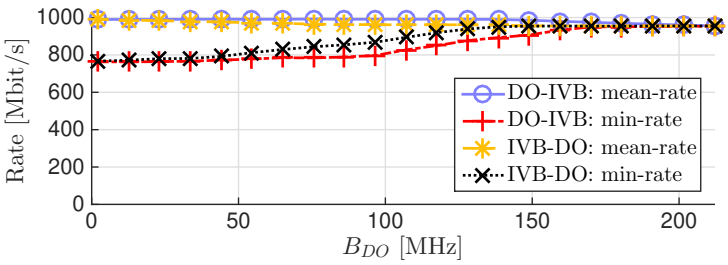

Figure 2.11.: Rates versus the amount of bandwidth B_{DO} assigned to DO. Frequency sharing between DO and IVB enables to adjust the trade off between mean and min-rate. For instance, both min-rate and mean-rate equal to $\sim 950\,\text{Mbps}$ for DO-IVB sharing with $B_{\text{DO}} = 212\,\text{MHz}$, but if we permit a slight decrease of minimum, we could have mean-rate $\sim 975\,\text{Mbps}$ while having minimum still $\sim 950\,\text{Mbps}$ (here $B_{\text{DO}} \simeq 170\,\text{MHz}$). Similarly, when mean-rate is priority, $B_{\text{DO}} \simeq 125\,\text{MHz}$ increases min-rate from $\sim 760\,\text{Mbps}$ ($B_{\text{DO}} \simeq 0\,\text{MHz}$) to $\sim 875\,\text{Mbps}$ keeping the same mean-rate.

where ordered QR decomposition (2.15) is used. Automatic gain control scaling g establishes the power constrain (2.2), i.e.,

$$E\left[|x_i|^2\right] = \frac{1}{g^2}\sum_{j=1}^{L}\left|\tilde{f}_{ij}\right|^2 \leq 1, \tag{2.21}$$

with labeling $\tilde{\mathbf{F}} = \mathbf{Q}\,\text{diag}(\mathbf{R})^{-1}$ and $\left[\tilde{\mathbf{F}}\right]_{ij} = \tilde{f}_{ij}$. The constraint is fulfilled by the following scaling using the $(2,\infty)$-mixed norm $\|\star\|_{2,\infty}$ as

$$g^2 = \left\|\tilde{\mathbf{F}}^T\right\|_{2,\infty}^2 \triangleq \max_i \sum_{j=1}^{L}\left|\tilde{f}_{ij}\right|^2 = \max_i \sum_{j=1}^{L} |q_{ij}|^2/r_{jj}^2. \tag{2.22}$$

Notice, an average power constrain is assumed in [41], [42], which leads to the scaling with Frobenius norm $\|\star\|_F$ as $g^2 = {}^1/_L \left\|\tilde{\mathbf{F}}\right\|_F^2 \triangleq {}^1/_L \,\text{tr}\left(\tilde{\mathbf{F}}\tilde{\mathbf{F}}^H\right)$. We confirm that ER-THP meets ZF condition (2.5) as

$$\mathbf{GHFB}^{-1}\mathbf{E} = g\mathbf{IPR}^H\mathbf{Q}^H\frac{1}{g}\mathbf{Q}\,\text{diag}(\mathbf{R})^{-1}\text{diag}(\mathbf{R})\mathbf{R}^{-H}\mathbf{P}^T = \mathbf{I}.$$

The decision variable $\hat{\mathbf{y}} = \mathbf{a} + g\mathbf{w}$ implies the output SNR to be

$$\gamma_i = \gamma_{base} \cdot {}^1/_{g^2}, \tag{2.23}$$

where γ_{base} denotes baseline SNR. Constant SNR yields the same bit-loading and the same modulo threshold $\boldsymbol{\tau} = [\tau,\ldots,\tau]^T$ on every line, therefore the vector of thresholds $\tilde{\boldsymbol{\tau}} = \boldsymbol{\tau}$ fulfills modulo condition (2.7).

2.3.5.2. VB Ordered and Lattice Reduced (LR) ER-THP

Performance of ER-THP is given by the scaling factor g^2. Using the inequality $1/r_{ii}^2 \leq 1/\min_i r_{ii}^2$, we rephrase (2.22) as

$$g^2 = \max_i \sum_{j=1}^{L} \frac{|q_{ij}|^2}{r_{jj}^2} \leq \max_i \sum_{j=1}^{L} \frac{|q_{ij}|^2}{\min_k r_{kk}^2} = \frac{1}{\min_k r_{kk}^2}. \tag{2.24}$$

We see that g^2 is minimized when $\min_k r_{kk}^2$ is as large as possible, therefore VB ordering (i.e., maximizing the minimum of $\{r_{ii}\}_{i=1}^{L}$) is again preferable. Reference [49] shows that even smaller value of g^2 is obtained with LR QR decomposition

$$\mathbf{H}^H = \mathbf{Q}\mathbf{R}\mathbf{T}^{-1}, \tag{2.25}$$

where QR decomposes the reduced channel as $\tilde{\mathbf{H}} = \mathbf{Q}\mathbf{R}$, the reduced channel is $\tilde{\mathbf{H}} = \mathbf{H}^H\mathbf{T}$, and $\mathbf{T}$ is a unimodular integer matrix. LR ER-THP is given by (2.20) using decomposition (2.25), where $\mathbf{E} = \mathbf{T}^H$. We use the common Lenstra–Lenstra–Lovász (LLL) implementation of LR with moderate algorithm complexity parameter $\delta = 3/4$ [39].

Unfortunately, LR decomposition (2.25) cannot be used in the proposed THP scheme (2.17) with $\mathbf{E} = \mathbf{T}^H$, as matrix $\mathbf{G} = \mathbf{T}^{-H}\,\mathrm{diag}(\mathbf{R})^{-1}\mathbf{T}^H$ (unlike in the case of ordering) is not diagonal anymore, and thus cannot be performed by non-cooperating CPEs. For the sake of comparison, we consider ER-THP scheme enhanced by both LR and VB ordering with complexity parameter set to an extreme value $\delta = 1$. This scheme has impractical implementation complexity, but achieves the highest SNR among the ER-THP methods, as confirmed by simulations in Fig. 2.12.

2.3.6. Performance Evaluation

2.3.6.1. Evaluation Procedure and Simulation Parameters

Bit-loading at the i-th line is computed according to [50] by insertion of SNR γ_i (2.14), (2.18), (2.23) into the gap formula

$$b_i = \lfloor \log_2 (1 + \gamma_i/\Gamma) \rfloor\,, \quad \text{for} \quad b_i \in [2, 12] \tag{2.26}$$

and $b_i = 0$ otherwise, where symbol $\lfloor \star \rfloor$ denotes floor operation and gap Γ = Shannon gap + margin − coding gain [dB]. Aggregated rates are obtained by summing the bit-loading (2.26) over all DMT tones multiplied by the tone spacing Δf (1 − Framing Overhead). Simulation parameters are listed in Table 2.2. We use bit-loading modification described in [37] to incorporate power increases ΔE (shown in Table 2.1) due to modulo $\mathbf{\Gamma}_{\boldsymbol{\tau}}$. The algorithm allocates bits according to (2.26), and then recomputes the SNR corrected by ΔE and update bit-allocation accordingly.

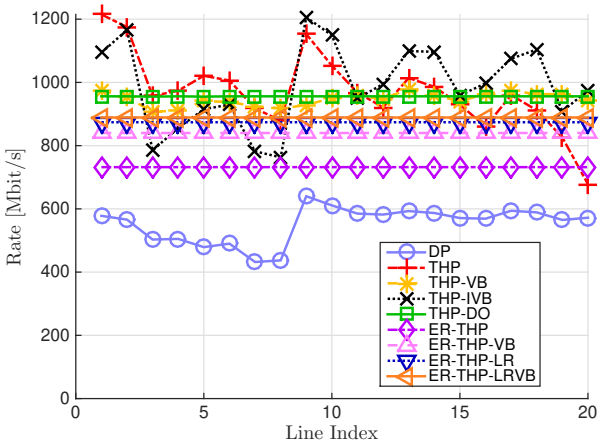

Figure 2.12.: Aggregated rates of considered precoding schemes over tested 100m long paper-insulated cable. The acronyms and basic rate statistics of considered precoding schemes are summarized in Table 2.3.

Table 2.2.: Simulation parameters [50]

Transmit PSD	−76 [dBm/Hz]	Coding Gain	5 [dB]
Noise PSD	−140 [dBm/Hz]	Shannon Gap	9.8 [dB]
Band	2.1 − 212 [MHz]	Bit Loading	2 − 12 [bits]
Tone Spacing Δf	51.750 [kHz]	Framing Overhead	12 %
Margin	6 [dB]		

2.3.6.2. Numerical Results

Numerical results in Fig. 2.12 and Table 2.3 compare several FEXT cancellation methods in DS. Non-linear precoding based on THP or ER-THP clearly outperforms linear DP precoding used in VDSL2 [25]. We confirm that ER-THP provides constant aggregated rates to all users, where gains by VB ordering and LR are significant. THP with un-equal rates provides higher sum-rate than ER-THP. As expected, VB ordered THP considerably increases min-rate, while IVB ordered THP considerably increases sum-rate. Proposed DO ordered THP provides the highest aggregated minimum rate among all considered methods. The achieved rates are fairly stable vs. line index being close to G.fast target of 1 Gbps.

Table 2.3.: Mean and minimum aggregated rates of several FEXT cancellation precoding schemes depicted in Fig. 2.12. The rates are in Mbits/s.

Acronym	Precoding Scheme	[mean,min]-rate
DP	Diagonal Precoding	[552, 432]
THP	Tomlinson-Harashima Precoding	[970, 678]
THP-VB	THP using VB ordering	[947, 907]
THP-IVB	THP using Inverse VB ordering	[990, 763]
THP-DO	THP using Dynamic Ordering	[956, 955]
ER-THP	Equal-Rate THP	[732, 732]
ER-THP-VB	ER-THP using VB ordering	[840, 840]
ER-THP-LR	ER-THP using Lattice Reduction	[874, 874]
ER-THP-LRVB	ER-THP-LR using VB ordering	[889, 889]

2.4. Lattice-Reduction Aided Non-Linear Precoding

In the section above, THP has been shown to be a valid solution for next generation G.fast systems, especially if combined with a properly chosen ordering strategy. However, besides these gains, THP poses the following issues: *i)* THP requires CPEs' receiver processing to be modified in order to implement the modulo operation, and *ii)* THP processing introduces an additional delay proportional to the number of lines due to the inherent nonlinear sequential processing. In particular, the latter is especially critical, being maximum latency of signal processing algorithms a primary concern in practical communication systems [51].

Mainly focusing on this second issue, the second part of the chapter discusses non-linear precoding based on Lattice Reduction aided Zero-Forcing (ZF-LR), as this provides an alternative to THP which allows for parallel implementation, thus avoiding any additional latency due to sequential interference cancellation. ZF-LR has been proposed for the wireless Multiple-Input Single-Output (MISO) broadcast channel in [52] using scalar the Frobenius Norm Scaling (FNS) to adjust average transmit power. We modify this scheme to comply with per-line per-carrier power constraint [23] by using the scalar maximum Row Norm Scaling (RNS), similarly to [37]. Scalar scaling in general implies that the line with the weakest channel determines the performance of all the other lines. This feature is undesirable especially in Fiber-To-The-distribution-point (FTTdp) deployments where different lengths of lines are expected (e.g., CPEs in different floors of the building). Therefore, we propose a novel ZF-LR scheme with vector scaling where each line has its own scaling gain to enable per-line individual power control (terminology illustrated in Fig. 2.13). Unlike the scalar scaling, vector scaling cannot be placed arbitrarily in the processing chain (diagonal matrix does not generally commute), which leads to an unusual position of the power controlling operation placed before ZF channel inversion (scheme depicted in Fig. 2.15).

We distinguish in this chapter between power allocation optimization combined

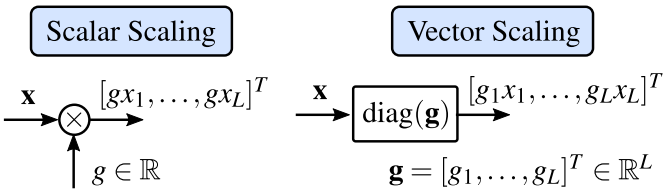

Figure 2.13.: Scalar scale $g \in \mathbb{R}$ controls transmit power per group of lines while vector of scales $\mathbf{g} \in \mathbb{R}^L$ controls transmit power per-line. Symbol diag($\mathbf{g}$) denotes diagonal matrix with vector components on the main diagonal.

with precoding, denoted here as Optimized Power Allocation (OPA), and power management used to handle uncoordinated interference (i.e., interference that cannot be mitigated by precoding), which we denote as Dynamic Spectrum Management (DSM) [36], although this division is not so strict in the literature. OPA for G.fast downstream is a challenging problem since there is not only the constraint on per-line per-carrier transmit power, but also the constraint on the total per-line transmit power aggregated over all carriers [23], where the optimal solution needs a joint optimization over all carriers. This is numerically demanding, and suboptimal approaches have been proposed for both linear [27] and non-linear precoding [53]. In this section, we show that OPA for ZF-LR precoding maximizing weighted sum-rate subject to per-line per-carrier constraint leads to the signomial optimization problem [54], [55], for which efficient solving methods are known [56, 57]. Signomial programming as a solution to power optimization appears recently e.g., in [58], [59]. Related work [60] presents ZF-LR concept supporting unequal-rates without optimized power control.

2.4.1. Lattice-Reduction Aided Zero-Forcing Precoding with Row Norm Scalar (RNS) Scaling Power Control

2.4.1.1. ZF-LR Precoding Scheme

ZF-LR scheme with scalar row norm scaling power control as introduced in [52], denoted here as ZF-LR-RNS, is depicted in Fig. 2.14. Symbol $\mathbf{a} \in \mathbb{C}^L$ denotes vector of uncorrelated constellation symbols where every component a_i is taken from M-QAM constellation of the same size M. Without loss of generality we assume unit mean symbol power, i.e., $E[\mathbf{a}\mathbf{a}^H] = \mathbf{I}$. Feedforward matrix $\mathbf{F}$ denotes precoding operation which is composed as

$$\mathbf{F} = g\tilde{\mathbf{F}}, \tag{2.27}$$

where $\tilde{\mathbf{F}}$ is a linear precoding filter and g is the scalar scale controlling the transmitted power. Unlike in the case of linear ZF precoding, where precoding matrix $\tilde{\mathbf{F}}$ implements channel inversion $\tilde{\mathbf{F}} = \mathbf{H}^{-1}$ to completely cancel the FEXT, ZF-LR

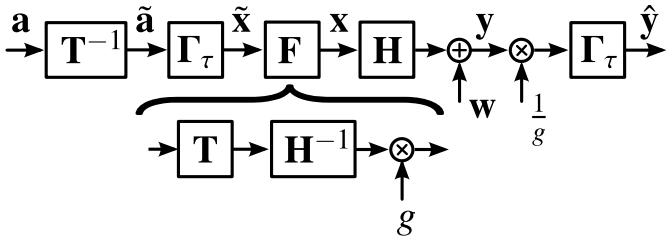

Figure 2.14.: Scheme of Lattice-Reduction (LR) aided Zero-Forcing (ZF) precoding using scalar scaling power control.

implements precoding by inverting the channel matrix which is reduced by lattice reduction as

$$\tilde{\mathbf{F}} = \mathbf{H}^{-1}\mathbf{T}. \tag{2.28}$$

The impact of lattice reduction, which is essentially described by the integer valued matrix $\mathbf{T}$, is eliminated by modulo $\mathbf{\Gamma}_\tau$ similarly as in THP. In fact, lattice-reduced channel inversion precoding cancels all the interference up to an integer multiple of τ, which is eliminated by the modulo $\mathbf{\Gamma}_\tau$. LR operation produces a reduced matrix whose columns (or rows) exhibit much better orthogonal properties with respect to the original matrix. In other words, the reduced matrix is easier to be inverted than the original one. As a result, performance gains come from the fact that the impact of noise enhancement due to channel inversion, which is the main drawback of ZF-based techniques, is less severe when inverting the lattice reduced channel matrix.

2.4.1.2. Lattice Reduction

Lattice is a discrete subgroup of $\mathbb{R}^L$ spanning $\mathbb{R}^L$. Lattices are mathematical structures with long history and many practical and theoretical features which find application also in signal processing and communication theory [61]. This chapter does not intent to provide comprehensive overview of lattice reduction which is well covered e.g., by [39]. We rather consider lattice reduction as a matrix decomposition of the type $\mathbf{A} = \mathbf{BT}$, where $\mathbf{A}$ is a matrix with lattice reduced columns of $\mathbf{B}$, i.e., both matrices are basis of the same lattice, but length of the base vectors of $\mathbf{A}$ is reduced. In our case, lattice reduction turns potentially ill-conditioned $\mathbf{H}^{-1}$ into reduced form $\mathbf{H}^{-1}\mathbf{T}$, which amplifies transmitted signal much less (i.e., scalar scale [as discussed later in Sec. 2.4.1.4] of reduced matrix is lower [49]). Matrix $\mathbf{T}$ is unimodular with integer components $[\mathbf{T}]_{ij} = t_{ij} \in \mathbb{Z}_\mathrm{j}$ and $|\mathbf{T}| = 1$, where $|\star|$ is the determinant operator.

2.4.1.3. Modulo $\mathbf{\Gamma}_{\boldsymbol{\tau}}$

The modulo operator $\mathbf{\Gamma}_{\boldsymbol{\tau}}$ is the same as defined in Sect 2.3.1.1. Here, we just remind the reader that $\boldsymbol{\tau} = [\tau_1, \tau_2, ..., \tau_L]^T$ is the vector containing the thresholds, where the size of τ_i is chosen to wrap each constellation within a $\tau_i \times \tau_i$ frame, such that the distance from the edge point to the boundary is half of its minimal distance $d_{\min}$. In the case of square-shaped M-QAM constellations considered for G.fast [35], we have $\tau_i = \sqrt{M_i} d_{\min}$, where M_i is the size of the constellation of the i-th symbol.

In certain cases, such as ZR-LR-RNS, where all the lines use the same constellation alphabet and thus $\tau_1 = \cdots = \tau_L$, we denote modulo gamma with a scalar subscript τ as

$$\mathbf{\Gamma}_{\tau}[\tilde{\mathbf{a}}] \triangleq \mathbf{\Gamma}_{\boldsymbol{\tau}}[\tilde{\mathbf{a}}], \quad \tau \triangleq \tau_1 = \cdots = \tau_L. \tag{2.29}$$

In general, every line uses different cardinality alphabet for which different modulo size is required (as shown in Table I), however LR processing strictly requires the same τ_i on each line, thus we need to select the maximal one, i.e., $\tau = \max_i \tau_i$.

2.4.1.4. Row Norm Scalar (RNS) Scaling Transmit Power Control

The per-line per-carrier transmit power constraints in (2.2) are enforced in ZF-LR-RNS by using a scalar scaling (see Fig. 2.14), which is obtained as

$$g = \frac{1}{\left\|\tilde{\mathbf{F}}\right\|_C}, \tag{2.30}$$

where row norm $\|\star\|_C$ can be expressed as $\left\|\tilde{\mathbf{F}}\right\|_C \triangleq \sqrt{\max_i \sum_{j=1}^{L} \left|\tilde{f}_{ij}\right|^2}$.

2.4.1.5. SNR Analysis

The decision variable at the CPEs side is

$$\hat{\mathbf{y}} = \mathbf{\Gamma}_{\boldsymbol{\tau}}\left[\mathrm{y}/g\right] = \mathbf{\Gamma}_{\boldsymbol{\tau}}\left[\left(\mathbf{HF}\tilde{\mathbf{x}} + \mathbf{w}\right) 1/g\right], \tag{2.31}$$

where $\tilde{\mathbf{x}} = \mathbf{\Gamma}_{\boldsymbol{\tau}}[\mathbf{T}^{-1}\mathbf{a}]$.

After some matrix and modulo arithmetic manipulations, the decision variable at i-th CPE reads

$$\hat{y}_i = \Gamma_{\tau}\left[a_i + {}^{w_i}/_g\right] \simeq a_i + {}^{w_i}/_g, \tag{2.32}$$

where in the last approx. equality we assume that in a well-designed system $\Pr\left(|{}^{w_i}/_{g}| > {}^{d_{min}}/_{2}\right)$ is very small [38], and the input of modulo Γ_τ is very unlikely to exceed the $\tau \times \tau$ frame. Equivalently, in multiple dimensions, the decision variable yields

$$\hat{\mathbf{y}} = {}^{1}/_{g}\left(\mathbf{HF}\tilde{\mathbf{x}} + \mathbf{w}\right) + \tilde{\mathbf{d}} = \mathbf{a} + \mathbf{Td} + {}^{\mathbf{w}}/_{g} + \tilde{\mathbf{d}} \simeq \mathbf{a} + {}^{\mathbf{w}}/_{g}, \tag{2.33}$$

where $\mathbf{Td} + \tilde{\mathbf{d}} \simeq \mathbf{0}$ summarizes the effect of modulo arithmetic. We conclude that SNR at the decision variable is

$$\gamma_i = g^2. \tag{2.34}$$

From 2.34 is directly follows that the SNR γ_i is the same for all lines and driven by the line with the weakest channel, which implies highly unfavorable performance in case of asymmetric strength of lines e.g., when the lines have different lengths.

2.4.2. Lattice-Reduction Aided Zero-Forcing Precoding with Vector Scaling Power Control

In this section, we propose a novel scheme, denoted ZF-LR-OPA, which enables the control and adaptation of transmitted power per-line individually. This is done modifying the ZF-LR-RNS by the introduction of per-line individual scaling matrix

$$\mathbf{G} = \mathrm{diag}\left(\mathbf{g}\right) = \mathrm{diag}\left(\left[g_1, g_2, \ldots, g_L\right]^T\right). \tag{2.35}$$

Let us consider the ZF-LR-RNS scheme in Fig. 2.14. Note that simply replacing scalar g with power allocation matrix $\mathbf{G}$ right after the feedforward matrix is not possible since the chain $\mathbf{H}^{-1}\mathbf{GHG}^{-1}$ would not simplify. Therefore matrix $\mathbf{G}$ is incorporated into the feedforward filter matrix as

$$\mathbf{F} = \mathbf{H}^{-1}\mathbf{GT}, \tag{2.36}$$

where matrix $\mathbf{T}$ is obtained by lattice reduction $\tilde{\mathbf{F}} = \mathbf{H}^{-1}\mathbf{T}$ applied to the columns of $\mathbf{H}^{-1}$. The block scheme of per-line power controlled ZF-LR is shown in Fig. 2.15.

Similarly to (2.33), the decision variable is

$$\hat{\mathbf{y}} = \mathbf{G}^{-1}\mathbf{y} + \tilde{\mathbf{d}} = \mathbf{G}^{-1}\left(\mathbf{HF}\tilde{\mathbf{x}} + \mathbf{w}\right) + \tilde{\mathbf{d}} \simeq \mathbf{a} + \mathbf{G}^{-1}\mathbf{w} \tag{2.37}$$

and the corresponding SNR at the line i-th

$$\gamma_i = g_i^2. \tag{2.38}$$

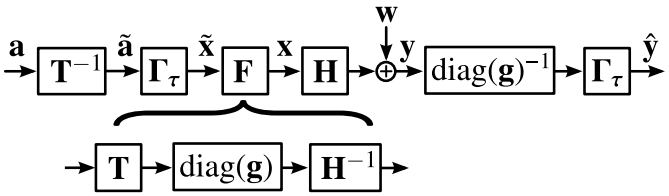

Figure 2.15.: Per-line power controlled Zero-Forcing (ZF) precoding scheme aided by Lattice-Reduction (LR).

2.4.2.1. Parallel Implementation of ZF-LR Precoding

If we denote $\mathbf{T}^{-1} = \tilde{\mathbf{T}} = [\mathbf{t}_1, \mathbf{t}_2, \dots \mathbf{t}_L]^T$, then the signal entering feedforward filter is

$$\tilde{\mathbf{x}} = \boldsymbol{\Gamma}_\tau[\tilde{\mathbf{a}}] = \boldsymbol{\Gamma}_\tau[\tilde{\mathbf{T}}\mathbf{a}] = \left[\Gamma_\tau\left[\mathbf{t}_1^T\mathbf{a}\right], \Gamma_\tau\left[\mathbf{t}_2^T\mathbf{a}\right], \dots, \Gamma_\tau\left[\mathbf{t}_L^T\mathbf{a}\right]\right]^T, \tag{2.39}$$

which can be implemented in parallel. This implies a substantial advantage in terms of latency with respect to THP (see Fig. 2.5, assume $\mathbf{E} = \mathbf{I}$), as the feedback loop implements the inversion of the triangular matrix $\mathbf{B} = \mathrm{diag}\,(\mathbf{R})^{-1}\,\mathbf{R}^H$ by back substitution, i.e., sequential interference cancellation, with modulo $\boldsymbol{\Gamma}_{\boldsymbol{\tau}}$. In particular, the feedback loop in Fig. 2.5, implements the operation described in Fig. 2.16 as

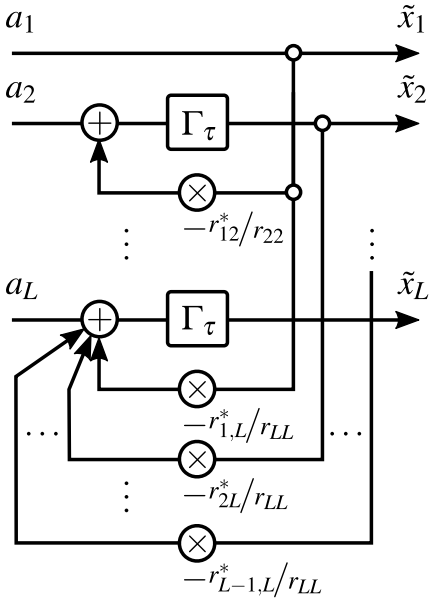

Figure 2.16.: Sequential processing of THP.

$$\tilde{x}_i = \Gamma_\tau \left[a_i - \frac{r^*_{1,i}}{r_{ii}} \tilde{x}_1 - \frac{r^*_{2,i}}{r_{ii}} \tilde{x}_2 \cdots - \frac{r^*_{i-1,i}}{r_{ii}} \tilde{x}_{i-1} \right]. \tag{2.40}$$

This confirms that, due to the sequential processing (2.40) (i.e.,$\{\tilde{x}_1, \ldots, \tilde{x}_{i-1}\}$ are required to obtain $\tilde{x}_i$), THP scheme generates additional processing delay which is linearly proportional to the number of lines L.

2.4.3. Optimized Power Allocation for ZF-LR Precoding

Controlling the power allocation of transmitted signal by scaling matrix $\mathbf{G}$ that is included into the definition of feedforward filter makes the optimization task more challenging.

Let us consider the weighted sum-rate utility function u to be optimized

$$u(\mathbf{g}) = \sum_{i=1}^{L} w_i \log_2 \left(1 + \frac{g_i^2}{\Gamma} \right), \tag{2.41}$$

where $\sum_{i=1}^{L} w_i = 1$ are the weights set to properly respect e.g., line lengths and Γ is Shannon gap to capacity [26].

Including per-line per-carrier power constraint (See (2.2)), the optimization problem yields

$$\begin{aligned} &\text{maximize} \quad u(\mathbf{g}) \\ &\text{subject to} \quad E\left[|x_i|^2 \right] \leq 1, \end{aligned} \tag{2.42}$$

where $E\left[|x_i|^2\right] = [\mathbf{\Phi}]_{ii} = \Phi_{ii}$ is the i-th diagonal entry of the covariance matrix $\mathbf{\Phi} = E[\mathbf{x}\mathbf{x}^H]$ of the transmitted signal $\mathbf{x} = \mathbf{F}\tilde{\mathbf{x}}$. Since signal $\tilde{\mathbf{x}}$ after modulo $\Gamma[\star]$ is approximately uncorrelated [62], its covariance matrix is approximately diagonal, i.e., $\tilde{\mathbf{\Phi}} = E\left[\tilde{\mathbf{x}}\tilde{\mathbf{x}}^H\right] \simeq \operatorname{diag}\left(\tilde{\Phi}_{11}, \ldots, \tilde{\Phi}_{LL}\right)$, where $\tilde{\Phi}_{ii} = E\left[|\tilde{x}_i|^2\right]$ represents the power at the i-th line. Finally, the transmitted signal power can be expressed as

$$E\left[|x_i|^2\right] = E\left[\left| \sum_{j=1}^{L} f_{ij} \tilde{x}_j \right|^2 \right] = \sum_{j=1}^{L} |f_{ij}|^2 E\left[|\tilde{x}_j|^2\right] = \sum_{j=1}^{L} |f_{ij}|^2 \tilde{\Phi}_{jj}. \tag{2.43}$$

Let us analyze the structure of $\mathbf{F} = \mathbf{H}^{-1}\mathbf{G}\mathbf{T}$ in more details in simple 2×2 example, where we denote $\tilde{\mathbf{H}} = \mathbf{H}^{-1}$ to ease the notation:

$$\mathbf{F} = \begin{bmatrix} \tilde{h}_{11} & \tilde{h}_{12} \\ \tilde{h}_{21} & \tilde{h}_{22} \end{bmatrix} \begin{bmatrix} g_1 & 0 \\ 0 & g_2 \end{bmatrix} \begin{bmatrix} t_{11} & t_{12} \\ t_{21} & t_{22} \end{bmatrix}, \tag{2.44}$$

so the generic ij-th element of $\mathbf{F}$ is $f_{ij} = \sum_{k=1}^{L} \tilde{h}_{ik} g_k t_{kj}$ and for instance

$$|f_{11}|^2 = g_1^2 \left|\tilde{h}_{11} t_{11}\right|^2 + g_2^2 \left|\tilde{h}_{12} t_{21}\right|^2 + 2 g_1 g_2 \Re\left[\tilde{h}_{11} t_{11} \tilde{h}_{12}^* t_{21}^*\right]. \tag{2.45}$$

Similarly to (2.45), general $|f_{ij}|^2$ is a quadratic form in variables g_i. Hence, considering the convex utility function (2.41), the optimization problem (2.42) is close to be a Signomial Program (SP), that is a generalization of the well known Geometric Program (GP)[54, 55]. It can be shown that $|f_{ij}|^2$ is a quadratic form even when $\tilde{\mathbf{x}}$ is slightly correlated after modulo $\Gamma[\star]$ and even if an average transmit power constraint is assumed. Notice that utility function (2.41) is not exactly in the form required by SP, however it is a well-known convex function and in the high SNR regime it can be easily approximated by a posynomial [54]. Although SPs cannot in general be turned into convex optimization problems, they can be solved by a number of efficient algorithms recently proposed in the literature [54, 55, 56, 57]. Here, in order to demonstrate the viability of ZF-LR-OPA, we use computationally efficient interior point method providing only a locally optimal solution to SP. We set starting values to be given by RNS obtaining a solution that cannot be worse than ZF-LR-RNS.

2.4.4. Performance Evaluation

2.4.4.1. Linear Precoding Reference Methods

For the reference and comparison purposes, we define linear canonical precoding methods considered here.

Zero-Forcing Precoding with Row Norm Scaling ZF-RNS depicted in Fig. 2.17 implements channel inversion as $\mathbf{F} = \mathbf{H}^{-1}$, where $g = \frac{1}{\|\mathbf{F}\|_C}$ is the scalar scaling factor set to fulfill the per-line per-carrier power constraint (2.2). SNR at the

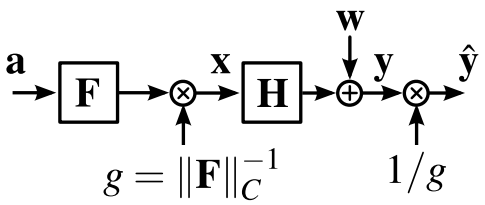

Figure 2.17.: Zero-Forcing (ZF) precoding scheme using Row Norm Scaling (RNS).

decision variable yields $\gamma_i = g^2$.

Diagonal Precoding DP, adopted in VDSL2, can be described similarly as ZF-RNS with $\mathbf{F} = \mathbf{H}^{-1}\text{diag}(\mathbf{H})$ [25].

Zero-Forcing Precoding with Per-line Optimized Power Allocation ZF-OPA depicted in Fig. 2.18 implements channel inversion as $\mathbf{F} = \mathbf{H}^{-1}$, however individual per-line power optimization matrix $\mathbf{G}$ is applied [27], [37]. The SNR at the decision

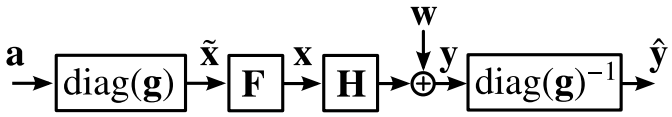

Figure 2.18.: Zero-Forcing (ZF) precoding scheme with per-line Optimized Allocation Power (OPA).

variable at the i-th line is the same as in (2.38) where the coefficients g_i are obtained maximizing the weighted sum-rate utility function (2.41) subject to per-line per-carrier power constraint (2.2) as

$$\begin{array}{ll} & \text{maximize} \quad u(\mathbf{g}) \\ \text{subject to} & E\left[|x_i|^2\right] = \sum_{j=1}^{L} g_j^2 \, |f_{ij}|^2 \leq 1 \end{array} , \tag{2.46}$$

where f_{ij} is the ij-th element of the inverse channel $\mathbf{H}^{-1}$. Notice that unlike in case of LRA-ZF, transmitted power constraint is a linear function in g_i^2 which makes the whole optimization problem (2.46) convex and thus relatively easy to solve [63].

2.4.4.2. Numerical Results

Aggregated rates over tested cable described in Section 2.2.2 are shown in Fig. 2.19 and Table 2.4 using the parameters summarized in Table 2.2. All the OPA schemes use utility function (2.41) with identical weights i.e., mean-rate utility function. To perform the LR step we employed the popular low-complexity LLL algorithm with parameter $\delta = 3/4$ [39]. We notice that ZF-LR-OPA outperforms all the reference linear precoding methods. The power optimization with identical weights leads to a fair scheme where the performance are similar among the lines and uniformly better then the standard ZF-LR-RNS. Notice that, in the considered scenario, ZF-LR-OPA provides the highest minimum rate among all the methods compared in this section, including canonical non-ordered THP [26]. However, from the comparison between 2.4 and 2.3, it follows that ZF-LR-OPA can be easily outperformed in terms of minimum rate by acting on the ordering of interference cancellation in THP, which is the price to pay in order to allow for the parallel implementation.

Table 2.4.: Mean and minimum aggregated rates of several FEXT cancellation precoding schemes depicted in Fig. 2.19. The rates are in Mbits/s.

Acronym	Precoding Scheme	[mean,min]-rate
DP	Diagonal Precoding	[552, 432]
ZF-RNS	Zero-Forcing with Row Norm Scaling	[528, 528]
ZF-OPA	ZF with Optimized Power Allocation	[680, 567]
ZF-LR-RNS	ZF aided by Lattice-Reduction with RNS	[724, 724]
ZF-LR-OPA	ZF aided by LR with OPA	[783, 754]
ZF-THP	ZF Tomlinson-Harashima Precoding	[970, 678]
Single Line	Single Line (without FEXT)	[861, 681]

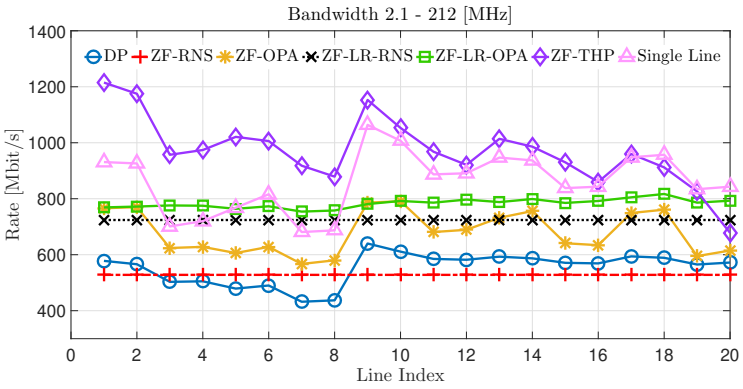

Figure 2.19.: Performance over paper insulated P-ALT 100m cable.

2.5. Concluding Remarks

In this chapter, non-linear Far-End-CrossTalk (FEXT) cancellation precoding techniques have been investigated for next generation DSL standard, namely G.fast.

In particular, the first part of the chapter has been devoted to the design of a novel ordered Tomlinson-Harashima Precoding (THP) scheme aided by a Dynamic Ordering (DO) strategy, which has been proved to provide the highest minimum rate in G.fast downstream for the considered scenario. Unlike existing ordered Equal Rate (ER) THP scheme, the proposed scheme better adapts to asymmetric channel statistics of G.fast channel. Although the results are related to concrete G.fast settings, the proposed scheme has universal application in general multiple-input multiple-output systems including wireless scenario (e.g., paper [48] shows that sum-rate of THP is always higher or equal than sum-rate of ER-THP when the same type of channel matrix decomposition is considered).

In the second part of the chapter, a novel nonlinear FEXT cancellation precoding

based on Lattice Reduction (LR) aided Zero-Forcing (ZF) with per-line individual power control has been proposed for G.fast downstream. The advantage with respect to THP-based precoding techniques is that LR-ZF-OPA allows for the parallelization of the nonlinear modulo operation, which does not cause additional processing delay. However, the price to pay for the parallel implementation of LR-ZF-OPA is in terms of minimum user rate, which is lower then the one achieved by THP with DO.

3. Parallelazing Tomlinson-Harashima Precoding in G.fast Downstream

3.1. Introduction

G.FAST is the latest Digital Subscriber Line (DSL) standard recently approved by the International Telecommunication Union (ITU) for ultra-broadband access technology utilizing existing copper line infrastructure to form a hybrid fiber-copper Fiber-To-The-distribution-point (FTTdp) architecture [22]. G.fast aims to achieve aggregated rates up to 1 Gbps over short length copper lines (typically 100 m) between Central Office (CO) and Consumer Premised Equipments (CPEs). The first G.fast standard release assumes 106 MHz bandwidth profile to be later extended to 212 MHz [23]. The usage of wider cable bandwidth allows for higher communication rates but, at the same, it also poses some serious challenges. As seen in Chapter 2, at these frequencies, Far-End-CrossTalk (FEXT), which is the crosstalk interference arising between pairs at the opposite ends of the cable binder, is very strong and often overcomes the direct lines. As a consequence, crosstalk mitigation techniques (denoted as precoding or vectoring) have a major impact on the system performance, and need to be carefully designed.

In DownStream (DS) direction covered here, DSL receivers, or CPEs, are usually decentralized, and thus they cannot cooperate for DS interference cancellation. As a consequence, DS FEXT mitigation techniques are usually performed centrally at the transmitter side by a Vector Processor (VP), which is hosted in the DSL Access Multiplexer (DSLAM) or directly in the Central Office (CO). The group of all lines that terminate in the same VP is denoted as vectored group. In a multiple vectored DSL system, where several vectored groups coexist in the same cable binder, FEXT among pairs belonging to the same vectored group, denoted here as In-Domain (ID) self-FEXT, is canceled through vectoring performed at the VP of each vectored group. However, uncanceled crosstalk due to other vectored groups, denoted here as Out-of-Domain (OD) FEXT, can cause a remarkable performance degradation to all the lines.

In this regards, Dynamic Spectrum Management (DSM) techniques [36], such as Optimal Spectrum Balancing (OSB) [64] and Joint DSM 2/3 [65], have been

proposed to cope with OD FEXT. OSB aims at maximizing the minimum DS data-rate for a specific vectored group, while the others are constrained to a target data rate. Joint DSM 2/3 exploits the properties of the channels to design precoding techniques to cancel FEXT within each group, while OSB algorithm is used to balance the usage among different vectored groups. Unfortunately, both techniques could be beneficial only for cable binders that contain few twisted-pairs, as they require an external processing unit that hosts the complex spectrum management algorithm to jointly balance all the lines.

Another possibility to cope with OD FEXT is by exploiting cooperation between the VPs of different vectored groups. By exchanging information through an external coordination engine, the VPs can cooperatively cancel OD FEXT in a centralized fashion by performing any of the interference mitigations techniques conventionally employed in DSL systems, and thus achieving full vectoring gain for all the vectored groups [66]. The most challenging task in designing DSL transmit precoding techniques is to achieve a satisfactory degree of FEXT mitigation, while limiting both computational complexity and latency of signal processing algorithms.

In this direction, in the previous chapter, two non-linear interference mitigation techniques, namely Tomlinson-Harashima Precoding with Dynamic Ordering (THP-DO) and Lattice-Reduction Aided Zero-Forcing Precoding with Optimal Power Allocation (ZF-LR-OPA), have been proposed for the DS of G.fast systems. From the one hand, THP-DO achieves the highest minimum rate among both linear and non-linear existing precoding techniques, however, it is not appropriate for large cable binders (e.g., that contain hundreds of twisted pairs) due to the sequential back-substitution processing delay and the complexity inherent of conventional THP. From the other hand, ZF-LR-OPA can be executed in parallel (i.e., without additional processing delay) but the price to pay is in term of user rate, which is significantly lower than the one achieved by THP-based techniques. Following these considerations, this chapter focuses on a novel parallel hybrid linear/nonlinear precoding architecture, whose goal is to achieve a good trade-off among complexity, performance, and latency.

3.1.1. Chapter Contribution

To provide a flexible and scalable precoding structure trading over computational complexity, achievable user rate, and processing delay, in this chapter we propose a novel DSL architecture in which a single DSL Access Multiplexer (DSLAM) hosts multiple VP modules. These VPs can either be hosted within a single integrated circuit with multiple boards interconnected though the backplane, or on multiple integrated circuits that are interconnected via ultra-high speed copper traces. The proposed architecture, referred to as Multi-VP THP, reduces both processing delay and complexity of conventional THP through the parallelization of THP over the multiple VPs, that cooperate (i.e., through cross-VP connections) by exchanging

the precoded data in order to minimize both OD FEXT and ID self-FEXT at the CPEs. Multi-VP THP contains a two level interference cancellation mechanism: OD FEXT mitigation is based on linear Block Diagonalization (BD) [67], while ID self-FEXT is cancelled by THP [26] performed simultaneously at each VP. The information exchanged enables all the VPs to perform vectoring at their local vectoring engine.

3.1.2. Contribution in International Conferences/Journals

Part of the material presented in this chapter has been published in:

- S. H. R. Naqvi, **A. Matera**, X. Wang, A. H. Fazlollahi, and U. Spagnolini, "Multi-Vector Tomlinson-Harashima Precoding in G.fast Downstream System" in *2016 IEEE International Conference on Communication Systems (ICCS)*, pp. 1–6, IEEE, 2016.

3.2. Multi-VP DSL System Model

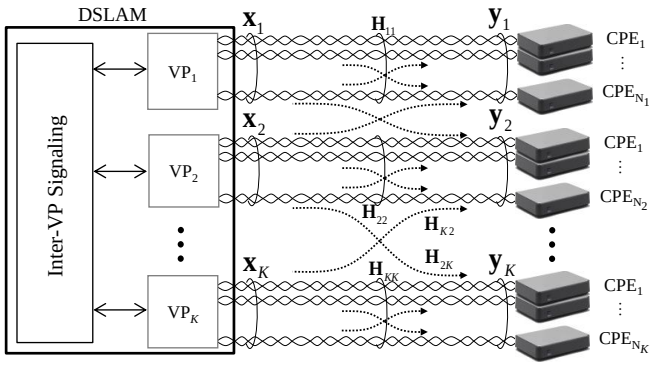

Figure 3.1.: Cooperative Multi-VP G.fast DSL system for K VPs with N_k CPEs each in downstream.

Multi-VP DSL system for DS is shown in Fig. 3.1, where K vectored groups share the same cable binder, and thus interfere with each other at the CPEs. The k-th VP serves N_k CPEs where the number of CPEs can be arbitrarily different, i.e., $N_1 \neq N_2 \neq \ldots \neq N_K$. The frame structure is tailored to have all the CPEs in the system synchronized in DS to avoid NEXT and inter-carrier interference due to any frequency drift.

The linear model for the signal received at the CPEs belonging to the k-th VP is

$$\mathbf{y}_k = \mathbf{H}_{kk}\mathbf{x}_k + \sum_{m \neq k} \mathbf{H}_{km}\mathbf{x}_m + \mathbf{w}_k, \tag{3.1}$$

where $\mathbf{x}_k$ and $\mathbf{x}_m$ denote the $N_k \times 1$ and $N_m \times 1$ ensemble of the signals transmitted to the CPEs belonging to k-th and m-th VPs, respectively. The Gaussian noise is $\mathbf{w}_k \sim \mathcal{CN}(0, \sigma_w^2 \mathbf{I})$. The $N_k \times N_m$ channel matrix $\mathbf{H}_{km}$ represents the $m \to k$ DSL channel from the m-th VP to the group of CPEs connected to k-th VP (i.e., CPE_1, CPE_2,...,CPE_{N_k}): it accounts for OD FEXT, for $k \neq m$, and for ID self-FEXT, for $k = m$. We assume that full Channel State Information (CSI) is locally available at each VP.

3.3. Multi-VP THP

The proposed multi-VP THP for multi-VP DSL systems (see Fig. 3.1) mitigates the OD FEXT using BD [67], thus turning the Multi-VP MISO (MVP-MISO) system in Fig. 3.1 into K parallel Single-VP MISO (SVP-MISO) systems. Then, channel matrix of each SVP-MISO can be diagonalized by using any methods such as the low-complexity technique recently proposed in [68] for next generation DSL systems. Here we assume that, after the BD step, conventional THP [26] is adopted to mitigate ID self-FEXT in parallel at each of the K SVP-MISO systems, thus making THP scalable by groups of lines.

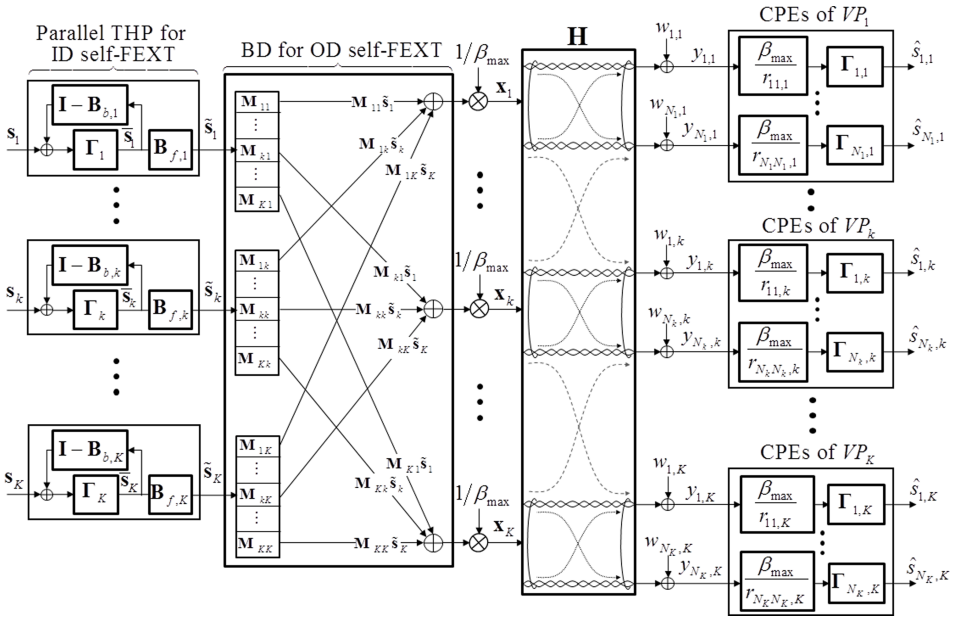

Figure 3.2.: Multi-Vector THP for K VPs.

3.3.1. Precoding Structure of Multi-VP THP

The precoded transmitted symbol vector $\mathbf{x}_k$ in (3.1) is computed locally at the k-th VP as the summation of the precoded symbols $\mathbf{F}_{kk}\mathbf{s}_k$ for the CPEs connected to k-th VP and the precoded symbols forwarded by all the other $K-1$ VPs to the k-th VP over the high-speed link. Hence, the aggregated transmit signal is

$$\mathbf{x}_k = \mathbf{F}_{kk}\mathbf{s}_k + \sum_{m\neq k} \mathbf{F}_{km}\mathbf{s}_m, \tag{3.2}$$

where $\mathbf{s}_m$ are the M-QAM constellation symbols intended to the CPEs connected to the m-th VP, and $\mathbf{F}_{km}$ is the matrix that precodes the signal intended to the CPEs connected to the m-th VP and relayed by the k-th VP. From (3.1) and (3.2), we obtain

$$\mathbf{y}_k = \underbrace{\mathbf{H}_{kk}\mathbf{F}_{kk}\mathbf{s}_k}_{A} + \underbrace{\sum_{m\neq k} \mathbf{H}_{km}\mathbf{F}_{mk}\mathbf{s}_k}_{B} + \underbrace{\sum_{m}\sum_{l\neq k} \mathbf{H}_{km}\mathbf{F}_{ml}\mathbf{s}_l}_{C} + \mathbf{w}_k, \tag{3.3}$$

where A is the ID self-FEXT, B is the signal relayed by the $K-1$ VPs toward the N_k CPEs of VP k-th, and C is OD-FEXT. Collecting the channels towards the CPEs of the k-th VP into the compound channel matrix

$$\mathbf{H}_k = [\mathbf{H}_{k1}, \mathbf{H}_{k2}, ..., \mathbf{H}_{kK}] \tag{3.4}$$

and, similarly, all the linear filters used to precode the signals for the CPEs of the k-th VP into the matrix

$$\mathbf{F}_k = \left[\mathbf{F}_{1k}^T, \mathbf{F}_{2k}^T, ..., \mathbf{F}_{Kk}^T\right]^T, \tag{3.5}$$

the model (3.3) conveniently reduces to

$$\mathbf{y}_k = \mathbf{H}_k\mathbf{F}_k\mathbf{s}_k + \sum_{l\neq k}\mathbf{H}_k\mathbf{F}_l\mathbf{s}_l + \mathbf{w}_k, \tag{3.6}$$

where the signal of interest and interference are decoupled. As it will be motivated below in Sec. 3.3.2, it is convenient to decompose $\mathbf{F}_k$ as

$$\mathbf{F}_k = \mathbf{M}_k\mathbf{B}_k, \tag{3.7}$$

where $\mathbf{M}_k$ is the $N_{Tot}\times N_k$ precoding matrix for all the VPs, $N_{Tot} = \sum_{k=1}^{K} N_k$ is the total number of CPEs in the system, and the $N_k \times N_k$ precoding $\mathbf{B}_k$ is related only to the k-th VP. Eq. ((3.6)) can be rearranged as

$$\mathbf{y}_k = (\mathbf{H}_k\mathbf{M}_k)\,\mathbf{B}_k\mathbf{s}_k + \sum_{l\neq k}(\mathbf{H}_k\mathbf{M}_l)\,\mathbf{B}_l\mathbf{s}_l + \mathbf{w}_k. \tag{3.8}$$

The OD FEXT is completely cancelled if $\mathbf{H}_k\mathbf{M}_l = \mathbf{0}$, for $\forall l \neq k$, or, equivalently, using algebraic arguments: $\text{Span}\{\mathbf{M}_l\} \subseteq \underset{l\neq k}{\cup} \text{Null}\{\mathbf{H}_k\}$ (Sec. 3.3.2). Once the OD FEXT is cancelled by a judicious choice of $\{\mathbf{M}_l\}$, the received signal in (3.8) becomes

$$\mathbf{y}_k = (\mathbf{H}_k\mathbf{M}_k)\,\mathbf{B}_k\mathbf{s}_k + \mathbf{w}_k. \tag{3.9}$$

$\mathbf{B}_k$ is designed to cancel the ID self-FEXT of the $N_k \times N_k$ effective SVP-MISO equivalent channel $\mathbf{H}_k\mathbf{M}_k$ employing THP. The THP precoding filter $\mathbf{B}_k$ is thus decomposed as $\mathbf{B}_k = \mathbf{B}_{f,k}\mathbf{B}_{b,k}^{-1}$ into a feedback filter ($\mathbf{B}_{b,k}$) and a feed-forward filter ($\mathbf{B}_{f,k}$), which are obtained by the QR decomposition of the effective SVP-MISO channel [26] as

$$(\mathbf{H}_k\mathbf{M}_k)^H = \mathbf{Q}_k\mathbf{R}_k, \tag{3.10}$$

where $\mathbf{Q}_k$ is a unitary matrix and $\mathbf{R}_k$ is a upper triangular matrix. The feed-forward filter at k-th VP for multi-VP THP is

$$\mathbf{B}_{f,k} = \mathbf{Q}_k. \tag{3.11}$$

The feedback branch at k-th VP (see Fig. 3.2) implements the inversion of the feedback filter

$$\mathbf{B}_{b,k} = \text{diag}\,(\mathbf{R}_k)^{-1}\,\mathbf{R}_k^H, \tag{3.12}$$

while limiting the transmitted signal power by the complex modulo operator $\mathbf{\Gamma}_k$ [37]. As common in THP (see Chapter 2), the symbols for the CPEs that belong to the k-th VP at the output of the feedback block, , denoted as $\bar{\mathbf{s}}_k = [\bar{s}_{1,k}, \bar{s}_{2,k}, ..., \bar{s}_{N_k,k}]^T$, are obtained by sequential back-substitutions as

$$\begin{cases} \bar{s}_{1,k} = s_1 \\ \bar{s}_{2,k} = \Gamma_{2,k}\left[s_{2,k} - \frac{r_{21,k}}{r_{22,k}}\bar{s}_{1,k}\right] \\ \vdots \\ \bar{s}_{N_k,k} = \Gamma_{N_k,k}\left[s_{N_k,k} - \overset{[}{m} = 1]N_k - 1\sum \frac{r_{N_k m,k}}{r_{N_k N_k,k}}\bar{s}_{m,k}\right] \end{cases}, \tag{3.13}$$

where the complex-valued modulo operator Γ for any precoded symbol z (i.e., $\Gamma[z]$) is defined as

$$\Gamma[z] = z - 2\sqrt{M}\left\lfloor \frac{\Re(z) + \sqrt{M}}{2\sqrt{M}} \right\rfloor - j2\sqrt{M}\left\lfloor \frac{\Im(z) + \sqrt{M}}{2\sqrt{M}} \right\rfloor. \tag{3.14}$$

Here $2\sqrt{M}$ defines the boundary region for M-QAM constellation to make sure that the precoded symbol z lies within the constellation boundaries, hence avoiding any undesired power increment. Notice that modulo operator Γ introduces a small signal power increment at the output of feedback block that is equal to $M/(M-1)$, hence the power of the transmitted signal must be scaled down accordingly for M-QAM constellation as discussed in [37]. To fulfill the per-line per-carrier power constraints typical of G.fast systems [35], after the BD linear precoding filter $\mathbf{M} = [\mathbf{M}_1, \mathbf{M}_2, \ldots, \mathbf{M}_K]$, the transmitted signal is normalized by a scaling factor $\beta_{max} = \sqrt{\max_i \sum_{j=1}^{N_{Tot}} |\mathbf{M}[i,j]|^2}$, as shown in Fig. 3.2. The signal at the CPEs of the k-th vectored group is

$$\mathbf{y}_k = \frac{1}{\beta_{max}} \text{diag}\left(\mathbf{R}_k\right) \mathbf{s}_k + \mathbf{w}_k. \tag{3.15}$$

Therefore, the decision variable of the j-th CPE connected to k-th VP is

$$\hat{s}_{j,k} = s_{j,k} + \beta_{max} w_{j,k} / r_{jj,k}, \tag{3.16}$$

where $r_{jj,k}$ is the j-th diagonal entry of the triangular matrix $\mathbf{R}_k$. It follows from (3.16) that the SNR at the decision variable is

$$SNR_{j,k} = \frac{r_{jj,k}^2}{\beta_{max}^2} SNR_{input}, \tag{3.17}$$

where SNR_{input} is the transmitted signal SNR.

3.3.2. OD FEXT Mitigation

OD FEXT mitigation is based on linear precoding in order to block diagonalize the compound channel matrix $\mathbf{H} = [\mathbf{H}_1^H, \mathbf{H}_2^H, ..., \mathbf{H}_K^H]^H$ [67]. The optimal precoding matrix $\mathbf{M}_k$ in (3.7) is computed at the k-th VP from the CSI available at k-th VP so that the range space of $\mathbf{M}_k$ lies in the null space of the channels of all the other $K-1$ VPs. In this perspective, the complementary channel matrix $\tilde{\mathbf{H}}_k$ for the k-th VP is the ensemble channel matrix that includes all the rows of the block partitioned channel matrix $\mathbf{H}$ except the k-th row belonging to the k-th group of CPEs:$\tilde{\mathbf{H}}_k = \left[\mathbf{H}_1^H, \ldots, \mathbf{H}_{k-1}^H, \mathbf{H}_{k+1}^H, \ldots, \mathbf{H}_K^H\right]^H$. The precoder $\mathbf{M}_k$ at k-th VP is computed by the Singular Value Decomposition (SVD) of $\tilde{\mathbf{H}}_k$ as

$$\tilde{\mathbf{H}}_k = \tilde{\mathbf{U}}_k \tilde{\mathbf{\Sigma}}_k \tilde{\mathbf{V}}_k^H = \tilde{\mathbf{U}}_k \tilde{\mathbf{\Sigma}}_k \begin{bmatrix} \tilde{\mathbf{V}}_k^{(1)} & \tilde{\mathbf{V}}_k^{(0)} \end{bmatrix}^H, \tag{3.18}$$

where $\tilde{\mathbf{U}}_k$, $\tilde{\mathbf{\Sigma}}_k$ and $\tilde{\mathbf{V}}_k$ contain respectively the left singular vectors, singular values and right singular vectors of $\tilde{\mathbf{H}}_k$.

3.3.2.1. Zero-Forcing BD (ZF-BD)

The last N_k right singular vectors of $\tilde{\mathbf{H}}_k$ (i.e., $\tilde{\mathbf{V}}_k^{(0)}$) provide the basis for the null space for $\tilde{\mathbf{H}}_k$, hence the precoding matrix $\mathbf{M}_k$ for ZF-BD at k-th VP is simply

$$\mathbf{M}_k = \tilde{\mathbf{V}}_k^{(0)}. \tag{3.19}$$

The overall channel matrix $\mathbf{H}$ after ZF-BD precoding $\mathbf{M} = [\mathbf{M}_1, \mathbf{M}_2, ..., \mathbf{M}_K]$ becomes perfectly block diagonal:

$$\mathbf{HM} = \text{blockdiag}[\mathbf{H}_1\mathbf{M}_1,\, \mathbf{H}_2\mathbf{M}_2,\, \ldots,\, \mathbf{H}_K\mathbf{M}_K]. \tag{3.20}$$

3.3.2.2. Minimum Mean Square Error BD (MMSE-BD)

Multi-VP THP based on ZF-BD mimics the centralized THP with comparable performances only if OD FEXT is not excessively high and in the high SNR region (see Sec. 3.4). Similarly to multi-user wireless systems, the BD can include some regularizing terms that trade some residual OD-FEXT at CPEs with the same level of background noise [69]:

$$\mathbf{M}_k = \tilde{\mathbf{V}}_k \left(\tilde{\mathbf{\Sigma}}_k^T \tilde{\mathbf{\Sigma}}_k + N_{Tot}\sigma_w^2 \mathbf{I} \right)^{-1/2}, \tag{3.21}$$

where $\tilde{\mathbf{\Sigma}}_k$ and $\tilde{\mathbf{V}}_k$ are computed as in (3.18). The QR factorization of the effective channel for MMSE-BD at k-th SP is

$$(\mathbf{H}_k\mathbf{M}_k)^H = \begin{bmatrix} \mathbf{Q}_{k1} & \mathbf{Q}_{k2} \end{bmatrix} \begin{bmatrix} \mathbf{R}_k \\ \mathbf{0} \end{bmatrix}, \tag{3.22}$$

where $\mathbf{Q}_{k1}$ and $\mathbf{R}_k$ are used to compute the feed-forward ($\mathbf{B}_{f,k} = \mathbf{Q}_{k1}$) and feedback ($\mathbf{B}_{b,k} = \text{diag}\left(\mathbf{R}_k\right)^{-1} \mathbf{R}_k^H$) filters in THP for ID self-FEXT mitigation as shown in (3.12) and (3.11).

Remark 3.1. In this chapter, a single-DSLAM multi-VP DSL scenario is considered, meanwhile, the proposed multi-VP THP system architecture can also be applied for multi-DSLAM scenarios in which there are proper coordination between DSLAMs, see [66, 70].

3.3.3. Complexity Analysis and Latency

All the steps and the corresponding computational cost per VP of multi-VP THP and centralized THP are summarized in Table 1. Both the schemes are

Table 3.1.: Downstream Multi-VP THP: Algorithm steps, per VP complexity and comparison. [*) denotes all preparation steps]

Processing Steps	**Multi-VP THP**	**Centralized THP**
*) SVD of $\tilde{\mathbf{H}}_k$ for $\mathbf{M}_k$	$\mathcal{O}_C\left(N_{Tot}^3 - N_k N_{Tot}^2\right)$	
*) $\mathbf{H}_k\mathbf{M}_k$	$\mathcal{O}_C\left(N_k^2 N_{Tot}\right)$	
*) QR decomposition	$\mathcal{O}_C\left(N_k^3\right)$	$\mathcal{O}_C\left(N_{Tot}^3\right)$
*) $\mathbf{B}_{f,k}$ and $\mathbf{B}_{b,k}$	$\mathcal{O}_C\left(\frac{1}{2}N_k^2\right)$	$\mathcal{O}_C\left(\frac{1}{2}N_{Tot}^2\right)$
Local THP for $\tilde{\mathbf{s}}_k$	$\mathcal{O}_C\left(\frac{3}{2}N_k^2\right)$	$\mathcal{O}_C\left(\frac{3}{2}N_{Tot}^2\right)$
$\mathbf{M}_{mk}\tilde{\mathbf{s}}_k$	$\mathcal{O}_C\left(N_k N_{Tot}\right)$	

based on set of preliminary steps (denoted in Table 1 by *) that are carried out to compute the filters given the CSI, hence those steps must be executed just once, unless the channels change. It follows that the computational complexity for the preliminary steps is $\mathcal{O}_C\left(N_{Tot}^3 - N_k\left(N_{Tot}^2 - N_k^2\right) + N_k^2\left(N_{Tot} + 0.5\right)\right)$ and $\mathcal{O}_C\left(N_{Tot}^2\left(N_{Tot} + 0.5\right)\right)$ for multi-VP and centralized THP, respectively.

The cost of every iteration (i.e., the cost of every data transmission) includes only the processing of the data by THP in centralized THP, while in multi-VP THP it accounts for the processing by THP and OD FEXT cancellation matrix $\mathbf{M}_k$ (i.e., $\mathbf{M}_k\tilde{\mathbf{s}}_k$). Therefore, it is $\mathcal{O}_C\left(N_k\left(N_{Tot} + 1.5N_k\right)\right)$ and $\mathcal{O}_C\left(1.5N_{Tot}^2\right)$ for multi-VP and centralized THP, respectively. Notice that the total computational cost for both schemes scales with the number of DMT tones that for G.fast 106 MHz and 212 MHz band profiles is N_{tones} =2005 or 4051 [35]. Table 1 shows that the multi-VP THP computation cost per VP per iteration, as well as the computational cost per VP for the preliminary steps, are always lower than those of centralized THP, and they further reduce with by increasing the number of VPs.

Moreover, the parallelization of THP over the K VPs leads to a latency reduction with respect to the centralized THP, which roughly ranges from $1/K$ to $1/K^2$ depending on the precoding implementation structure.

3.4. Numerical Results

Performance of the proposed multi-VP THP schemes are validated and compared with the centralized precoding where a single VP performs conventional centralized THP for FEXT mitigation. We consider a DSL deployment where $K = 2$ and $K = 3$ VPs coexist in the same DSLAM. The performance of multi-VP THP is evaluated for fixed and variable cable length scenarios for G.fast Band-2 frequency (2-212 MHz) to validate the method in practical and challenging scenarios. The test loops considered here are for 20 pairs 0.6mm PE4D-ALT [71] and 10 pairs 0.5mm BT cables [72], where the parameters for direct links $[\mathbf{H}_{kk}]_{pp}$, ID self-FEXT ($[\mathbf{H}_{kk}]_{pq}$, $\forall p \neq q$) and OD FEXT channels ($\mathbf{H}_{km}$, $\forall k \neq m$) are measured

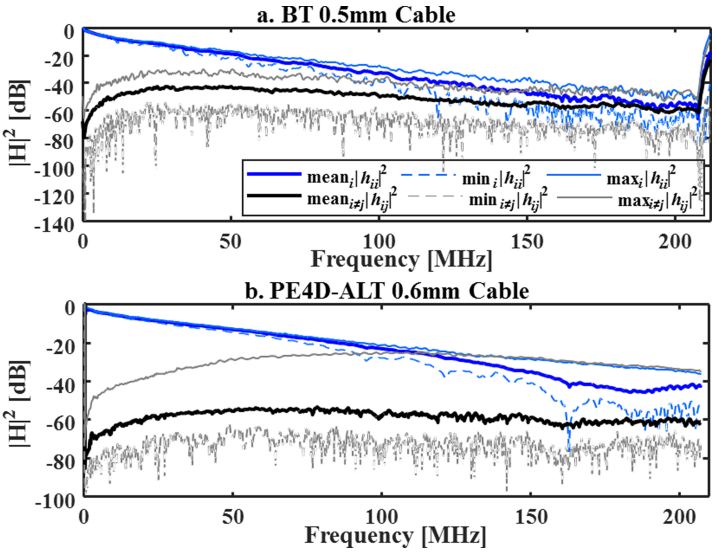

Figure 3.3.: Channel Characteristics of 100m PE4D-ALT (20 pairs) [71] and BT (10 pairs) [72] cables for G.fast frequency (2-212 MHz).

for G.fast frequency band as shown in Fig. 3.3. The data symbols "**s**" for each CPE depend on the SNR at the decision variable (SNR_D) for particular carrier frequency, and belong to M-QAM constellation that is normalized to unit energy for numerical convenience. The bit loading on the l-th sub-carrier depends on SNR_D according to the "gap-formula" widely adopted by the DSL community [73, 21]: $b_\ell = log_2\,(1 + SNR_{D,\ell}/Gap)$ with the Gap=10.8dB=6dB(SNR margin)+9.8dB(SNR gap)-5dB(coding gain). Loading bits range from 1 to 12 bits with 12% framing overhead. The power spectral density of the transmitted signal is set to -76dBm/Hz while the noise floor is assumed to be at -140dBm/Hz as customary [73, 21], therefore the maximum transmitted signal SNR is $SNR_{input} = 64dB$.

Fig. 3.4 shows the average spectral efficiency (average bit loading over frequency) for every CPE with $K = 2$ (solid lines) and $K = 3$ (dashed lines) VPs. The equal number of CPEs are connected to each VP that is 6 (i.e., $N_1 = N_2 = N_3 = 6$) for PE4D-ALT and 3 (i.e., $N_1 = N_2 = N_3 = 3$) for BT cables. Hence, the total number of CPEs for $K = 2$ and $K = 3$ VPs scenarios is $N_{Tot} = 12$ (or $N_{Tot} = 6$) and $N_{Tot} = 18$ (or $N_{Tot} = 9$) for PE4D-ALT (or BT) cable, respectively. All the CPEs are located 100m far away from the vectoring engine. Performance of the proposed multi-VP THP scheme are compared with two extreme cases: *i)* no-cooperation ($\times$), where each VP independently applies THP and treats OD FEXT as noise and *ii)* centralized THP vectoring ($*$). The SNR_D is used to compute the average sum throughput in Table 2. The ZF-BD multi-VP THP shows similar performance to centralized THP in the low frequency region (say up to $\approx 120MHz$) due to low level of OD FEXT. On the other hand, some minor

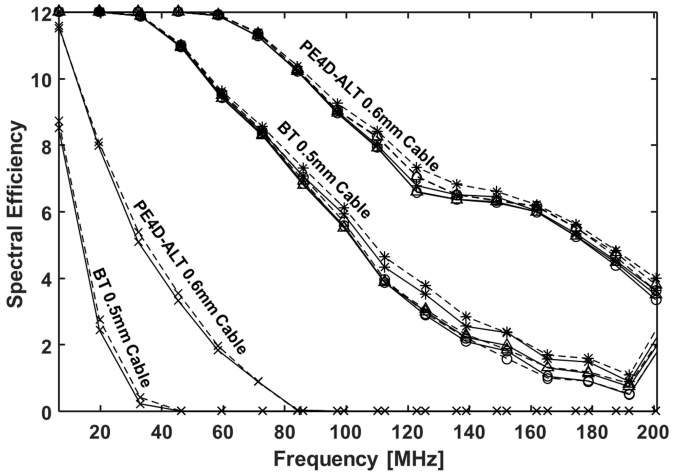

Figure 3.4.: Spectral efficiency vs frequency in G.fast (2-212 MHz) for $K = 2$ (solid), $K = 3$ (dashed) VPs with 6 CPEs each ($N_1 = N_2 = N_3 = 6$) for PE4D-ALT and 3 CPEs each ($N_1 = N_2 = N_3 = 3$) for BT cables at 100m distance. Precoding Method: Centralized THP ($*$), Multi-VP THP (ZF-BD) ($\bigcirc$), Multi-VP THP (MMSE-BD) ($\triangle$), No Cooperation THP ($\times$).

Table 3.2.: Average sum throughput per line (Mbps) vs VP cooperation (K=2, 3) for G. Fast band 2-212 MHz ($N_{PE4D-ALT}$=6, N_{BT}=3, cable:100m)

Precoding Scheme	PE4D-ALT		BT	
	K=2	K=3	K=2	K=3
Centralized THP	1570	1634	1133	1140
Multi-VP THP (ZF-BD)	1556	1601	1078	1035
Multi-VP THP (MMSE-BD)	1560	1605	1091	1046
No Cooperation THP	348	360	130	138

degradation can be noticed in the high frequency region where the channel is not row wise diagonal dominant. The performance improves in high frequency region by MMSE-BD multi-VP THP that attains centralized THP performance used as upper bound. Fig. 3.4 also shows the severe performance degradation of the non-cooperating scenario confirming the importance of inter-VP cooperation in order to achieve the maximum vectoring gain.

Near-far scenario is analyzed in Fig. 3.5. Here the distance between CO and CPEs connected to VP_1 is kept fixed at $L_1 = 100m$ while the distance L_2 between CPEs connected to VP_2 and CO varies from 20m to 200m with 20m increment ratio: $L_2 \in \{20, 40, ..., 200\}m$. The sum throughput of ZF-BD multi-VP THP ($\bigcirc$) and MMSE-BD multi-VP THP ($\triangle$) are compared with scenarios where *i)* only one of the two VPs (either VP_1 or VP_2) is active ($\star$), *ii)* centralized THP vectoring

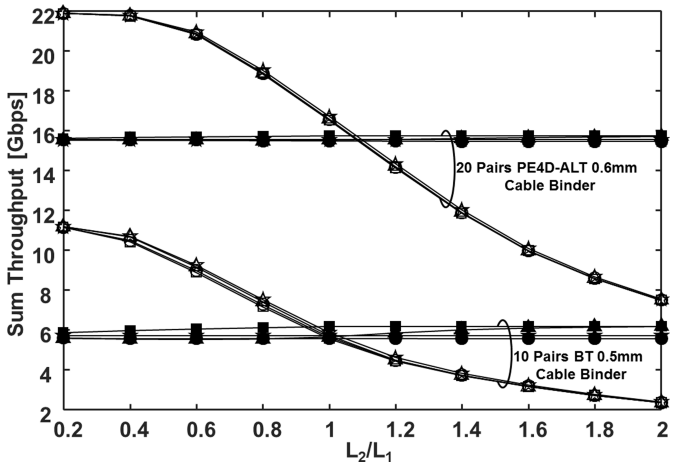

Figure 3.5.: Sum throughput of all pairs vs loop length ratio between the CO and CPEs of VP_1 (filled markers) and VP_2 (empty markers) for $K = 2$ VPs. Number of CPEs are $N_1 = N_2 = 10$ for PE4D-ALT and $N_1 = N_2 = 5$ for BT cables. Precoding Schemes: ZF THP for single line without OD FEXT ($\star$), Centralized THP (square marker), Multi-VP THP (ZF-BD) ($\bigcirc$), Multi-VP THP (MMSE-BD) ($\triangle$).

is performed (square marker). The sum throughput is constant at VP_1 for all the cooperation modes due to fixed length L_1 as compared to VP_2 where it is decreasing due to increasing loop length L_2. Fig. 3.5 shows that the performance of the proposed multi-VP THP is not sensitive to near-far scenario where line variations (IL and FEXT) of one VP do not affect the performance of other VPs. The performance of ZF-BD multi-VP THP MMSE-BD multi-VP THP in near-far scenario is consistent with Fig. 3.4, and the sum-throughput for single CPE using PE4D-ALT cable is bounded between 748.2 Mbps (471 Mbps for BT cable) and 2.187 Gbps (2.2 Gbps for BT cable) Gbps for loop length variation between 200m and 20m at VP_2, respectively.

3.5. Concluding Remarks

In this chapter, we propose a distributed non linear precoding architecture in order to reduce latency and complexity of conventional Tomlinson-Harashima Precoding (THP). To parallelize conventional THP, we consider a DSL system with a single DSL Access Multiplexer (DSLAM) hosting multiple Vector Processors (VPs). In such single-DSLAM multi-VP DSL system, Out-of-Domain (OD) FEXT mitigation between different vectored groups is carried out by linear block diagonalization, that is enabled by VPs cooperation, while In-Domain (ID) self-FEXT

cancellation, which is performed locally and in parallel at each VP, is based on conventional non-linear THP. Numerical simulations have been performed for two different cable types, and the results show that the performance of proposed multi-VP THP is comparable with that of fully non-linear centralized THP in both cases, but with much less latency and complexity. Moreover, it has been shown that multi-VP THP is not sensitive to the practical near-far scenario. Further degrees of freedom in the design of the system are provided by the choice of the number of VPs to be used, as well as the criterion to group the lines together. A design criterion could be to organize the lines into groups such that the resulting interference between the groups at the VPs is minimized and, consequently, the OD FEXT processing is eased.

Part II.

Interference Mitigation Techinques for Wireless Communications Systems

4. Cooperative Precoding in Multi-Operator Wireless Systems

4.1. Introduction

INTERFERENCE, in traditional mobile wireless networks, is commonly considered as an obstacle which requires additional resources for its complete elimination, thus lowering the overall system efficiency. Current 4G networks are so saturated by interference that are denoted as interference-limited, rather than noise-limited. In most of the cases, this interference is treated as an unstructured random noise, and mitigated by power control and dynamic spectrum management strategies. However, when the interference structure is properly addressed to exploit the degrees of freedom available in the system, interference can be theoretically turned into benefits [74].

Coordinated (also referred to as cooperative) transmission in the form of joint signal transceiver and/or receiver processing is one way how to obtain these benefits [75], and thus it is supported in modern network architectures such as Coordinated Multi-Point (CoMP) [76] or Cloud Radio Access Network (C-RAN) [5]. These architectures are based on the concept of *virtual* multi-user Multiple-Input Multiple-Output (MIMO) system, which refers to a system where the Base Stations (BSs) cooperate to form a Distributed Antenna System (DAS) in order to obtain MIMO gains which would not be available for them as single entities.

The ideas of BS cooperation and information sharing, originally introduced to combat inter-cell interference (e.g., created by adjacent cells with frequency reuse factor 1), have been recently proposed for mobile networks in which multiple operators share the same physical resources. This radio access strategy, denoted as multi-operator Non-Orthogonal Spectrum Sharing (NOSS), is considered in this chapter, as it has been recently proved to outperform traditional Orthogonal Spectrum Sharing (OSS) technique, in which disjoint resources are allocated to different operators [77]. In multi-operator NOSS scenarios, cooperation among different operators appears to be the only viable solution for handling the resulting inter-operator interference. However, operators are usually reluctant to share any sensitive information like users' data, thus complicating the design of a privacy preserving cooperative communication system, which is the focus of this chapter.

4.1.1. Chapter Contribution

The chapter is divided into two macro-parts, each of which addressing different aspects of the same problem. In particular, inspired by the hybrid linear-non-linear precoding architecture proposed in Chapter 3 for wired communication systems, the first part of the chapter tackles the problem of multi-operator NOSS by proposing a novel cooperative mechanism for interference cancellation. As such, the proposed cooperative precoding strategy enables multiple operators to perform joint transmission/precoding without exchanging any private data among them. In turn, operators only need to share each other interference, i.e., a part of the precoding matrix (unknown to the other operators) mixed by the users' signal.

The proposed mechanism is shown to perform close to the fully centralized system, i.e., a system in which operators fully share their sensitive data. Nevertheless, the following questions still remain unanswered: *i)* Does the proposed interference sharing mechanism really preserve privacy for all the operators? *ii)* Is it possible for the operators to retrieve any sensitive information from the interference received from the other operators (e.g., by blind equalization techniques etc.)? In the second part of the chapter, a simple single-antenna information theoretical model is introduced in order to answer these questions, and to confirm the possibility to implement the proposed multi-operator interference sharing precoding while guaranteeing privacy for the operators. By leveraging information theoretical tools, the secrecy analysis performed in this second part of the chapter is based on the concept of physical layer security.

4.1.2. Contribution in International Conferences/Journals

Part of the material presented in this chapter has been published in:

- M. Hekrdla, **A. Matera**, S. H. R. Naqvi, and U. Spagnolini, "Interference Sharing Multi-Operator Cooperation for Downlink Precoding in Cloud-RAN Architecture" in *2016 IEEE International Conference on Communications Workshops (ICC Workshops)*, pp. 128–133, IEEE, 2016.
- **A. Matera**, P.-H. Lin, E. A. Jorswieck, and U. Spagnolini, "Secure 2-user Gaussian Interference Channel with Limited Information Exchange at the Transmitters" in *2016 IEEE Global Communications Conference Workshops (GLOBECOM Workshops)*, pp. 1–6, IEEE, 2016.

4.2. Interference-Sharing Multi-Operator Cooperation in C-RAN Architecture

This first part of the chapter describes a novel cooperative interference cancellation technique considering the downlink of a Multiple-Input Single-Output Inter-

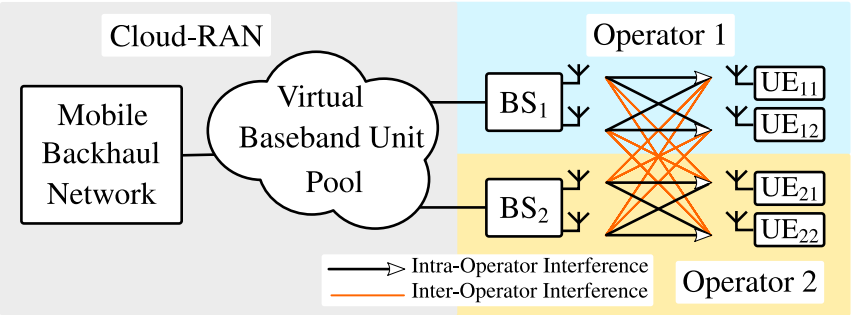

Figure 4.1.: Cloud Radio Access Network (C-RAN) architecture in multi-operator MISO Interference Channel (IC). Inter- and intra-operator interference are marked by black and red lines, respectively.

ference Channel (MISO-IC). The MISO-IC comprises two mobile operators that serve multiple single-antenna users through their own multi-antenna BSs, as depicted in Fig 4.1. Unlike cooperation adopting well known precoding schemes developed for single-user MISO/MIMO Broadcast Channel (BC) (e.g., optimal non-linear Dirty Paper Coding (DPC) implemented as Tomlinson-Harashima Precoding (THP) [46, 62], suboptimal linear Zero-Forcing (ZF), Minimum Mean Square Error (MMSE) [78], or general linear beamforming methods), the scheme proposed here does not require any exchange of sensitive user's signals or Channel State Information (CSI) among the operators. Instead, the operators share each other's interference, i.e., a part of precoding matrix mixed by the users' signals. The proposed interference sharing mechanism is based on the two levels interference cancellation precoding divided into inter- and intra-operator precoding. Regularized Block Diagonalization (RBD) [69], originally proposed for multi-user MIMO-BC, is adopted here to cancel the inter-operator interference, while the intra-operator precoding is based on THP. We denote our interference-sharing mechanism as Distributed-(D)-RBD-THP reflecting decentralization and the two level precoding. D-RBD-THP performance is comparable to the utmost fully coordinated THP where operators share all sensitive information, and it is a suboptimal scheme which does not require multiple iterations among operators, as in common multi-operator solutions based on game theoretical approaches [77], [79]. Furthermore, D-RBD-THP is a flexible precoding architecture which is not constrained to any specific linear or nonlinear beamforming method [80], [81]. C-RAN architecture, already adopted in current mobile systems, is seen as a natural architecture for D-RBD-THP, where coordinated processing and interference sharing mechanism can be performed centrally in the virtual pool of BaseBand Units (BBU) without significant increase in backhauling traffic [5].

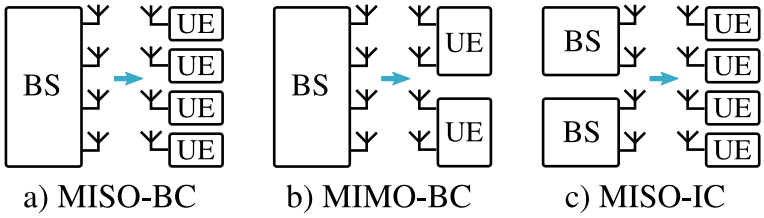

Figure 4.2.: Schematic description of considered cooperative scenarios.

4.2.1. System Model

Even though our interference sharing mechanism is proposed for the MISO-IC channel, its core parts are presented in this section in the different scenarios for which they have been originally proposed [69, 46, 62]. All the scenarios considered here have a similar structure, which allows us to describe them by using a common notation. We denote each scenario as BC or IC according to the number of receiver and transmitter terminals, and MISO or MIMO according to the number of antennas placed on every terminal, as illustrated by Fig. 4.2.

Let the number of BSs be denoted as K and the number of UEs be L. The total number of transmitting antennas $N_t = \sum_{i=1}^{K} n_{t,i}$ is the sum of all transmitting antennas at all BSs. In the same way, the total number of receiving antennas is $N_r = \sum_{i=1}^{L} n_{r,i}$, where $n_{r,i}$ is the number of antennas at the i-th receiver. To alleviate heavy notation, we assume a symmetric setting where $n_{r,i}$ and $n_{t,i}$ are constant for all i. We demonstrate all aspects of our approach in the simplest representative model with $N_t = N_r = 4$ as illustrated in Fig. 4.1, 4.2. Let the downlink channel be the canonical linear model

$$\mathbf{y} = \mathbf{H}\mathbf{x} + \mathbf{w}, \tag{4.1}$$

where $\mathbf{x}$ is the concatenation of all transmitted signals from all K BSs arranged in an $N_t \times 1$ vector. Vector $\mathbf{y} \in \mathbb{C}^{N_r}$ contains the received signals at all L UEs. Vector $\mathbf{w} \sim \mathcal{CN}(0, \sigma_w^2 \mathbf{I})$ represents uncorrelated complex Gaussian noise that has identical statistics over all UEs. The $N_r \times N_t$ channel matrix $\mathbf{H}$ is assumed to be frequency-flat uncorrelated Rayleigh fading.

It is convenient to block partition the channel matrix into inter- and intra-operator parts. In the 4×4 MIMO illustrative case, the channel is decomposed into 2×2 blocks as

$$\begin{bmatrix} \mathbf{y}_1 \\ \mathbf{y}_2 \end{bmatrix} = \begin{bmatrix} \mathbf{H}_{11} & \mathbf{H}_{12} \\ \mathbf{H}_{21} & \mathbf{H}_{22} \end{bmatrix} \begin{bmatrix} \mathbf{x}_1 \\ \mathbf{x}_2 \end{bmatrix} + \begin{bmatrix} \mathbf{w}_1 \\ \mathbf{w}_2 \end{bmatrix}, \tag{4.2}$$

where the transmitted signal $\mathbf{x}_i = [x_{i,1}, x_{i,2}]^T \in \mathbb{C}^2$, the received signal $\mathbf{y}_i \in \mathbb{C}^2$, and the noise vector noise $\mathbf{w}_i = [w_{i,1}, w_{i,2}]^T \in \mathbb{C}^2$ are related to the i-th operator.

We denote the power of the transmitted symbols as $E[|x_{i,j}|^2]$, and the variance of the noise as $E[|w_{i,j}|]^2 = \sigma_w^2$. The main diagonal channel blocks $\mathbf{H}_{ii}$ account for the intra-operator interference, while the off-diagonal channel blocks $\mathbf{H}_{ij}$ account for inter-operator interference.

We do not consider large scale fading in our model, although we make the inter-operator statistics to be scaled relative to intra-operator statistics by the parameter α, which is denoted as relative inter-operator channel power. Accordingly, intra-operator channels are distributed as $[\mathbf{H}_{ii}]_{kl} \sim \mathcal{CN}(0,1)$, and inter-operator channel are parametrized as $[\mathbf{H}_{ij}]_{kl} \sim \mathcal{CN}(0,\alpha^2)$. Parametrization by α represents various level of inter- and intra-operator channel quality corresponding to various level of large scale fading, and it enables to better study the capability of the considered precoding methods to mitigate inter-operator interference.

MIMO processing usually relies on the assumption of perfect CSI knowledge at both transmitter and receiver sides. In the multi-operator MISO-IC proposed here, we assume that the BS of each operator knows only the CSI of the channels from all BSs *toward* the group of UEs belonging to the same operator. Referring to the 4×4 MIMO in (4.2), this means that BS_1 knows not only $\mathbf{H}_{11}$, but also $\mathbf{H}_{12}$. The technicalities for this assumption can be obtained as a part of the mutual cooperation among operators for channel estimation proposed in [70]. Estimation of these off-diagonal blocks is quite straightforward when using channel uplink/downlink reciprocities of Time Division Duplexing (TDD). Alternatively, CSI can be obtained by channel estimation with orthogonal trainings as routinely performed in CDMA systems for soft-handover.

4.2.2. Regularized Block Diagonalization in Single-Operator Broadcast Channel

This section presents the RBD precoding method for the single-operator MIMO-BC where every UE is equipped with multiple antennas. After the block-diagonalization precoding performed by RBD, MIMO-BC channel decomposes into two independent and parallel MIMO channels where Singular Value Decomposition (SVD) processing is applied as depicted in Fig. 4.3. We denote the original RBD for MIMO-BC as RBD-SVD [69]. However, in MISO-BC there are only single antenna receivers available which cannot cooperate to jointly perform SVD. Therefore, we propose to shift all the signal processing at the transmitter side (i.e., precoding) by using THP instead of SVD equalization, which leads to RBD-THP. Our novel interference-sharing mechanism is a way how to implement RBD-THP in uncoordinated manner in multi-operator MISO-BC as will be discussed in Sec. 4.2.3.

4.2.2.1. Regularized Block-Diagonalization

Regularized block diagonalization is a processing common to both RBD-SVD and RBD-THP. The UEs' data vector $\mathbf{s}$ is precoded by a matrix $\mathbf{F}$ to form the trans-

mitted signal $\mathbf{x} = \mathbf{Fs}$. Precoding matrix $\mathbf{F}$ is composed by two matrices $\mathbf{A}$ and $\mathbf{B}$ corresponding to the two steps of precoding as

$$\mathbf{F} = \beta \mathbf{AB}, \tag{4.3}$$

where the power scaling constant β is equal $\beta = \sqrt{N_t} / \|\mathbf{AB}\|_F$ to ensure per-antenna unit average transmitted power, where $\|\mathbf{X}\|_F \triangleq \sqrt{\mathrm{tr}\left(\mathbf{XX}^H\right)}$ denotes Frobenius norm and $\mathrm{tr}\left(\star\right)$ denotes trace operation. Precoding matrix $\mathbf{A}$ is arranged as

$$\mathbf{A} = \left[\mathbf{A}_1, \mathbf{A}_2, \ldots, \mathbf{A}_L\right], \tag{4.4}$$

and the structure of precoding matrix $\mathbf{B}$ is block diagonal

$$\mathbf{B} = \mathrm{diag}\left(\mathbf{B}_1, \mathbf{B}_2 \ldots \mathbf{B}_L\right), \tag{4.5}$$

where L denotes the number of UEs and operation $\mathrm{diag}\left(\star\right)$ denotes a block diagonal matrix with input matrices on the main diagonal. In the 4×4 MIMO example, the precoding matrices are

$$\mathbf{A} = \left[\mathbf{A}_1, \mathbf{A}_2\right], \quad \mathbf{B} = \mathrm{diag}\left(\mathbf{B}_1, \mathbf{B}_2\right) = \begin{bmatrix} \mathbf{B}_1 & \mathbf{0} \\ \mathbf{0} & \mathbf{B}_2 \end{bmatrix}, \tag{4.6}$$

where matrix block $\mathbf{A}_i \in \mathbb{C}^{4\times 4}$, $\mathbf{B}_i \in \mathbb{C}^{4\times 2}$, and the vectors $\mathbf{x} = [\mathbf{x}_1^T, \mathbf{x}_2^T]^T \in \mathbb{C}^4$ and $\mathbf{s} = [\mathbf{s}_1^T, \mathbf{s}_2^T]^T \in \mathbb{C}^4$. Let us define the auxiliary channel matrix $\tilde{\mathbf{H}}_i$, which describes the stack of matrices containing all matrix row blocks except of the i-th one as

$$\tilde{\mathbf{H}}_i = \left[\mathbf{H}_1^T, \mathbf{H}_2^T, \ldots, \mathbf{H}_{i-1}^T, \mathbf{H}_{i+1}^T, \ldots, \mathbf{H}_L^T\right]^T. \tag{4.7}$$

In the 4×4 MIMO reference channel

$$\mathbf{H} = \begin{bmatrix} \mathbf{H}_{11} & \mathbf{H}_{12} \\ \mathbf{H}_{21} & \mathbf{H}_{22} \end{bmatrix} = \begin{bmatrix} \mathbf{H}_1 \\ \mathbf{H}_2 \end{bmatrix}, \tag{4.8}$$

the auxiliary matrices reduce to

$$\tilde{\mathbf{H}}_1 = \mathbf{H}_2, \quad \tilde{\mathbf{H}}_2 = \mathbf{H}_1, \tag{4.9}$$

where the i-th matrix row yields $\mathbf{H}_i = [\mathbf{H}_{i1}, \mathbf{H}_{i2}] \in \mathbb{C}^{2\times 4}$. Precoding matrix $\mathbf{A}_i$ is obtained by SVD algorithm of $\tilde{\mathbf{H}}_i$ as

$$\tilde{\mathbf{H}}_i = \tilde{\mathbf{U}}_i \tilde{\mathbf{\Sigma}}_i \tilde{\mathbf{V}}_i^H. \tag{4.10}$$

The size of matrices in (4.10) is $[2 \times 4] = [2 \times 2][2 \times 4][4 \times 4]$. The i-th precoding block $\mathbf{A}_i$ is given by regularized inversion [69] as

$$\mathbf{A}_i = \tilde{\mathbf{V}}_i \left(\tilde{\mathbf{\Sigma}}_i^H \tilde{\mathbf{\Sigma}}_i + n_{r,i}\sigma_w^2 \mathbf{I}\right)^{-\frac{1}{2}}, \tag{4.11}$$

where we assume unit mean symbol power of the transmitted signals and AWGN with power σ_w^2. Precoding matrix $\mathbf{B}$ depends on the strategy used for precoding in the decoupled channel (i.e., SVD for MIMO, THP for MISO) later on. In both cases, the overall channel is block-diagonalized in MMSE sense, which we denote as $\sim \mathbf{0}$, and thus

$$\mathbf{HF} = \beta \begin{bmatrix} \mathbf{H}_1\mathbf{A}_1\mathbf{B}_1 & \mathbf{H}_1\mathbf{A}_2\mathbf{B}_2 \\ \mathbf{H}_2\mathbf{A}_1\mathbf{B}_1 & \mathbf{H}_2\mathbf{A}_2\mathbf{B}_2 \end{bmatrix} = \beta \begin{bmatrix} \mathbf{H}_1\mathbf{A}_1\mathbf{B}_1 & \sim \mathbf{0} \\ \sim \mathbf{0} & \mathbf{H}_2\mathbf{A}_2\mathbf{B}_2 \end{bmatrix}.$$

In a single-operator scenario, the decision variable at every UE is obtained from $\mathbf{y}$ by local decoding, that for the ensemble analysis corresponds to a multiplication with a block-diagonal matrix $\mathbf{G}$ as $\hat{\mathbf{y}} = \mathbf{G}\mathbf{y}$. Decoding $\mathbf{G}$ accounts for the arbitrary linear receiver processing and it has the block-diagonal structure

$$\mathbf{G} = \beta^{-1}\mathrm{diag}\left(\mathbf{G}_1, \mathbf{G}_2, \ldots, \mathbf{G}_L\right), \tag{4.12}$$

which shrinks for $N_t = N_r = 4$ into

$$\mathbf{G} = \beta^{-1}\mathrm{diag}\left(\mathbf{G}_1, \mathbf{G}_2\right) = \beta^{-1} \begin{bmatrix} \mathbf{G}_1 & \mathbf{0} \\ \mathbf{0} & \mathbf{G}_2 \end{bmatrix}. \tag{4.13}$$

The design of *the* i-th block $\mathbf{G}_i \in \mathbb{C}^{2\times 2}$ is paired with the design of the precoding $\mathbf{B}_i$ as detailed below for the MIMO-BC and MISO-BC, respectively.

4.2.2.2. RBD-SVD in MIMO-BC

After the block-diagonalization precoding, MIMO-BC channel decomposes into two independent MIMO channels as illustrated in Fig. 4.3. SVD of each effec-

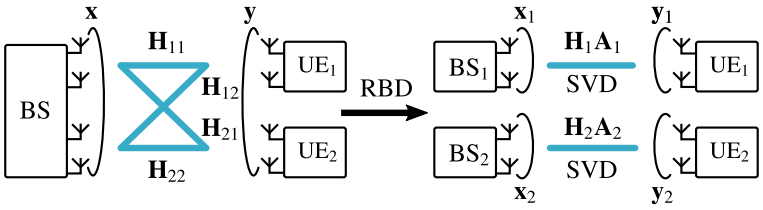

Figure 4.3.: Scheme of RBD-SVD in MIMO-BC. RBD decomposes MIMO-BC channel into two independent MIMO channels where SVD is employed. Every thick blue line denotes 2×2 MIMO link.

tive decomposed channel $\mathbf{H}_i\mathbf{A}_i = \mathbf{U}_i\left[\mathbf{\Sigma}_i, \mathbf{0}\right]\left[\mathbf{V}_{i1}, \mathbf{V}_{i2}\right]^H$ determines the remaining precoding matrix $\mathbf{B}_i$ and the receiver processing matrix $\mathbf{G}_i$ as

$$\mathbf{B}_i = \mathbf{V}_{i1}, \quad \mathbf{G}_i = \mathbf{\Sigma}_i^{-1}\mathbf{U}_i^H. \tag{4.14}$$

4.2.2.3. RBD-THP in MISO-BC

Similarly to the case of MIMO-BC, block-diagonalization decomposes the channel into two independent MISO-BC channels each having effective channel $\mathbf{H}_i\mathbf{A}_i$ as shown in Fig. 4.4. RBD-THP implementation is defined by the feedback filter $\mathbf{B}_{b,i}$

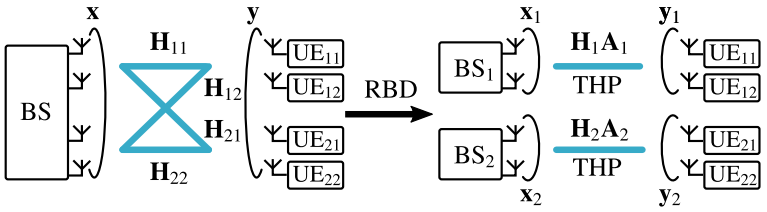

Figure 4.4.: Scheme of RBD-THP in MISO-BC. RBD decomposes MISO-BC channel into two independent MISO-BC channels where THP is employed.

and the feed-forward filter $\mathbf{B}_{f,i}$ as shown in Fig. 4.5. The matrices are obtained

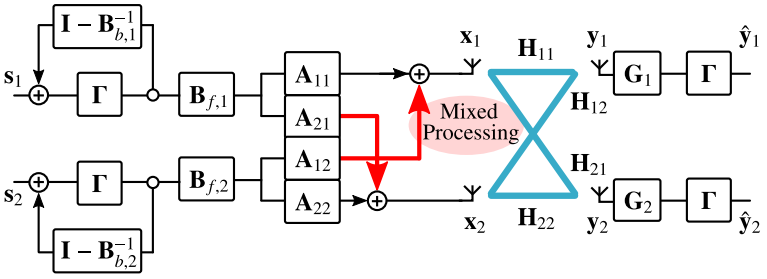

Figure 4.5.: RBD-THP implementation. Thick red arrows highlighted parts where independent processing of users signals $\mathbf{s}_1$ and $\mathbf{s}_2$ is mixed together.

by the QR decomposition of the Hermitian transposed effective channel as

$$(\mathbf{H}_i\mathbf{A}_i)^H = [\mathbf{Q}_{i1}, \mathbf{Q}_{i2}] \begin{bmatrix} \mathbf{R}_i \\ \mathbf{0} \end{bmatrix}. \tag{4.15}$$

There are two different types of possible THP implementation that can be considered here. We choose the one with potentially higher sum-rate performance [46] where the feedback matrix is given by

$$\mathbf{B}_{b,i} = \left(\mathbf{G}_i\mathbf{R}_i^H\right)^{-1} \tag{4.16}$$

and feed-forward matrix as

$$\mathbf{B}_{f,i} = \mathbf{Q}_{i1}. \tag{4.17}$$

The i-th diagonal matrix which describes the receiver processing is equal to the inverse of the diagonal elements taken from $\mathbf{R}_i$ as $\mathbf{G}_i = \mathrm{diag}\left(\mathbf{R}_i\right)^{-1}$. Matrix $\mathbf{B}_i$ from (4.6) is composed as

$$\mathbf{B}_i = \mathbf{B}_{f,i}\mathbf{B}_{b,i}. \tag{4.18}$$

Implementation of RBD-THP in the reference 4×4 MIMO is shown in Fig. 4.5, where matrix $\mathbf{A}$ is composed by 2×4 blocks as

$$\mathbf{A} = \begin{bmatrix} \mathbf{A}_{11} & \mathbf{A}_{12} \\ \mathbf{A}_{21} & \mathbf{A}_{22} \end{bmatrix} \tag{4.19}$$

and $\mathbf{\Gamma}[\star]$ denotes THP modulo [46]. The implementation presented in Fig. 4.5 can be easily analyzed by linearizing the modulo $\mathbf{\Gamma}$ block with the addition of a certain data-channel dependent vector $\mathbf{d}_i$ [62]. Since the added vector $\mathbf{d}_i$ is removed by modulo performed by receivers, we can express the resulting transmitted signals as

$$\mathbf{x}_1 = \mathbf{A}_{11}\mathbf{B}_1\mathbf{s}_1 + \mathbf{A}_{12}\mathbf{B}_2\mathbf{s}_2, \tag{4.20}$$

$$\mathbf{x}_2 = \mathbf{A}_{21}\mathbf{B}_1\mathbf{s}_1 + \mathbf{A}_{22}\mathbf{B}_2\mathbf{s}_2. \tag{4.21}$$

4.2.3. Distributed RBD Tomlinson-Harashima Precoding in Multi-Operator MISO-IC

In the previous section, we have developed RBD-THP for the single-operator MISO-BC channel. Here, we introduce its distributed implementation, where multiple operators cooperate to cancel inter-operator interference by RBD and consequently use THP in the decoupled MISO-BC channels as illustrated in Fig. 4.6. Possible distributed implementation of RBD-THP is analyzed using equations

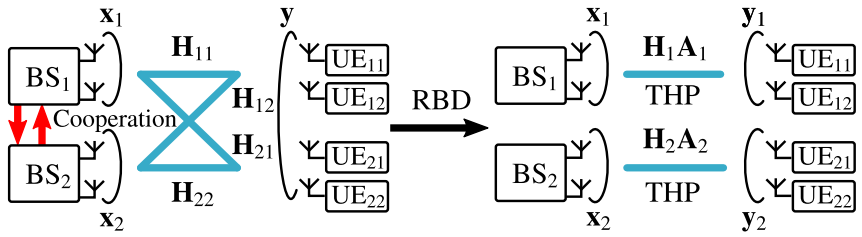

Figure 4.6.: Multi-operator cooperation implementing Distributed (D)-RBD-THP in MISO-IC. Thick red arrows correspond to red arrows in Fig. 4.5 highlighting part of the processing requiring cooperation.

(4.20), (4.21). Fig. 4.5 illustrates the only parts which require cooperation between parallel processing of $\mathbf{x}_i$ by thick red arrow.

First of all, it is important to recall what is known by each operator. We describe the knowledge of each operator from the perspective of operator 1 since the scheme is symmetrical. Operator 1 knows user signal $\mathbf{s}_1$ and CSI related to UE_{11} and UE_{12}, which corresponds to $\mathbf{H}_{11}$, $\mathbf{H}_{12}$ forming $\mathbf{H}_1 = [\mathbf{H}_{11}, \mathbf{H}_{12}]$. According to (4.9), operator 1 knows also $\tilde{\mathbf{H}}_2$ as $\tilde{\mathbf{H}}_2 = \mathbf{H}_1$. This way, operator 1 can compute $\mathbf{A}_2 = \left[\mathbf{A}_{12}^T, \mathbf{A}_{22}^T\right]^T$ by using (4.11). In order to completely build the signal $\mathbf{x}_1$ in (4.20) which is transmitted when centralized RBD-THP is used, operator 1 would need to know $\mathbf{A}_{11}\mathbf{B}_1$ and $\mathbf{B}_2\mathbf{s}_2$. The core observation is that it is not required the knowledge of individual matrices and the vector, but just their product.

The proposed cooperation mechanism exchanges $\mathbf{A}_i$ and $\mathbf{B}_j\mathbf{s}_j$ between operators to implement RBD-THP in the distributed way. Let us check the functionality from the perspective of operator 1 who obtained $\mathbf{A}_1$ and $\mathbf{B}_2\mathbf{s}_2$ from operator 2. With knowledge of $\mathbf{A}_1$ and its own channel $\mathbf{H}_1$, precoding matrix $\mathbf{B}_1$ is computed from (4.15), (4.16), (4.17), (4.18). To close the cooperation loop, operator 1 needs to make the same favor for operator 2 which means to send $\mathbf{A}_2$ (known without cooperation) and $\mathbf{B}_1\mathbf{s}_1$ (based on known users' signals and $\mathbf{B}_1$ obtained through the cooperation). One loop of the cooperation is shown in Table 4.1.

Table 4.1.: One loop of the cooperation between operators exchanging $\mathbf{A}_i$ and $\mathbf{B}_j\mathbf{s}_j$.

Operator 1	Operator 2
Step 1	
know: $\mathbf{H}_1, \mathbf{s}_1$	know: $\mathbf{H}_2, \mathbf{s}_2$
compute: $\mathbf{A}_2$ (11)	compute: $\mathbf{A}_1$ (11)
exchange: $\mathbf{A}_2$ $\leftarrow$ / $\rightarrow$ $\mathbf{A}_1$	exchange: $\mathbf{A}_1$
Step 2	
know: $\mathbf{H}_1, \mathbf{s}_1, \mathbf{A}_2, \mathbf{A}_1$	know: $\mathbf{H}_2, \mathbf{s}_2, \mathbf{A}_1, \mathbf{A}_2$
compute: $\mathbf{B}_1$ (18)	compute: $\mathbf{B}_2$ (18)
exchange: $\mathbf{B}_1\mathbf{s}_1$ $\rightarrow$ / $\leftarrow$ $\mathbf{B}_2\mathbf{s}_2$	exchange: $\mathbf{B}_2\mathbf{s}_2$
Final Step	
compute: $\mathbf{x}_1$ (20)	compute: $\mathbf{x}_2$ (21)

4.2.3.1. Backhaul Overloading

Apparently, $\mathbf{A}_i$ and $\mathbf{B}_j\mathbf{s}_j$ must be exchanged for every transmitted symbol. This may generate considerable load, if not prohibitive, on the backhauling links. This is in contrast to the coordinated beamforming schemes which cooperate only to steer the beamforming vectors such that the interference is reasonably diminished [77], [79], [80], [81]. We see a great implementation potential of our method in C-RAN

architecture where backhauling issues are a priori eliminated since all coordinated processing and interference-exchange appear at the same place in the virtual pool of BBUs [5].

4.2.4. Numerical Results

Simulation settings are used to validate the effectiveness of the multi-operator technique in fully-overlapped spectrum assignment compared to conventional methods for multi-operator coexistence. The system is composed of $K = 2$ operators and $L = 4$ or $L = 8$ UEs that for the symmetric setting correspond to 2 and 4 UEs per operator, respectively. We show the mean rate per user for various relative inter-operator channel power α, and for signal to additive Gaussian noise ratio $1/\sigma_w^2 = 10\,\text{dB}$ (Fig.4.7) and $1/\sigma_w^2 = 20\,\text{dB}$ (Fig.4.8). Rate has been evaluated

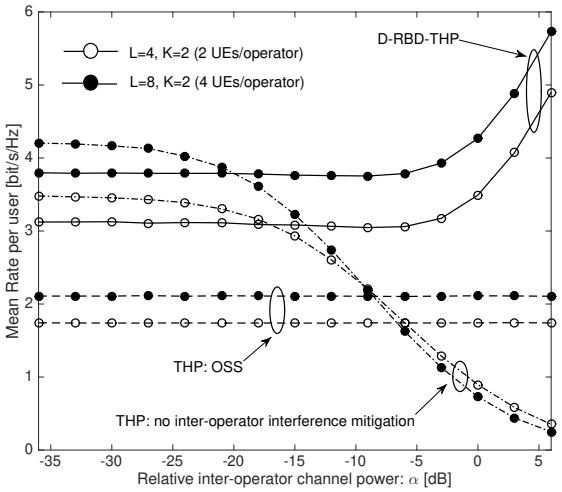

Figure 4.7.: Mean rate per user versus α for $1/\sigma_w^2 = 10$ dB for $K = 2$, $L = 4$ (empty dots) and for $K = 2$, $L = 8$ (filled dots). Mean rate is compared for D-RBD-THP (solid lines), orthogonal spectrum sharing (dashed lines) and no inter-operator interference mitigation (dash-dot lines).

from the signal to noise ratio at the decision variable at UE side assuming QPSK as reference modulation. The mean rate for D-RBD-THP (solid-lines) is almost constant for weak inter-operator coupling ($\alpha < -5\,\text{dB}$) and increases while increasing the coupling ($\alpha > 0\,\text{dB}$) due to the inter-operator cooperation that let every operator exploit the capability of the other operator in creating an augmented space-diversity toward all the UEs. Performance vs α is consistent for 2 UEs per operator ($L = 4$, empty dots) and 4 UEs per operator ($L = 8$, filled dots), and for

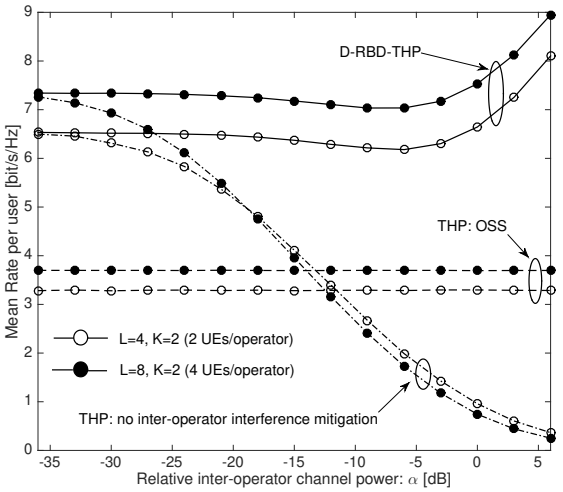

Figure 4.8.: Mean rate per user versus α for $1/\sigma_w^2 = 20$ dB for $K = 2$, $L = 4$ (empty dots) and for $K = 2$, $L = 8$ (filled dots). Mean rate is compared for D-RBD-THP (solid lines), orthogonal spectrum sharing (dashed lines) and no inter-operator interference mitigation (dash-dot lines).

$1/\sigma_w^2 = 10\,\text{dB}$ (Fig.4.7) and $1/\sigma_w^2 = 20\,\text{dB}$ (Fig.4.8). Mean rate for disjoint spectrum usage where each BS is allocated to $1/K = 1/2$ of the total spectrum assignment is also shown as reference in Fig.4.7 and Fig.4.8 (dashed lines) as this corresponds to Orthogonal Spectrum Sharing (OSS) in multi-operator setting. Since there is no inter-operator interference, performance is independent on α. The comparison with D-RBD-THP confirms that there is a definite advantage (i.e., close to $\times 2$ in mean rate per user, or even more for larger α) to have multiple-operator to cooperate while sharing the same spectrum assignment. Alternatively, the BSs can coexist on the same bandwidth as for full-spectrum sharing and the mean rate for the multi-operator interference channel (dash-dot lines) is surely optimum for weak interference, while it decreases considerably when increasing α, far below the orthogonal spectrum sharing for $\alpha > -15\,\text{dB}$. Since D-RBD-THP (solid lines) embeds non-linear operations (e.g. THP) and regularization steps (4.11), there is a small loss of performance when compared to BSs coexistence (dash-dot lines) for $\alpha < -20\,\text{dB}$ when noise is too large (Fig.4.7 for $1/\sigma_w^2 = 10\,\text{dB}$), and the difference disappears for small σ_w^2 (Fig.4.8 for $1/\sigma_w^2 = 20\,\text{dB}$). Since any multi-operator cooperation based on dynamic spectrum sharing allocates spectrum depending on instantaneous inter-operator interference, the expected mean rate is in the order of the best of the two spectrum policies. However, spectrum-sharing offers no-cooperation gain as for D-RBD-THP, that for heavy inter-operator interference is remarkably better.

D-RBD-THP is essentially a distributed interference cancellation technique and

it is relevant to evaluate the loss compared to centralized THP that is used as upper-bound reference. Fig.4.9 shows the sum-rate of D-RBD-THP (filled dots)

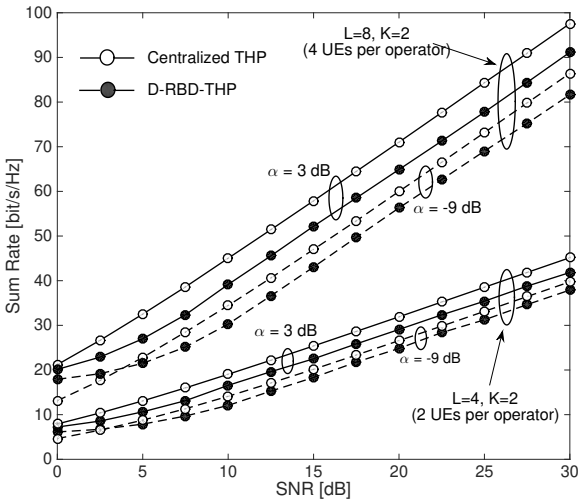

Figure 4.9.: Sum rate versus $1/\sigma_w^2$ for $\alpha = -9\,\mathrm{dB}$ (dashed lines) and $\alpha = 3\,\mathrm{dB}$ (solid lines) for $K = 2$, $L = 4$ and for $K = 2$, $L = 8$. Sum rate has been compared for D-RBD-THP (filled dots) and centralized THP (empty dots).

and centralized THP (empty dots) vs $1/\sigma_w^2$ for the same setting of Fig.4.7 and Fig.4.8 and mild ($\alpha = -9\,\mathrm{dB}$, dashed lines) or severe ($\alpha = 3\,\mathrm{dB}$, solid lines) inter-operator interference. Compared to Fig.4.7 and Fig.4.8 the sum-rate is used only for graphical convenience to separate $L = 4$ and $L = 8$. Inspection of the performance confirms a loss due to the block diagonalization procedure that is negligible (approx. 7-8%) if compared to the gain shown in Fig.4.7 and Fig.4.8 for conventional spectrum sharing methods. Recall that centralized THP is a sequential interference cancellation method that is impaired by the delay due to the sequential cancellation procedure. Therefore, usage in latency-limited settings (e.g. in 5G systems) needs to be carefully traded for the rate gain.

4.3. Privacy Preserving Multi-Operator Cooperation: The Secure 2-User Gaussian Interference Channel with Limited Information Exchange at the Transmitters

In the previous section, a cooperative precoding scheme has been proposed which enables two BSs belonging to two different network operators to design their precoders without directly exchanging private information (e.g., Channel State Information (CSI) and/or users' data). Instead, they only exchange precoding matrices and precoded data. However, the analysis of the degree of privacy preserved for both transmitters in such information exchanges is missing, and is the focus of this section. By considering a simple single-antenna information theoretical model, the problem of enabling cooperation among multiple transmitters, while guaranteeing privacy, is analyzed in this section from a physical layer security perspective.

Certainly, operators are reluctant to share any sensitive information like users' data. Sharing part of precoding matrix $\mathbf{A}_i$ is not harmful in this sense. Much more critical is sharing of $\mathbf{B}_j\mathbf{s}_j$. Note that the data carrying signal $\mathbf{s}_j$ of potential interest is mixed by unknown matrix $\mathbf{B}_j$ which cannot be obtained since it would require knowledge of channel $\mathbf{H}_j$ which is not known. Moreover, the proposed interference-sharing approach works with whatever users' signals, so we could assume that signal $\mathbf{s}_i$ was encrypted by some type of function $\prod_i$ and $\mathbf{s}_j$ by $\prod_j \neq \prod_i$ which only receivers of operator i and j can invert. In wireless communication, natural type for this privacy increasing function is temporal-frequency-space interleaver which may be already implemented to obtain diversity. Besides the interleaving, we can imagine sharing of $\mathbf{B}_j\mathbf{s}_j$ where arbitrary noise of carefully selected power is added to conform with the theory of physical layer security [82], which the approach used here.

Although key-based enciphering is traditionally used to ensure the security of data transmission, key distribution and management may be challenging tasks [83] for secure wireless communications. This is mainly due to the additional control signaling and feedback channel management, which introduce significant overhead and complicate the system design. By contrast, the physical-layer security approach, considered here, is appealing because of its keyless nature [84, 85]. Physical layer security is based on the concept of secrecy capacity, which is defined as the maximum achievable secrecy rate between a transmitter and a legitimate receiver when a secrecy constraint is imposed to prevent the information from being available to an eavesdropper. This simple information theoretical model is called wiretap channel. The secrecy capacity of a discrete memoryless non-degraded wiretap channel was first derived in [85] in the form of channel prefixing, i.e., precoding, which is based on the optimization over the distribution which relates the the original information signal with the (pre)coded one. For degraded, less noisy, or more capable wiretap channels, such prefixing can be removed and the

optimization problem is highly simplified. As an example, for Gaussian wiretap channels with full channel state information at the transmitter, Gaussian channel input is optimal [86, 87, 88].

In multi-user/multi-operator wireless communications, the issue of providing security guarantees becomes even more pressing. In fact, due to the broadcast nature of the medium, the users belonging to different operators not only experience interference, but also the communications become vulnerable to undesired eavesdropping. Physical-layer security in the 2-user Interference Channel (IC) has been analyzed in [89], where the Broadcast Channel (BC) and the IC with independent confidential messages are considered, and the achievable scheme is found to be capacity-optimal in some specific cases. The extension to the K-user Gaussian IC (GIC) with secrecy constraints is considered in [90] adopting interference alignment. Finally, the secrecy capacity region of the multi-antenna Gaussian BC with confidential messages has been investigated in [91].

The effect of cooperation on secrecy has been explored in [92, 93] for the Multiple Access Channel (MAC) and BC, respectively, while in [94, 95, 96] the achievable secrecy rates have been studied for the IC with both transmitter and receiver cooperation using the deterministic model introduced in [97]. However, the impact on secrecy in a GIC with limited information exchange at the transmitters that do not trust each other, which accurately captures the nature of the cooperative multi-operator scenario introduced in the previous section, has not been explored in literature and is the focus of this section. Along this section, we will refer to the D-RBD-THP previously discussed as peaceful multi-operator IC, as security has not been considered as a design parameter. In turn, this section focuses on physical layer security for the 2-user GIC with a novel Limited Information Exchange mechanism at the Transmitters (LIET), which is achieved by an infinite rate link. In addition to the peaceful multi-operator IC, here we design the GIC-LIET including secrecy constraints, and specializing the secrecy rate analysis to the single-antenna case. Artificial Noise (AN) [98] is injected at each of the two transmitters such that the received signal at the potential eavesdroppers (i.e., the other transmitter and receiver) is a degraded version of the signal received at the desired receiver. As for D-RBD-THP, the proposed scheme is tailored for practical RBD precoding scheme [69] designed to mitigate inter-channel interference .

4.3.1. System Model

We consider a GIC with two transmitter/receiver pairs equipped with a single-antenna each where the two transmitters can exchange information through an infinite rate link as depicted in Fig. 4.10. The signal received at the k-th Receiver (RX_k) is

$$y_k = h_{k1}x_1 + h_{k2}x_2 + w_k, \tag{4.22}$$

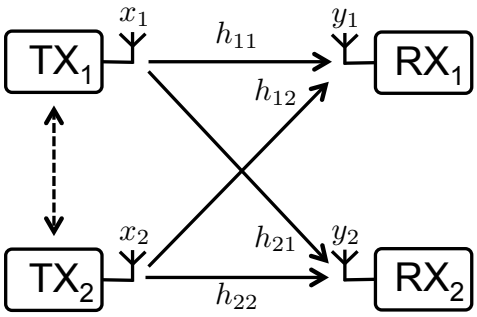

Figure 4.10.: 2-user Gaussian Interference Channel with Limited Information Exchange at the Transmitters (GIC-LIET) with single-antenna nodes.

where h_{kj} is the channel coefficient from the j-th Transmitter (TX_j) to RX_k, x_k is the precoded signal transmitted by TX_k and $w_k \sim \mathcal{CN}(0,1)$ is the additive white Gaussian noise. The ensemble of the symbols $\mathbf{y} = [y_1, y_2]^T \in \mathbb{C}^{2\times 1}$ is

$$\mathbf{y} = \mathbf{H}\mathbf{x} + \mathbf{w}, \tag{4.23}$$

where $\mathbf{x} = [x_1, x_2]^T \in \mathbb{C}^{2\times 1}$ is the ensemble of the signals transmitted by both transmitters, $\mathbf{w}$ is the Gaussian noise independent among the two receivers and the overall channel matrix (possibly complex) is represented as $\mathbf{H} \in \mathbb{C}^{2\times 2}$, where $[\mathbf{H}]_{k,j} = h_{kj}$.

In order to evaluate the impact of different power constraints on the system performance, in this work we consider either per-transmitter (per-TX) power constraints

$$\mathrm{E}[|x_i|^2] \leq P_{T_i},\ \forall\, i = 1, 2, \tag{4.24}$$

or sum-transmitter (sum-TX) power constraint

$$\mathrm{E}[\mathrm{tr}(\mathbf{x}\mathbf{x}^H)] \leq P_T, \tag{4.25}$$

where $P_T = P_{T_1} + P_{T_2}$.

The CSI is perfectly available at each transmitter and this is obtained by exploiting the uplink/downlink channel reciprocity of Time Division Duplex (TDD) systems. We assume that generic TX_k has the knowledge only of the ensemble of the channels from both the transmitters to his RX_k

$$\mathbf{h}_k^T = [h_{k1}, h_{k2}] \in \mathbb{C}^{1\times 2} \tag{4.26}$$

as a result of the cooperative uplink channel estimation algorithm proposed in [70].

4.3.2. Precoding Structure without Artificial Noise

Let us consider the signal received at RX_k in (4.22). Precoded symbol x_j is computed locally at TX_j as the summation of the precoded symbol for its own RX_j and the precoded symbol to be relayed on behalf of the other transmitter obtained by the infinite rate link:

$$x_j = f_{jj}s_j + f_{jm}s_m,\ j \neq m, \tag{4.27}$$

where $s_m \sim \mathcal{CN}(0, P_{s_m})$ is the Gaussian signal with power P_{s_m} intended to RX_m and f_{jm} is the coefficient that precodes the symbol intended to RX_m and transmitted by TX_j. From equations (4.22) and (4.27) we obtain

$$y_k = \underbrace{h_{kk}f_{kk}s_k}_{A} + \underbrace{h_{kj}f_{jk}s_k}_{B} + \underbrace{\sum_{m=1}^{2} h_{km}f_{mj}s_j}_{C} + w_k,\ j \neq k, \tag{4.28}$$

where A is the signal intended to RX_k sent by TX_k, B is the signal intended to RX_k relayed by TX_j and C is the inter-channel interference as the interference coming from the signal intended to the other RX_j (with $j \neq k$). Collecting the channel coefficients towards RX_k into the vector channel $\mathbf{h}_k^T$ in (4.26) and, similarly, the weights used to precode the signal for RX_k into the vector $\mathbf{f}_k = [f_{1k}, f_{2,k}]^T \in \mathbb{C}^{2\times 1}$, equation (4.28) simplifies to

$$y_k = \mathbf{h}_k^T\mathbf{f}_k s_k + \mathbf{h}_k^T\mathbf{f}_j s_j + w_k. \tag{4.29}$$

In order to obtain a signal which is free from the inter-channel interference, the following condition must be satisfied

$$\mathbf{h}_k^T\mathbf{f}_j = 0,\ \forall\, j \neq k, \tag{4.30}$$

or, equivalently, the precoding vector $\mathbf{f}_j$ for RX_j must lie in the null space of the channel towards the other receiver [67]: $\mathbf{f}_j \in \mathrm{Null}(\mathbf{h}_k^T),\ \forall\, j \neq k$. Hence, with a proper selection of the precoding vector, the interference-free signal at RX_k yields

$$y_k = h_k^e s_k + w_k, \tag{4.31}$$

where $h_k^e = \mathbf{h}_k^T\mathbf{f}_k$ is the scalar effective channel for RX_k.

In the following, the distributed precoding scheme proposed in Sect. 4.2 is adapted for the considered single-antenna case using both BD [67] and RBD [69] for the design of the precoders $\{\mathbf{f}_j\}$. The exchange of information required to construct the precoded symbols x_1 and x_2 in (4.27) locally at each transmitter depends on the design criteria for the precoders $\{\mathbf{f}_j\}$ and it will be addressed in the following sections.

4.3.2.1. Distributed Zero-Forcing BD

In the case of ZF-BD [67], the precoding vector $\mathbf{f}_j$ for RX_j is obtained by the Singular Value Decomposition (SVD) of the vector channel $\mathbf{h}_k^T$ to RX_k (with $k \neq j$) as

$$\mathbf{h}_k^T = u_j \boldsymbol{\sigma}_j^T \mathbf{V}_j = u_j \left[\sigma_j, 0\right] \left[\mathbf{v}_j^{(1)}, \mathbf{v}_j^{(0)}\right], \tag{4.32}$$

where u_j, $\boldsymbol{\sigma}_j^T$ and $\mathbf{V}_j$ contain respectively the left singular vectors, the singular values and right singular vectors of $\mathbf{h}_k^T$. Vector $\mathbf{v}_j^{(0)} \in \mathbb{C}^{2\times 1}$ represents a basis for the null space of $\mathbf{h}_k^T$, hence we select

$$\mathbf{f}_j = \mathbf{v}_j^{(0)}. \tag{4.33}$$

The scalar effective channel for the k-th receiver after ZF-BD precoding is $h_k^e = \mathbf{h}_k^T \mathbf{v}_k^{(0)}$.

Remark 4.1. Two kinds of information exchange are needed to enable the Distributed implementation of ZF-BD (D-ZF-BD)

1. the precoder $\mathbf{f}_j$ for TX_j in (4.33) depends only on the channel $\mathbf{h}_k^T$ towards RX_k (with $k \neq j$). Therefore, TX_k, that knows $\mathbf{h}_k^T$, computes the vector $\mathbf{f}_j$ on behalf of TX_j. Then TX_k exchanges the precoder $\mathbf{f}_j$ with TX_j in trade of $\mathbf{f}_k$ (similarly computed by TX_j);
2. TX_1 and TX_2 must exchange directly the users signals s_1 and s_1 in order to build locally the precoded symbols x_1 and x_2 in (4.27).

Remark 4.2. Distributed-ZF-BD (D-ZF-BD) in this simple single-antenna scenario is equivalent to channel inversion at the transmitter side (i.e., the precoding matrix is $\mathbf{H}^{-1}$). However, D-ZF-BD enables each transmitter to build its precoded symbol without directly exchanging the channel matrix with the other transmitter (they only exchange the precoders $\{\mathbf{f}_j\}$ and the users data $\{s_j\}$). This is fundamental in scenarios where the transmitters are reluctant to share their CSI with others such as the multi-operator scenario considered here.

4.3.2.2. Distributed RBD

RBD aims to design the precoder allowing for some inter-channel interference to find the optimum (in MMSE sense) trade-off between interference and noise level [69]. In the case of RBD it is convenient to decompose the precoder as

$$\mathbf{f}_j = \mathbf{M}_j \mathbf{b}_j, \tag{4.34}$$

where $\mathbf{M}_j \in \mathbb{C}^{2\times 2}$ and $\mathbf{b}_j \in \mathbb{C}^{2\times 1}$. $\mathbf{M}_j$ is responsible for inter-channel interference minimization and it is computed as

$$\mathbf{M}_j = \mathbf{V}_j \left(\boldsymbol{\sigma}_j^T \boldsymbol{\sigma}_j + \mu \mathbf{I}\right)^{-1/2}, \tag{4.35}$$

where $\mathbf{V}_j$ and $\boldsymbol{\sigma}_j$ are obtained by (4.32) and $\mu = \frac{N_r}{P_T}$ is a regularization factor that depends on the total number of receiving antennas (here $N_r = 2$) and on the total sum power P_T. The equivalent channel after RBD precoding becomes block diagonal in MMSE sense which we denote as $\sim \mathbf{0}$, and thus

$$\mathbf{HM} = \begin{bmatrix} \mathbf{h}_1^T\mathbf{M}_1 & \mathbf{h}_1^T\mathbf{M}_2 \sim \mathbf{0} \\ \mathbf{h}_2^T\mathbf{M}_1 \sim \mathbf{0} & \mathbf{h}_2^T\mathbf{M}_2 \end{bmatrix}, \tag{4.36}$$

where $\mathbf{M} = [\mathbf{M}_1, \mathbf{M}_2]$ is the overall RBD precoding matrix and $\widetilde{\mathbf{h}}_{kj}^T \triangleq \mathbf{h}_k^T\mathbf{M}_j \in \mathbb{C}^{2\times 1}$ represent the direct equivalent channels (for $k = j$) and the equivalent residual interference channels obtained after the RBD step (for $k \neq j$). Vector $\mathbf{b}_j$ is chosen to pre-equalize the direct RBD channel $\tilde{\mathbf{h}}_{jj}^T$ as

$$\mathbf{b}_j = \frac{\tilde{\mathbf{h}}_{jj}}{\left\|\tilde{\mathbf{h}}_{jj}\right\|}, \tag{4.37}$$

where $\|\cdot\|$ denotes the Euclidean norm. The scalar effective channel of RX_k is $h_k^e = \mathbf{h}_k^T\mathbf{M}_k\mathbf{b}_k = \left\|\tilde{\mathbf{h}}_{jj}\right\|$.

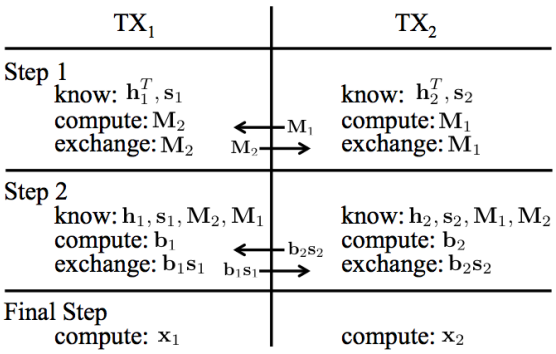

Figure 4.11.: Limited Information Exchange between TX_1 and TX_2 in RBD without artificial noise

Remark 4.3. The two steps of the information exchange needed in Distributed RBD (D-RBD), which are similar to those described in Sect. 4.2, are shown in Fig. 4.11 for the single-antenna case. Differently from the case of D-BD (Remark 4.1), in D-RBD the RBD precoding matrices $\{\mathbf{M}_k\}$ are exchanged only in the first step, while in the second step the transmitters exchange the precoded data $\{\mathbf{b}_k s_k\}$ (and not directly the users data $\{s_k\}$ as in D-BD). In Sect. 4.2, it is claimed that since TX_j does not know $\mathbf{b}_k$ (with $k \neq j$), in principle, TX_j is not able to distinguish between the vector $\mathbf{s}_k$ and $\mathbf{b}_k$ from the observed mixture $\mathbf{b}_k\mathbf{s}_k$, providing a certain degree of protection. However, as addressed in the next section, the system cannot be considered secure from a physical layer security perspective.

4.3.3. Secure Precoding with Artificial Noise

From the previous discussion we conclude that the exchange of explicit (i.e., in D-ZF-BD) or precoded (i.e., in D-RBD) users data between the two transmitters is mandatory in order to enable the two transmitters to cooperate in precoding the data without inter-channel interference as in (4.27). However, such information exchange may be harmful from a secrecy perspective. In fact, even in the case of RBD where only precoded users data $\{\mathbf{b}_k\mathbf{s}_k\}$ are exchanged, one could claim that the TX_j ($j \neq k$) could attempt to extract the information $\mathbf{s}_k$ from the observed mixture $\mathbf{b}_k\mathbf{s}_k$ by means of any available blind estimation or source separation technique.

To prevent the other transmitter from decoding the private data intended to its own receiver, each transmitter injects AN [98] together with its precoded data in order to create two virtual wiretap channels. In each wiretap channel the other transmitter and receiver represent potential eavesdroppers. The motivation for using AN is to deteriorate the infinite rate link between the two transmitters up to the limit that makes the wiretap code to guarantee the secrecy.

In the following we first prove that D-ZF-BD with AN does not provide any non-zero secrecy rate. Then we derive the secrecy rate region of the GIC-LIET based on RBD precoding with AN.

4.3.3.1. Secure D-ZF-BD with AN

In the case of D-ZF-BD with AN, the precoded symbols in (4.27) transmitted by TX_1 and TX_2 are

$$\begin{aligned} x_1 &= f_{11}(s_1 + v_1) + f_{12}(s_2 + v_2), \\ x_2 &= f_{21}(s_1 + v_1) + f_{22}(s_2 + v_2), \end{aligned} \tag{4.38}$$

where $v_j \sim \mathcal{CN}(0, P_{v_j})$ is the zero-mean Gaussian AN with power P_{v_j} injected by TX_j. Notice that TX_j adds AN to both the signal exchanged with TX_k (i.e., $f_{kj}(s_j + v_j)$) and the signal sent directly to RX_j (i.e., $f_{jj}(s_j + v_j)$) so that both s_j, v_j are precoded by the BD filter without any signal leaking to RX_k.

In the following the performance of the system will be analyzed from the view point of TX_1(being symmetrical for TX_2). The signals received at the intended receiver RX_1 and at the potential eavesdropper TX_2 are respectively

$$y_1 = h_1^e(s_1 + v_1) + w_1, \quad \bar{y}_{21} = f_{21}(s_1 + v_1), \tag{4.39}$$

where $\bar{y}_{kj}$ denotes the information received at TX_k from TX_j. We do not need to consider RX_2 as a second potential eavesdropper since it is guaranteed that no information about s_1 is leaked toward RX_2 by ZF-BD.

The secrecy rate R_{s_1} for RX_1 is

$$R_{s_1} \leq [I(s_1; y_1) - I(s_1; \bar{y}_{21})]^+, \tag{4.40}$$

where $[x]^+ = \max(x, 0)$ and

$$I(s_1; y_1) = \log_2 \left(1 + \frac{P_{s_1}|h_1^e|^2}{1 + P_{v_1}|h_1^e|^2}\right), \tag{4.41}$$

$$I(s_1; \bar{y}_{21}) = \log_2 \left(1 + \frac{P_{s_1}}{P_{v_1}}\right). \tag{4.42}$$

Lemma 4.1. *For the 2-user GIC using the LIET scheme, D-ZF-BD with AN cannot achieve a non-zero secrecy rate.*

Proof. To achieve a non-zero positive secrecy rate we need $\frac{P_{s_1}|h_1^e|^2}{1+P_{v_1}|h_1^e|^2} > \frac{P_{s_1}}{P_{v_1}}$. However we can easily observe that there is no solution for positive values of the signal power P_{s_1} and the power of AN P_{v_1}. □

The reason why D-ZF-BD fails in providing a secure communication is that the same AN used to confuse TX_2 corrupts also the channel towards RX_1. We conclude that a non-zero secrecy rate could be achieved by a choice of the AN that prevents the other operator from recovering user's information, but at the same time it *does not degrade* the channel towards the intended receiver. A solution adopting RBD precoding for this problem is described in the next section.

4.3.3.2. Secure D-RBD with AN

In the case of RBD, the precoding coefficient f_{jk} for the symbol s_k intended to RX_k and transmitted by TX_j is decomposed as

$$f_{jk} = \mathbf{m}_{jk}^T \mathbf{b}_k, \tag{4.43}$$

where $\mathbf{m}_{jk}^T \in \mathbb{C}^{1\times 2}$ is the j-th row block of the k-th RBD precoding matrix $\mathbf{M}_k$ in (4.35). The precoded symbols yield

$$\begin{aligned} x_1 &= \mathbf{m}_{11}^T(\mathbf{b}_1 s_1 + \mathbf{t}_1 v_1) + \mathbf{m}_{12}^T(\mathbf{b}_2 s_2 + \mathbf{t}_2 v_2), \\ x_2 &= \mathbf{m}_{21}^T(\mathbf{b}_1 s_1 + \mathbf{t}_1 v_1) + \mathbf{m}_{22}^T(\mathbf{b}_2 s_2 + \mathbf{t}_2 v_2), \end{aligned} \tag{4.44}$$

where definitions of s_k, v_k and $\mathbf{b}_k$ are the same as before and $\mathbf{t}_k$ is chosen such that the AN v_k is aligned in the null space of the direct RBD channel $\tilde{\mathbf{h}}_{kk}^T = \mathbf{h}_k^T \mathbf{M}_k$: $\mathbf{t}_k = \tilde{\mathbf{v}}_k^{(0)}$, where $\tilde{\mathbf{v}}_k^{(0)}$ is the right singular vector of $\tilde{\mathbf{h}}_{kk}^T$ corresponding to the smallest singular value. In order to gain insight about this criterion, we analyze the signal received at RX_k in (4.29). After some manipulations (4.29) becomes

$$y_k = \mathbf{h}_k^T \mathbf{M}_k(\mathbf{b}_k s_k + \mathbf{t}_k v_k) + \mathbf{h}_k^T \mathbf{M}_j(\mathbf{b}_j s_j + \mathbf{t}_j v_j) + w_k, \tag{4.45}$$

where we consider also the effect of the interference coming from signal s_j and AN v_j (with $j \neq k$) since RBD does not completely cancel the interference (i.e., $\mathbf{h}_k^T \mathbf{M}_j \sim \mathbf{0}$, $\forall\, j \neq k$ in 4.36). Key point is that since the AN v_k lies in the null space of the corresponding RBD direct channel (i.e., $\mathbf{h}_k^T \mathbf{M}_k \mathbf{t}_k = 0$) the AN v_k does not degrade the channel to RX_k while it still corrupts the channel from TX_k to TX_j. The signals received respectively at RX_k and at TX_j ($j \neq k$) are

$$y_k = h_k^e s_k + \tilde{\mathbf{h}}_{kj}^T (\mathbf{b}_j s_j + \mathbf{t}_j v_j) + w_k, \quad \bar{y}_{jk} = \mathbf{m}_{jk}^T (\mathbf{b}_k s_k + \mathbf{t}_k v_k) \tag{4.46}$$

Remark 4.4. It has been proved in [69] that the choice of the regularization parameter $\mu = \frac{N_r}{P_T}$ in the definition of the RBD filter in (4.35) is MMSE-optimal for the peaceful downlink Multi-User (MU) MIMO. However, it does not imply that such μ is optimal also for the secure GIC-LIET considered here. In [99] authors derive the optimal regularization factor μ that maximizes the secrecy sum-rate in MU-MIMO broadcast channel with regularized channel inversion at the transmitter using large-scale analysis. However, the results in [99] do not apply to our GIC-LIET since we have single-antenna nodes and the transmitters exchange only limited amount of information. Since μ affects the approximation of the non-diagonal block terms in (4.36), an improper selection of μ can degrade the secrecy rate region due to the interference or underestimate Eve's capacity (i.e., the system is no longer secure). For simplicity in this chapter we use a sub-optimal value of μ obtained by comparing the corresponding achievable secrecy rate regions (derived in the next section). This approach indeed takes the complete matrix (4.36) into account without any approximation in terms of block-diagonal matrix, as this reflects a real scenario and guarantees that the resulting secrecy rate region is truly achievable. The derivation of the optimal regularization factor for the considered GIC-LIET is left as a future research topic.

4.3.4. Secrecy Rate Region of the GIC-LIET with RBD precoding and AN

Due to MMSE inter-channel interference cancellation (RBD precoding), we must consider that each TX_k has two potential eavesdroppers, TX_j and RX_j with $j \neq k$. This has been taken into account into the secrecy rate derivation by considering the worst case result as from the concept of compound wiretap channel [100]. Per-TX power constraint in (4.24) becomes

$$\alpha_k P_{s_k} + \beta_k P_{s_j} + \gamma_k P_{v_k} + \eta_k P_{v_j} \leq P_{T_k},\ k, j, = 1, 2,\ j \neq k,$$

where $\alpha_k = |\mathbf{m}_{kk}^T \mathbf{b}_k|^2$, $\beta_k = |\mathbf{m}_{kj}^T \mathbf{b}_j|^2$, $\gamma_k = |\mathbf{m}_{kk}^T \mathbf{t}_k|^2$ and $\eta_k = |\mathbf{m}_{kj}^T \mathbf{t}_j|^2$ are constant terms that depend on the channel matrices.

Lemma 4.2. *An achievable secrecy rate region of the* 2*-user GIC using the LIET*

scheme is

$$\begin{aligned}\mathcal{R}_{\mathcal{S}} = \bigcup_{\substack{P_{s_1},P_{s_2},P_{v_1},P_{v_2}\geq 0 \\ \alpha_1 P_{s_1}+\beta_1 P_{s_2}+\gamma_1 P_{v_1}+\eta_1 P_{v_2}\leq P_{T_1} \\ \alpha_2 P_{s_2}+\beta_2 P_{s_1}+\gamma_2 P_{v_2}+\eta_2 P_{v_1}\leq P_{T_2}}} \Big\{ (R_{s_1}, R_{s_2}) : \\ R_{s1} \leq \left[I(s_1;y_1) - \max\left\{I(s_1;y_2), I(s_1;\bar{y}_{21})\right\}\right]^+ \\ R_{s2} \leq \left[I(s_2;y_2) - \max\left\{I(s_2;y_1), I(s_2;\bar{y}_{12})\right\}\right]^+ \Big\},\end{aligned} \tag{4.47}$$

where $\forall\, j,k = 1,2$ *and* $j \neq k$

$$I(s_k;y_k) = \log_2\left(1 + \frac{P_{s_k}\left\|h_k^e\right\|^2}{1 + a_k P_{s_j} + b_k P_{v_j}}\right), \tag{4.48}$$

$$I(s_k;y_j) = \log_2\left(1 + \frac{P_{s_k} a_j}{1 + b_j P_{v_k}}\right), \tag{4.49}$$

$$I(s_k;\bar{y}_{jk}) = \log_2\left(1 + \frac{c_k P_{s_k}}{d_k P_{v_k}}\right) \tag{4.50}$$

and the terms $a_k = |\tilde{\mathbf{h}}_{kj}^T \mathbf{b}_j|^2$, $b_k = |\tilde{\mathbf{h}}_{kj}^T \mathbf{t}_j|^2$, $c_k = |\mathbf{m}_{jk}^T \mathbf{b}_k|^2$ *and* $d_k = |\mathbf{m}_{jk}^T \mathbf{t}_k|^2$ *are known constants that depend on the specific channel matrices.*

The above secrecy rate region can be easily adapted to the case of sum power constraints considering the sum-TX constraint in (4.25), instead of the per-TX constraints in (4.24).

Remark 4.5. In (4.49) the term that depends on the power P_{s_j} of the signal s_j is not considered in the denominator since RX_j can apply the successive interference cancellation: RX_j first decodes and strips out its information s_j from the received signal, then RX_j attempts to decode the private information s_k intended to RX_k.

4.3.5. Numerical Results

We compare the secrecy rate region of the proposed GIC-LIET with two extreme cases: without information exchange at the transmitters and full information exchange at the transmitters. These reference schemes are attainable respectively by the secure GIC with Confidential Messages and AN (GIC-CM with AN) without transmitters cooperation [89] and by the secure Gaussian Broadcast Channel

with Confidential Messages (GBC-CM) with two transmitting antennas and two single-antenna receivers [91]. To make a fair comparison, here we consider the three methods by adopting the standard form GIC model [101]

$$\mathbf{H} = \begin{bmatrix} 1 & \nu_1 \\ \nu_2 & 1 \end{bmatrix},$$

where ν_i are normalized crossover channel gains. As in [89] we consider a symmetric case with $\nu_1 = \nu_2 = 0.2$. In Fig. 4.12 and Fig. 4.13 we compare the proposed

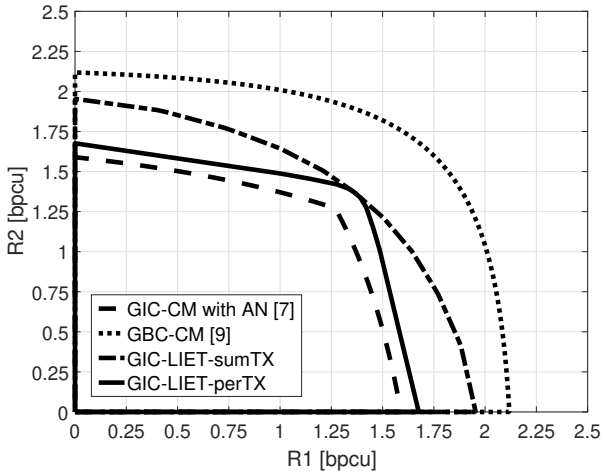

Figure 4.12.: Rate region comparison between the proposed GIC-LIET, Gaussian Interference Channel with Confidential Messages and Artificial Noise (GIC-CM with AN) and Gaussian Broadcast Channel with Confidential Messages (GBC-CM) for $P_{T_1} = P_{T_2} = 10$.

GIC-LIET subject to both per-TX (4.24) and sum-TX (4.25) power constraints with GIC-CM-AN and GBC-CM for two different values of $P_{T_1} = P_{T_2} = 10$ (Fig. 4.12) and $P_{T_1} = P_{T_2} = 100$ (Fig. 4.13). From both figures we can observe that the secrecy rate region of the proposed GIC-LIET is larger than that of the traditional secure IC without information exchange (GIC-CM with AN). The gain is due to the limited information exchange at the transmitter side which still preserves privacy for both the transmitters. Obviously the rate region of GIC-LIET is smaller than that achieved by full information exchange (GBC-CM), to be considered here as an upper bound. In fact, our proposed scheme is different from the GBC-CM because the exchanged information is wiretap coded by the addition of AN, hence it cannot be decoded by the other transmitter. The rate region of GIC-LIET-sumTX is broader then the one obtained by IC-LIE-perTX and they coincide in the point of maximum sum rate. The rate regions achieved by secure GIC-LIET with both per-TX and sum-TX power constraints have been

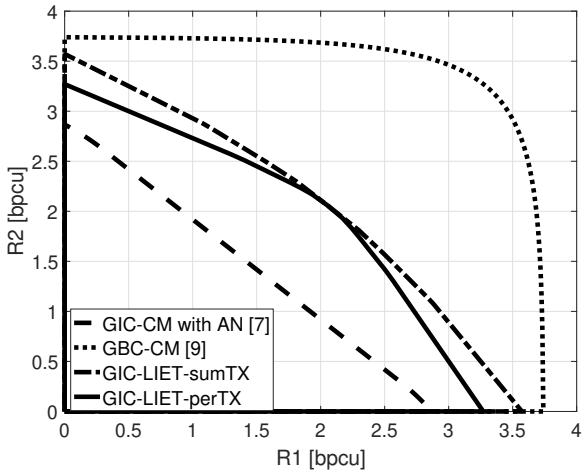

Figure 4.13.: Rate region comparison between the proposed GIC-LIET, Gaussian Interference Channel with Confidential Messages and Artificial Noise (GIC-CM with AN) and Gaussian Broadcast Channel with Confidential Messages (GBC-CM) for $P_{T_1} = P_{T_2} = 100$.

compared to the ones obtained in case of peaceful systems in Fig. 4.14 for both $P_{T_1} = P_{T_2} = 10$ and $P_{T_1} = P_{T_2} = 100$. We notice that the cost to pay to ensure information-theoretic secure transmission for both transmitter/receiver pairs is reasonably small for the case with $P_{T_1} = P_{T_2} = 10$, while in the case of high power (i.e., $P_{T_1} = P_{T_2} = 100$) the loss in the achievable rate is higher.

4.4. Concluding Remarks

In this chapter, we considered a Non-Orthogonal Spectrum Sharing (NOSS) cellular scenario where multiple operators coexist in the same spectrum bandwidth.

In particular, in the first part of the chapter, it has been presented a precoding technique based on the cooperation among multiple operators that jointly precode the downlink data streams intended for the own users. Inter-operator interference is mutually canceled among operators by adopting Regularized Block Diagonalization (RBD) precoding. RBD, originally proposed for multi-user Multiple-Input Multiple-Output (MIMO) Broadcast Channel (BC) settings, is tailored here to the considered multi-operator Multiple-Input Single-Output (MISO) Interference Channel (IC) to avoid that operators exchange any sensitive data about their own users. The overall analytical framework for multi-operator is proved to be a natural evolution of conventional precoding for MISO-BC. The only difference with

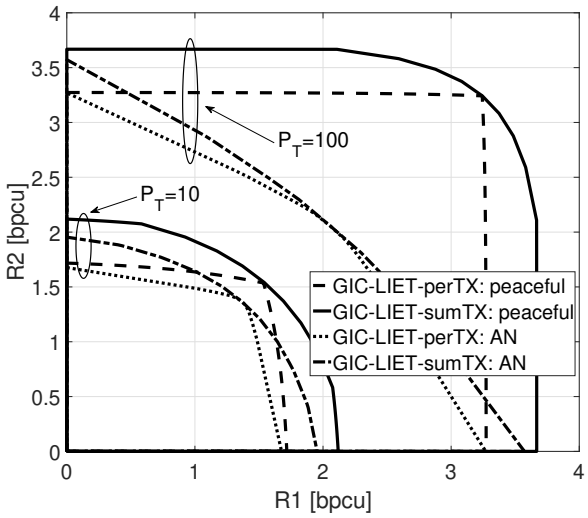

Figure 4.14.: Rate region comparison for the proposed GIC-LIET between the peaceful and the secure systems with per-TX and sum-TX power constraints and for both $P_{T_1} = P_{T_2} = 10$ and $P_{T_1} = P_{T_2} = 100$.

respect to conventional MISO-BC is that in the considered multi-operator MISO-IC, while there is no-cooperation among users, the cooperation among operators is only partial and based on mutual interference-exchange. Tomlinson-Harashima Precoding (THP) is adopted for intra-operator MISO-BC after RBD, and it has been shown to be very effective in handling intra-operator interference while limiting the transmitted power. Numerical analysis has proved that the proposed D-RBD-THP method enables the interference-sharing based cooperation mechanism among operators, and provides a considerable gain when the inter-operator interfering channel is large (say at least $-3\,\mathrm{dB}$). Comparison with conventional spectrum allocation methods proved the benefits of D-RBD-THP, that is capable to at least double the rate achieved by Orthogonal Spectrum Sharing (OSS).

Even if D-RBD-THP has been detailed for MISO-IC setting with $K = 2$ operators, the extension to any arbitrary K and to MIMO-IC scenario where receivers have multiple antennas is just a matter of algebraic and notation complexity purposely avoided here for the sake of clarity. Furthermore, similarly to the parallel precoding algorithm proposed for wireline communications in Chapter 3, the proposed RBD-THP can be interpreted as a novel low-complexity way to carry out the MISO-BC precoding, as it decomposes the sequential interference cancellation of precoding into parallel cancellations with minimal loss. In fact, parallel precoding reduces the overall system latency, which is a critical parameter in dense and delay sensitive networks as for future 5G systems.

In order to complete the discussion on multi-operator cooperation, the second part of the chapter is devoted to the investigation of the degree of privacy guaranteed to operators in the exchange of precoded data. The problem is tackled from a physical layer security view point. In particular, a simple information-theoretical model capturing the main characteristics of the proposed multi-operator scenario has been introduced. A secure communication scheme has been proposed for a sample multi-operator system, which is modeled as a 2-user Gaussian Interference Channel (GIC) with Limited Information Exchange at the Transmitters (GIC-LIET). The information exchanged is wiretap coded so that each transmitter is not able to decode the private information of the other. The performance of the proposed GIC-LIET have been compared with well-established information-theoretical bounds. In particular, simulation results show that the proposed GIC-LIET allows for secure communication over the 2-user IC at higher rates than those allowed by the traditional IC with Confidential Messages (GIC-CM). The performance of GIC-LIET are in between those of the GIC-CM with AN (no information exchange at the transmitters) and those achieved by the secure Gaussian Broadcast Channel with Confidential Messages (full information exchange at the transmitters), considered here as an upper bound. We also show that the rate loss of our secure system with respect to the peaceful system is relatively small for practical values of the transmitted power (i.e., $P_T = 10$) while it increases for higher maximum transmitted power (i.e., $P_T = 100$). Concluding, the overall analysis demonstrated the feasibility of the proposed interference-sharing multi-operator precoding algorithm, confirming that secure communication can be achieved for all the operators with only a small loss in the achievable user rates.

5. Non-Linear Precoding for Visible Light Communications

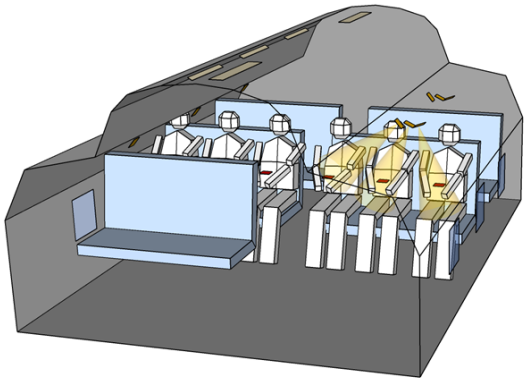

Figure 5.1.: In-Flight VLC Communications Systems

5.1. Introduction to VLC for In-Flight Systems

Visible Light Communications (VLC) are emerging as a promising alternative to radio communications in harsh environments. Their inherent advantages are: use of unlicensed bands, E.M. pollution free, and availability of low cost transmitters (LED lights) that offer a potentially high capacity per unit area system [102]. Among the various VLC applications, on-aircraft VLC systems are gaining large attention in recent years as a possible technique to provide low cost, ubiquitous and green access to high speed Internet through the usage of the LED reading lamps, for which the communication function would be superposed to their natural illumination one. VLC offers an inexpensive and scalable alternative to the existing low-bandwidth Wi-Fi-based infrastructure [103], which adapts to the asymmetric traffic conditions of the entertaining and multimedia services. VLC-based solution mimics femto-cell systems by exploiting the available LED reading lamps to serve the passengers' terminals (which can be added into or externally

to laptops, tablets, smartphones etc.) with a point-to-point wireless downlink Intensity-Modulated/Direct-Detected (IM/DD) visible light communication. The reading lamps can be connected to the external communications system by any technology (e.g., power line communication [104] or optical fiber [105]). Each user device logs on to "its own" cell through a proper uplink transmission protocol (typically InfraRed, IR). High Quality of Service (QoS) is dependent on adequate values of Signal-to-Interference-plus-Noise Ratio (SINR).

In practice, the deployment of in-flight VLC systems presents several issues. In particular, the large number of closely spaced non-directive transmitters makes the communication challenging, due to the interference that is generated while many sources of light inside the cabin (e.g., ceiling, sidewall, dome lights, solar radiation entering through the fuselage windows) contribute to increase the noise at the receivers' front-end. The possibility of in-flight VLC was already introduced and investigated in [106, 107], while the specific problem of exploring interference and Signal-to-Interference Ratio (SIR) was reported in [108] for a simple airplane cabin geometry and sources-receivers configuration. A complete characterization of the SINR inside a realistic airplane cabin has been presented in [109] under the hypothesis of perfect alignment between transmitters and receivers, and showing promising results in case of highly directive lamps. However, as soon as the device is moved (e.g., user moves the device from hand to hand) performance dramatically drop due to transmitter-receiver misalignment. In this regard, the use of LEDs with wider beamwidths could be a viable solution to guarantee seamless connectivity, but this should be designed side-by-side with proper techniques in order to reduce the resulting Mutual Light Interference (MLI) to acceptable values. Apart from the most common Frequency or Time Division Multiplexing schemes (FDM/TDM, respectively) that cannot be accommodated within the limited electrical bandwidth of common LED lamps [110], MLI reduction could be based on Colour Division Multiplexing (CDM) [111][112], in which a different colour is assigned to each data-stream. Despite the spectral efficiency of CDM approach (each source transmits on the same electrical bandwidth), it has the inherent disadvantage of having to equip the receiving terminals with more additional optical components and analog decoding chains to receive separately every possible colour, thus increasing the costs and the complexity of the realization.

In this chapter, we explore the possibility of using a multi-stream Transmitter Precoding (TP) approach to mitigate MLI at the receivers, by exploiting the knowledge of the channel characteristics from each transmitter to each receiver. When multiple sources are coordinated (acting as a single, whole transmitter) to transmit information to multiple devices equipped with one single receiver, the system is called Multi-User-Multiple-Input Single-Output (MU-MISO), and the one-to-many communication channel is identified as “broadcast”. In particular, motivated by the promising results obtained for wireline MU-MISO communication systems (see Part I of this thesis), this chapter focuses on the design of non-linear Tomlinson-Harashima Precoding (THP) [41, 42] for in-flight VLC systems. Even if the literature on MU-MISO systems is well detailed, the VLC scenario contains

some peculiarities:

- VLC is a special type of IM/DD Optical Wireless Communication (IM/DD OWC), so the transmitter uses real-valued and non-negative signals instead of complex and bipolar ones;
- each LED transmitting unit has two power constraints: the average value of the emitted signal (average optical intensity intended for illumination) and the maximum peak amplitude (maximum optical intensity) limited by the LED technology or by its input linearity range.

5.1.1. Related Works

The concept of MU-MISO VLC systems is close to that of multiple-input multiple-output (MIMO) optical wireless communication, which dates back to [113]. More recently, Hsu et al. [114] proposed and demonstrated a 3x3 single-user MIMO VLC system using commercial available phosphorescent white LEDs and performing Zero-Forcing (ZF) channel equalization at the single receiver. However, the MU-MISO VLC system considered here is for multiple devices that are geographically distributed so that no joint receiver processing can be performed. Instead, signal processing should be entirely shifted at the transmitter side and applied prior to signal transmission is form of precoding. Transmitter precoding techniques for MU-MISO VLC systems are in [115][116][117][118]. These papers proposed linear or non-linear techniques for ideal VLC scenarios within an empty room, thus not accounting for complex reverberating environments. In Li et al [115], Zero-Forcing (ZF) and Minimum Mean Squared Error (MMSE) linear precoding techniques were analyzed in terms of average Bit Error Rate (BER) and Mean Square Error (MSE) performance through simulations in an empty room, where an arbitrary number of receivers were randomly placed. In Ma et al. [116] the application scenario is again an empty room, and authors proposed two linear precoding schemes, obtained through sum-MSE minimization and minimal illumination level. A different approach has been followed by Pham et al. [118], who proposed a MU-MISO VLC system optimization in terms of VLC channel capacity (i.e., mutual information between input and output) in terms of lower and upper bounds of VLC channel capacity and linear ZF precoding techniques. Non-linear precoding for VLC have been first considered in Yu et al. [117], that compared a linear ZF precoding scheme with a non-linear one based on Zero-Forcing-Dirty Paper Coding (ZF-DPC) with a remarkable spectral efficiency gain. ZF-DPC represents a theoretical upper bound that can be attained by pre-canceling methods such as the proposed THP, that is compared herein to ZF-DPC.

5.1.2. Chapter Contributions

In this chapter, motivated by the promising results obtained for wired communication systems (see Part I of this thesis), we adapted Tomlinson-Harashima

Precoding (THP) to a VLC system and evaluated the performance for a realistic highly-reverberating scenario inside an airplane passenger cabin. The choice is mainly motivated by the fact that the non-linear transmitter precoding allows to mitigate multi-user interference still bounding the transmitted power. THP is very promising for VLC applications, since the amplitude constraint to be imposed on the emitted signal can be inherently fulfilled. Moreover, inside an airplane cabin the users' mobility is very limited and the optical channel is quasi-static, or slowly time varying. This condition is suited for the application of a computationally complex algorithm such as THP, as the precoding matrix can recalculated much less frequently.

In particular, the contributions of the chapter are three-fold:

1. we first developed a realistic model of a passenger cabin with a certain number of reading lamps and receivers to compute the VL channel matrixes with [109];
2. we adapted THP to VLC and demonstrated the performance gain with respect to ZFP, comparing THP with the ZF-DPC upper bound as indicated in [117], for varying emission angles and degree of coordination by the size of the precoding matrix;
3. we identified an optimal configuration of the precoding system that guarantees the best compromise among channel capacity maximization, precoding complexity, robustness against source-receiver misalignments, and lamps directivity (in order not to dazzle the adjacent passengers and avoid discomfort situations).

5.1.3. Contribution in International Conferences/Journals

Part of the material presented in this chapter has been published in:

- D. Tagliaferri, **A. Matera**, C. Capsoni, and U. Spagnolini, "Nonlinear Visible Light Communications Broadcast Channel Precoding: A New Solution for In-Flight Systems" in *IEEE Photonics Journal*, vol. 10, no. 4, pp. 1–14, Aug. 2018.

5.2. Channel Generation by Ray Tracing

In order to test the performance of the proposed algorithms, the optical channel matrixes have been generated, together with the SINR values, by using the Modified MonteCarlo (MMC) ray tracer tool detailed in [109], originally developed for the characterization of visible and IR light propagation inside any arbitrary-shaped space. The tool in [109] provides the Channel Impulse Response (CIR) from each modulated light source to each receiver in the space, together with the

background light level (which is the amount of optical power due to all the non-modulated sources of radiation), and the SINR at the receiving side. The CIRs are computed for a set of testing wavelengths chosen either in visible or in near-IR range and considering an arbitrary number of reflections. The final result is a function of the specific source-receiver pair (j, k), the wavelength λ and the time t: CIR is hereafter indicated with $h[t, j, k, \lambda]$. The background light levels composed by the optical power from the illumination fixtures and from the solar radiation entering through the windows (the latter being modeled according to [119] and [120]). The SINR at the k-th photodiode receiver is

$$\mathrm{SINR}_k = \frac{i_{s,k}^2}{i_{int,k}^2 + \sigma_{n,k}^2}, \tag{5.1}$$

where the numerator is the squared electrical current generated by the useful modulated light sources and the denominator is the sum of the squared electrical current generated by the interfering light signals (which are in the same electrical band of the useful ones) plus the overall electrical noise power $\sigma_{n,k}^2$. As motivated in the introduction, in this chapter we consider standard phosphor-based LED as VLC sources, thus we choose as testing wavelengths for every simulation the red, green and blue peaks (i.e. 460 nm, 532 nm and 650 nm) as in [121]. Hereafter, we consider the channel as frequency-flat within the bandwidth of interest that is set to $B = 20$ MHz. The electrical current for the signal of interest is expressed as

$$i_{s,k} = \sum_{t=0}^{N_t} \sum_{j \in \mathcal{K}_{\mathcal{U}}} \sum_{\lambda \in \mathcal{W}} \underbrace{P_T[j, \lambda] \cdot h[t, j, k, \lambda] \cdot \eta\,[k, \lambda]}_{i_R[t,j,k,\lambda]}, \tag{5.2}$$

where $P_T\,[j, \lambda]\,[W]$ is the optical power transmitted by the j-th source at wavelength λ and $\eta\,[k, \lambda]$ is the k-th photodetector spectral responsivity measured in $[A/W]$. The product of the three terms is the generated photocurrent at the receiver $i_R\,[t, j, k, \lambda]$. The total electrical current at the receiver is the obtained by summing over the time grid on which the CIR is computed (thanks to the frequency-flat hypothesis), the set of wavelengths $\mathcal{W}$ and the set of useful sources $(\mathcal{K}_{\mathcal{U}})$. The interfering current $i_{int,k}$ has the same expression of Eq. (5.2), with the only difference that the summation spans the set of interfering sources, while the electrical noise power $\sigma_{n,k}^2$ is computed as:

$$\sigma_{n,k}^2 = 2\,e\,B\,\{i_{bg,k} + i_{s,k} + i_{int,k} + i_{dark,k}\} + \sigma_{th,k}^2, \tag{5.3}$$

where the first term is the overall shot noise caused by the sum of the electrical currents generated respectively by the background light $(i_{bg,k})$, the signal and interfering lights $(i_{s,k} + i_{int,k})$ and the dark current of the photodector $(i_{dark,k})$ [122] while the second one is the thermal noise variance (the input referred noise density $i_{rms}\ \left[A/\sqrt{H_z}\right]$ of the front-end's first amplifying stage).

The channel matrix is then computed as an intensity-one:

$$\mathbf{H} = \{h_{j,k}\}, \qquad h_{j,k} = \sum_{t=0}^{N_t} \sum_{\lambda \in \mathcal{W}} h[t, j, k, \lambda], \tag{5.4}$$

where $h_{j,k}$ is the channel coefficient between the k-th transmitter and the j-th receiver, and results from the summation over the time grid on which the complete CIR $h[t, j, k, \lambda]$ is computed and over the set of wavelengths $\mathcal{W}$ for white-light VLC.

5.3. System Model

In this chapter, we consider the downlink of a general MU-MISO VLC system consisting in N_t LED transmitters serving N_r single-photodiode users (i.e., aircraft passengers), as shown in Fig 5.2.

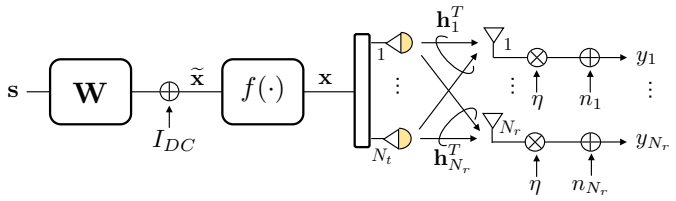

Figure 5.2.: Downlink VLC system model with transmitter precoding. The N_t signals (vector $\mathbf{s}$) are precoded by matrix $\mathbf{W}$ and then transmitted onto the VLC channel by means of N_t non-directive sources (LEDs) to N_r single-PD users.

5.3.1. VLC Downlink Channel

The downlink channel from the LEDs to the users is a frequency-flat VLC channel, such that the signal received at the k-th user is

$$y_k = \eta \mathbf{h}_k^T \mathbf{x} + n_k, \tag{5.5}$$

where η is the PhotoDiode (PD) responsivity, $\mathbf{h}_k^T \in \mathbb{R}_{\geq 0}^{1 \times N_t} = [h_{1,k}, h_{2,k}, ..., h_{N_t,k}]$ is the non-negative, real-valued vector denoting the channel coefficients from all the LEDs to the k-th single-photodetector user, $\mathbf{x} \in \mathbb{R}_{\geq 0}^{N_t \times 1}$ represents the emitted optical power signal and $n_k \sim \mathcal{N}(0, \sigma_{n,k}^2)$ is the overall noise fluctuation current at the k-th receiver which can be reasonably modeled as zero-mean additive Gaussian process [123] with variance $\sigma_{n,k}^2$ (computed with (5.3)). Gathering all the received user signals, we obtain the canonical MU-MISO model as

$$\mathbf{y} = \eta \mathbf{H} \mathbf{x} + \mathbf{n}, \tag{5.6}$$

where $\mathbf{y} = [y_1, y_2, ..., y_{N_r}]^T$ is the signal received by all the users, $\mathbf{H} = [\mathbf{h}_1, \mathbf{h}_2, ..., \mathbf{h}_{N_r}]^T \in \mathbb{R}_{\geq 0}^{N_r \times N_t}$ is the compound channel matrix defined as in (5.4) and $\mathbf{n} \sim \mathcal{N}(\mathbf{0}, \mathbf{R}_n)$ is the overall zero-mean additive uncorrelated colored Gaussian noise with covariance $\mathbf{R}_n = \text{diag}(\sigma_{n,1}^2, \sigma_{n,2}^2, ..., \sigma_{n,N_r}^2)$.

5.3.2. Transmitter Constraints

The transmitted signals $\mathbf{x}$ are obtained as

$$\mathbf{x} = f(\tilde{\mathbf{x}}), \tag{5.7}$$

where $\tilde{\mathbf{x}}$ are the electrical drive current signals at the LEDs input and $f(\tilde{\mathbf{x}})$ is the LED optical power (or, equivalently, luminous intensity) vs drive current characteristic , assumed hereafter to be the same for each LED. As typical for white phosphorescent LEDs [124], for a drive input current $\tilde{x}_k$ in the range [0, $I_{\max}$] it is approximately linear as

$$f(\tilde{x}) \approx \gamma \cdot \tilde{x}, \tag{5.8}$$

where γ is the so-called LED conversion factor that maps $[0, I_{\max}]$ into optical power $[0, P_{\max}]$ [116].

Since we use a transmitter precoding technique, the drive current signals at the LEDs input are obtained as

$$\tilde{\mathbf{x}} = \mathbf{W}\mathbf{s} + \mathbf{i}_{DC}, \tag{5.9}$$

where $\mathbf{s} = [s_1, s_2, .., s_{N_r}]^T \in \mathbb{R}^{N_r \times 1}$ are the zero-mean, uncorrelated symbols to be transmitted to the N_r users, whose amplitudes are limited as

$$|s_k| \in [-d_k, +d_k], \tag{5.10}$$

$\mathbf{W} \in \mathbb{R}^{N_t \times N_r}$ is the precoding matrix, and $\mathbf{i}_{DC} \in \mathbb{R}_{\geq 0}^{N_t \times 1}$ is the vector of DC offset currents added to the signal in order to ensure the non-negativity of the output. Vector $\mathbf{s}$ can include either pulse-amplitude modulated (PAM) symbols or quadrature-amplitude modulated (QAM) ones (see *Remark 1*). In the following, we assume without loss of generality that the DC currents I_{DC}^k are the same for all the LEDs, so $\mathbf{i}_{DC} = I_{DC}\mathbf{1}$ where $\mathbf{1}$ is a column vector of all ones. Therefore, the average transmitted optical power at each LED is

$$\text{E}[x_k] = \gamma \text{E}[\tilde{x}_k] = \gamma \text{E}[\mathbf{w}_k^T \mathbf{s} + I_{DC}] = \gamma I_{DC} = P_T. \tag{5.11}$$

From (5.9), the amplitude constraints on the transmitted signals can be written as:

$$0 \leq \mathbf{w}_k^T \mathbf{s} + I_{DC} \leq I_{\max}, \tag{5.12}$$

where, $\mathbf{w}_k^T$ is the k-th row of the precoding matrix $\mathbf{W}$. Without loss of generality, we choose the DC current I_{DC} to be exactly half of the LED dynamics ($I_{DC} = I_{\max}/2$), and the maximum amplitude of the electrical PAM modulated symbol to be $d_k = I_{DC}$, so as to exploit the full dynamic range of the transmitter. From (5.10) and considering all the previous assumptions, it follows that

$$0 \leq \mathbf{w}_k^T \mathbf{s} \leq I_{DC} \quad \rightarrow \quad \left\|\mathbf{w}_k^T\right\|_1 d_k \leq I_{DC}, \quad \rightarrow \quad \left\|\mathbf{w}_k^T\right\|_1 \leq 1 \qquad \forall k = 1, .., N_t. \tag{5.13}$$

It is easy to show that under these assumptions the constraint in (5.12) is always satisfied.

To tackle the VLC downlink amplitude constraint at the transmitting LEDs, it is convenient to scale the precoding operator $\mathbf{W}$ as

$$\mathbf{W} = \tilde{\mathbf{W}} \frac{1}{\beta}, \tag{5.14}$$

where $\tilde{\mathbf{W}}$ is the MU-MISO precoder and β enforces the power constraint $I_{\max}$ (5.12), which can be rewritten as

$$\left\|\mathbf{w}_k^T\right\|_1 = \frac{1}{\beta} \left\|\tilde{\mathbf{w}}_k^T\right\|_1 \leq 1, \quad \forall k = 1, .., N_t, \tag{5.15}$$

where $\tilde{\mathbf{w}}_k^T$ is the row of the matrix $\tilde{\mathbf{W}}$ which precodes the signal to be transmitted by the k-th LED. From (5.15) the VLC amplitude constraint is always fulfilled for

$$\beta = \left\|\tilde{\mathbf{W}}^T\right\|_\infty = \max_k \left\|\tilde{\mathbf{w}}_k^T\right\|_1, \tag{5.16}$$

with the $(\infty)-$norm $\|\mathbf{A}\|_\infty$ denoting the maximum absolute column sum of the matrix $\mathbf{A}$ (i.e., the maximum column l_1-norm of matrix $\mathbf{A}$).

Remark 1. The analytical treatment of the precoding problem adopted here applies both to conventional single-carrier and to multi-carrier transmissions, such as the MU-MISO OFDM system discussed in [125]. In this last case, Eq. (5.9) describes the precoding operation applied to each OFDM subcarrier.

5.3.3. Signal-to-Interference-plus-Noise Ratio with Precoding

At this point, it is useful to rewrite the expression of the k-th user's SINR highlighting the precoding scheme defined by $\mathbf{W}$ in terms of the elements of the equivalent channel matrix

$$\widetilde{\mathbf{H}} = \mathbf{H}\mathbf{W}. \tag{5.17}$$

To get it, we note that if the constraints in (5.13) are satisfied, the overall signal (5.6) received at the users becomes

$$\mathbf{y} = \eta\gamma\mathbf{HWs} + \eta\gamma I_{DC}\mathbf{H1} + \mathbf{n}, \tag{5.18}$$

where the DC current is removed by a filter at the receiver leading to the equivalent MU-MISO model

$$\mathbf{y} = \eta\gamma\widetilde{\mathbf{H}}\mathbf{s} + \mathbf{n}. \tag{5.19}$$

It follows that the electrical signal received at the k-th single-PD user yields

$$y_k = \eta\gamma\widetilde{h}_{kk}s_k + \eta\gamma\sum_{j\neq k}\widetilde{h}_{kj}s_j + n_k, \tag{5.20}$$

where the first term is the information of interest, the second term represents the residual interference light from all the other transmitters and the last one is the noise. The achievable SINR is therefore:

$$\widetilde{\mathrm{SINR}}_k = \frac{i_{s,k}^2}{i_{int,k}^2 + \sigma_{n,k}^2} = \frac{\gamma^2\eta^2 I_{DC}^2\widetilde{h}_{kk}^2}{\gamma^2\eta^2 I_{DC}^2\sum_{j\neq k}\widetilde{h}_{kj}^2 + \sigma_{n,k}^2} = \frac{\eta^2\widetilde{h}_{kk}^2 P_T^2}{\eta^2 P_T^2\sum_{j\neq k}\widetilde{h}_{kj}^2 + \sigma_{n,k}^2}. \tag{5.21}$$

Hence, the transmission rate for user k-th and the sum rate can be computed respectively as

$$r_k = \frac{1}{2}\log_2\left(1 + \widetilde{\mathrm{SINR}}_k\right), \qquad R = \sum_{k=1}^{N_r} r_k, \tag{5.22}$$

assuming the overall disturbance at the denominator in (5.21) is modeled as a zero-mean Gaussian process with variance $\eta^2 P_T^2\sum_{j\neq k}\widetilde{h}_{kj}^2 + \sigma_{n,k}^2$.

5.4. VLC Downlink Precoding

In this section, the VLC precoding scheme is detailed with the aim to take benefit from interference, which is conventionally perceived as an impairment for the communication. In particular, here we focus on Zero-Forcing (ZF) precoding which forces to zero all the interference between the N_r users. Hence, the precoding matrix $\mathbf{W}$ is designed to fully cancel the MLI in the VLC channel, which is mathematically described by the diagonalization of the VLC channel matrix $\mathbf{H}$ as [67]

$$\widetilde{\mathbf{H}} = \mathbf{HW} = \mathrm{diag}(\widetilde{h}_{11}, \widetilde{h}_{22}, ..., \widetilde{h}_{N_rN_r}), \tag{5.23}$$

where $\widetilde{h}_{kk}$ denotes the equivalent channel gain for the k-th user.

It follows that in the case of ZF precoding the decision variable at the k-th single-PD user in (5.20) yields

$$y_k = \eta\gamma\widetilde{h}_{kk}s_k + n_k, \tag{5.24}$$

and the corresponding SINR simplifies to

$$\widetilde{\mathrm{SINR}}_k = \frac{\eta^2\widetilde{h}_{kk}^2 P_T^2}{\sigma_{n,k}^2}. \tag{5.25}$$

Finally the transmission rate r_k with precoding is computed as

$$r_k = \frac{1}{2}\log_2\left(1 + \frac{\eta^2\widetilde{h}_{kk}^2 P_T^2}{\sigma_{n,k}^2}\right). \tag{5.26}$$

By the comparison between (5.21) and (5.25), it can be noticed that the interference term in the SINR expression in (5.21) is completely cancelled due to the effect of precoding.

In the following, linear and non-linear zero forcing precoding approaches are reviewed and adapted to the peculiarities of the VLC scenario.

5.4.1. Linear Zero Forcing Precoding

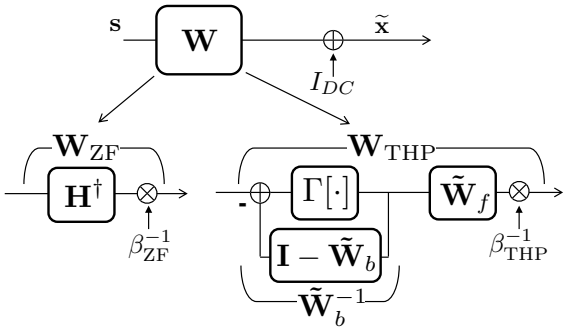

Figure 5.3.: VLC precoding schemes: linear Zero-Forcing (ZF) vs Tomlinson-Harashima Precoding (THP)

In linear ZF the VLC channel $\mathbf{H}$ is inverted by the linear transformation $\tilde{\mathbf{W}}_{\mathrm{ZF}}$ as

$$\tilde{\mathbf{W}}_{\mathrm{ZF}} = \mathbf{H}^{\dagger}, \tag{5.27}$$

where $\mathbf{A}^{\dagger} = \mathbf{A}^H\left(\mathbf{A}\mathbf{A}^H\right)^{-1}$denotes the right Moore–Penrose pseudo-inverse of matrix $\mathbf{A}$. It is easy to prove that the ZF condition (5.23) is satisfied, i.e.,

$$\mathbf{H}\mathbf{W}_{\mathrm{ZF}} = \frac{1}{\beta_{\mathrm{ZF}}}\mathbf{I}, \tag{5.28}$$

and that the rate for user k-th is

$$r_k \leq \frac{1}{2}\log_2\left(1+\frac{1}{\beta_{\mathrm{ZF}}^2}\cdot\frac{\eta^2 P_T^2}{\sigma_{n,k}^2}\right), \tag{5.29}$$

where β_{ZF} is computed by (5.16).

5.4.2. Tomlinson-Harashima Precoding

Linear ZF precoding is known to lead to an extremely high scaling factor $\beta_{\mathrm{ZF}} \gg 1$ to contrast the amplitude peaks of the encoded symbols which severely degrades the transmission rates for all the users (5.29).

Tomlinson-Harashima Precoding (THP) for the VLC downlink is a non-linear successive interference cancellation precoding scheme, conventionally based on ZF criteria, that inherently accounts for amplitude dynamics. The main idea behind THP is to implement the VLC channel inversion by successively canceling previously encoded symbols, still limiting their amplitude by a non-linear modulo operation on amplitudes. The THP scheme is depicted in Fig. 5.3, where the precoding matrix $\tilde{\mathbf{W}}_{\mathrm{THP}}$ is decomposed in two sub-matrices as

$$\tilde{\mathbf{W}}_{\mathrm{THP}} = \tilde{\mathbf{W}}_f \tilde{\mathbf{W}}_b^{-1}, \tag{5.30}$$

where $\tilde{\mathbf{W}}_f \in \mathbb{R}^{N_t \times N_r}$ is a linear matrix with orthonormal columns (i.e., feed-forward filter) and $\tilde{\mathbf{W}}_b \in \mathbb{R}^{N_r \times N_r}$ (feedback filter) is a lower-triangular matrix with unit values along the main diagonal. As anticipated before, the key characteristic which makes THP an attractive solution for applications with strict transmit power (or amplitude in this case) constraints (e.g., DSL communication systems see Part I of the thesis) is that the inversion of the triangular matrix $\tilde{\mathbf{W}}_b$ is performed by backward substitution together with a non-linear modulo operator $\Gamma[\cdot]$ (see feedback block in Fig. 5.3) which limits the amplitude of the encoded symbols within the boundaries of the original signal constellation.

Feed-forward filter $\tilde{\mathbf{W}}_f$ and feedback filter $\tilde{\mathbf{W}}_b$ are typically obtained [26] by the QR decomposition of the VLC channel matrix $\mathbf{H}$ as

$$\mathbf{H}^T = \mathbf{Q}\mathbf{R} = [\mathbf{Q}_1, \mathbf{Q}_2]\begin{bmatrix}\mathbf{R}_1 \\ \mathbf{0}\end{bmatrix}, \tag{5.31}$$

then

$$\tilde{\mathbf{W}}_f = \mathbf{Q}_1, \quad \tilde{\mathbf{W}}_b = \mathrm{diag}(\mathbf{R}_1)^{-1}\mathbf{R}_1^T, \tag{5.32}$$

where $\mathbf{Q}_1 \in \mathbb{R}^{N_t \times N_r}$ contains the first N_r orthonormal columns of the unitary matrix $\mathbf{Q} \in \mathbb{R}^{N_t \times N_t}$, $\mathbf{R}_1 \in \mathbb{R}^{N_r \times N_r}$ is an upper triangular matrix and $\mathrm{diag}(\mathbf{R}_1) \in$

$\mathbb{R}^{N_r \times N_r}$ is a diagonal matrix that contains the main diagonal entries of $\mathbf{R}_1$. It can be shown that the ZF condition (5.23) is satisfied:

$$\begin{aligned}\mathbf{H}\mathbf{W}_{\text{THP}} &= \mathbf{H}\mathbf{W}_f\tilde{\mathbf{W}}_b^{-1}/\beta_{\text{THP}} \\ &= \mathbf{R}_1^T\mathbf{Q}^T\mathbf{Q}\mathbf{R}_1^{-T}\text{diag}(\mathbf{R}_1)/\beta_{\text{THP}} \\ &= \text{diag}(\mathbf{R}_1)/\beta_{\text{THP}}.\end{aligned} \tag{5.33}$$

Similarly to (5.22), (5.26), the rate of user k-th is therefore

$$r_k \leq \log_2\left(1 + \frac{|r_{kk}|^2}{\beta_{\text{THP}}^2} \cdot \frac{\eta^2 P_T^2}{\sigma_{n,k}^2}\right), \tag{5.34}$$

where r_{kk} is the k-th diagonal entry of matrix $\text{diag}(\mathbf{R}_1)$ and β_{THP}^2 is computed as in (5.16).

To prove the benefits of THP with respect to linear ZFP for the considered VLC architecture, let us focus on the interpretation of the scaling factor β, whose value is proportional to the amplitude penalty to be paid by performing a complete channel inversion at the transmitter side. Let us consider the Tomlinson-Harashima precoded symbols $\tilde{\mathbf{x}} = \tilde{\mathbf{W}}_b^{-1}\mathbf{s}$ at the output of the feedback block. Notice that in case of M-ary square QAM input symbols $\mathbf{s}$, the encoded symbols $\tilde{\mathbf{x}}$ are approximately uncorrelated with only a slight power increment with respect to the input symbols [41] (i.e., $\sigma_{\tilde{x}}^2 = \frac{M}{M-1}\sigma_s^2$) that is bounded to maximum 1.25 dB (see Chapter 2, Table 2.1), hence neglected in simulation results (Sect. 5.5). As a consequence of the modulo operation in THP and of the aforementioned assumption, the maximum amplitude of the symbols at the output of the feedback filter is approx. the same as the maximum signal amplitude at the input, i.e.,

$$\max_k |\tilde{x}_k| \approx \max |s_k| \,. \tag{5.35}$$

Let us now consider the k-th precoded symbol

$$x_k = \frac{1}{\beta_{\text{THP}}}\left[\tilde{\mathbf{W}}_f\tilde{\mathbf{x}}\right]_k = \frac{1}{\beta_{\text{THP}}}\left[\mathbf{Q}_1\tilde{\mathbf{x}}\right]_k = \frac{1}{\beta_{\text{THP}}}\mathbf{q}_{1,k}^T\tilde{\mathbf{x}}, \tag{5.36}$$

with $[\mathbf{a}]_k$ denoting the k-th element of vector $\mathbf{a}$ and $\mathbf{q}_{1,k}^T \in \mathbb{R}^{1\times N_r}$ the k-th row of matrix $\mathbf{Q}_1$. It directly follows from (5.13) and (5.36) that the amplitude of the k-th transmit symbol x_k is constrained by

$$|x_k| = \frac{1}{\beta_{\text{THP}}}\left\|\mathbf{q}_{1,k}^T\right\|_1 \leq 1 \quad . \tag{5.37}$$

Therefore, the VLC amplitude constraint is always satisfied if

$$\beta_{\text{THP}} = \max_k \left\|\mathbf{q}_{1,k}^T\right\|_1 . \tag{5.38}$$

The key observation is that $\mathbf{q}_{1,k}^T \in \mathbb{R}^{1\times N_r}$ contains only the first N_r entries of the k-th unit-length row $\mathbf{q}_k^T$ of the original unitary matrix $\mathbf{Q}$ coming from (5.31), hence,

$$\beta_{\text{THP}} = \max_k \left\|\mathbf{q}_{1,k}^T\right\|_1 \overset{(a)}{\leq} \max_k \left\|\mathbf{q}_k^T\right\|_1 \overset{(b)}{\leq} \sqrt{N_t}\left\|\mathbf{q}_k^T\right\|_2 = \sqrt{N_t}, \tag{5.39}$$

where the equality in $^{(a)}$ holds if $N_t = N_r$ (i.e., the VLC channel to be precoded is squared) and $^{(b)}$ comes from the inequality between l_2- and l_1-norm. Therefore, if THP is employed for VLC, the power penalty to be paid is bounded by the square root of the number of transmitting LEDs N_t, which is in general much lower than β_{ZF}.

5.5. Simulation Settings and Numerical Results

5.5.1. Airplane Cabin Generation and Simulation Settings

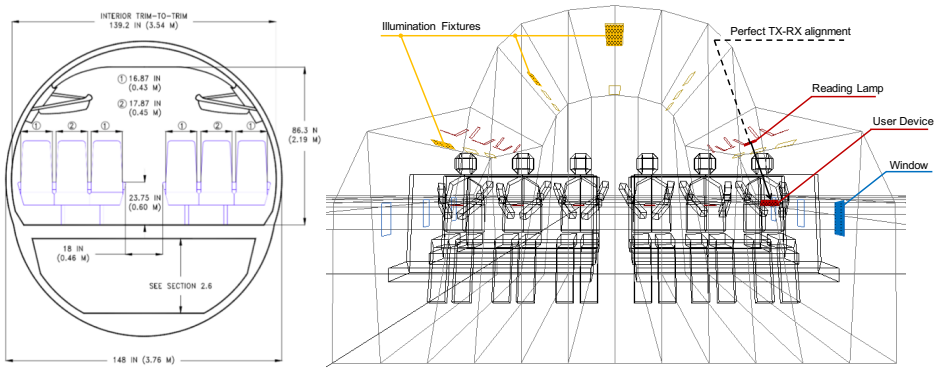

(a) Section **(b)** Frontal view (Autodesk 3DS Max)

Figure 5.4.: Boing 737 fuselage

By using Autodesk 3DS Max, we generated a section of the internal part of a Boeing 737 fuselage as in Fig. 5.4a [126], that considers 3 seat tiers, each one including 6 adjacent seats divided by the central corridor in two 3-seats groups. Each seat is equipped with its own reading lamp perfectly pointed on the users (receivers) so that overall there are $N_{t,tot} = 18$ transmitting LEDs in the system. For performance evaluation, we considered only the $N_r = 6$ passenger's models sitting in the central tier, each one with a receiving terminal. As proved in [109], with the purpose of simulating the visible light propagation in the space and successively compute the channel matrixes $\{\mathbf{H}\}$ and the electrical noise powers $\{\sigma_{n,k}^2\}$

(see Sect. 5.2), it is sufficient to model 3 seat tiers only. This is due to the fact that the effect of further emitting devices has not significant impact on the considered N_r central-tier passengers. In particular, in this work we assumed user devices equipped with a single Osram BPW 34 Si-PIN photodetector (PD) characterized by a 7.02 mm^2 area, 60° Field-Of-View (FOV), 23 MHz bandwidth (with 10 V reverse voltage), 2 nA dark current and an average responsivity over the visible spectrum $\eta = 0.3$. Moreover, with the aim of computing the receivers' noise, the analog front-end is modeled as a single amplifier stage (TIA) operated by a LTC6268-10 operational amplifier with 1 $pA/\sqrt{Hz}$ overall input-referred current noise. We further assumed that the N_r central-tier passengers were jointly served by $N_t \leq N_{t,tot}$ LEDs depending on the degree of coordination between emitting LEDs, while the remaining $N_I = N_{t,tot} - N_t$ LEDs contributed as uncoordinated interference that cannot be canceled by any mean, thus degrading the system performance. Following the avionic layout for lightings proposed in [127] and [128], we inserted 6 wash lights near the luggage compartment and pointed toward the ceiling, 2 ceiling lights in the center of the corridor ceiling and pointed downward and 6 side wall lights, as general LED illumination fixtures emitting a luminous intensity of 1980 lm (assuming a LED luminous efficacy of 90 lm/W) distributed on a neutral white spectrum of 5000 K and a beam angle of 70 degrees. Moreover, in order to consider the worst situation, we associated to each 3-seats group an airplane window of 25×25 cm size from which both the direct sunlight and the diffuse one (skylight) got into. We computed the solar radiation in clear sky conditions (above clouds) at a reference altitude of 10000 m. Finally, the reading lamps were modeled by employing typical parameters for avionic applications [129] such as 100 lm average emitted luminous power, corresponding to $P_T = 0.58\,W$, and the same 5000 K neutral white spectrum, while we let the lamp emission angle (i.e. directivity) varied in the simulations to find the optimal configuration for this specific application. In particular, we tested 5 beam angles Θ: 10, 13, 20, 30, 45 degrees, being the first two (10, 13) the most commonly deployed in today's airplane cabins [129] and the other three (20, 30, 45) chosen to investigate new possible solutions more suitable for the considered VLC on board Internet system where each passenger may reasonably move its the terminal deviating from the perfect alignment condition, but still maintaining the connectivity. The aim of our valuation was twofold: *i)* show the impact of Θ on the average amount of performance degradation (in terms of channel capacity) due to misalignment with respect to the ideal static case; *ii)* investigate the performance gain provided by precoding the transmitted signal when varying Θ and the degree of emitting LEDs coordination, i.e, the number of sources that are jointly precoding and transmitting signals to the same set of users. We considered different degrees of transmitters coordination, so that the number of transmitting LEDs that perform joint precoding and transmission can be either 3 (the reading lamps belonging to the same 3-seats group), 6 (the lamps of the same seat-tier) or all the $N_{t,tot}$ lamps (i.e., fully coordinated system). In practice, since we assumed that each passenger can reasonably move its terminal around the perfect alignment condition, we generated for each passenger a set of 10 realistic movements chosen to efficiently sample the user's

available space and assuming that the receiver displacement from the best light-beam alignment position along each of the three dimensions can range from 15 to 25 *cm*. Then, for each value of the beam angle Θ, we evaluated the performance by averaging the user-capacity (computed as in (5.26)) over 60 channel realizations. Precoder design under imperfect channel state information conditions is beyond the scope of the chapter, hence, the precoding matrixes for ZFP in (5.27) and THP in (5.32) have been computed by assuming perfect channel knowledge at the transmitter side.

5.5.2. Results

The first set of results we present are plotted in Fig. 5.5. When the reading lamps are perfectly pointed toward the users' equipment (dashed line), the data-rate capacity of the links (computed with (5.22)) exhibits a monotonic decrease as the beam angle of the sources Θ increases: this effect is due to the increase of the MLI as well as to the decrease of the optical power density that impinges the receivers. When the receiving terminals move away (even slightly) from the center of the light cone of the lamps (solid lines), the performance degrades rapidly and the channel capacity, in case of precoding (considered here of degree 6), shows a peak for $\Theta_{max} = 20°$. In fact, when $\Theta < \Theta_{max}$, the light cone of each LED is so narrow that when the users move, they can easily fall out of the coverage region, hence experiencing a drastic loss of signal power (inversely proportional to Θ) which limits the performance. By contrast, as $\Theta > \Theta_{max}$, the coverage area is enlarged and thus the misalignments' effect is less effective, but at the same time this implies a strong increment of MLI, from both coordinated and uncoordinated sources. As detailed in Sect. 5.4, TP completely cancels the MLI from the 6 coordinated sources, however, the performance of the system slightly decrease with Θ both for the residual, uncoordinated interference and for the loss of signal power (as for the static case). In this regard, $\Theta_{max} = 20°$ turns out to be the best solution for dynamic scenarios, since it provides the best balancing between signal coverage (power) and residual MLI. As expected, the overall performance gain provided by TP increases proportionally to Θ (and thus to the amount of MLI): in particular, when employing THP, the achievable channel capacity for $\Theta = \Theta_{max} = 20°$ is 7.88 bps/Hz, that can be considered high if compared to 5G point-to-point communications (whose associated maximum modulation format that can be employed is 256-QAM) [130]. The performance is upper-bounded by the theoretical limit provided by ZF-DPC (dotted line) [117], although THP almost matches such limit for most of the angles. Regarding the emission angle of the lamps, it is worth noting that, since their angular light distribution is optimized for providing a good passenger comfort (avoiding glare), the standard commercially available reading lamps for airplanes emit on a beam angle between 10° and 15°. When those lamps are also intended for communication, the average emitted power (and the consequent illumination level) is diminished to a certain extent with respect to the nominal one (e.g. halved as here): we can therefore think

to relax the tight constraint on the angle, tolerating a wider one such as $\Theta = 20°$, proved here to achieve the best performance even in case of transmitter-receiver misalignment.

The user-rate obtained for different levels of TX coordination when employing THP are depicted in Fig. 5.6, emphasizing the trade-off between achievable performance and system complexity of the implementation. As expected, the latter can be reduced, at the price of a performance loss, by decreasing the level of transmitters' cooperation from 6 (empty circle marker, used as reference in the previous result) to 3 (filled circle marker), which still provides remarkable benefits with respect to the unprecoded case (dashed line). Moreover, Fig. 5.6 shows that the utmost performance limit can be reached by fully centralizing the transmission (diamond marker): all the $N_{t,tot} = 18$ sources in the cabin are coordinated to serve the $N_r = 6$ users. In this case all the MLI is suppressed by precoding, thus the performance match the SNR-limited ones. This condition is, however, unpractical in conventional aircraft VLC systems. Apart from the exponentially increasing precoder complexity of a fully centralized transmission, the coordination among sources of different tiers of seats is unfeasible: since the airplane fuselage in Fig. 5.4 is only a slice of the real one, precoding groups of 18 sources contemporarily leads to an undesirable unfairness in users' performance, inasmuch the passengers belonging to the frontal and rear seat tiers of each group (e.g., edge users) are affected by the interference of the adjacent, uncoordinated ones.

Remark 2. Here the focus is on the Boeing 737 airplane cabin. However, some considerations on the possible effects of considering different scenarios can be made, since airplane cabins mainly differ from each other in the spatial arrangements of seats. Let us consider as an example the case of a two-corridor cabin (i.e., Boeing 777 [131]): in this case each seat-tier includes 10 seats divided into 3 groups of 3-4-3 (for Boeing 777-200) or 11 seats divided into 3-5-3 (for Boeing 777-300). The 4 (or 5) central passengers are mutually interfering while also interfered both by the passengers on the left and by those on the right. This challenging scenario is therefore characterized by stronger interference than the Boeing 737 considered in this chapter, and that is the reason why the impact of the proposed non-linear precoding techniques will be even more evident.

5.6. Concluding Remarks

In this chapter, Tomlinson-Harashima Precoding (THP) scheme is proposed for onboard Visible Light Communications (VLC) systems in order to pre-compensate for the strong Multi Light Interference (MLI) arising from the high number of adjacent transmitters (i.e., LED reading lamps). The choice of THP relies in the fact that, as already emphasized in Part I of this thesis, THP is a particularly suitable precoding algorithm for communication scenarios characterized by strict transmit

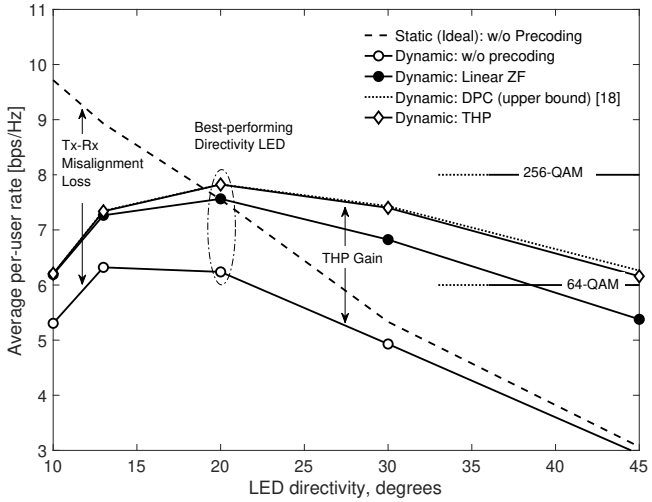

Figure 5.5.: Static (ideal) versus dynamic scenario: performance comparison by varying the LED directivity for different precoding schemes

power constraints, such as wireline communications (see Part I, "Interference Cancellation Techniques for Wired Communication Systems: *Next Generation Digital Subscriber Lines"*), or VLC covered here. To assess the benefits of the proposed on-board VLC system based on THP, we performed numerical evaluations based on ray tracing-generated channels for a standard-equipped Boeing 737 fuselage. Numerical results confirmed the effectiveness of the proposed THP-based VLC system in providing high-speed connectivity to all the passengers. In particular, THP guarantees a fair user performance even in the challenging case of transmitter-receiver misalignment due to the user terminals' movements. THP has been shown not only to outperform conventional unprecoded VLC systems by more then 1.5 bps/Hz, but also linear Zero-Forcing precoding. Furthermore, it has been shown that coordinating the 6 transmitters belonging to the same seat tier and employing 20° LED directivity presents the best trade-off between received power (high LED directivity), the amount of MLI (low LED directivity), and overall system complexity, thus providing robustness with respect to users' movements and still achieving almost 8 bps/Hz (256-QAM), used as ultimate target spectral efficiency for 5G communication systems.

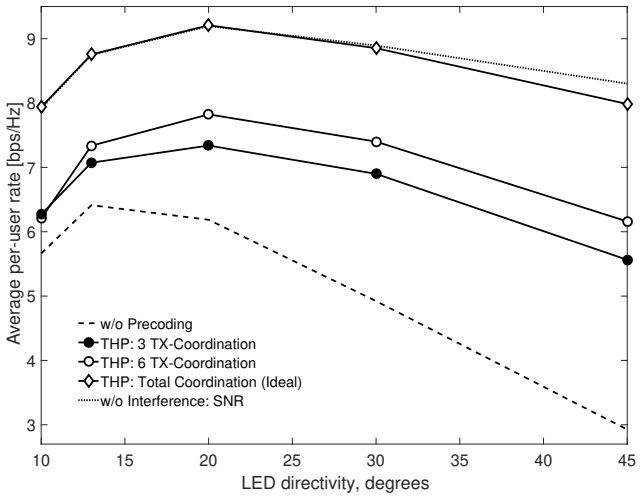

Figure 5.6.: Performance comparison varying the degree of transmitter coordination

Part III.

Interference Mitigation Techniques for Hybrid Wired-Wireless Communications Systems: *The Analog MIMO Radio-over-Copper Architecture*

6. The Genesis of Analog MIMO-RoC: Do LAN Cables Provide Enough Bandwidth for Fronthaul Applications?

6.1. Introduction

Next generation (5G and beyond) mobile systems are completely changing the Radio Access Network (RAN) paradigm due to the ever-growing traffic demand, and calling for the fulfillment of strict requirements in terms of throughput, mobility, and latency. Pervasive deployment of a large number of antennas appears to be the only viable solution to meet such requirements [4], though introducing complicated interference scenarios. In this context, Centralized RAN (C-RAN) [5] is a promising architecture able to address such challenging interference management task. Leveraging centralized signal processing, C-RAN allows to handle a massive number of antennas/cells, taking benefits from their mutual cooperation for interference mitigation. Key enablers for C-RAN is the co-location of BaseBand Units (BBUs) in so-called BBU pools, that allows centralized processing and provides remarkable benefits in terms of programmability, scalability, and cost reduction. The antennas, with all the Radio-Frequency (RF) functionalities, are hosted at the Remote Antenna Units (RAUs), while modulation/demodulation and precoding are performed at the BBUs.

The FrontHaul (FH) link between RAUs and BBUs is conventionally designed to exchange digital In-phase and Quadrature (I/Q) signals streaming according to the CPRI protocol [7], demanding analog/digital conversion at the RAU. As a consequence, the expected increase in RF signal bandwidth and the massive number of antennas call into question the effectiveness of this digital I/Q streaming, that would introduce a bandwidth expansion of RF signals over the FH that can be as severe as 30x. Compression of digital I/Q signals [8] or more flexible RAN functional split options [9] are not enough for bandwidth reduction. In contrast with these newly proposed FH architectures, which are mostly digital, one possible solution for high-rate/low-latency/synchronized RAU applications is to employ a fully analog FH link [30, 12, 132].

In analog FH, the RAUs relay the Intermediate Frequency (IF) signals to/from

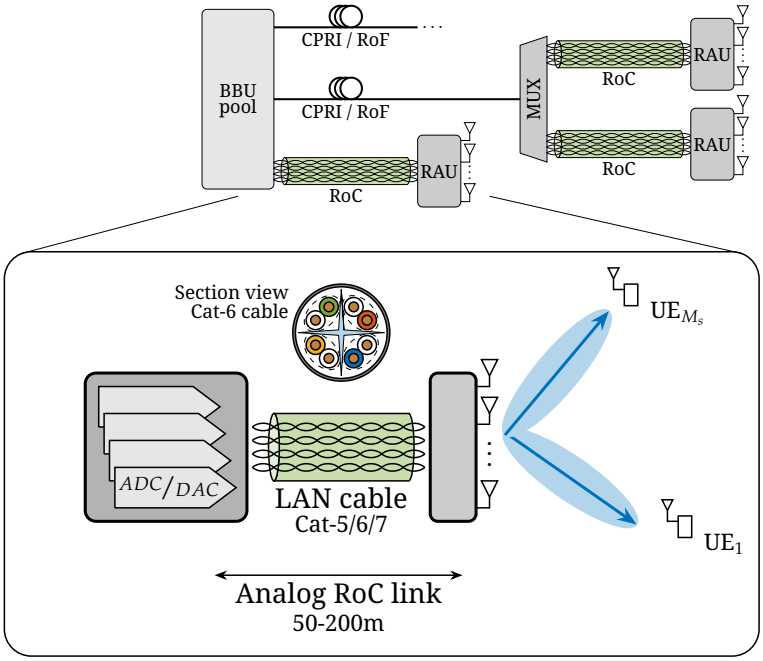

Figure 6.1.: C-RAN architecture with joint deployment of fiber and copper

the BBUs after heterodyning, thus avoiding any bandwidth expansion due to digitization or latency (up to the propagation only), which enables fairly precise bit/carrier-frequency synchronized RAUs. Analog FH simplifies the FH, improves the energy efficiency, and reduces hardware cost. Analog Radio-over-Fiber (A-RoF) provides an effective example of analog FH, due to its capability to carry several Gbit/s in terms of equivalent data-rate [133, 12]. However, A-RoF architecture would require the deployment of a large-scale and pervasive fiber optic infrastructure whose cost can be excessive. Even if RoF could be based on Passive Optical Networks (PON), the RAUs still need the power supply for optical sources and electronics. As a consequence, this could make the economical benefits of using PON questionable, thus pushing to look for novel cost-effective solutions such as Analog Radio-over-Copper (A-RoC), which has been gaining much attention over the last years [30, 31, 134], and it is the focus of this chapter.

A-RoC is a complementary/alternative technology for FH that makes use of Local Area Network (LAN) cables, which are nowadays already largely deployed in buildings and enterprises, thus cutting the costs of the deployment of a brand-new network infrastructure, mostly if considering indoor coverage. LAN cables contain 4 twisted pairs bonded together to provide at least 4 separated cable-pairs (or space) channels with a bandwidth of up to 1GHz/pair (depending on the cable type). Cat-5/6/7 cables enable the design of all-analog and low-cost fronthauling

(at least for the last 100-200m), which, in principle, is capable of supporting a large number of independent radio access channels (possibly corresponding to different Radio Access Technologies, RATs) or a massive number of antennas at each RAU.

Despite of the potentially huge bandwidth capability offered by LAN cables, existing A-RoC solutions exploit mainly the low-frequency cable bandwidth [33, 31], which is characterized by low attention and crosstalk interference. Moreover, they are based on a 1-to-1 mapping between antennas and twisted-pairs, i.e., each twisted-pair carries the signal coming to/from a single RAU antenna, which allows to serve up to 4 antennas (e.g., 4x4 MIMO) per LAN cable, if all the 4 twisted-pairs are employed. The goal of this chapter is to show the great transport capability provided by LAN cables, whose cable frequency can be exploited far beyond the first few tens of MHz, thus providing enough bandwidth for indoor fronthaul applications.

6.1.1. Chapter Contribution

In this chapter, we extend the conventional A-RoC FH architecture by introducing a more flexible and efficient utilization of the transport capabilities of indoor LAN cables. This novel architecture, referred to as A-MIMO-RoC, allows radio signals coming to/from multiple RAU antennas to be freely mapped over the LAN cable multiplexed over both space (i.e., the 4 space channels provided by the 4 twisted-pairs) and frequency (i.e., the 1 GHz bandwidth available for each twisted-pair) dimensions. The name *A-MIMO-RoC* comes from the structure of the overall channel between the BBU and the end-users, which is modeled as the cascade of a MIMO radio channel and a MIMO cable channel.

The characteristics of the most commonly employed LAN cables, e.g., Cat-5/6/7, are revised in this chapter to delineate the link budget for the cascade of air and copper links. Based on the link-budget, a feasibility study is conducted in order to define the maximum number of independent RAT channels (or independent antennas at every RAU) that can be allocated over different twisted-pairs/frequency channels of a single LAN cable, while taking into account the maximum power spectral density over cables to avoid extra-cable interference.

The numerical analysis shows that the equivalent data-rate that can be achieved over copper-cable systems is large enough to make A-MIMO-RoC a more than valid solution for 5G indoor networks over the last 100-200m.

6.1.2. Contribution in International Conferences/Journals

Part of the material presented in this chapter has been published in:

- S. H. R. Naqvi, **A. Matera**, L. Combi, and U. Spagnolini, "On the Transport Capability of LAN Cables in All-Analog MIMO-RoC Fronthaul" in *2017*

IEEE Wireless Communications and Networking Conference (WCNC), pp. 1–6, IEEE, 2017.

6.2. System Model and Parameters

The system model for the proposed A-MIMO-RoC architecture is shown in Fig. 6.2 for uplink transmission (downlink would be similar, see Chapter 8), where N antennas at the RAU are connected to the BBU by a LAN cable with $N_c = 4$ twisted pairs to serve M_S users. To simplify the reasoning here, users are equipped with one antenna each, but any generalization is straightforward. Each RAU relays towards the BBU (or any other mid-way equipment) the analog signals received from the users after a proper Analog-to-Analog (A/A) conversion, which comprises frequency downconversion of RF signal to match the cable frequency band and signal amplification, as detailed later.

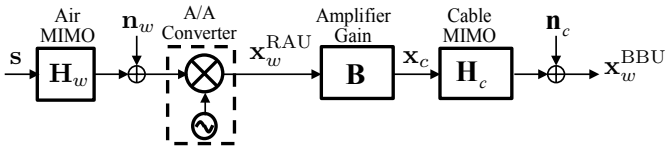

Figure 6.2.: Block diagram of A-MIMO-RoC.

The signal $\mathbf{x}_w^{\mathrm{RAU}} \in \mathbb{C}^N$ received at the RAU antenna array (after downconversion) is modeled as flat-fading (e.g., it corresponds to one subcarrier of OFDM/OFDMA modulation) as

$$\mathbf{x}_w^{\mathrm{RAU}} = \mathbf{H}_w \mathbf{s} + \mathbf{n}_w, \tag{6.1}$$

where $\mathbf{H}_w \in \mathbb{C}^{N \times M_S}$ is the air-link channel matrix from the M_S users to the N antennas, $\mathbf{s} \in \mathbb{C}^{M_S}$ is the users signal, and $\mathbf{n}_w \sim \mathcal{CN}(\mathbf{0}, \sigma_n^2 \mathbf{I})$ is the air-link noise at the antenna array with power σ_n^2. The signal $\mathbf{x}_w^{\mathrm{BBU}} \in \mathbb{C}^N$ received at the BBU after A/A is

$$\mathbf{x}_w^{\mathrm{BBU}} = \mathbf{H}_c \mathbf{B} \mathbf{x}_w^{\mathrm{RAU}} + \mathbf{n}_c, \tag{6.2}$$

where $\mathbf{H}_c \in \mathbb{C}^{N \times N}$ is the space-frequency MIMO cable channel accounting for the frequency-dependent Insertion Loss (IL, on the main diagonal elements $[\mathbf{H}_c]_{i,i}$) and for the frequency-dependent Far-End Crosstalk (FEXT, on the off-diagonal terms $[\mathbf{H}_c]_{i,j}$). The N signals are channelized into Space and Frequency Division Multiplexing (SDM/FDM, respectively) over N_c twisted-pairs, each equipped with

N_f cable bands. The overall LAN cable channel presents a block-diagonal structure to guarantee the orthogonality of the cable-bands:

$$\mathbf{H}_c = \mathrm{diag}\big[\mathbf{H}_{c,1}, \mathbf{H}_{c,2}, \ldots, \mathbf{H}_{c,N_f}\big]. \tag{6.3}$$

Cable channel at the k-th frequency band $\mathbf{H}_{c,k} \in \mathbb{C}^{N_c \times N_c}$ contains the IL and FEXT elements for the N_c spatial cable channels. The total bandwidth available over the $N_f \cdot N_c$ space-frequency cable channels should be $N_f N_c \geq N$ for a given Signal-to-Interference-plus-Noise (SINR) ratio degradation of the cable (Sect. 6.3.2).

In order to cope with the impairments of the analog FH without any digital signal processing at the RAU, the only degrees of freedom are the antenna mapping onto cable and the design of the amplification for each copper/frequency-link. In this regards, $\mathbf{B}$ is the amplifier gain matrix that is designed to minimize the cable crosstalk effect by adjusting the transmitted power over each space-frequency cable channel as detailed in Sect.6.4. The additive noise introduced by the cable is $\mathbf{n}_c \sim \mathcal{CN}(\mathbf{0}, \sigma_c^2 \mathbf{I})$, and (6.2) becomes

$$\mathbf{x}_w^{\mathrm{BBU}} = \mathbf{H}_c \mathbf{x}_c + \mathbf{n}_c, \tag{6.4}$$

where $\mathbf{x}_c = \mathbf{B}\mathbf{x}_w^{\mathrm{RAU}}$ contains the signals transmitted from RAU to BBU over the N_c twisted pairs and N_f cable frequency bands.

For LAN cables $N_c = 4$, and the total bandwidth depends on cable length and type. Even if their bandwidth can be as high as approx. 1 GHz, here the analysis is only for the first 500 MHz for the availability of experimental measurements and models. Moreover, the analysis is for multiple antennas LTE system with 20-MHz bandwidth that uses a global bandwidth of $B_w = 22$ MHz comprehensive of 10% of guard band overhead for FDM over cables.

6.3. LAN Cables for Analog MIMO-RoC

The fronthaul capacity of the A-RoC architecture in [30] can be greatly enhanced through A-MIMO-RoC, that efficiently exploits cables with multiple twisted pairs as the 4-pairs of LAN cables detailed below.

6.3.1. Cables Characteristic

Standard LAN cables (Cat-5/6/7) are considered here for A-MIMO-RoC. Cat-5 cables are Unshielded Twisted Pair (UTP) cables, commonly deployed for computer networks (e.g., Gigabit Ethernet) and their performances are mostly affected by the system noise. Cat-6 cables are high-grade UTP cables with additional foil

underneath the cable jacket, in which better noise and interference immunity is achieved by increasing the twists density ($>$ 2 twists/cm for Cat-6, compared to 1.5 twists/cm for Cat-5). Cat-7 cables offer lower signal attenuation and reduced intra-cable interference through extensive shielding and foiling over each individual twisted pair, and therefore can be used in a noisy environment, or to remarkably increase the transport capability with respect to Cat-5 cables.

The transmission bandwidth over each copper link is typically considered up to 212 MHz for 100-m cables (e.g., G.fast as next generation DSL, see Part I of this thesis), but it can reach as much as 1 GHz for LAN cables, especially for shorter distances ($\leq$ 50 m). Cable lengths can vary in a range between few meters up to several hundreds of meters, but higher IL is associated with longer cables, thus reducing the practically available transmission bandwidth as shown in Fig. 6.3. The analysis is limited here to 50-m, 100-m and 200-m LAN cables over maximum bandwidth of 500 MHz (limit due to the reliability of available measurements). Notice that, even thought the total available bandwidth of each pair is $B_{c,max} = 500$ MHz, the useful bandwidth for signal transmission B_c is reduced for the joint effect of IL and FEXT, i.e., $B_c \leq B_{c,\max}$.

Fig.6.3 shows the characteristics of the 3 categories of cables in terms of average (over pairs) IL versus frequency for varying cable length (Fig.6.3a), and in terms of average IL and FEXT for 100-m length for varying Cat-type (Fig.6.3b). In Fig.6.3b the noise-floor is highlighted assuming that its power spectral density (typ. is -140 dBm/Hz) is normalized to the maximum spectral mask of signal (-80 dBm/Hz). Cables have a low-pass characteristic that increases with cable length as shown in Fig.6.3a. For the scope of having a transparent RoC, it is meaningful to derive from Fig.6.3 the SINR versus frequency that is illustrated in Fig.6.4 for Cat-6 cable and varying cable lengths (50, 100 and 200 m). It can be noticed from Fig.6.4 that in case of longer cables (i.e., 200 m) the noise dominates over FEXT limiting its usage up to 200 MHz.

Remark 6.1. In this chapter, as well as in the upcoming Chapters 7 and 8, we assume for the sake of simplicity in numerical analysis that the cable channel matrix $\mathbf{H}_c$ is approximately constant within each B_w-band (i.e., corresponding to the radio signal bandwidth). However, in the reality the cable is not flat, i.e., Fig. 6.3 shows that for Cat-5 and Cat-6 cables 100m long the IL within 22-MHz varies approx. 2 dB and 1.5 dB, respectively. Hence, we set the IL and FEXT coefficients of the kth matrix $\mathbf{H}_{c,k}$ in (6.3) as the mean of the channel measurements over the kth frequency band (see Fig. 6.3). If necessary, one could perform a sub-band analysis within each 22-MHz band to resume this assumption without any relevant changes to the analysis and final results.

6.3.2. Cable Resources Analysis

In the proposed A-MIMO-RoC fronthauling architecture, the signal from each antenna is mapped over one of the different 22-MHz bands of LAN cable, as

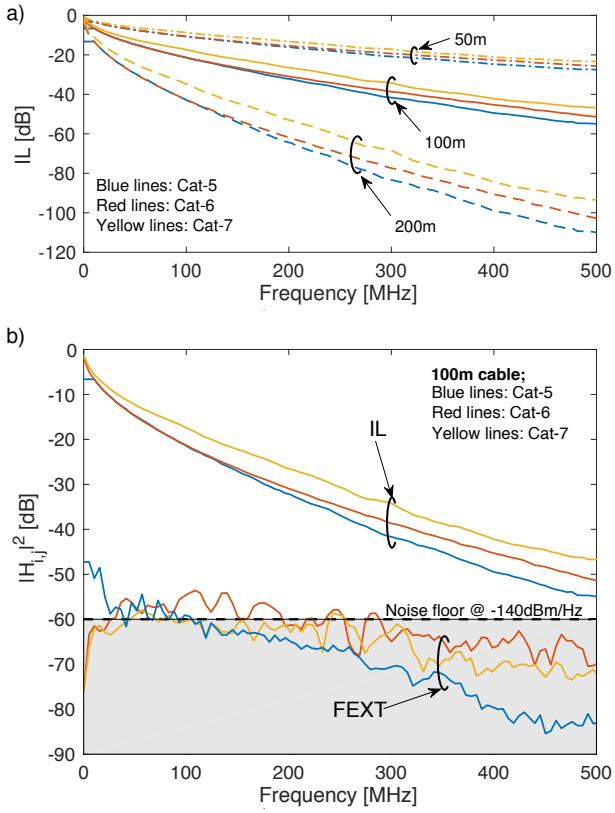

Figure 6.3.: Cable characteristics: a) IL vs frequency for 50m, 100m and 200m and Cat-5/6/7 cables; b) cable IL and FEXT vs frequency for 100-m cables (noise-floor is scaled from standard cable-design parameters)

shown in Fig.6.4. Given the bandwidth of each air-link B_w (that in the numerical analysis is $B_w = 22$ MHz), the bandwidth to transport over cable the overall N antennas is NB_w, hence the cable transport capability must be

$$\sum_{\ell=1}^{N_c} B_{c,\ell} \geq NB_w, \tag{6.5}$$

where $B_{c,\ell}$ is the useful transmission bandwidth on the ℓ-th twisted pair of the N_c in a cable subject to a minimal SINR level induced by the cable from Fig.6.4. From (6.5), $N \leq N_{max}$ and thus

$$N_{max} = \sum_{\ell=1}^{N_c} \left\lfloor \frac{B_{c,\ell}}{B_w} \right\rfloor \tag{6.6}$$

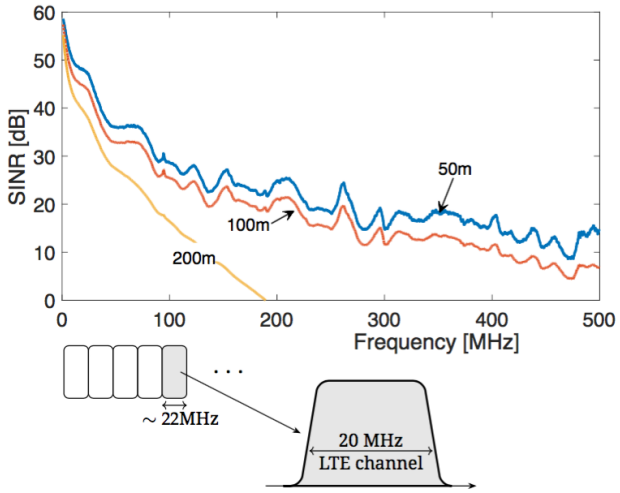

Figure 6.4.: Bandwidth of LTE signals and SINR vs frequency for Cat-6 cable, 100m length and its extrapolation to 50m, 200m

is the maximum number of independent RAT channels (or RAU antennas) that can be allocated over a single LAN cable.

6.4. Power Allocation in A-MIMO-RoC

The main limitation in LAN cables is the crosstalk among twisted-pairs. Crosstalk cancellation is the obvious solution to maximize the throughput over the copper, but it requires the digitization and the corresponding digital signal processing at the RAU, that is too energy and latency consuming compared to the all-analog relaying (not to mention the cost). Instead, in A-MIMO-RoC power allocation is used to optimize the power of the transmit signal $\tilde{\mathbf{x}}$ over the space-frequency copper channels such that the crosstalk among the cable pairs is minimized. Since copper channel gains (IL and FEXT) are time-invariant compared to the air-links, the power allocation problem consists in optimizing the gains of the diagonal matrix $\mathbf{B}$ that scales the power of the input signal $\mathbf{x}$ prior to transmission over the cable. This can be solved by adapting the Optimum Spectrum Balancing (OSB) algorithm [64] to A-MIMO-RoC.

The SINR at the BBU follows from (6.4), and it can be represented for line n-th and k-th subcarrier as

$$\mathrm{SINR}_k^n = \frac{|h_k^{n,n}|^2 p_k^n}{\sum\limits_{m \neq n} |h_k^{n,m}|^2 p_k^m + \sigma_k^n}, \tag{6.7}$$

where $h_k^{n,m} = [\mathbf{H}_{c,k}]_{n,m}$ is the channel gain from cable pair m towards n ($m \rightarrow n$), and p_k^n is the transmit signal power over the n-th cable pair at k-th frequency band such that

$$p_k^n = \mathrm{E}\{\, |x_{c,k}^n|^2 \,\}. \tag{6.8}$$

The power p_k^n is optimized to minimize the crosstalk toward the other lines ($n \neq m$), and the optimization problem for all the cable pairs (n) and sub-carriers (k) can be stated as

$$\begin{aligned} &\max_{\mathbf{p}^1,\ldots,\mathbf{p}^{N_c}} \sum_{n=1}^{N_c} R^n \\ &\quad \text{s.t. } P^n \leq P^{n,Tot}, \qquad n = 1...N_c, \\ &\qquad 0 \leq p_k^n \leq p_k^{n,\,mask}, n = 1...N_c \text{ and } k = 1...N_f. \end{aligned} \tag{6.9}$$

In (6.9), R^n is the throughput of the n-th pair obtained by summing the contributions from N_f sub-carriers with frequency spacing $f_s = 22$ MHz (as in Fig. 6.4) as

$$R^n = f_s \sum_k \log_2 \left(1 + \mathrm{SINR}_k^n\right). \tag{6.10}$$

$P^n = \sum_{k=1}^{N_f} p_k^n$ is the sum power of all the sub carriers for line n, and it is constrained by the maximum transmit power of the cable amplifier $P^{n,Tot}$. The maximum transmit power per subcarrier is also constrained to $p_k^{n,\,mask}$. The required transmit power on k-th subcarrier for all the cable pairs is [64]

$$\mathbf{p}_k = \left(\mathbf{D}_k - \mathbf{\Lambda}_k \mathbf{A}_k\right)^{-1} \mathbf{\Lambda}_k \boldsymbol{\sigma}_k, \tag{6.11}$$

where

$$\mathbf{D}_k = \mathrm{diag}\left[|h_k^{1,1}|^2,\, |h_k^{2,2}|^2,\, \ldots,\, |h_k^{N_c,N_c}|^2\right] \tag{6.12}$$

$$\mathbf{\Lambda}_k = \mathrm{diag}\left[\mathrm{SINR}_k^1,\, \mathrm{SINR}_k^2 \quad ,\, \ldots,\, \mathrm{SINR}_k^{N_c}\right] \tag{6.13}$$

$$[\mathbf{A}_k]_{n,m} = \begin{cases} 0 & m = n \\ |h_k^{n,m}|^2 & m \neq n \end{cases}, \tag{6.14}$$

and the required SINRs in (6.13) are selected iteratively for different M-QAM constellations to guarantee that power allocation is positive valued. The numerical values here are derived from the LTE specifications [135]. The spectrum balancing algorithm in [64] provides an efficient solution for the optimization problem in (6.9), in the form of an amplifier gain matrix $\mathbf{B} \in \mathbb{R}^{N \times N}$. Such matrix is block diagonal as in (6.3): $\mathbf{B} = \mathrm{diag}(\mathbf{B}_1, \ldots, \mathbf{B}_{N_f})$ and the $N_c \times N_c$ amplifier gain matrix $\mathbf{B}_k$ for k-th subcarrier is

$$\mathbf{B}_k = \mathrm{diag}\left[\sqrt{p_k^1},\, \sqrt{p_k^2},\, \ldots,\, \sqrt{p_k^{N_c}}\right]. \tag{6.15}$$

To comply with the air-link specification for LTE, the spectral efficiency is upper-limited to 8 bps/Hz, corresponding to the maximum constellation of the evolution of LTE that supports up to 256-QAM.

6.5. Numerical Results

Simulation results for different cable types and lengths, based on the input parameters summarized in Table 6.1, are presented here to show the effectiveness of the proposed A-MIMO-RoC fronthauling architecture. In particular, the number of independent 20-MHz LTE signals (assumed to be equal to the number of antennas N_{max}) available on the cable channel is evaluated by considering modulation parameters according to the LTE specifications [135]. The copper bandwidth B_c is limited here up to 500 MHz even if the usage can be expanded up to 1 GHz and beyond, as foreseen for future broadband access networks [136].

The results of OSB as defined in (6.9) are shown in Fig. 6.5 for a Cat-5 cable, and reported in Tables 6.2, 6.3 for Cat-5/6/7. In order to compare the OSB for A-MIMO-RoC with digital pre-compensation of FEXT at the RAU, the performance of conventional Tomlinson-Harashima Precoding (THP) for FEXT compensation in multi-pair copper cables (see Chapter 2 for further details) is shown as reference in Fig. 6.5b, d, and in Table 6.3. In particular, the averaged (over the N_c pairs) OSB transmit powers over the 22-MHz frequency bins are in the upper part of Fig. 6.5, while the powers for each of the 4 twisted pairs are in gray lines. The corresponding spectral efficiency, which is related to the M-QAM modulations of LTE according to the specifications, is in the lower part of the same figure. The power required for any given modulation scheme increases with cable impairments, and consequently with frequency and length.

We observe that the 256-QAM (spectral efficiency of 8 bps/Hz) is guaranteed for the entire 500-MHz bandwidth when using the 50-m cables. Increasing the cable length, the 256-QAM requirements can be fulfilled over a reduced bandwidth up to approx. 175 MHz and 25 MHz for 100 and 200-m cables. Comparison with digital FEXT compensation shows a modest improvement compared to the cost. The maximum useful bandwidth for transmission on each pair ($B_{c,\ell}$, second to last column in Tables 6.2, 6.3) is obtained from Fig. 6.5c,d as the spectrum portion corresponding to non-zero spectral efficiency and the total number of antennas is computed for the useful transmission bandwidth as in (6.6). It is to be noticed that the average sum power per line is always lower than 4dBm, that is the limit of commercially available power driver for twisted-pairs. As expected, the maximum throughput is achieved by Cat-7 cables, due to its higher FEXT protection capabilities.

The total number of allocable independent 20-MHz LTE channels that corresponds to the number of antennas N_{max} versus cable length is in Fig. 6.6 for all cable types and considering also the impact of FEXT processing at the RAU as design

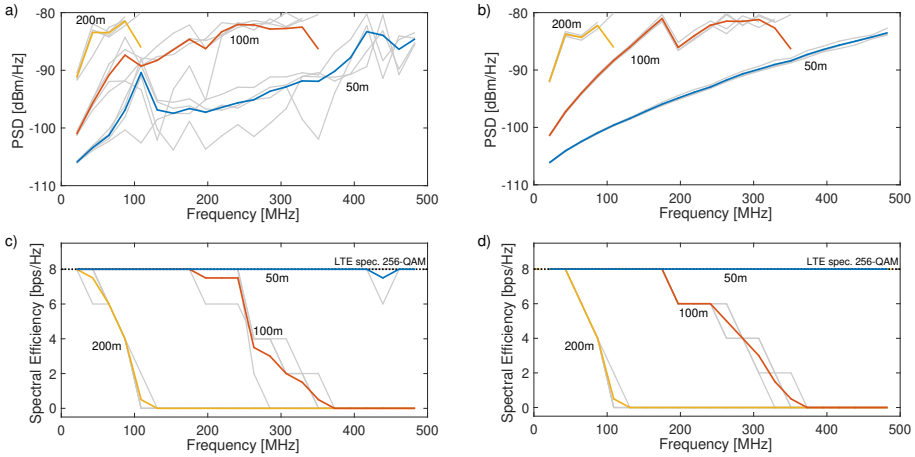

Figure 6.5.: Transmit PSD (top) and average spectral efficiency vs frequency (bottom), with OSB and with (right) or without (left) cable crosstalk compensation for different lengths, Cat-5 cable.

parameter. Up to around 75 m, any cable (regardless the use of FEXT compensation) allows to serve the maximum number of antennas compatible with 500-MHz bandwidth that is $88 \simeq 4 \times 500$ MHz/22 MHz (i.e., 22 LTE channels on each pair), which is limited by the 500-MHz bandwidth for reliable cable measurements. Distance of 100 m on a LAN cable is considered as a reference, and at least 55 independent LTE channels (or independent antennas) can be transported using A-MIMO-RoC on Cat-5, thus proving the effectiveness of A-MIMO-RoC fronthauling for the last 100 m of the C-RAN architecture. It is important to notice that the beneficial effects of crosstalk compensation are modest, and can be appreciated only for lower cable lengths where the interference dominates over noise. This is a strong argument in favor of the usage of all-analog processing of judicious power allocation in all-analog A-MIMO-RoC fronthauling to minimize any latency of the I/Q signal transport.

6.6. Concluding Remarks

In this chapter, we considered the implementation of a novel fully-analog Radio-over-Copper (RoC) fronthauling architecture, which exploits the pre-existing LAN cabling infrastructure of buildings and enterprises for enhancing indoor coverage. The proposed architecture, referred to as Analog MIMO-RoC (A-MIMO-RoC) due to the cascade of a MIMO radio- over a MIMO cable-channel, enables a more flexible and efficient exploitation of the transport capabilities of LAN cables. In particular, the great potential provided by multi-pair LAN cables has been

LTE Tx. Bw. (B_w)	22 MHz
LTE M-QAM Modulation	4, 16, 64, 256
LAN Cable	Cat-5/6/7
Cable Pairs (N_c)	4
Cable Length	50,100 and 200 m
Copper Bw. (B_c)	500 MHz
Sum Power per line $\left(P^{n,Tot}\right)$	4 dBm
Max. Tx. Signal PSD $\left(p_k^{n,\,mask}\right)$	-80 dBm/Hz
Cable Noise PSD (σ_c^2)	-140 dBm/Hz

Table 6.1.: System Parameters for A-MIMO-RoC.

Cable Type	Cable Length [m]	Av. Sum Power per Line [dBm]	Sum Thr. per Cable [Gbps]	Max. Bw. $B_{c,1}/B_{c,2}/B_{c,3}/B_{c,4}$ [MHz]	No. of Ant. N_{max}
Cat-5	50	-3.17	12.35	500/500/500/500	88
	100	0.15	6.82	264/330/352/330	58
	200	-3.78	1.83	88/88/88/110	17
Cat-6	50	-8.93	12.39	500/500/500/500	88
	100	1.49	7.63	374/374/374/396	69
	200	-3.65	1.83	88/88/110/110	18
Cat-7	50	-6.42	12.39	500/500/500/500	88
	100	1.64	8.83	418/352/440/440	75
	200	-1.24	2.88	132/154/132/154	26

Table 6.2.: Cable resources and OSB parameters without cable crosstalk compensation.

proved by evaluating the maximum number of antennas, or multi Radio Access Technology (RAT) channels, that can be served by a single LAN cable for different cable lengths and types. By numerical evaluation, we proved that the maximum number of antennas (or 20-MHz LTE channels) that can be served by a 50-m Cat-5 cable is 88, and this value is limited by the cable bandwidth of 500 MHz considered here. In particular, at least 60 antennas can be served by a cable of practical length (100 m), thus enabling the design of A-MIMO-RoC fronthauling to serve a RAU with a large number of antenna elements. The proposed radio-MIMO over cable-MIMO allows the joint exploitation of space and frequency multiplexing on both cable (multiple pairs) and air (multiple antennas) channels. Hence, a further degree of freedom in the design of A-MIMO-RoC is given by the mapping between the space-frequency channels, defined by antennas and radio spectrum, onto the cable-pairs and cable-spectrum. This mapping, referred to as Space-Frequency to Space-Frequency multiplexing, is discussed in the following chapters.

Cable Type	Cable Length [m]	Av. Sum Power per Line [dBm]	Sum Thr. per Cable [Gbps]	Max. Bw. $B_{c,1}/B_{c,2}/B_{c,3}/B_{c,4}$ [MHz]	No. of Ant. N_{max}
Cat-5	50	-2.5	12.39	500/500/500/500	88
	100	1.17	6.75	308/330/352/330	60
	200	-4.35	1.86	88/88/88/110	17
Cat-6	50	-4.20	12.39	500/500/500/500	88
	100	2.04	7.63	374/374/374/374	68
	200	-3.41	1.93	110/88/110/110	19
Cat-7	50	-6.11	12.39	500/500/500/500	88
	100	2.22	8.94	440/440/440/440	80
	200	-1.98	2.88	132/154/132/154	26

Table 6.3.: Cable resources and OSB parameters with cable crosstalk compensation.

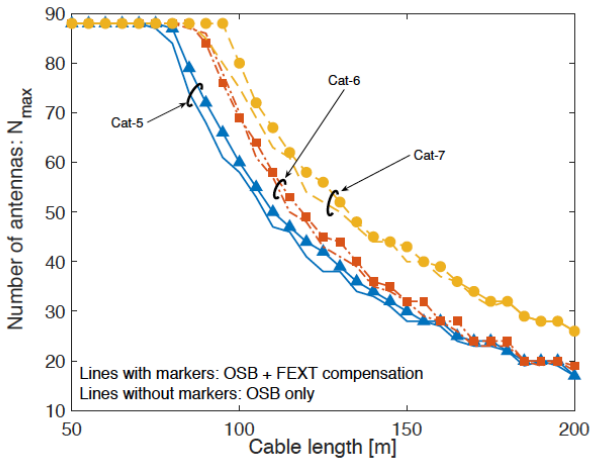

Figure 6.6.: Number of antennas vs cables length for Cat-5/6/7 with OSB and with or without cable crosstalk cancellation

7. Analog MIMO RoC Uplink with Space-Frequency to Space-Frequency Multiplexing

7.1. Introduction

Centralized Radio Access Network (C-RAN) with analog fronthauling based on LAN cables, namely Analog MIMO Radio-over-Copper (A-MIMO-RoC), has been introduced in the previous chapter as an attractive solution to extend indoor coverage over distances longer than 100 m. A-MIMO-RoC encompasses both the advantages of analog FrontHaul (FH) architectures and the cost-benefit of reusing the pre-existing LAN cabling infrastructure of buildings. In summary, the benefits of A-MIMO-RoC are as follows: *i)* large analog bandwidth availability, *ii)* reduced deployment cost, *iii)* low-complexity of RF equipments powered over the same copper cable (i.e., Power-over-Ethernet, PoE [31]), *iv)* low-latency communication (i.e., limited to signal propagation only), and *v)* precise bit/carrier frequency synchronization among multiple-antenna RAUs for MIMO joint processing. Moreover, differently from existing indoor solutions that utilize mainly low cable frequencies [31, 33], A-MIMO-RoC considered here pushes the frequency cable usage up to several hundreds of MHz, thus fully exploiting the transport capabilities of LAN cables.

Key enabler for A-MIMO-RoC is a more flexible and efficient usage of the space-frequency cable resources, which are defined by the 4 mutually interfering twisted-pairs (i.e., Space Division Multiplexing, SDM), each of which disposes of up to 1 GHz bandwidth (i.e., Frequency Division Multiplexing, FDM). In A-MIMO-RoC, SDM and FDM dimensions are jointly exploited in order to take full advantage of the LAN cables bandwidth capabilities. The overall channel between the BBU and the end-user is thus modeled as a cascade of a MIMO radio channel over a MIMO cable channel, where the multiple radio signals at the RAU antenna need to be properly mapped onto the available cable resources. The main contribution of this chapter is to show the potential of this mapping between antennas/radio-spectrum and cable-pairs/cable spectrum, which is referred to as Space-Frequency to Space-Frequency (SF2SF) multiplexing. In particular, the goal is to show the potential of the SF2SF technique *alone* to cope with cable impairments (in particular cable crosstalk), without getting the performance influenced by any other

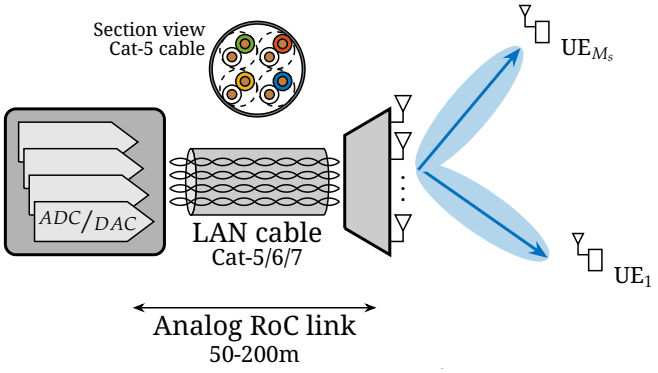

Figure 7.1.: RoC-based C-RAN employing LAN cables for SDM

cable equalization or power optimization technique, which are therefore not considered in this chapter. For the same reason, the analysis here is limited to the uplink of the A-MIMO-RoC architecture in single-user settings. Once asserted the potential of SF2SF alone for this simple A-MIMO-RoC system, the SF2SF technique has been extended in Chapter 8 to the more challenging multi-user settings, and in combination with the precoding of the overall cascade of wired and wireless channels.

7.1.1. Chapter Contribution

As a first step, the considered A-MIMO-RoC uplink system model and the algebraic structure of the SF2SF multiplexing technique are detailed. Then, the chapter is divided into two macro-sections, each of which considering a different problem. The first part of the chapter considers the uplink of an outdoor multi-cell mobile networks, in which the BBU serves a single-user through a RAU equipped with multiple antennas. SF2SF multiplexing technique is designed in order to jointly mitigate the impairments of the analog fronthauling and the interference coming from neighboring cells. Following the A-MIMO-RoC concept, the analog FH link is made by a single LAN cable which, in this first part of the chapter, is assumed to be entirely dedicated to FH transmission. However, in indoor office scenarios, the pre-existing building LAN cabling infrastructure may be already used for other services, i.e., xDSL, PoE, other RAUs, etc. In this regards, in order to consider a more realistic setting, it is mandatory to assess the performance of the system by assuming that only a subset of the twisted-pairs contained into the LAN cables is used for FH transmissions, while the remaining act as a source of uncoordinated interference. This last case is discussed in the second part of the chapter.

7.1.2. Contribution in International Conferences/Journals

Part of the material presented in this chapter has been published in:

- **A. Matera**, L. Combi, S. H. R. Naqvi, and U. Spagnolini, "Space-Frequency to Space-Frequency for MIMO Radio over Copper" in *2017 IEEE International Conference on Communications (ICC)*, pp. 1–6, IEEE, 2017.
- **A. Matera,** and U. Spagnolini, "On the Optimal Space-Frequency to Frequency Mapping in Indoor Single-Pair RoC Fronthaul" in *2017 IEEE European Conference on Networks and Communications (EuCNC)*, pp. 1–6, IEEE, 2017.

7.2. A-MIMO-RoC Uplink System Model

In this chapter, we consider the uplink of the A-MIMO-RoC architecture, where signal multiplexing over the FH channel is achieved through space and frequency division: the wireless signals at the RAU antennas, defined in the Space-Frequency domain, are mapped onto the Space-Frequency channels of the wired access link (SF2SF). In particular, copper cables (e.g., LAN cables) are considered, where the space dimension is defined by the four twisted pairs bounded together into the cable.

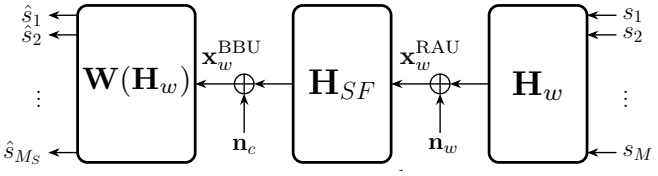

Figure 7.2.: A-MIMO-RoC uplink general system model

Even if the analysis performed in this chapter is for a single-user, the system model is described for a more general scenario with an arbitrary number of users M. In particular, the uplink signals from M_S users served by a specific antenna array are interfered by the signals coming from M_I users deployed in a neighboring area, where $M = M_S + M_I$ is the total number of users in the system. The uplink radio signals are received at the RAU by N antennas, and then directly relayed in an all-analog fashion towards the BBU, where receiver processing is performed (e.g., beamforming). Fig. 7.2 shows the main blocks that form the A-MIMO-RoC architecture, whose details are given in the next sections (see Fig. 7.3 for a more detailed block scheme). The considered system model is described in Fig. 7.2 and Fig. 7.3 as the cascade of wireless and cable links, where the quantities related to wireless and cable links have been denoted by subscript $(\cdot)_w$ and $(\cdot)_c$, respectively. The equivalent end-to-end signal model describing the signal $\mathbf{x}_w^{\mathrm{BBU}}$, which is the

signal that is first received at the RAU antennas from the users and then forwarded to the BBU over the cable FH, is

$$\mathbf{x}_w^{\mathrm{BBU}} = \mathbf{H}_{SF}(\mathbf{H}_w\mathbf{s} + \mathbf{n}_w) + \mathbf{n}_c, \tag{7.1}$$

where $\mathbf{H}_w$ is the channel matrix describing the wireless radio environment defined in Sect. 7.2.1, and $\mathbf{H}_{SF}$ is the equivalent FH cable channel matrix (referred to as SF channel) comprising of SF2SF multiplexing operation (details are in Sect. 7.2.2). Vectors $\mathbf{s}$ and $\mathbf{n}_w$, defined in details in Sect. 7.2.1, contain the uplink user signals and the noise at the antenna array, respectively.

A sample scenario is considered for performance evaluation in which beamforming is performed at the BBU to separate the useful uplink signal from interference arising from neighboring cells: the estimated user signal $\hat{\mathbf{s}}$ at the BBU is described by

$$\hat{\mathbf{s}} = \mathbf{W}(\mathbf{H}_w)\mathbf{x}_w^{\mathrm{BBU}}. \tag{7.2}$$

The SF channel is assumed to be maximally transparent to the beamformer $\mathbf{W}(\mathbf{H}_w)$, which is designed based only on the knowledge of the radio channel. For simplicity, no fading nor multi-path propagation are considered in the following, but extension would just include a temporal processing to the channel model. Furthermore, it is assumed a single user to be served in the area of interest ($M_S = 1$) just to avoid that the performance analysis is affected by the multiuser processing. Accordingly, the single user signal s can be estimated from the signal $\mathbf{x}_w^{\mathrm{BBU}}$ received at the BBU as

$$\hat{s} = \mathbf{w}^H(\mathbf{H}_w)\,\mathbf{x}_w^{\mathrm{BBU}}, \tag{7.3}$$

where $\mathbf{w} \in \mathbb{C}^N$ is the spatial filter for the intended user.

In the following sections, each of the blocks shown in Fig. 7.2 is discussed in details.

7.2.1. Radio Channel

The uplink radio signals received by the N antennas at the RAU, arranged in a vector, are

$$\mathbf{x}_w^{\mathrm{RAU}} = \mathbf{H}_w\mathbf{s} + \mathbf{n}_r, \tag{7.4}$$

where vector $\mathbf{s} \in \mathbb{C}^M$ collects the signals with power σ_s^2 transmitted by all the $M = M_S + M_I$ users, and it is approximated as Gaussian distributed: $\mathbf{s} \sim \mathcal{CN}(\mathbf{0}, \sigma_s^2\mathbf{I})$.

$\mathbf{H}_w \in \mathbb{C}^{N\times M}$ is the wireless channel matrix and $\mathbf{n}_w \sim \mathcal{CN}(\mathbf{0}, \sigma_n^2\mathbf{I})$ is the $N \times 1$ wireless noise vector, white with power σ_n^2. The wireless channel model is based on the far field approximation, and it accounts for the Directions of Arrival (DoAs) of the signals as

$$\mathbf{H}_w = \begin{bmatrix}\beta_1\mathbf{a}(\theta_1) & \beta_2\mathbf{a}(\theta_2) & \cdots & \beta_M\mathbf{a}(\theta_M)\end{bmatrix}, \tag{7.5}$$

where $\beta_i^2 = 1/d_i^2$ is the path loss attenuation related to the distance d_i from the i-th user to the array and $\mathbf{a}(\theta_i) \in \mathbb{C}^N$ is the steering vector for the DoA θ_i of the i-th user. Under the assumption of half-wavelength spaced Uniform Linear Array (ULA) at the RAU, the steering vector for the i-th user is

$$\mathbf{a}(\theta_i) = \begin{bmatrix}1 & e^{j\pi\sin(\theta_i)} & \cdots & e^{j\pi(N-1)\sin(\theta_i)}\end{bmatrix}^T, \tag{7.6}$$

where no fading nor multi-path propagation are considered.

7.2.2. Analog Transmission over the Cable Fronthaul Channel

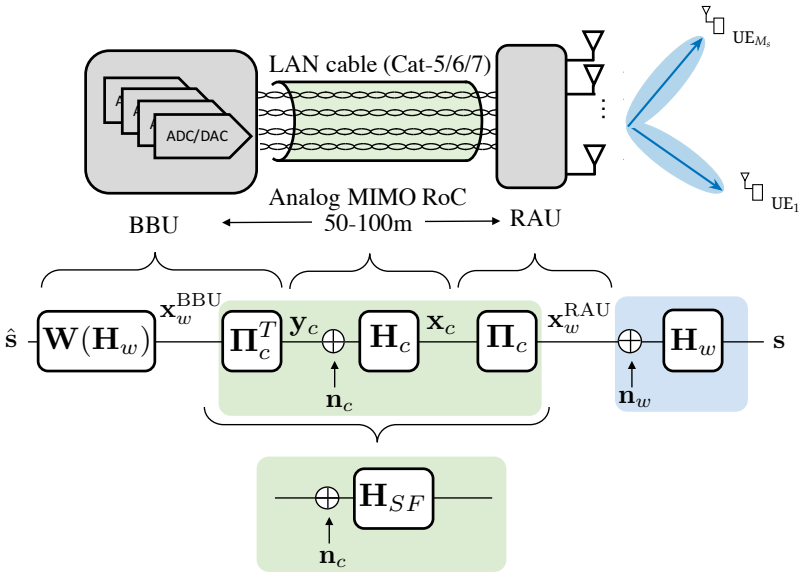

Figure 7.3.: Detailed block scheme of A-MIMO-RoC operations, including signal mapping ($\mathbf{\Pi}_c$) and demapping ($\mathbf{\Pi}_c^T$) by SF2SF multiplexing

A-MIMO-RoC architecture is an attractive solution for low-latency/low-complexity applications that require full RAU synchronization, and this is due to the full analog transmission of radio signals over the FH. In this regards, no complex digital

signal processing is allowed at the RAU, which acts as an amplify-and-forward relay node, and whose only task is to relay the radio signals $\mathbf{x}_w^{\mathrm{RAU}}$ to the BBU multiplexed both in space and frequency dimensions over the cable FH. A detailed block scheme of the A-MIMO-RoC operations, including signal mapping/demapping by SF2SF, is in Fig. 7.3. The signal received at the BBU over the cable link prior to beamforming ($\mathbf{W}(\mathbf{H}_w)$) and signal demapping ($\mathbf{\Pi}_c^T$) is thus

$$\mathbf{y}_c = \mathbf{H}_c\mathbf{x}_c + \mathbf{n}_c, \tag{7.7}$$

where $\mathbf{H}_c \in \mathbb{C}^{N_c \times N_c}$ is the FH wired access link detailed in Sect. 7.2.2.1 and $\mathbf{x}_c \in \mathbb{C}^{N_c \times 1}$ is the transmit cable signal forwarded by the RAU over the cable FH, which is obtained by opportunely mapping the radio received signal $\mathbf{x}_w^{\mathrm{RAU}}$ in (7.4) over the SF cable resources, as detailed in Sect.7.2.2.2. Finally, vector $\mathbf{n}_c$ accounts for those impairments introduced by the wired FH access link that cannot be mitigated by any signal processing technique, and thus need to be treated as noise at the receiver (e.g., additive noise or uncoordinated/uncanceled interference). Vector $\mathbf{n}_c$ is distributed as $\mathbf{n}_c \sim \mathcal{CN}(\mathbf{0}, \mathbf{R}_c)$, where the structure of the spatial cable covariance matrix $\mathbf{R}_c$ depends on the considered scenario. In Sect. 7.4, where the FH signal is jointly transmitted over all the four twisted-pairs of the LAN cable, $\mathbf{R}_c$ contains only additive white Gaussian noise uncorrelated over pairs, i.e.,

$$\mathbf{R}_c = \sigma_c^2\mathbf{I}. \tag{7.8}$$

However, in Sect. 7.5, where only one pair is used for FH transmission, while the others are used to carry different services acting as sources of uncoordinated interference, the cable covariance matrix $\mathbf{R}_c$ accounts also for the FEXT coming from the interfering pairs as

$$\mathbf{R}_c = \sigma_c^2\mathbf{I} + \mathbf{R}_{\mathrm{FEXT}}. \tag{7.9}$$

7.2.2.1. Space-Frequency Cable Fronthaul Channel

The FH cable channel $\mathbf{H}_c$ in (8.6) is equivalent to a large MIMO system in the Space-Frequency (SF) domain defined by N_s SDM channels (i.e., the N_s twisted-pairs bonded together into the cable, $N_s = 4$ is typical for LAN cables) and N_f FDM channels for a total of $N_c = N_s \cdot N_f$ SF resource blocks on cable. To simplify the discussion here, it is assumed that the total number of available SF cable channels N_c exactly equals the total number of RAU antennas N (i.e., $N_c = N$), even if in practice it could be relaxed to $N_c > N$ with further benefits. The matrix cable channel $\mathbf{H}_c$ accounts for cable IL (diagonal terms, $[\mathbf{H}_c]_{i,i}$) and for cable FEXT between all the N cable channels (off-diagonal terms, $[\mathbf{H}_c]_{i,j}$). Since cross-cable interference occurs only among spatial channels at the same frequency, it is straightforward to describe $\mathbf{H}_c$ by the block diagonal matrix

$$\mathbf{H}_c = \mathrm{diag}(\mathbf{H}_{c,1}, \mathbf{H}_{c,2}, \ldots, \mathbf{H}_{c,N_f}), \tag{7.10}$$

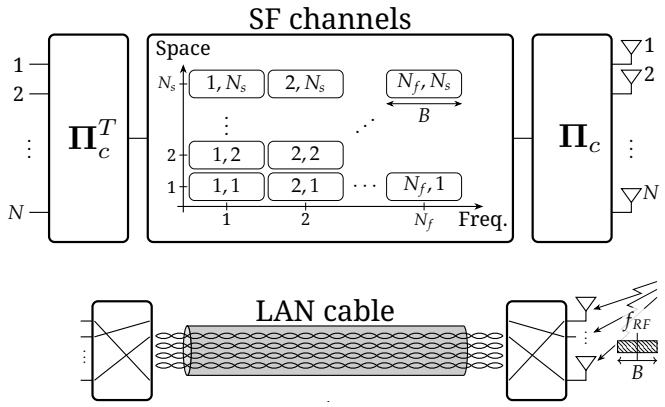

Figure 7.4.: General Space-Frequency wired access link: (upper) mathematical and (lower) physical model

where each of the N_f diagonal blocks $\mathbf{H}_{c,f} \in \mathbb{C}^{N_s \times N_s}$ is the cable channel matrix at the f-th frequency band (frequency bands are disjointed). In particular, the main diagonal element $[\mathbf{H}_{c,f}]_{ii}$ contains the IL for the i-th twisted-pair at the f-th frequency band, while the off-diagonal element $[\mathbf{H}_{c,f}]_{ij}$, with $i \neq j$, represents the FEXT between twisted-pair j-th and i-th at the f-th frequency band.

7.2.2.2. RAU Transmit Cable Signal

The RAU transmit cable signal $\mathbf{x}_c$ is relayed to the BBU over the cable FH multiplexed in space and frequency dimensions, hence, it is conveniently defined as

$$\mathbf{x}_c = [\mathbf{x}_{c,1}^T, \mathbf{x}_{c,2}^T, ..., \mathbf{x}_{c,N_f}^T]^T, \tag{7.11}$$

where $\mathbf{x}_{c,f} \in \mathbb{C}^{N_s \times 1}$ are the symbols transmitted over the N_s twisted-pairs at the f-th frequency band. In particular, $[\mathbf{x}_{c,f}]_j$ denotes the RAU symbol transmitted over the j-the twisted-pair at the f-th cable frequency band.

The cable symbols $\mathbf{x}_c$ are obtained at the RAU by mapping the N symbols $\mathbf{x}_w^{\text{RAU}} = [x_{w,1}^{\text{RAU}}, x_{w,2}^{\text{RAU}}, ..., x_{w,N}^{\text{RAU}}]^T$ received from the users over the radio channel onto the N SF cable channels. This mapping operation is described by

$$\mathbf{x}_c = \mathbf{\Pi}_c \mathbf{x}_w^{\text{RAU}}, \tag{7.12}$$

where $\mathbf{\Pi}_c$ is a permutation matrix that maps the radio symbols $\mathbf{x}_w^{\text{RAU}}$ received at the N RAU antennas onto N SF blocks over the cable properly selected according to SF2SF multiplexing criteria (see Sect. 7.3). In other words, $[\mathbf{x}_w^{\text{RAU}}]_n$ denotes

the RAU symbol which is first received at the n-th RAU antenna, and then relayed over the cable FH in a specific SF block defined by matrix $\mathbf{\Pi}_c$.

SF2SF multiplexing operators $\mathbf{\Pi}_c$ are mutually signaled between RAU and BBU. In practice, the choice of the optimal SF2SF multiplexing $\mathbf{\Pi}_c$ is taken at the BBU. Then, this information is signaled to the RAU that maps the symbols from the N antennas onto the N SF cable blocks by the matrix $\mathbf{\Pi}_c$. Finally, the BBU applies an inverse permutation $\mathbf{\Pi}_c^T$ to the received symbols $\mathbf{y}_c$, in order to map the symbols back from the SF cable FH blocks as

$$\mathbf{x}_w^{\text{BBU}} = \mathbf{\Pi}_c^T \mathbf{y}_c. \tag{7.13}$$

The overall model describing the communication between RAU and BBU over cable is then described by

$$\mathbf{x}_w^{\text{BBU}} = \mathbf{H}_{SF} \mathbf{x}_w^{\text{RAU}} + \mathbf{n}_c, \tag{7.14}$$

where

$$\mathbf{H}_{SF} = \mathbf{\Pi}_c^T \mathbf{H}_c \mathbf{\Pi}_c \tag{7.15}$$

is the equivalent SF permuted cable channel, and the statistical properties of $\mathbf{n}_c$ are invariant for permutations so that $\mathbf{\Pi}_c^T \mathbf{n}_c \rightarrow \mathbf{n}_c$. Notice that Eq. 8.12 is fully equivalent to the end-to-end signal model previously introduced in Eq. (7.1).

7.3. Algebraic Structure of Space-Frequency to Space-Frequency Multiplexing

An effective technique to mitigate the cable FH impairments for the considered scenario, which requires low-cost/complexity/latency RAUs, is given by the resource allocation between the SF resource blocks over the cable and the SF resources over the wireless link, referred here to as SF2SF multiplexing. This multiplexing operation determines on which cable SF channel each of the RAU signals $\mathbf{x}_{\text{RAU}}$ must be relayed efficiently to the BBU. This is described by

$$\mathbf{x}_c = \mathbf{\Pi}_c \mathbf{x}_w^{\text{RAU}}, \tag{7.16}$$

where the permutation matrix $\mathbf{\Pi}_c \in \{0,1\}^{N \times N}$ is a unitary (i.e., $\mathbf{\Pi}_c \mathbf{\Pi}_c^T = \mathbf{\Pi}_c^T \mathbf{\Pi}_c = \mathbf{I}$) binary matrix having a single non-zero entry per row/column. Matrix $\mathbf{\Pi}_c$ describes how the RAU symbols $\mathbf{x}_{\text{RAU}}$, received by the N RAU antennas, are multiplexed onto the cable transmit symbols $\mathbf{x}_c$ in both space and frequency dimensions, and then transmitted to the BBU. Consistently with the definition of the transmit

cable symbols $\mathbf{x}_c$, the following notation is adopted to highlight the partitioning in mapping operation performed by $\mathbf{\Pi}_c$:

$$\mathbf{\Pi}_c = [\underbrace{\mathbf{p}_{11}, ..., \mathbf{p}_{1N_s}}_{1^{\text{st}}\text{ freq}}, ..., \underbrace{\mathbf{p}_{21}, ..., \mathbf{p}_{2N_s}}_{k^{\text{th}}\text{ freq}}, ..., \underbrace{\mathbf{p}_{N_f 1}, ..., \mathbf{p}_{N_f N_s}}_{N_f^{\text{th}}\text{ freq}}]^T.$$

The row of $\mathbf{\Pi}_c$ is $\mathbf{p}_{fj}^T = [p_{fj}^1, p_{fj}^2, ..., p_{fj}^N]$, where the single non-zero entry p_{fj}^n selects the RAU symbol $[\mathbf{x}_{\text{RAU}}]_n$ received at the n-th RAU antenna, and to be relayed toward the BBU over the j-th pair at the f-th frequency band of the copper cable:

$$[\mathbf{x}_{c,f}]_j = \mathbf{p}_{fj}^T \mathbf{x}_w^{\text{RAU}}. \tag{7.17}$$

Each permutation matrix $\mathbf{\Pi}_c$ is univocally identified by a vector $\boldsymbol{\pi} = [\pi_1, \pi_2, ..., \pi_N]^T$ storing all the indexes of the non-zero elements of the rows of matrix $\mathbf{\Pi}_c$, i.e., π_n is the index of the non-zero element of the n-th row of matrix $\mathbf{\Pi}_c$.

Example To gain some insights on the multiplexing performed by $\mathbf{\Pi}_c$, let us assume a very simple 4×4 reference channel model $\mathbf{H}_c$ compound of 2 frequencies defined as

$$\mathbf{H}_c = \begin{bmatrix} \alpha_{(1,1)} & \beta_1 & 0 & 0 \\ \beta_1 & \alpha_{(2,1)} & 0 & 0 \\ 0 & 0 & \alpha_{(1,2)} & \beta_2 \\ 0 & 0 & \beta_2 & \alpha_{(2,2)} \end{bmatrix}, \tag{7.18}$$

where $\alpha_{(i,f)} = [\mathbf{H}_{c,f}]_{ii}$ is the IL coefficient for the i-th twisted-pair (tp_i) at f-th cable frequency band (f_f) and $\beta_f = [\mathbf{H}_{c,f}]_{ij}, \forall i \neq j$, is the FEXT coefficient at f_f (for simplicity in this example we assume symmetric FEXT coefficients for the two pairs at each frequency, although this is not true in general). Let us consider the RAU signal $\mathbf{x}_w^{\text{RAU}} \in \mathbb{C}^{4\times 1}$, which is first received by a RAU with 4 antennas over the radio channel, and then transmitted over the cable channel to the BBU. Let us assume the following desired SF2SF multiplexing between cable and air resources: $\text{Ant}_1 \rightarrow(\text{tp}_1,\text{f}_2)$, $\text{Ant}_2 \rightarrow(\text{tp}_1,\text{f}_1)$, $\text{Ant}_3 \rightarrow(\text{tp}_2,\text{f}_2)$, $\text{Ant}_4 \rightarrow(\text{tp}_2,\text{f}_1)$, where $\text{Ant}_n \rightarrow(\text{tp}_i,\text{f}_f)$ means that the RAU signal $[\mathbf{x}_{\text{RAU}}]_n$, that has been received at the n-th RAU antenna Ant_n, is transmitted to the BBU over the i-th cable pair at the f-th frequency band. This operation is performed by the permutation matrix

$$\mathbf{\Pi}_c = \begin{bmatrix} 0 & 1 & 0 & 0 \\ 0 & 0 & 0 & 1 \\ 1 & 0 & 0 & 0 \\ 0 & 0 & 1 & 0 \end{bmatrix} \tag{7.19}$$

leading to the permuted channel matrix $\mathbf{H}_{SF} = \mathbf{\Pi}_c^T \mathbf{H}_c \mathbf{\Pi}_c$. Hence, according to (8.12), the transmitted signal at the RAU yields

$$\overbrace{\begin{bmatrix} x_{w,1} \\ x_{w,2} \\ x_{w,3} \\ x_{w,4} \end{bmatrix}}^{\mathbf{x}_w^{\mathrm{BBU}}} = \begin{bmatrix} \alpha_{(1,2)} & 0 & \beta_2 & 0 \\ 0 & \alpha_{(1,1)} & 0 & \beta_1 \\ \beta_2 & 0 & \alpha_{(2,2)} & 0 \\ 0 & \beta_1 & 0 & \alpha_{(2,1)} \end{bmatrix} \overbrace{\begin{bmatrix} x_{w,1} \\ x_{w,2} \\ x_{w,3} \\ x_{w,4} \end{bmatrix}}^{\mathbf{x}_w^{\mathrm{RAU}}} + \mathbf{n}_c, \tag{7.20}$$

which shows that the above mapping rules are met: e.g., the RAU signal $\left[\mathbf{x}_w^{\mathrm{RAU}}\right]_2$, received at the 2$^{\mathrm{nd}}$ RAU antenna, is relayed to the BBU over the 1$^{\mathrm{st}}$ pair at the 1$^{\mathrm{st}}$ frequency band, (tp_1,f_1)$\rightarrow$ Ant_2. However, it is important to notice also that the relay over the cable introduces interference among the RAU symbols which needs to be carefully handled. The aim of this chapter is to show that by a proper SF2SF multiplexing, this interference can be mitigated, leading to significant performance improvement at virtually no-cost at RAU, and transparently to the end-to-end link.

7.4. Analog MIMO-RoC for Outdoor Multi-Cell Mobile Systems with Dedicated LAN Cable

In this section, the potential of SF2SF technique is evaluated in the uplink of a multi-cell outdoor mobile network in which the analog FH cable is entirely dedicated to FH signal transmission. In the scenario considered here, the BBU serves through a multiple-antenna/all-analog RAU a single-user, which gets interference from two neighboring cells. To have meaningful results, SF2SF performance evaluation is carried out assuming that beamforming is performed at the BBU to separate the single-user useful uplink signal from from inter-cell interference. The wired channel is assumed to be maximally transparent to the beamformer that is designed based only on statistical (i.e., not instantaneous) knowledge of the radio channel.

In more details, the contributions of this first part of the chapter are three-fold: *i)* we propose Space-Frequency to Space-Frequency (SF2SF) multiplexing for A-MIMO-RoC, which is a novel resource allocation strategy based on the mapping of multiple radio signals at the RAU antennas onto multiple space-frequency resource blocks over the LAN cable, *ii)* we evaluate the performance of the proposed A-MIMO-RoC architecture in terms of radio-link performance metrics considering a realistic uplink radio scenario, and *iii)* we show that, even without any pre-/post-equalization of the MIMO cable at the BBU, the performance of the proposed architecture attains that of the ideal fronthauling when properly designing SF2SF multiplexing.

7.4.1. BBU Processing: Minimum Variance Distortionless Response Beamforming

Digital beamforming is performed at the BBU in order to separate the signal of the user of interest from the interference coming from neighboring cells. We consider Minimum Variance Distortionless Response (MVDR) beamforming [137, 138], for which vector $\mathbf{w} \in \mathbb{C}^N$ in (7.3) is the spatial filter for the DoA of the user defined as

$$\mathbf{w} = \frac{\mathbf{R}_x^{-1}\mathbf{a}(\theta_{UE})}{\mathbf{a}^H(\theta_{UE})\mathbf{R}_x^{-1}\mathbf{a}(\theta_{UE})}. \tag{7.21}$$

$\mathbf{R}_x$ is the covariance matrix of the radio received signal $\mathbf{x}$ in (7.4), which contains both the signal of interest and the interference plus noise as

$$\mathbf{R}_x = \beta_{UE}^2\mathbf{a}(\theta_{UE})\mathbf{a}^H(\theta_{UE}) + \mathbf{R}_{n+i}, \tag{7.22}$$

where β_{UE}^2 is the received power at the array from the user of interest, and $\mathbf{R}_{n+i} = \mathbf{R}_I + \sigma_n^2\mathbf{I}$ is the spatial covariance matrix at the antenna array comprising both the interference coming from neighboring cells, i.e., $\mathbf{R}_I$, and the radio noise, i.e., $\sigma_n^2\mathbf{I}$.

It is realistic to assume that, while the DoAs of the users in the served area are known (or separately estimated), information about the interference is not available instantaneously, but rather in terms of spatial covariance for the beamforming design at the BBU. In the following, the interference covariance matrix $\mathbf{R}_I$ is computed assuming a set of interferers uniformly distributed over one or more interfering areas. A detailed description of the statistical interference model is in Appendix A.1.

7.4.2. Performance Metrics and Cable Degradation

The performance degradation due to the spatial crosstalk introduced by the FH link is evaluated primarily in terms of SINR at the decision variable $\hat{s}$ for the user. SINR after beamforming, in the ideal case of transparent fronthauling where BBU and RAU are co-located (i.e., $\mathbf{H}_{SF} = \mathbf{I}$), is

$$\mathrm{SINR}_{\mathrm{ideal}}(\theta_{UE}) = \frac{\sigma_s^2|\mathbf{w}^H\mathbf{a}(\theta_{UE})|^2}{\mathbf{w}^H\mathbf{R}_{n+i}\mathbf{w}}. \tag{7.23}$$

For a non-ideal SF fronthauling, the received signal at the beamformer is that of (7.1), and the SF channel matrix $\mathbf{H}_{SF}$ is included in the SINR expression accordingly:

$$\mathrm{SINR}(\theta_{UE}) = \frac{\sigma_s^2 |\mathbf{w}^H \mathbf{H}_{SF} \mathbf{a}(\theta_{UE})|^2}{\mathbf{w}^H \mathbf{H}_{SF} (\mathbf{R}_{n+i} + \mathbf{R}_c) \mathbf{H}_{SF}^H \mathbf{w}}, \tag{7.24}$$

where we recall that in this case the cable covariance matrix is $\mathbf{R}_c = \sigma_c^2 \mathbf{I}$, as in (7.8).

Moreover, to gain insight into how the system performances scale with the antenna array dimension, an average SINR per user is also evaluated by assuming that θ_{UE} is uniformly distributed and averaging $\mathrm{SINR}(\theta_{UE})$ over θ_{UE} as $\mathrm{SINR} = \mathrm{E}_{\theta_{UE}}[\mathrm{SINR}(\theta_{UE})]$.

7.4.3. Hill-Climbing Approach for SF2SF Mapping

The optimal SF2SF mapping of each antenna onto each cable and frequency can be found by solving a non-trivial integer programming optimization problem, whose complexity is $\mathcal{O}(N!)$. This is the number of possible permutations for a $N \times N$ matrix and the number of all possible SF2SF mappings. It is therefore mandatory to adopt a sub-optimal, but still effective, resource allocation algorithm, especially when dealing with a massive number of antennas (say $N > 100$). In this chapter, we propose to find a suboptimal solution through an iterative local search with relatively low computational cost. In general, the optimization problem set by the SF2SF mapping consists in defining an optimal mapping between the N radio signals from the antennas of the array and all the $N_s \cdot N_f \geq N$ available SF channels. The problem is considered here in a simplified version, in which we assume that $N_s \cdot N_f = N$ and $N_s = 4$, to gain insight into the interplay between the crosstalk introduced by $\mathbf{H}_{SF}$ and the SF channel mapping. In Section 7.4.4.3, unless otherwise explicitly stated, it is assumed that, for N antennas, the first $N_f = N/4$ frequency bands of 22-MHz are allocated (i.e., the channels are allocated by increasing level of crosstalk).

In particular, the hill-climbing approach, adapted from Intelligence Artificial problems [139], is used to find the (sub)optimal SF channel mapping based on a local search iterative algorithm, explained in the following and summarized in Algorithm 7.1. For any permutation, univocally defined by a vector $\boldsymbol{\pi} = [\pi_1, \ldots, \pi_N]^T$ as in Section 7.3, the set of all the neighboring permutations at a (integer) distance d_p is defined as the set of all vectors obtained by permuting in any way all subset of d_p elements in $\boldsymbol{\pi}$. The algorithm starts from an initial permutation $\boldsymbol{\pi}_0$, randomly chosen, and updates the solution as follows: at the k-th step all the neighbors $\{\boldsymbol{\pi}_{near,k}\}$ at distance lower than or equal to d_p from the present solution $\boldsymbol{\pi}_{\mathrm{opt},k}$ are computed, together with the corresponding SINR values (7.24). The

best neighbor $\boldsymbol{\pi}_{\text{near},k}^{\text{best}}$ is compared to $\boldsymbol{\pi}_{\text{opt},k}$ in terms of associated SINR: if the best neighbor has greater SINR with respect to $\boldsymbol{\pi}_{\text{opt},k}$ the solution is updated to $\boldsymbol{\pi}_{\text{opt},k+1} = \boldsymbol{\pi}_{\text{near},k}^{\text{best}}$ and another iteration is performed, otherwise the final solution is $\boldsymbol{\pi}_{\text{opt},k}$. The number of iterations N_{it} needed to reach the solution is proportional to the dispersion of the solution set (i.e., high dispersion means that there is room for channel assignment optimization), and it depends both on the radio-link SNR and on the number of RAU antennas N. However, it cannot be known in advance and needs to be evaluated numerically. The hill-climbing algorithm is clearly sub-optimal as it will select as solution the first local maximum for the SINR, but the performances are close to the exhaustive $\mathcal{O}(N!)$ search as shown in Section 7.4.4.3.

Algorithm 7.1 Iterative hill-climbing algorithm for (sub)optimal SF2SF mapping

1. Input: radio scenario parameters, cable characteristics, max. neighbor distance d_p;
2. Initialize $\boldsymbol{\pi}_0$ and compute $\text{SINR}(\boldsymbol{\pi}_0)$ from (7.15) and (7.24);
3. **while** $\text{SINR}(\boldsymbol{\pi}_{best,k}) > \text{SINR}(\boldsymbol{\pi}_{best,k-1})$
   a) compute neighboring permutations $\{\boldsymbol{\pi}_{near,k}\}$ at distance $d \leq d_p$ from $\boldsymbol{\pi}_{best,k-1}$;
   b) $\boldsymbol{\pi}_{best,k} = \arg\max_{\boldsymbol{\pi}} \text{SINR}(\boldsymbol{\pi}_{near,k})$;
4. **end while**
5. Output: $\boldsymbol{\pi}_{best,k}$.

7.4.3.1. Hill-Climbing Computational Complexity

The evaluation of the optimal SF2SF multiplexing $\boldsymbol{\Pi}_c$ matrix follows from the positions of UEs by the directional channel $\mathbf{H}_w$, and, for each specific setting, the choice of $\boldsymbol{\Pi}_c$ remains unchanged. In perspective, a number of possible configurations between UEs' positions and corresponding optimal SF2SF permutation matrices can be pre-computed and indexed when needed. This follows a learning approach of the context (not covered here, left as future work) which represents an obvious solution for practical implementations.

In any case, the hill-climbing algorithm should be run for each UEs configuration, and its computational complexity can be measured by the total number of times, denoted by K, that the SINR value in (7.24) needs to be evaluated in order to reach the solution. In the case of the SF2SF multiplexing by exhaustive search, for example, it corresponds to the total number of possible reference channel permutations: $K_{\text{exh}} = N!$. The computational complexity of the hill-climbing algorithm

needs to account for the fact that, for each of the N_{it} hill-climbing iterations, an exhaustive search over all the neighboring permutations must be performed according to the neighboring distance d_π. Given a specific neighboring distance d_π, the cardinality of the neighboring permutations set K_{d_π} is

$$K_{d_\pi} = \sum_{n=2}^{d_\pi} \binom{N}{n} \cdot !n, \tag{7.25}$$

where $!n = n! \cdot \sum_{i=0}^{n} \frac{(-1)^i}{n!}$ is known as *derangement number* or *de Montmort number*, which is defined as the number of permutations of the elements of a set, such that no element appears in its original position (details are in Appendix A.2). Then, the overall computational complexity is obtained as

$$K = K_{d_\pi} \cdot N_{\text{it}}. \tag{7.26}$$

N	4	20	36	52	68	84	100	116	132	148	164	180
K_{d_π}	6	190	630	1326	2278	3486	4950	6670	8646	10878	13366	16110

Table 7.1.: Cardinality of the neighboring set K_{d_π} for different values of RAU antennas N and $d_\pi = 2$

The values of the cardinality of the neighboring permutation set K_{d_π} corresponding to the values of the number of RAU antennas N considered in the numerical evaluation are reported in Table 7.1 for $d_\pi = 2$.

7.4.4. Simulation Settings and Results

7.4.4.1. Radio Scenario

The scenario considered in this section includes interference coming from two areas in the surroundings of the antenna array. The interference spatial covariance matrix $\mathbf{R}_I$ at the RAU antenna array in (7.22) is computed for the average number of active interfering users M_I and the angular position γ, the size r and the distance d of the two interfering areas (e.g., cells, hot-spots, access points, etc..). In the following numerical evaluations, we consider the presence of $M_I/2 = 2$ active users (on average) in each of the two interfering areas, which differ both in size and distance. The first one is at $\gamma_1 = -50°$, $r_1 = 100$m, $d_1 = 250$m while the second at $\gamma_2 = 50°$, $r_2 = 30$m, and $d_2 = 150$m as in Fig. 7.6a. In all the results, a 20-dB radio-link SNR is considered.

7.4.4.2. Cable Scenario

As discussed in the previous chapter, LAN cables (Cat-5/6/7) contain $N_s = 4$ twisted pairs providing the space multiplexing dimension, where each pair can

accommodate a bandwidth up to 1 GHz (depending on cable type, length, etc..). In this section, we assume that all the twisted pairs are used for the FH signal. In particular, IL and FEXT vary in frequency as shown in Fig. 7.5 for a measured Cat-6 cable, which is the cable type used here for performance evaluation. It is assumed that the frequency division is made by 22-MHz bands, corresponding to 20-MHz LTE-like channels plus an additional 10% guard interval, and that the cable channel is approximately frequency-flat within each 22-MHz band for the construction of the channel matrix $\mathbf{H}_c$. Hence, since the cable is not flat, for the sake of numerical analysis (Section 7.4.4), the coefficients of the k-th matrix $\mathbf{H}_k$ in (8.7) are obtained as the mean of the channel measurements over the k-th frequency band.

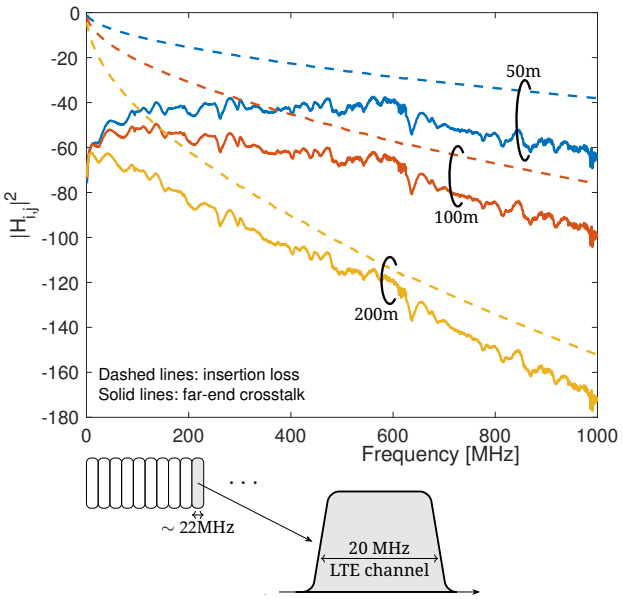

Figure 7.5.: Cat-6 cable characterization for 50m length and its extrapolation to 100m and 200m

7.4.4.3. Numerical results

Numerical validation for the proposed fronthauling architecture has been carried out evaluating the SINR at the decision variable by varying the angular position θ_{UE} of the user of interest within the coverage area of the antenna array (i.e., [-60°,60°]). An experimentally measured Cat-6 LAN cable of 50m with 1GHz/pair bandwidth is used for the FH link in all the settings, using typical parameters as -76dBm/Hz transmit power spectral density per pair and -140dBm/Hz noise floor.

The attenuation of the signals received over each twisted-pair and frequency band has been compensated at the BBU, which amplifies the received signals (both interference and noise have been scaled accordingly) prior to receive beamforming. Fig. 7.6 shows the results for $N = 8$ antennas at the RAU. To highlight the effect of SF2SF mapping, we assume that the $N = N_s \cdot N_f$ SF channels are obtained with $N_f = 2$ frequency slots allocated over the $N_s = 4$ twisted pairs contained in the LAN cable. The two frequency slots are taken around 300MHz to investigate the impact of SF2SF in case of relatively severe crosstalk. Moreover, in Fig. 5 the accuracy provided by the hill-climbing algorithm with respect to an exhaustive search over all the possible $N!$ SF2SF channel mappings is proved.

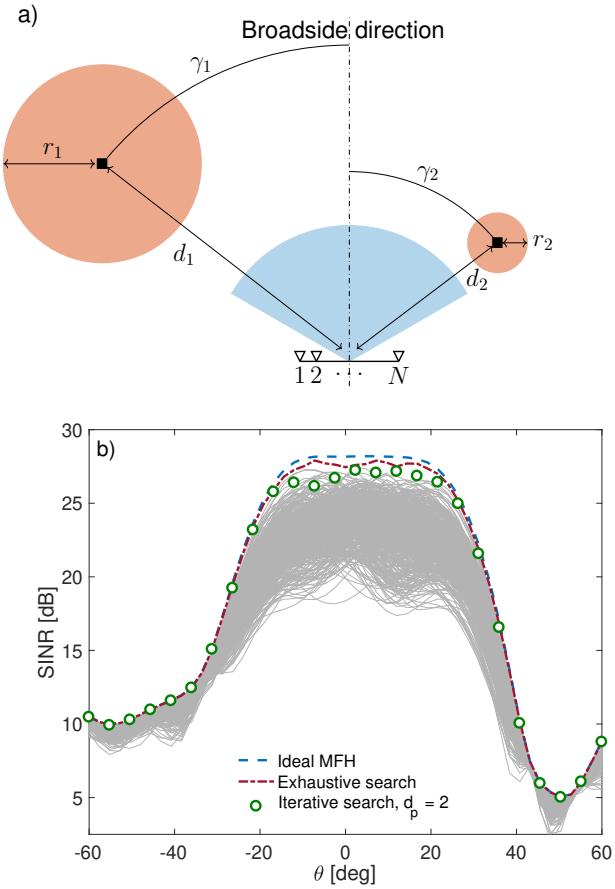

Figure 7.6.: a) Interference scenario and b) SINR versus θ highlighting the effect of all possible SF2SF mapping (gray lines) and the optimum values (red dash-dotted line)

The SINR degradation due to the two interfering areas at $\pm 50°$ is apparent. The

gray lines represent the SINR for some of the possible cable channel assignments to antennas versus the angles, showing the great gain the can be achieved by selecting the best permutation at each angle (dashed-dotted red line) which attains the performance of ideal fronthauling (i.e., $\mathbf{H}_{SF} = \mathbf{I}$, dashed blue line). Moreover, the iterative search algorithm, although suboptimal, approaches the performance guaranteed by the exhaustive search with much lower computational complexity that is a major issue with large antenna arrays.

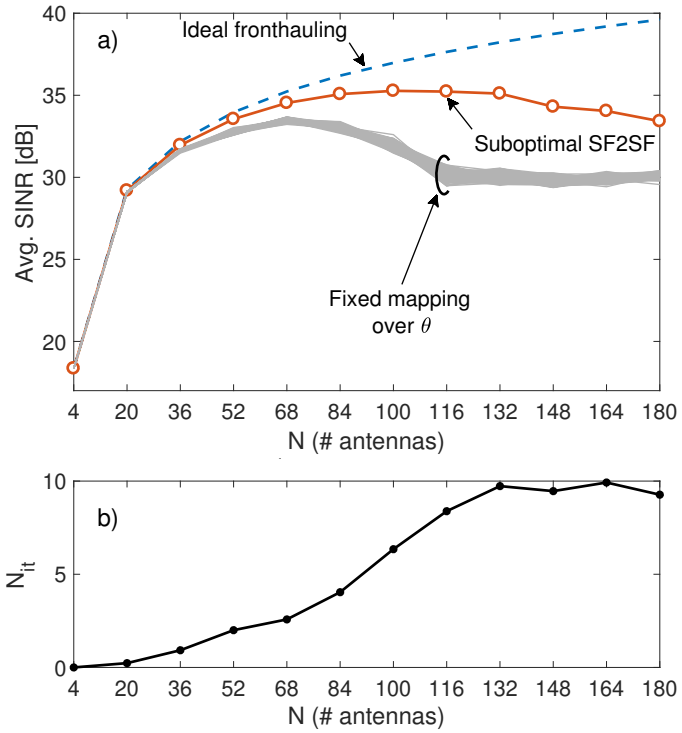

Figure 7.7.: a) Average SINR at the decision variable $\hat{s}$ vs number of antennas (N), b) cost of the optimization algorithm in terms of number of iterations (N_{it})

The performances obtained increasing dramatically the number of RAU antennas are shown in Fig. 7.7 in terms of mean SINR (averaged over the DoAs θ_{UE}) and cost of the iterative algorithm used, identified with the number of iterations N_{it} (Section 7.4.3). The gray lines are obtained averaging the SINR achieved by a representative number of random permutations (fixed SF2SF mapping for all θ_{UE}).

It is to be noticed that, being the overall available spectrum in the LAN cable approximately equal to $N_s \cdot 1\text{GHz} = 4\text{GHz}$, and considering 22-MHz RF signals at each antenna, the maximum number of allocable antennas by SF2SF mapping

is approx. 180. However, from Fig. 7.7 we observe that it seems to be counter-productive to allocate more then 116 RAU antennas (corresponding to approx. 650 MHz) due to the joint effect of FEXT and noise. For a relatively small number of antennas (< 36), since at low frequencies the impact of crosstalk is limited (see Fig. 7.5), the effect of (sub)optimal SF2SF mapping is negligible. On the contrary, increasing the number of antennas, those should be allocated on the high-frequency spectrum, for which the impact of crosstalk is severe and allocation should be judiciously chosen. As a result, and confirmed by Fig. 7.7, when using such spectrum portion it is mandatory to employ the SF2SF mapping, which provides up to approx. 6-dB gain in SINR approaching the ideal fronthauling, at least up to 650 MHz (i.e., $N = 116$).

The cost associated with such result is proportional to the gain provided: the SINR improvement with respect to a fixed channel mapping presents the same behavior of the cost curve, where the cost is defined as N_{it} (averaged over θ_{UE}). Just to take a practical example, the heuristic SF2SF solution for $N = 68$ antennas requires the computation of $K = K_{d_\pi} \cdot N_{it} = 2278 \cdot 2.5 \approx 5.7 \cdot 10^3$ (values taken from Fig. 7.7b and Table 7.1) values for the SINR, which is greatly lower than the $K_{\text{exh}} = N! = 2.5 \cdot 10^{96}$ searches required by the optimal solution obtained by exhaustive search.

7.5. Analog MIMO RoC for Indoor Office Scenario with Other-Services Interference

In the section above, it has been shown the gain that SF2SF multiplexing can achieve in A-MIMO-RoC by a judicious mapping between multiple-antennas/radio-spectrum to/from cable-pairs/cable-spectrum. SF2SF allows to cope with cable impairments without any digital RAU processing. So far, we have considered an outdoor multi-cell system in which a dedicated LAN cable has been entirely devoted to the transmission of FH signals. In this section, we consider a more realistic indoor office scenario in which only one out of the 4 twisted-pairs contained in the LAN cable is used for FH transmission, as the others are assumed to be already employed for other services (i.e., Power Over Ethernet, DSL, other RAUs, etc.), and act as additional source of interference.

In particular, we consider the in-building A-MIMO-RoC solution in Fig.7.8, specializing the analysis of the section above to the case of single-pair copper cable (i.e., $N_s = 1$). As a result, for this specific case, the multiplexing dimension over the FH cable-link is provided over frequency only, and the resource allocation strategy is referred to as Space-Frequency to Frequency (SF2F) multiplexing.

As discussed, the computation complexity of the optimal SF2SF requires an exhaustive search over all the possible air-link channel assignments onto the available cable-links, which is impractical for a large number of RAU antennas and/or bandwidths (say when $\gg 10$). An iterative hill-climbing algorithm has been proposed

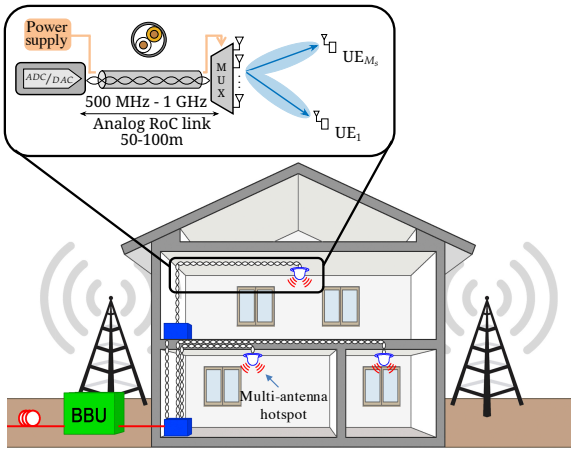

Figure 7.8.: RoC fronthauling for in-building solutions

to find a sub-optimal mapping at relatively low computational complexity. In particular, in this section, we show that for the special case of a single twisted-pair, the SF2F multiplexing problem reduces to an Integer Linear Programming (ILP) problem, which can be *optimally* solved at low complexity by conventional solving algorithms. The main goal is to gain insights into the role of the optimal SF2F mapping between the air antennas/spectrum (or air-services) and the cable-link spectrum allocable, showing the potential of the proposed strategy.

To validate the method in a realistic scenario, the performance of the SF2F are evaluated for a sample scenario in which digital beamforming is performed at the BBU to separate the useful signal of a single indoor user from the uncoordinated interference arising from outdoor users.

In details, the contributions of this section are as follows: *i)* we propose an in-building solution based one single-pair A-MIMO-RoC fronthauling, *ii)* we optimally solve the SF2F mapping optimization problem for the single-pair case, and *iii)* we prove the advantages of the proposed architecture whose performance are greatly improved by the optimal SF2F mapping, without any manipulation of RF signals to cope with cable impairments.

7.5.1. Single-Pair Copper Fronthauling in the Frequency Domain

In this section, we assume the FH transmission is over a single pair, as the other pairs act as additional interference. As a consequence, the FH cable multiplexing dimension is here over frequency only. In the case of single-pair FH link, the channel matrix in (9.16), denoted here as $\mathbf{H}_f$ emphasizing that frequency is the only FH multiplexing dimension, can be thus defined starting from the diagonal

matrix

$$\mathbf{H}_{c,\text{single}} = \text{diag}(h_1, h_2, ..., h_{N_f}), \tag{7.27}$$

that accounts for the cable loss h_j of the considered twisted-pair at the j-th frequency band. Moreover, to simplify the analysis, it is assumed that the total number of antennas N served by the cable is equal to the total number of available frequency resource blocks (i.e., $N = N_f$).

Once again, the SF2F mapping between air-link spectrum-antennas and cable-link frequency resource blocks is a fundamental free-design parameter in the all-analog interference management at the RAU. As a result, the cable channel matrix $\mathbf{H}_f$ can be conveniently reframed by the FDM permutation of the reference channel matrix $\mathbf{H}_{c,\text{single}}$ as

$$\mathbf{H}_f = \mathbf{\Pi}_c^T \mathbf{H}_{c,\text{single}} \mathbf{\Pi}_c, \tag{7.28}$$

where the mapping between air and cable channels is described by the permutation matrix $\mathbf{\Pi}_c \in \{0,1\}^{N \times N}$ as in 7.3. An illustrative description of the FH channel based on FDM over a single-pair copper cable is given in Fig.7.9.

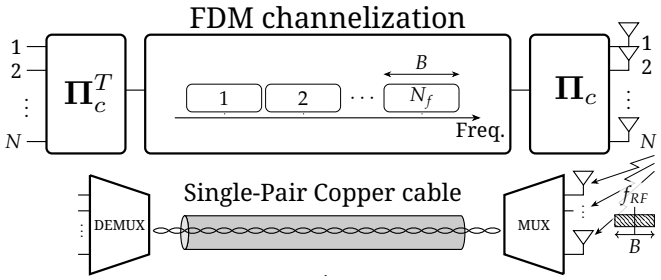

Figure 7.9.: FDM wired access link: (upper) mathematical and (lower) physical model

7.5.2. BBU Processing: Maximum Signal-to-Interference Ratio Beamforming

The digital spatial processing is performed at the BBU side. Hence, instead of acting directly on the signals received at the antenna array, beamforming acts on the signals $\mathbf{x}_w^{\text{BBU}} = \mathbf{H}_f \mathbf{x}_w^{\text{RAU}} + \mathbf{n}_c$ received at the BBU after the FH channel $\mathbf{H}_f$, which is expected to be transparent for the beamforming design.

As example of receiver processing for performance evaluation, here we adopt Maximum Signal-to-Interference Ratio (Max-SIR) beamforming [137, 138], since it requires the knowledge of the covariance matrices of signal and interference (plus noise) only, and not the knowledge of the exact DoAs (impractical in many settings). The signal of the desired user is estimated at the BBU as

$$\hat{s} = \mathbf{w}^H \mathbf{y}, \tag{7.29}$$

where $\mathbf{w} \in \mathbb{C}^N$ is the spatial filter maximizing the radio-link SIR after the beamforming and defined as

$$\mathbf{w} = \mathbf{R}_n^{-1/2} \, \mathrm{eig}_{\max}\{\mathbf{R}_n^{-H/2} \mathbf{R}_x \mathbf{R}_n^{-1/2}\}, \tag{7.30}$$

where $\mathrm{eig}_{\max}\{\mathbf{A}\}$ denotes the eigenvector of $\mathbf{A}$ corresponding to its maximum eigenvalue, $\mathbf{R}_x = \beta_{UE}^2 \gamma_{UE}^2 \mathbf{a}(\theta_{UE})\mathbf{a}(\theta_{UE})^H$ is the covariance matrix of the signal of the user of interest and $\mathbf{R}_n = \mathbf{R}_I + \sigma_n^2 \mathbf{I}$ is the spatial covariance matrix at the antenna array containing the interference coming from outdoor cells $\mathbf{R}_I$ and the radio noise $\sigma_n^2 \mathbf{I}$. The interference spatial covariance matrix $\mathbf{R}_I$ at the RAU in (7.30) considers M_I interfering users uniformly randomly distributed over each outdoor cell and with radio channel modeled as the one in (7.5). As mentioned, only the covariances matrices of user and interference signals are needed in order to design the digital beamformer at the BBU.

7.5.3. Performance Metrics and Cable Degradation

The performance degradation due to the analog cable FH link $\mathbf{H}_f$ is evaluated primarily in terms of SINR at the decision variable $\hat{s}$ for the indoor user. The received signal at the BBU after beamforming is the one in (7.3), and the corresponding SINR is

$$\mathrm{SINR}(\theta_{UE}) = \frac{\sigma_s^2 |\mathbf{w}^H \mathbf{H}_f \mathbf{a}(\theta_{UE})|^2}{\mathbf{w}^H \mathbf{H}_f \mathbf{R}_n \mathbf{H}_f^H \mathbf{w}}. \tag{7.31}$$

Performance are evaluated in terms of equivalent wireless channel capacity

$$\mathrm{C}(\theta_{UE}) = \log_2(1 + \mathrm{SINR}(\theta_{UE})), \tag{7.32}$$

and SINR degradation with respect to the ideal case as

$$\Delta_{\mathrm{SINR}}(\theta_{UE}) = \mathrm{SINR}_{\mathrm{ideal}}(\theta_{UE}) - \mathrm{SINR}(\theta_{UE}), \tag{7.33}$$

where $\mathrm{SINR}_{\mathrm{ideal}}(\theta_{UE})$ is the SINR in the case of transparent fronthauling with co-located BBU and RAU: $\mathbf{H}_f = \mathbf{I}$.

7.5.4. Optimal Space-Frequency to Frequency Mapping in Single-Pair Copper Cables

The computation of the optimal SF2F mapping requires an exhaustive search over all the $N!$ possible permutations $\mathbf{\Pi}_c$ of the FH channel $\mathbf{H}_f$, which is impractical for a large number of antennas ($\gg 10$). In the previous section, an iterative algorithm has been proposed to find a sub-optimal $\mathbf{\Pi}_c$ for the multi-pair case at relatively low computational complexity. However, no general mapping-rule for multiple antennas has been provided so far. Here, we formulate the optimization problem for the case of single-pair copper cable where the permutation $\mathbf{\Pi}_c$ is designed to cope with cable attenuation of the considered pair only (i.e., $\mathbf{\Pi}_c$ has no effect on FEXT, treated as additive noise).

From (7.31) it follows that the radio performance degradation is due to the impairment caused by $\mathbf{H}_f$ on the original beamforming weights $\{w_i\}_{i=1}^N$ (recall that $M = 1$, single-user case) as

$$\mathbf{w}_f^H(\mathbf{\Pi}_c) = \mathbf{w}^H \mathbf{H}_f, \tag{7.34}$$

where $\mathbf{H}_f = \mathbf{\Pi}_c^T \mathbf{H}_{c,\text{single}} \mathbf{\Pi}_c$. We characterize the optimal SF2F mapping as that specific permutation matrix $\mathbf{\Pi}_c$ which limits the impact of $\mathbf{H}_{c,\text{single}}$ on the performance of the system, thus leading to an impaired beamforming vector $\mathbf{w}_f(\mathbf{\Pi}_c)$ which is the closest in a least square sense to the original beamformer $\mathbf{w}$:

$$\mathbf{\Pi}_{c,\text{opt}} = \arg\min_{\mathbf{\Pi}_c} \left\| \mathbf{w}^H - \mathbf{w}_f^H(\mathbf{\Pi}_c) \right\|_2^2 . \tag{7.35}$$

After some algebraic manipulations exploiting the diagonal structure of $\mathbf{H}_f$, and considering the properties of the permutation $\mathbf{\Pi}_c$ (see Sect.), it is easy to reformulate problem (7.35) as an Integer Linear Program (ILP), which can be efficiently solved by any of the solvers conventionally employed in mathematical optimization (i.e., Gurobi [140]).

7.5.5. Simulation settings and results

7.5.5.1. Radio Scenario

The scenario considered in this section is shown in plan view in Fig. 7.11a.. It includes interference coming from two outdoor areas (e.g., macro-cells) located in the surroundings of the building at angular positions $\gamma_1 = -60\,\text{deg}$ and $\gamma_2 = 20\,\text{deg}$, with radial size $r_1 = 50\text{m}$ and $r_2 = 100\text{m}$, and distance $d_1 = 125\text{m}$ and $d_2 = 250\text{m}$ from the antenna array. It is assumed to have $M_I = 5$ interfering users uniformly randomly distributed over each outdoor cell. In all the following numerical results, we assume an air-link SNR $1/\sigma_n^2 = 15$ dB, and we consider LOS-dominant radio links whose gains follow a Rician distribution with shape

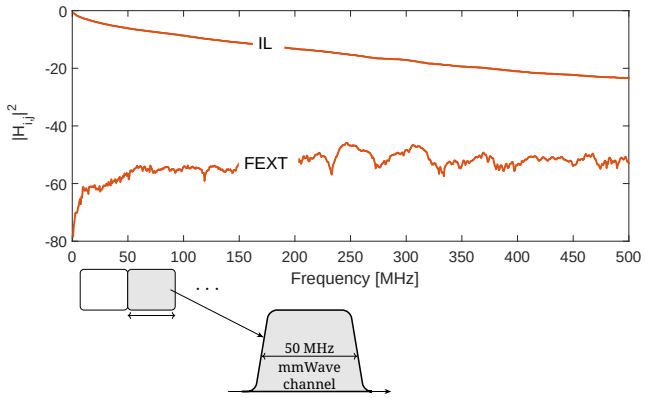

Figure 7.10.: IL and FEXT measurements on a 50m Cat-7 cable

parameter $K = 10\,\text{dB}$ to model a typical mm-Wave small-scale fading [141]. For the considered indoor architecture, we assume that the RAU is equipped with $N = 10$ antennas, each of which carries a 50-MHz bandwidth mm-Wave signal. The RAU maps the incoming signals onto $N_f = N$ frequency slots over the twisted pair. Notice that $N = 10$ antennas corresponds to the whole 500-MHz cable bandwidth if considering 50-MHz RF signals at each antenna.

7.5.5.2. Cable Scenario

The in-building A-MIMO-RoC fronthauling architecture considered here is based on a 50m Cat-7 LAN cable, for which IL and FEXT vary vs frequency as shown in Fig. 7.10 for the cable measurements over a 500-MHz bandwidth [142]. The frequency division over the cable is made by 50-MHz bands, corresponding to the bandwidth of the considered RF signals. Notice that the values of cable IL and FEXT may change significantly over each 50-MHz bandwidth due to their behavior over frequency. However, for the sake of numerical analysis, we simplify the reasoning by assuming that the cable channel is approximately frequency-flat within each 50-MHz band considering the IL coefficient h_k in $\mathbf{H}_{c,\text{single}}$ (7.27) and the FEXT affecting the k-th FDM channel (accounted by the degradation in interference plus noise covariance matrix $\mathbf{R}_c$ in (7.9)) as the mean of the channel measurements over the k-th frequency band.

7.5.5.3. Numerical results

Numerical validation for the proposed fronthauling architecture has been carried out by evaluating the wireless capacity $C(\theta_{UE})$ when varying the angular position θ_{UE} of the user of interest within the coverage area of the antenna array (i.e., $[-60\,\text{deg}, 60\,\text{deg}]$). The values of IL and FEXT for the FH link are drawn from an experimentally measured Cat-7 LAN cable of 50m with 500 MHz bandwidth [142]

(Fig. 7.10), using typical parameters as -76dBm/Hz for transmitter spectral mask and -140dBm/Hz noise floor. As for the outdoor scenario, the attenuation of the received signals has been compensated at the BBU by signal amplification prior to the receive beamforming. Fig. 7.11 shows the outage capacity at 5% where the capacity degradation due to the interferers around $\gamma_1 = -60\,\text{deg}$ and $\gamma_2 = 20\,\text{deg}$ is apparent. The gray dash-dotted line is obtained by randomly selecting an

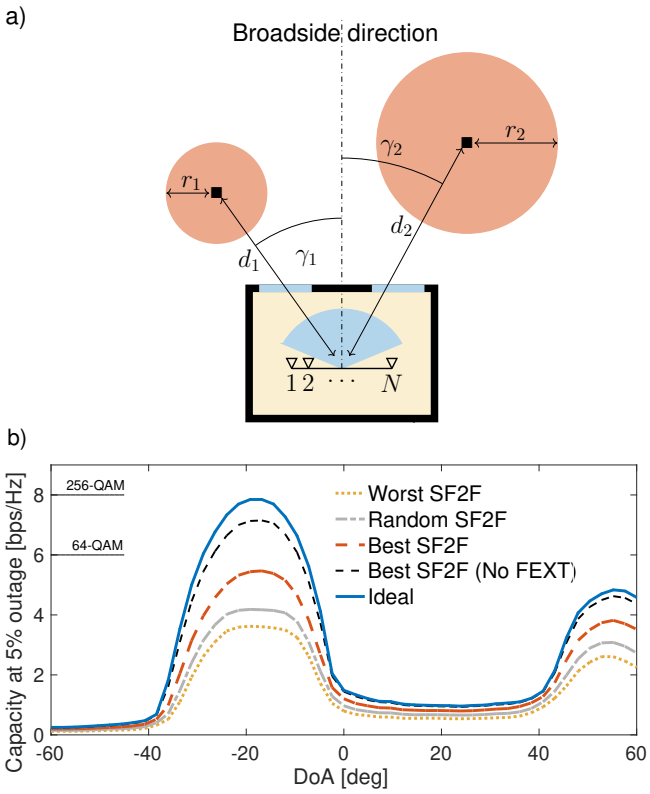

Figure 7.11.: a) Indoor deployment scenario with two non-coordinated interferers (plan view of the building room) and b) Capacity at 5% outage versus the DoA of the user θ_{UE} for different SF2F mappings ($N = 10$ antennas).

antennas-cable channels assignment for each θ_{UE} while the yellow dotted line is obtained for the worst channel permutation, showing the maximum gain the can be achieved by the optimal SF2F mapping at each angle (dashed red line) which at least halves the performance degradation from the ideal fronthauling (solid blue line). The dashed black line approaching the ideal performance shows the capacity achieved by the optimal SF2F mapping assuming that no FEXT from the other pairs degrades the signal of interest (i.e., the cable-link only attenuates the signal) which quantifies the performance degradation due to FEXT (approx. 2 bps/Hz).

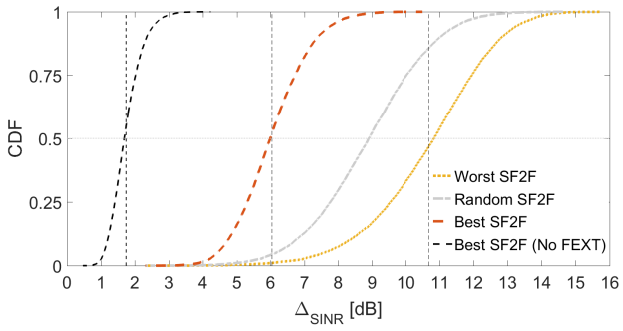

Figure 7.12.: CDF of the $\Delta_{\text{SINR}}(\theta_{UE} = -20\,\text{deg}\,)$ for different SF2F mappings

The Cumulative Distribution Function of the $\Delta_{\text{SINR}}(\theta_{UE} = -20\,\text{deg})$ is in Fig. 7.12 confirming the advantages in terms of SINR degradation from the ideal fronthauling provided by the optimal SF2F mapping while emphasizing again the loss due to the FEXT coming from the other pairs.

7.6. Concluding Remarks

In this chapter, we considered Analog MIMO-RoC (A-MIMO-RoC) architecture as an alternative solution to conventional mobile fronthauling based on fiber optics. The focus is on the A-MIMO-RoC uplink, in which LAN cables are employed for the analog connections between RAUs and BBUs, since they are already largely deployed in buildings and enterprises, and therefore no additional cost/time for a new network infrastructure is required. LAN cables contain 4 twisted pairs that allow transmissions over at least 4 space-separated channels with up to 1GHz/pair bandwidth, enabling the design of a joint Space/Frequency Division Multiplexing (SDM/FDM) fronthauling for a massive number of RAU antennas. In particular, the main contribution of the chapter is to investigate the impact of a novel mapping between the antenna/frequency dimensions of the air link and the twisted pair/frequency dimensions of the cable links, referred to as Space-Frequency to Space-Frequency (SF2SF) multiplexing.

The first part of the chapter focuses on a multi-cell mobile network in which a dedicated LAN cable is entirely devoted to the transmission of FH radio signals. To validate the effectiveness of the proposed architecture, a statistical interference model has been used to consider a realistic radio scenario, and MVDR beamforming (transparent to the copper channel) has been considered to evaluate the impact of the impairments introduced by the LAN cable. Numerical results proved that by means of a dynamic SF2SF mapping between air link and cable link resources, it is possible to overcome the crosstalk limitations of the copper FH approaching the ideal performances, at least up to approx. 650 MHz (corresponding to 116 RAU antennas).

In the second part of the chapter, an indoor office scenario is considered. In this case, it is assumed that only one pair out of the four contained into the LAN cable is used for FH transmission, while the others are used for other services, and act as sources of uncoordinated interference. In the single-pair case, frequency is the only multiplexing dimension available over the FH, and thus the problem is formulated in order to efficiently find the optimal Space-Frequency to Frequency (SF2F) mapping between the antennas at the RAU and the cable frequency channels. The validation of the proposed architecture has been performed considering a realistic radio scenario in which an indoor user is interfered by several outdoor users located in neighboring outdoor cells. Max-SIR beamforming has been considered as example of eigen-beamforming based spatial receiver processing at the BBU to evaluate the impact of the impairments introduced by the copper FH, which is again assumed to be completely transparent for the beamforming design. Numerical results confirmed the effectiveness of the proposed SF2F mapping.

Concluding, the proposed space-frequency domain resource allocation strategy between radio and cable resources has been shown to provide substantial benefits in the A-MIMO-RoC architecture. SF2SF enables the design of a C-RAN architecture based on the joint exploitation of SDM and FDM even without performing any digital processing and the RAU and any crosstalk mitigation techniques at the BBU to compensate for the copper channel, which is assumed to be fully transparent to the overall transmission from BBUs to the end-user. The extension to the case of multiple users and to the A-MIMO-RoC downlink is not trivial, as the effect of multi-user interference needs to be taken into account in the SF2SF multiplexing design. Moreover, in downlink direction, different power constraints must be fulfilled both at the RAU antennas and at the BBU. These issues are covered in the next chapter.

8. Analog MIMO RoC Downlink with Space-Frequency to Space-Frequency Multiplexing

8.1. Introduction

Centralized Radio Access Networks (C-RAN) with analog FrontHauling (FH) is an attractive solution for high-rate/low-latency/synchronized RAU applications [30, 12, 132]. The key feature of analog FH is that multiple geographically distributed Remote Antenna Units (RAUs) directly relay the Intermediate Frequency (IF) signals to/from the BaseBand Units (BBUs) after heterodyning, thus avoiding any bandwidth expansion due to digitization or latency (up to the propagation only), improving the energy efficiency, and reducing hardware cost.

In Chapter 6, a bandwidth-efficient and low-cost analog C-RAN architecture, referred to as Analog MIMO Radio-over-Copper (A-MIMO-RoC), has been proposed for extending indoor over the last 100-200m. A-MIMO-RoC leverages the LAN cables that are already largely deployed in buildings and enterprises. Contrarily to already existing indoor solutions based on LAN cables that use mainly the low frequency portion of cable bandwidth, e.g., [31, 33], A-MIMO-RoC pushes the usage of cable frequency up to several hundreds of MHz. The lesson learned from Chapter 6 is that LAN cables offer great bandwidth capability, which is more than enough to accommodated the transmission of analog signals for indoor fronthaul applications. In particular, it is shown by numerical evaluations that A-MIMO-RoC, by employing a 100m Cat-5 cable with approx. 500 MHz bandwidth/pair, is capable to serve up to 60 RAU antennas carrying a 20-MHz LTE channel/ea. The number of antennas increases even more for shorter cable lengths.

Beside the aforementioned advantages of the conceptual architecture presented in Chapter 6, in practice, the design and optimization of A-MIMO-RoC poses several technical challenges: *i)* Far-End CrossTalk (FEXT) among the 4 pairs and Insertion Loss (IL) severely limit the performance of LAN cables, if not properly handled, *ii)* for a large number of RAU antennas, it arises the problem of how to map the signal to/from each antenna onto the available cable resources, *iii)* the RAU equipment (e.g., home-device) should be as simple/cheap as possible, but in the meanwhile able to handle up to several tens of antennas, *iv)* LAN cables are subject to strict power constraints that must be carefully taken care of in

the system design, especially in downlink direction, and *v)* in case of multiple-users, interference cancellation techniques for compound A-MIMO-RoC should be properly designed, but still releasing the RAU from any computationally complex signal processing.

In Chapter 7, a single-user uplink A-MIMO-RoC architecture based on LAN cables is presented to address the critical aspects *i), ii)* and *iii)* mentioned above. In particular, it is demonstrated that by optimally mapping the RF signals of each RAU antenna onto a combination of twisted-pair/frequency allocations over the cable, referred to as Space-Frequency to Space-Frequency (SF2SF) multiplexing, it is possible to substantially mitigate the impairments introduced by the cable FH, once evaluated in terms of uplink end-user throughput. Moreover, the coexistence over the same LAN cable between FH signals and other services (e.g., DSL, PoE, etc.) has been tested for indoor, thus confirming the performance boost provided by SF2SF multiplexing technique.

Beyond the usage of A-MIMO-RoC with SF2SF for uplink FH scenarios, there are several open issues of practical interest, such as the A-MIMO-RoC downlink system design (complicated by power constraints) and the multi-user setting, both covered in this chapter.

In multi-user settings, the downlink problem requires an overall system optimization over the cascade of two MIMO channels (i.e., the FH cable channel and the wireless channel), and problem resembles the optimization of a two-hop Amplify-and-Forward (AF) MIMO relay system, first addressed in [143, 144]. Among the numerous valuable works dealing with AF systems that followed [143, 144] (for an excellent survey on the topic we refer the reader to [145] and references herein), the one by Chae *et al.* [146] is of particular interest for our purposes, since it focuses on the downlink channel of a cellular system in which the base station communicates with multiple single-antenna users through a single-relay node equipped with multiple-transceivers.

This chapter investigates the downlink multi-user A-MIMO-RoC architecture for 5G indoor deployments by optimizing the AF structure that, in A-MIMO-RoC, is constrained to perform the mapping of radio carriers for each antenna onto suitably chosen IL/FEXT impaired resources over the copper FH.

8.1.1. Chapter Contribution

In particular, the contributions of this chapter can be summarized as follows: *i)* we propose a single-user downlink A-MIMO-RoC architecture based on SF2SF multiplexing, and compliant with standardized LAN cables and heterodyne-only low-complexity RAU; *ii)* we extend the results in *i)* to multi-user settings by proposing a system design based on the joint optimization of the SF2SF multiplexing between air- and cable-link resources and the precoding algorithm performed at the BBU, and *iii)* we validate numerically the proposed architecture on geometrical air-link

MIMO channel models and 100 m cable (as reference length in copper cabling); performance are compared with the Singular Value Decomposition (SVD) relay design scheme proposed in [146], assumed here as a performance benchmark.

8.1.2. Contribution on International Conferences/Journals

Part of the material presented in this chapter has been published in:

- **A. Matera** and U. Spagnolini, "Analog MIMO-RoC Downlink with SF2SF" in *IEEE Wireless Communications Letters*, pp. 1–1, 2018.
- **A. Matera** and U. Spagnolini, "Analog MIMO Radio-over-Copper Downlink with Space-Frequency to Space-Frequency Multiplexing for Multi-User 5G Indoor Deployments" submitted to *IEEE Transactions on Wireless Communications*.

8.2. A-MIMO-RoC Downlink System Model

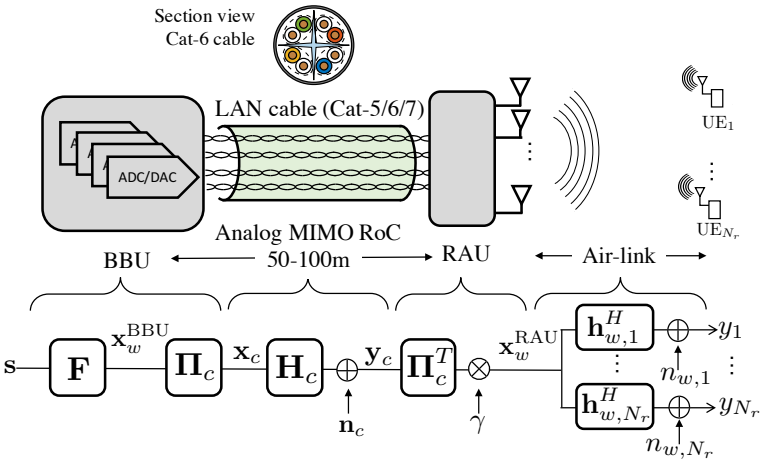

Figure 8.1.: System model: MIMO RoC architecture based on LAN cables, two-hop amplify-and-forward downlink channel

The Analog MIMO-RoC fronthauling for C-RAN architecture is in Fig. 8.1. The system is a cascade of cable and wireless links, denoted by subscript $(\cdot)_c$ and $(\cdot)_w$, respectively. In this chapter, the A-MIMO-RoC downlink is shortly described, as it is symmetric with respect to the A-MIMO-RoC uplink channel detailed in Chapter 7. In downlink direction, the BBU communicates with N_r User Equipments (UEs) through a RAU equipped with $N \geq N_r$ antennas, which acts as an AF relay node

comprehensive of frequency conversions. Without any loss of generality, UEs are single-antenna (or single-stream).

The downlink signals are precoded at the BBU, before being channelized into Space and Frequency Division Multiplexing (SDM and FDM, respectively) over the 4-pair wired access link. These are transmitted over the air-link by the RAU. Each of the N RAU antennas is assumed to carry a single wireless channel with bandwidth B_w so that, overall, at least a cable bandwidth

$$B_c \geq N \cdot B_w \tag{8.1}$$

is needed to transport all the fronthaul radio signal. The inequality in (8.1) provides degrees of freedom to cope with cable impairments (Sect. 8.3). The system in Fig. 8.1 can thus be regarded as a chain of two heterogeneous channels with different peculiarities.

8.2.1. Radio Channel

For reasoning simplicity, let the downlink radio channel RAU→UEs be narrowband frequency-flat block-fading (e.g., it might correspond to one sub-carrier of OFDM modulations) such that the signal received at the k-th user

$$y_k = \mathbf{h}_{w,k}^H \mathbf{x}_w^{\mathrm{RAU}} + n_{w,k} \tag{8.2}$$

involves the channel vector for the k-th user $\mathbf{h}_{w,k} \in \mathbb{C}^{N\times 1}$, the additive white Gaussian noise $n_{w,k} \sim \mathcal{CN}(0, \sigma_w^2)$, and the signal transmitted by the RAU $\mathbf{x}_w^{\mathrm{RAU}} \in \mathbb{C}^{N\times 1}$ subject to the average power constraint

$$\mathrm{E}\left[\left\|\mathbf{x}_w^{\mathrm{RAU}}\right\|_2^2\right] \leq P_w. \tag{8.3}$$

Otherwise explicitly stated (see Sect. 8.5.1.1), in this chapter we consider a geometrical channel model based on the Angles of Departure (AoDs) of signals [147], which accurately captures the mathematical structure of a mmWave systems (say $>$ 6-10 GHz), but it can also be extended to lower spectrum systems. In particular, it is assumed here that the channel $\mathbf{h}_{w,k}$ from the RAU to the k-th UE is the sum of the contribution of L_k propagating paths as

$$\mathbf{h}_{w,k} = \rho_k \sum_{l=1}^{L_k} \alpha_{k,l} \mathbf{a}(\phi_{k,l}, \theta_{k,l}), \tag{8.4}$$

where $\rho_k = \sqrt{N/L_k}$ is a normalization factor, $\alpha_{k,l} \sim \mathcal{CN}(0,1)$ is the complex gain for the l-th path, and $\mathbf{a}_{k,l}(\phi_{k,l}, \theta_{k,l})$ is the array response toward the k-th UE with $\phi_{k,l}$ and $\theta_{k,l}$ denoting the azimuth and elevation AoDs, respectively. Under the

assumption of half-wavelength spaced antenna elements, the array response of the $D_1 \times D_2$ Uniform Planar Array (UPA) is the $N \times 1$ vector

$$\mathbf{a}_{\text{UPA}}(\phi,\theta) = \frac{1}{\sqrt{N}} \Big[1, ..., e^{j\pi(d_1 \sin\phi \sin\theta + d_2 \cos\theta)}, ..., e^{j\pi((D_1-1)\sin\phi\sin\theta + (N-1)\cos\theta)}\Big]^T , \tag{8.5}$$

with $d_1 \in \{0, 1, ..., D_1 - 1\}$, $d_2 \in \{0, 1, ..., D_2 - 1\}$ and $N = D_1 D_2$.

8.2.2. Space-Frequency Cable Fronthaul Channel

Targeting no digital-processing at the RAU implies that its functionalities are limited to signal amplification, with possibly intra-cable frequency bands swapping to comply with cable capability (Sect. 8.4). The transmit signal $\mathbf{x}_w^{\text{RAU}}$ is just a scaled and frequency up-converted version of the signal

$$\mathbf{y}_c = \mathbf{H}_c \mathbf{x}_c + \mathbf{n}_c, \tag{8.6}$$

received from the BBU over the FH wired access link $\mathbf{H}_c \in \mathbb{C}^{N_c \times N_c}$, where $\mathbf{n}_c \sim \mathcal{CN}(\mathbf{0}, \sigma_c^2 \mathbf{I})$ is the uncorrelated white Gaussian cable noise with power σ_c^2 and $\mathbf{x}_c \in \mathbb{C}^{N_c \times 1}$ is the signal transmitted by the BBU over the cable.

As detailed in the previous chapter, the FH cable channel $\mathbf{H}_c$ is equivalent to a large MIMO system in the Space-Frequency (SF) domain defined by N_s SDM channels (i.e., the N_s twisted-pairs bonded together into the cable) and N_f FDM channels for a total of $N_c = N_s \cdot N_f$ SF resource blocks on cable. It is assumed that the total number of available SF cable channels N_c exactly equals the total number of RAU antennas N (i.e., $N_c = N$), even if in practice it could be relaxed to $N_c > N$ with further benefits. The matrix cable channel $\mathbf{H}_c$ accounts for the cable IL (diagonal terms, $[\mathbf{H}_c]_{i,i}$) and for the cable FEXT between all the N cable channels (off-diagonal terms, $[\mathbf{H}_c]_{i,j}$). As cross-cable interference occurs only among spatial channels at the same frequency, it is straightforward to describe $\mathbf{H}_c$ by the block diagonal matrix

$$\mathbf{H}_c = \text{diag}(\mathbf{H}_{c,1}, \mathbf{H}_{c,2}, \ldots, \mathbf{H}_{c,N_f}), \tag{8.7}$$

where each of the N_f diagonal blocks $\mathbf{H}_{c,f} \in \mathbb{C}^{N_s \times N_s}$ is the cable channel matrix at the f-th frequency band (frequency bands are disjointed). In particular, the main diagonal element $[\mathbf{H}_{c,f}]_{ii}$ contains the IL for the i-th twisted-pair at the f-th frequency band, while the off-diagonal element $[\mathbf{H}_{c,f}]_{ij}$, with $i \neq j$, represents the FEXT between twisted-pair j-th and i-th at the f-th frequency band.

The BBU signal $\mathbf{x}_c$ is transmitted to the RAU over the SF cable resource to be allocated, hence, it is conveniently defined as

$$\mathbf{x}_c = [\mathbf{x}_{c,1}^T, \mathbf{x}_{c,2}^T, ..., \mathbf{x}_{c,N_f}^T]^T, \tag{8.8}$$

where $\mathbf{x}_{c,f} \in \mathbb{C}^{N_s \times 1}$ are the symbols transmitted over the N_s twisted-pairs at the f-th frequency band. In particular, $[\mathbf{x}_{c,f}]_j$ denotes the BBU symbol transmitted over the j-the twisted-pair at the f-th cable frequency band.

The cable symbols $\mathbf{x}_c$ are obtained at the BBU by precoding ($\mathbf{F}$) and mapping ($\mathbf{\Pi}_c$) onto the N SF cable channels the N_r uncorrelated and normalized to unit-power UE information symbols $\mathbf{s} = [s_1, s_2, ..., s_{N_r}]^T$ as

$$\mathbf{x}_c = \mathbf{\Pi}_c \mathbf{x}_w^{\text{BBU}}, \quad \mathbf{x}_w^{\text{BBU}} = \mathbf{F}\mathbf{s}, \tag{8.9}$$

where matrix $\mathbf{\Pi}_c$ is the SF2SF multiplexing operator that maps the precoded symbols $\mathbf{x}_w^{\text{BBU}}$ intended to the N RAU antennas onto N SF blocks over the cable properly selected (for a detailed description of the algebraic structure of the SF2SF operator please refer to Chapter 7, Sect. 7.3). Symbol $[\mathbf{x}_w^{\text{BBU}}]_n$ denotes the BBU symbol that is relayed over the cable towards the n-th RAU antenna. Eq. (8.9) models a system in which the radio signal $\mathbf{s}$ carried over one subcarrier with bandwidth B_w is transported to the N RAU antennas after being mapped over N SF cable fronthaul channels. To comply with standardized cable constraints [35], $\mathbf{x}_c$ is subject to Per-Line Per-Carrier (PLPC) transmit power constraints at the cable input, also known as Power Spectral Density (PSD) masks, as

$$\mathrm{E}\left[|[\mathbf{x}_{c,f}]_j|^2\right] \leq P_c, \quad \forall\, f = 1, ..., N_f,\ \forall\, j = 1, ..., N_s, \tag{8.10}$$

and also per-line Aggregate Transmit Power (ATP) constraint

$$\sum_{f=1}^{Nf} \mathrm{E}\left[|[\mathbf{x}_{c,f}]_j|^2\right] \leq P_{ATP}, \quad ,\forall\, j = 1, ..., N_s. \tag{8.11}$$

Both the technological constraints typical of copper cables [35] complicate the SF2SF design.

Permutations $\mathbf{\Pi}_c$ are mutually signaled between RAU and BBU: once the specific SF2SF multiplexing $\mathbf{\Pi}_c$ is chosen at the BBU, this information is signaled to the RAU that scales the signal power to match the power constraint and maps back the symbols from the SF cable blocks to the corresponding antennas by performing an inverse permutation $\mathbf{x}_w^{\text{RAU}} = \gamma \mathbf{\Pi}_c^T \mathbf{y}_c$. Hence, the overall model describing the communication between RAU and BBU over cable is described by

$$\mathbf{x}_w^{\text{RAU}} = \gamma \mathbf{H}_{SF} \mathbf{x}_w^{\text{BBU}} + \gamma \mathbf{n}_c, \tag{8.12}$$

where $\mathbf{H}_{SF} = \mathbf{\Pi}_c^T \mathbf{H}_c \mathbf{\Pi}_c$ is the equivalent SF permuted cable channel, statistical properties of $\mathbf{n}_c$ are invariant for permutations so that $\mathbf{\Pi}_c^T \mathbf{n}_c \to \mathbf{n}_c$, and γ is the power scaling factor.

8.2.3. Power Constraints

Three different types of power constraints have to be *jointly* fulfilled in the considered hybrid wireless-wired MIMO AF system: *i)* a total power constraint at the RAU (8.3), *ii)* PLPC power constraints at the input of the cable channel (8.10) and *iii)* ATP constraint over each twisted-pair (8.11). Consistently with the assumption of unit mean power constellation symbols, we consider here a total power constraint at the RAU $P_w = N$ (i.e., unit mean power per transmitting antenna) as well as unit power PLPC constraints $P_c = 1$ at the cable input.

PSD optimization is beyond the scope of this work (we refer interest readers to [28] and references herein), but per-line ATP constraints are met here by properly choosing a transmit PSD value constant over all the lines/frequency bands (Sect. 8.5).

The RAU average power constraint is fulfilled by introducing the scaling factor γ in (8.12) such that it acts as a global gain scaling the power of the RAU transmit signal to meet the constraint. From (8.9) and (8.12), the constraint (8.3) can be re-framed as

$$\begin{aligned} \mathrm{E}\left[\left\|\mathbf{x}_w^{\mathrm{RAU}}\right\|_2^2\right] &= \mathrm{E}\left[\mathrm{tr}\left(\mathbf{x}_w^{\mathrm{RAU}}\mathbf{x}_w^{\mathrm{RAU},H}\right)\right] \\ &= \gamma^2 \mathrm{tr}(\mathbf{H}_{SF}\mathbf{F}\mathbf{F}^H\mathbf{H}_{SF}^H + \sigma_c^2\mathbf{I}) \leq N \end{aligned}, \tag{8.13}$$

and $\gamma = \gamma_{\max}$, where $\gamma_{\max}$ follows from the equality in (8.13).

To tackle the PLPC power constraints at the cable input, it is convenient to decompose the precoding operator $\mathbf{F}$ at the BBU as follows:

$$\mathbf{F} = \tilde{\mathbf{F}}\frac{1}{\beta}, \tag{8.14}$$

where $\tilde{\mathbf{F}}$ is the channel precoding matrix and β enforces the power constraints (8.10). This can be rewritten as

$$\begin{aligned} \mathrm{E}\left[\left|[\mathbf{x}_{c,f}]_j\right|^2\right] &= \frac{1}{\beta^2}\mathrm{E}\left[\left|\tilde{\mathbf{f}}_{fj}^T\mathbf{s}\right|^2\right] \\ &= \frac{1}{\beta^2}\left\|\tilde{\mathbf{f}}_{fj}^T\right\|_2^2 \leq 1, \quad f = 1,...,N_f,\ \forall j = 1,...,N_s \end{aligned}, \tag{8.15}$$

where $\tilde{\mathbf{f}}_{fj}^T$ is the row of the matrix $\tilde{\mathbf{F}}$ which precodes the signal to be relayed over the j-th twisted-pair of the f-th cable frequency band. From (8.15) it follows that the PLPC power constraints are fulfilled by choosing β as

$$\beta^2 = \left\|\tilde{\mathbf{F}}^T\right\|_{2,\infty}^2, \tag{8.16}$$

using the $(2,\infty)-$mixed norm, i.e., $\|\mathbf{A}\|_{2,\infty}$ denotes the maximum column l_2-norm of matrix $\mathbf{A}$.

8.3. Base Band Unit Precoding

In A-MIMO-RoC all the computationally complex digital signal processing is shifted to the BBU, which performs an overall (digital) precoding of the end-to-end wired-plus-wireless cascade channel from the BBU to all the intended UEs. Wireless and cable channels are assumed perfectly known at the BBU, as channel estimation techniques and precoder design under imperfect channel state information are beyond the scope of this work.

To describe this overall signal model, let us gather the received signals as

$$\mathbf{y} = \mathbf{H}_w \mathbf{x}_w^{\mathrm{RAU}} + \mathbf{n}_w, \tag{8.17}$$

where vector $\mathbf{y} = [y_1, y_2, ..., y_{N_r}]^T$ contains the signals received by all the N_r UEs, $\mathbf{H}_w = [\mathbf{h}_{w,1}, \mathbf{h}_{w,2}, ..., \mathbf{h}_{w,N_r}]^T \in \mathbb{C}^{N_r \times N}$ is the compound wireless channel matrix whose k-th row is the vector channel from the RAU to UE k-th, and $\mathbf{n}_w$ is the additive white Gaussian noise vector. Therefore, equation (8.17) becomes

$$\mathbf{y} = \mathbf{H}_\pi \mathbf{F}\mathbf{s} \cdot \gamma + \mathbf{n}, \tag{8.18}$$

where $\mathbf{H}_\pi = \mathbf{H}_w \mathbf{H}_{SF} \in \mathbb{C}^{N_r \times N}$ is the cascade of the permuted wired ($\mathbf{H}_{SF}$) and wireless ($\mathbf{H}_w$) channels with the sub-index π empathizing the dependence on the specific SF2SF multiplexing operator $\mathbf{\Pi}_c$, and vector $\mathbf{n} = [n_1, n_2, ..., n_{N_r}]^T$ collects the noise samples at all the receivers with $n_k \sim \mathcal{CN}\left(0, \gamma^2 \sigma_c^2 \left\|\mathbf{h}_{w,k}\right\|_2^2 + \sigma_w^2\right)$ denoting the noise at the k-th UE.

As BBU-side processing, in this chapter we consider Zero-Forcing (ZF) precoding which forces to zero all the interference among the N_r UEs. The precoding $\mathbf{F}$ is designed to fully diagonalize the compound wired-plus-wireless channel $\mathbf{H}_\pi$ to obtain an equivalent channel [67]

$$\mathbf{H}_e = \mathbf{H}_\pi \mathbf{F} = \mathrm{diag}(h_{e,1}, h_{e,2}, ..., h_{e,N_r}), \tag{8.19}$$

where here $h_{e,k}$ denotes the equivalent channel gain from the BBU to the k-th UE. This equivalent channel $h_{e,k}$ depends either on $\mathbf{F}$ and on the specific SF2SF multiplexing matrix $\mathbf{\Pi}_c$.

Directly from (8.18), it follows that for ZF precoding the decision variable at the k-th UE simplifies to

$$y_k = \gamma h_{e,k} s_k + n_k. \tag{8.20}$$

The corresponding UE rate r_k is conventionally computed as

$$r_k = \log_2 \left(1 + \frac{|h_{e,k}|^2}{\sigma_c^2 \left\|\mathbf{h}_{w,k}\right\|_2^2 + \sigma_w^2/\gamma^2}\right), \tag{8.21}$$

and the sum-rate for the whole UEs yields

$$R = \sum_{k=1}^{N_r} r_k. \tag{8.22}$$

In the following, both linear and non-linear ZF precoding approaches are reviewed and adapted to the A-MIMO-RoC scenario.

8.3.1. Linear Zero Forcing

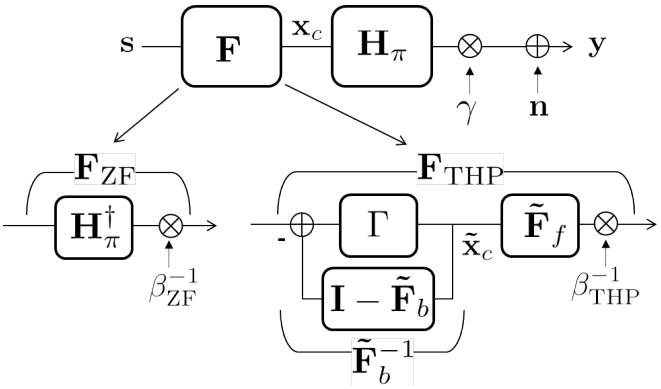

Figure 8.2.: BBU precoding schemes: linear Zero-Forcing (ZF) and Tomlinson-Harashima Precoding (THP)

In linear ZF the compound cascade of wired-plus-wireless channel $\mathbf{H}_\pi$ is compensated by the linear transformation

$$\tilde{\mathbf{F}}_{\mathrm{ZF}} = \mathbf{H}_\pi^\dagger, \tag{8.23}$$

where $\mathbf{A}^\dagger = \mathbf{A}^H \left(\mathbf{A}\mathbf{A}^H\right)^{-1}$denotes the right Moore–Penrose pseudo-inverse of matrix $\mathbf{A}$. It is easy to prove that the ZF condition (8.19) is satisfied and the equivalent channel matrix is

$$\mathbf{H}_{e,\mathrm{ZF}} = \mathbf{H}_\pi \mathbf{F}_{\mathrm{ZF}} = \frac{1}{\beta_{\mathrm{ZF}}} \mathbf{I}, \tag{8.24}$$

where β_{ZF} is computed by (8.16).

8.3.2. Tomlinson-Harashima Precoding

Linear ZF precoding usually suffers from a severe power increment due to the hard-inversion of the channel matrix. To overcome the problem, here we propose to

employ Tomlinson-Harashima Precoding (THP), which is a non-linear Successive Interference Cancellation (SIC) precoding scheme, conventionally based on ZF criterion [62]. The THP block scheme is depicted in Fig. 8.2, where the precoding matrix $\tilde{\mathbf{F}}$ is decomposed into two sub-matrices as

$$\tilde{\mathbf{F}}_{\text{THP}} = \tilde{\mathbf{F}}_f \tilde{\mathbf{F}}_b^{-1}, \tag{8.25}$$

where $\tilde{\mathbf{F}}_f \in \mathbb{C}^{N \times N_r}$ is a linear matrix with orthonormal columns, usually referred to as feed-forward filter, and $\tilde{\mathbf{F}}_b \in \mathbb{C}^{N_r \times N_r}$ is a lower-triangular matrix with units along the main diagonal, referred to as feed-back filter. The key characteristic which makes THP an attractive solution for applications with strict transmit power constraints is that the inversion of the triangular matrix $\tilde{\mathbf{F}}_b$ is performed by backward substitution together with a non-linear modulo operator Γ (see Fig. 8.2), which limits the power of the encoded symbols within the boundaries of the original signal constellation, hence avoiding the typical noise enhancement which is the main performance limitation of ZF-based techniques.

Feed-forward filter $\tilde{\mathbf{F}}_f$ and feedback filter $\tilde{\mathbf{F}}_b$ are obtained by the QR decomposition of the compound channel matrix $\mathbf{H}_\pi$ as [26]

$$\mathbf{H}_\pi{}^H = \mathbf{Q}\mathbf{R} = [\mathbf{Q}_1, \mathbf{Q}_2] \begin{bmatrix} \mathbf{R}_1 \\ \mathbf{0} \end{bmatrix}, \tag{8.26}$$

then

$$\tilde{\mathbf{F}}_f = \mathbf{Q}_1, \quad \tilde{\mathbf{F}}_b = \text{diag}(\mathbf{R}_1)^{-1} \mathbf{R}_1^H, \tag{8.27}$$

where $\mathbf{Q}_1 \in \mathbb{C}^{N \times N_r}$ contains the first N_r orthonormal columns of the unitary matrix $\mathbf{Q} \in \mathbb{C}^{N \times N}$, $\mathbf{R}_1 \in \mathbb{C}^{N_r \times N_r}$ is an upper triangular matrix and $\text{diag}(\mathbf{R}_1) \in \mathbb{C}^{N_r \times N_r}$ is a diagonal matrix that contains the main diagonal entries of $\mathbf{R}_1$. It is easy to show that the ZF condition (8.19) is satisfied and the equivalent channel matrix simplifies to

$$\mathbf{H}_{e,\text{THP}} = \mathbf{H}_\pi \mathbf{F}_{\text{THP}} = \text{diag}(\mathbf{R}_1)/\beta_{\text{THP}} \quad . \tag{8.28}$$

Remark 8.1. In THP, the encoded symbols $\tilde{\mathbf{x}}_c$ at the output of the modulo operator (see Fig. 8.2) show a power increment with respect to the input symbols as $\sigma_{\tilde{x}}^2 = \frac{M}{M-1}\sigma_s^2$, where M is the size of the M-QAM signal constellation. However, this terms becomes negligible for high modulation formats such as 256-QAM of LTE, hence it has been neglected here.

8.3.3. User Ordering Optimization

The UE signals encoding order in the SIC procedure of THP strongly impacts the performance for all the UEs [148]. Such ordering operation is described here by any possible row permutation of the compound wired-plus-wireless channel as

$\bar{\mathbf{H}}_\pi = \mathbf{\Pi}_w \mathbf{H}_\pi$, where $\mathbf{\Pi}_w \in \{0,1\}^{N_r \times N_r}$ is another permutation matrix (not to be confused with cable mapping $\mathbf{\Pi}_c$) which is used *prior* to the feedback filter to enforce the desired UE encoding order. Permutations $\mathbf{\Pi}_w$ should be carefully chosen in order to optimize the desired performance metric (e.g., system sum-rate or minimum user rate). However, an exhaustive search over all the possible $N!$ channel permutations is unpractical, especially for a large number of UEs. Instead, in this chapter we incorporate the computation of the UE ordering matrix $\mathbf{\Pi}_w$ in the QR procedure of THP with no additional computational complexity with respect to to conventional non-ordered (i.e., $\mathbf{\Pi}_w = \mathbf{I}$) THP. Ordering has no impact on the system sum-rate (see Appendix B.3), hence, we consider here the *minimum-rate maximization* heuristic ordering algorithm proposed in Chapter 2 for DSL systems (see Chapter 2, Sect. 2.3), denoted herein as *Worst First* (WF).

8.4. Downlink Space-Frequency to Space-Frequency Multiplexing Optimization

In this section, we detail the downlink SF2SF multiplexing optimization technique by starting with a simple single-UE downlink system, as it is useful to gain insights into the gain provided by the SF2SF technique alone without being affected by multi-user processing (FEXT mitigation or IL compensation). It is shown that the SF2SF problem for the single-UE multiple-input single-output case (SU-MISO) is equivalent the maximum Quadratic Assignment Problem (QAP), that is an NP-hard problem for which there is no known polynomial-time solving algorithm. Starting from these considerations, we adapt the efficient hill-climbing algorithm proposed for the A-MIMO-RoC uplink (see Chapter 7, Sect. 7.4.3) to the downlink SU-MISO SF2SF problem. The single-user MISO downlink hill-climbing algorithm is later extended to the multi-user case by jointly designing the SF2SF multiplexing matrix $\mathbf{\Pi}_c$, the precoding matrix $\mathbf{F}$ and the user ordering matrix $\mathbf{\Pi}_w$ for multi-user systems.

8.4.1. SF2SF Problem for SU-MISO System

The end-to-end capacity of the A-MIMO-RoC architecture is derived below for the SU-MISO case by setting the power scaling factors as $\gamma = \beta = 1$, as for the single-UE case all power constraints are satisfied. From (8.18), the single-UE received signal yields

$$y = \mathbf{h}^H \mathbf{f} s + n, \tag{8.29}$$

where $\mathbf{h}^H = \mathbf{h}_w^H \mathbf{H}_{SF}$ is the cascade of radio ($\mathbf{h}_w$) and cable ($\mathbf{H}_{SF} = \mathbf{\Pi}_c^T \mathbf{H}_c \mathbf{\Pi}_c$) channels, $\mathbf{f} = \mathbf{h} / \|\mathbf{h}\|$ is the conventional MISO beamforming for the overall Gaussian noise at the BBU $n \sim \mathcal{CN}(0, \sigma_n^2)$ with $\sigma_n^2 = \|\mathbf{h}_w\|_2^2 \sigma_c^2 + \sigma_w^2$.

The end-to-end capacity of the system for a certain radio channel realization $\mathbf{h}_w$ depends on the SF2SF mapping $\mathbf{\Pi}_c$ as

$$C(\mathbf{\Pi}_c) = \log_2 \left(1 + \left(\|\mathbf{h}_w\|_2^2 \sigma_c^2 + \sigma_w^2\right)^{-1} \cdot \Gamma(\mathbf{\Pi}_c)\right), \tag{8.30}$$

where

$$\Gamma(\mathbf{\Pi}_c) = \mathrm{tr}\left(\mathbf{\Pi}_c^T \mathbf{H}_c \mathbf{H}_c^H \mathbf{\Pi}_c \mathbf{h}_w \mathbf{h}_w^H\right) \tag{8.31}$$

is the signal power at the decision variable.

8.4.1.1. SF2SF Problem Formulation

For the SU-MISO case, we define the optimal SF2SF multiplexing as that specific permutation matrix $\mathbf{\Pi}_c$ that maximizes the single-UE end-to-end capacity $C(\mathbf{\Pi}_c)$ in (8.30), or equivalently $\Gamma(\mathbf{\Pi}_c)$ (8.31), leading to the following non-linear integer program:

$$\begin{aligned} \max_{\mathbf{\Pi}_c} \quad & \Gamma(\mathbf{\Pi}_c) \\ \text{s. t.} \quad & \sum_{n=1}^{N} p_{jf}^n = 1, \, \forall f = 1, ..., N_f, \, \forall j = 1, ..., N_s, \\ & \sum_{j=1}^{N_s} \sum_{f=1}^{N_f} p_{jf}^n = 1, \, \forall n = 1, ..., N, \\ & p_{jf}^n \in \{0, 1\} \, \forall f, j, n, \end{aligned} \tag{8.32}$$

where p_{jk}^n is the n-th entry of the row of matrix $\mathbf{\Pi}_c$ responsible for the signal mapping over the j-th pair at the f-th band as defined in Sect. 7.3, and the constraints ensure that each symbol is mapped onto only 1 SF channel and, symmetrically, each SF channel carries only 1 symbol (i.e., $\mathbf{\Pi}_c \in \mathcal{P}$, with $\mathcal{P}$ denoting the set of permutation matrices).

The downlink SF2SF problem (8.32) reduces to the maximum QAP, which is a combinatorial optimization problem proved to be NP-hard [149, 150]. Many linearization techniques have been proposed to turn the QAP into an Integer Linear Program (ILP) [149, 151], but these require the use of several auxiliary variables and constraints that make it difficult to efficiently get the solution, thus pushing us to explore for an heuristic algorithm shaped to SF2SF that (sub)optimally solves (8.32) at low computational-complexity.

8.4.1.2. An Hill-Climbing Approach to the SF2SF Problem

A sub-optimal solution to (8.32) can be found through an iterative local search with relatively low computational cost even when the number of RAU antennas N grows up to several tens. The (sub)optimal SF2SF multiplexing is computed here by using an hill-climbing approach, which is an heuristic iterative optimization technique adapted from artificial intelligence problems [139]. The hill climbing algorithm, first proposed for the A-MIMO-RoC SF2SF uplink problem (see Chapter 7, Sect. 7.4.3), is adapted in the following to the downlink SU-MISO case.

The hill-climbing procedure for the downlink SF2SF problem is based on the concept of *neighboring permutations*, which is recalled here: for an arbitrary permutation matrix $\mathbf{\Pi}_c$, univocally defined by a vector $\boldsymbol{\pi} = [\pi_1, \ldots, \pi_N]^T$ (see Chapter 7, Sect. 7.3), the set of all the neighboring permutations at a (integer) distance d_π is defined as the set of all vectors obtained permuting in any way all subsets of d_π elements in $\boldsymbol{\pi}$. The algorithm starts from an initial, randomly chosen, permutation $\boldsymbol{\pi}_0$ and updates the solution as follows: at the k-th step, all the neighbors $\{\boldsymbol{\pi}_{\text{near},k}\}$ at distance lower than or equal to d_π from the present solution $\boldsymbol{\pi}_{\text{best},k}$ are computed, together with the corresponding values of the the signal power at the decision variable $\Gamma(\boldsymbol{\pi})$. The best neighbor, i.e., $\boldsymbol{\pi}^{\text{best}}_{\text{near},k} = \arg\max_{\pi} \Gamma(\boldsymbol{\pi}_{\text{near},k})$, is obtained and compared to $\boldsymbol{\pi}_{\text{best},k}$ in terms of associated signal power before being updated to $\boldsymbol{\pi}_{\text{best},k+1} = \boldsymbol{\pi}^{\text{best}}_{\text{near},k}$ and another iteration is performed, otherwise the final solution is $\boldsymbol{\pi}_{\text{best},k}$. The total number of iterations N_{it} needed to reach the solution depends both on the radio SNR $1/\sigma_w^2$ and on the number of RAU antennas N, but it cannot be known in advance and needs to be evaluated numerically. The hill-climbing algorithm is clearly sub-optimal as it selects as solution the first local maximum of the objective but it can be updated to the change of $\mathbf{H}_w$, and degradation with respect to exact solution of (8.32) is negligible (Sect. 8.5).

8.4.2. SF2SF Problem for MU-MISO System

For the multi-user MISO (MU-MISO) scenario considered in this section, two different SF2SF optimization problems are exploited: *i) sum-rate maximization* problem maximizing the overall system performance as

$$\max_{\mathbf{\Pi}_c \in \mathcal{P}} \quad R(\mathbf{\Pi}_c) = \sum_{k=1}^{Nr} r_k(\mathbf{\Pi}_c), \tag{8.33}$$

where r_k is the rate for the k-th UE as defined in (8.21); *ii) min-rate maximization* problem maximizing the minimum rate among the UEs defined as

$$\max_{\mathbf{\Pi}_c \in \mathcal{P}} \quad \min_k r_k(\mathbf{\Pi}_c) \quad . \tag{8.34}$$

As for the SU-MISO case, both the MU-MISO min-rate maximization (8.34) and max-rate maximization (8.33) SF2SF optimization problems are NP-hard. For the

special case of $N = N_r$ (i.e., the number of UEs N_r equals the number of antennas N) under THP design, this can be proved to follow similar steps as for SU-MISO systems (Sect. 8.4.1). However, in the general $N \geq N_r$ case, in MU-MISO scenario it is fairly complicated to derive analytically tractable expressions for the UE rate $r_k(\mathbf{\Pi}_c)$ and the sum-rate $R(\mathbf{\Pi}_c)$ due to the fact that both the scalar gains β and γ depend on the SF2SF mapping $\mathbf{\Pi}_c$. Hence, MU-MISO considered here is for $N = N_r$ to provide the reader with an intuitive insight of the overall problem. In any case, the system design does not depend in any way by this assumption and it can be straightforwardly extended to the general $N \geq N_r$ case.

Problems (8.33) and (8.34) can be optimally solved only by an exhaustive search over all the possible $N!$ permutations of the cable channel matrix $\mathbf{H}_c$, which is unpractical when the number of RAU antennas grows large (i.e., $N \gg 10$). As a low-complexity heuristic solution to the problem, we again adopt the hill-climbing approach, which can be generalized to the MU-MISO case by making just minor adjustments to the algorithm described in Sect. 8.4.1.2. The generalized hill-climbing algorithm is reported in Algorithm 8.1, where the precoding matrix $\tilde{\mathbf{F}}$ be designed following both the linear ZF (Sect. 8.3.1) or the THP (either ordered or not, Sect. 8.3.2) criteria, and the objective function $f(\boldsymbol{\pi})$ can be either the minimum user rate in (8.34) or the sum-rate in (8.33). Recall that UEs permutations $\mathbf{\Pi}_w$ is accounted separately.

Algorithm 8.1 Generalized hill-climbing algorithm for (sub)optimal SF2SF mapping

1. Input: wireless channel $\mathbf{H}_w$, cable reference channel $\mathbf{H}_c$, max. neighbor distance d_π;
2. Initialize $\boldsymbol{\pi}_0$ and compute $\tilde{\mathbf{F}}$, β, g and $f(\boldsymbol{\pi}_0)$;
3. **while** $f(\boldsymbol{\pi}_{\text{best},k}) > f(\boldsymbol{\pi}_{\text{best},k-1})$
   a) compute neighboring permutations $\{\boldsymbol{\pi}_{\text{near},k}\}$ at distance $d \leq d_\pi$ from $\boldsymbol{\pi}_{\text{best},k-1}$;
   b) $\boldsymbol{\pi}_{\text{best},k} = \arg\max_{\pi} f(\boldsymbol{\pi}_{\text{near},k})$;
4. **end while**
5. Output: $\boldsymbol{\pi}_{\text{best},k-1}$.

8.4.3. Hill-Climbing Computational Complexity for Downlink SF2SF

The computational complexity of the hill-climbing solution to the downlink SU/MU-MISO SF2SF problem is the same as for the A-MIMO-RoC uplink (Chapter 7,

Sect.), which is recalled here for completeness. Notice that, for each of the N_{it} hill-climbing iterations, an exhaustive search over all the neighboring permutations must be performed according to the neighboring distance d_π. Hence, the computational complexity of the hill-climbing algorithm needs to account for the cardinality of the neighboring permutations set K_{d_π} , which is defined as

$$K_{d_\pi} = \sum_{n=2}^{d_\pi} \binom{N}{n} \cdot !n, \tag{8.35}$$

where $!n = n! \cdot \sum_{i=0}^{n} \frac{(-1)^i}{n!}$ is known as *derangement number* or *de Montmort number*, which is defined as the number of permutations of the elements of a set, such that no element appears in its original position (details can be found in Appendix A.2). The overall computational complexity is thus computed as

$$K = K_{d_\pi} \cdot N_{\text{it}}. \tag{8.36}$$

Notice that Eq. (8.36) must be multiplied by $N!$ if another exhaustive search is performed to find the optimal UE ordering matrix $\mathbf{\Pi}_w$ in Sect. 8.3.3.

8.5. Numerical Results

Technique	Radio SNR, $1/\sigma_w^2$ [dB]						Complexity (K) at $1/\sigma_w^2 = 25$ dB
	5	10	15	20	25	30	
SF2SF: optimal (exh. search)	0.007	0.023	0.068	0.207	0.541	1.245	40320
SF2SF: hill-climb., $d_\pi = 4$	0.007	0.022	0.066	0.206	0.540	1.244	1148 ($N_{it} = 1.49$)
SF2SF: hill-climb., $d_\pi = 2$	0.006	0.020	0.060	0.195	0.530	1.234	39 ($N_{it} = 1.38$)
w/o SF2SF	0.005	0.015	0.046	0.141	0.382	0.933	-

Table 8.1.: SU-MISO rates [bps/Hz]: optimal vs hill-climbing by varying neighboring distance d_π, $N = 8$ RAU antennas, $N_s = 2$ frequency bands at 300 and 500 MHz

To validate and prove the effectiveness of the proposed downlink A-MIMO-RoC architecture based on LAN cables, here we perform numerical evaluation based on cable channel measurements from the IEEE 802.3 Ethernet Working Group [152]. The cable is a 4-pairs Cat-6 cable with length 100 m as this is conventionally used as reference distance, the bandwidth/pair is ≈ 500 MHz, and FH link uses typical parameters such as -140 dBm/Hz noise floor PSD and -80 dBm/Hz/pair transmit PSD, which meets the 8dBm cable per-line ATP constraint [35] in (8.11) even if the whole 500 MHz cable bandwidth is employed. Otherwise explicitly stated, the radio channel toward each UE is the one in (8.4), and it is assumed to have $L = 3$ paths for all the UEs, while, per each radio channel, the azimuths AoDs $\phi_{k,l}$ and the elevation AoDs $\theta_{k,l}$ at the RAU have been assumed uniformly random

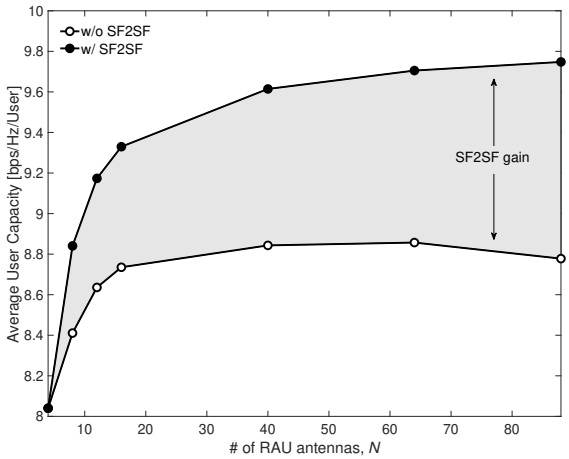

Figure 8.3.: SF2SF gain in SU-MISO: average user rate vs number of RAU antennas N ($\approx N \cdot 22$ MHz bandwidth), $1/\sigma_w^2 = 25$ dB

distributed as $\phi_{k,l} \sim \mathcal{U}(0, 2\pi)$ and $\theta_{k,l} \sim \mathcal{U}(-\pi/4, \pi/4)$ for indoor multi-path. The performance are evaluated in terms of user rate averaged over 1000 radio channel realizations. We assume that the frequency division over the cable is made by bands of $B_w = 22$ MHz, corresponding to the bandwidth of the considered RF signals (according to recent measurements on indoor deployments, it is reasonable to assume the wireless channel as frequency-flat within this range [153, 154]), and the cable channel is approximately frequency-flat within each 22-MHz band (if necessary, OFDM structure of wireless link can be used to resume this assumption without any relevant changes to the analysis and final results). Since cable is not flat, for the sake of numerical analysis, we consider the IL and FEXT coefficients of the k-th matrix $\mathbf{H}_{c,k}$ in (8.7) as the mean of the channel measurements over the k-th frequency band (see Chapter 6 for further details). Unless otherwise explicitly stated, it is assumed in the following that to serve N antennas at the RAU, the first $N_f = N/N_s$ 22-MHz frequency bands are allocated over the cable (i.e., the channels are allocated by increasing level of IL and FEXT), and all the $N_s = 4$ twisted-pair spatial channels are always used. To make a practical example, a total bandwidth of approx. $5 \cdot 22 = 110$ MHz is needed over the 4-pairs to transport the signal for $N = 20$ RAU antennas by 22 MHz/ea. A maximum number of antennas $N = 88$ is considered here, corresponding approx. to the usage of the whole 500 MHz bandwidth over the copper cable. Numerical results for the SU-MISO case are presented in Section 8.5.1, while in Section 8.5.2 the MU-MISO scenario is considered.

8.5.1. SU-MISO with SF2SF

In this section, we make a few considerations about the SU-MISO case. First of all, in Table 8.1 the rate obtained by optimally and heuristically solving the SF2SF multiplexing problem are compared by varying the neighboring distance d_π, together with the computational complexity for a radio SNR $1/\sigma_w^2 = 25$ dB (used in the following as reference radio SNR). The parameter N_{it}, evaluated numerically, is the average number of hill-climbing iterations needed to reach the solution. The $N!$ computational complexity of the optimal solution forces us to consider here a relatively small problem instance: $N = 8$ RAU antennas relay to the user the BBU signals carried over $N_f = 2$ cable bands at 300MHz and 500MHz, to stress a condition where IL and FEXT are more severe (see Chapter 6). Table 8.1 confirms that the hill-climbing approach leads to a solution which is quite close to the optimal one at much lower complexity: e.g., for $1/\sigma_w^2 = 25$ dB and $d_\pi = 2$ (used as reference neighboring distance for all the following numerical evaluations) the gap from the optimum is ≈ 0.01 bps/Hz, and this is achieved by performing only $K = 39$ out of the total $K_{\text{exh}} = 40320$ searches required by the exhaustive search.

In Fig. 8.3 the average UE rates with and without SF2SF multiplexing (filled and empty markers, respectively) are shown by progressively increasing the number of antennas N (i.e., increasing the portion of allocated cable bandwidth) for a fixed radio SNR $1/\sigma_w^2 = 25$ dB. It is interesting to observe that the UE rate achieved without any mapping starts to decrease when reaching approx. $N = 40$ RAU antennas (≈ 220 MHz cable bandwidth): in fact, in order to serve a greater number of antennas, a higher frequency portion of the cable bandwidth should be allocated for which IL and FEXT are so severe that any improvement in the SINR at the decision variable becomes negligible. In other words, there is no point in using more antennas if cable excessively degrades the wireless rate and antennas are almost randomly multiplexed over the cable resources. On the contrary, the UE rate achieved with SF2SF multiplexing increases with the number of antennas/cable bandwidth. This confirms that, by means of an optimized cable resources management, SF2SF is capable to cope with the cable impairments enabling the usage of the available cable bandwidth and improving the user rate by more then 1 bps/Hz. This can be explained by the fact that signal quality at the UE is mostly determined by a small subset of RAU antennas, which is not known in advance and depends on the specific UE configuration. SF2SF multiplexing technique selects and prioritizes those antennas by assigning them SF cable channels for which cable impairments are less severe, thus creating virtual sub-arrays at the RAU that are minimally cable interfered. Others are progressively assigned to cable SF resources.

8.5.1.1. SU-MISO with SF2SF in Sub-6GHz Scenario

For completeness, a similar result is presented in Fig. 8.5, in which the downlink SF2SF techniques has been tested also for a sub-6GHz downlink system. In particular, it is assumed that the single-user radio channel $\mathbf{h}_w$ in (8.4) is modeled as Rayleigh faded, i.e., $\mathbf{h}_{w,k} \sim \mathcal{CN}(\mathbf{0}, \mathbf{R}_t)$, with correlation between i-th and j-th elements given by $[\mathbf{R}_t]_{ij} = \rho^{|i-j|}$, with $0 < \rho < 1$. Numerical results are shown in Fig. 8.5 in terms of average (over radio channel realizations) UE rate and assuming an array correlation across antennas $\rho = 0.95$. Moreover, the wireless channel bandwidth is assumed to be $B_a = 540\,\text{kHz}$ (e.g., this can be seen as a group of 3 LTE resource blocks, or even a single 5G carrier). Accordingly, the FDM over the cable is by B_a-bands.

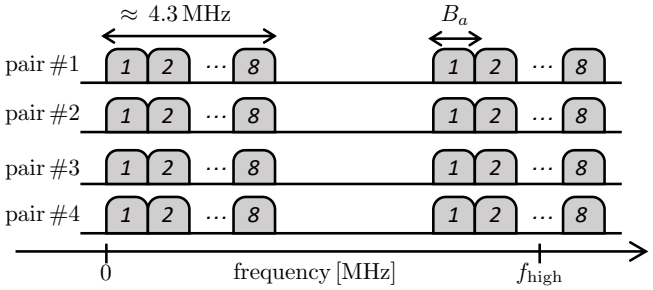

Figure 8.4.: Cable frequency bands utilized for FH

For the results in Fig. 8.5, it is assumed that $N = 64$ RAU antennas, each carrying a B_w-bandwidth channel, relay to the UE the signals transported over $N_c = 64$ SF cable channels. As shown in Fig. 8.4, we assume that half of the N channels are transported over low cable frequency (i.e., $N/2$ signals are mapped over the first $32/N_s = 8$ B_a-bands of the 4-pairs LAN cable, corresponding to approx. 4.3 MHz), while the remaining $N/2$ are transported over an higher cable frequency portion centered around f_{high} (this resembles the situation where due to the coexistence with other services it may be convenient to allocate the FH signal over higher frequency cable bands). For each f_{high}, the SF2SF algorithm looks for the optimal multiplexing of the N radio signals over the overall N SF channels (both at low and high cable frequencies). Fig. 8.5 shows how performance without SF2SF multiplexing (i.e., $\mathbf{\Pi}_c = \mathbf{I}$) quickly degrade by progressively increasing such f_{high}, until they converge to those achieved be employing only $N/2$ antennas allocated at low cable frequency (recall that the RAU is constrained to unit power for all the simulation settings). As observed in Fig. 8.3, this is suggesting that there is no point in using more antennas if cable excessively degrades the wireless rate and antennas are almost randomly multiplexed over the cable resources. The effect of SF2SF multiplexing is almost negligible for low f_{high}, while the gain becomes apparent by increasing it, and thus by employing frequency bands for which cable impairments are more severe (see Chapter 6). Concluding, Fig. 8.5 confirms the

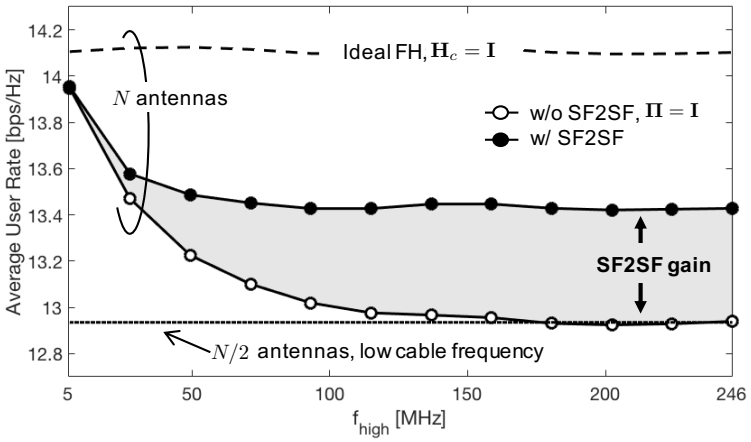

Figure 8.5.: SF2SF average UE-rate vs f_{high} for $N = 64$ RAN antennas and for radio SNR $1/\sigma_w^2$=25 dB

benefits of SF2SF technique also in a sub-6GHz scenario: by leveraging on a more efficient exploitation of the cable resources, SF2SF multiplexing almost halves the performance gap from the ideal FH (i.e., $\mathbf{H}_c = \mathbf{I}$).

8.5.2. MU-MISO with SF2SF

Technique	Radio SNR, $1/\sigma_w^2$ [dB]						Complexity (K) at $1/\sigma_w^2 = 25$ dB
	5	10	15	20	25	30	
SF2SF: optimal (exh. search)	0.361	0.693	1.014	1.281	1.312	1.335	40320
SF2SF: hill-climb., $d_\pi = 4$	0.355	0.689	1.008	1.274	1.307	1.329	1547 ($N_{it} = 2.01$)
SF2SF: hill-climb., $d_\pi = 2$	0.321	0.652	0.976	1.225	1.255	1.266	64 ($N_{it} = 2.27$)
w/o SF2SF	0.202	0.402	0.624	0.790	0.799	0.802	-

Table 8.2.: MU-MISO rates [bps/Hz] with non-ordered THP, max min-rate optimal solution vs hill-climbing by varying the neighboring distance d_π, $N = 8$ RAU antennas, $N_s = 2$ frequency bands at 300 and 500 MHz. Rates are in [bps/Hz]

The performance of the A-MIMO-RoC architecture are evaluated here in presence of multiple single-antenna UEs, which mandatorily requires BBU precoding to mitigate the multi-user interference due to the cascade of wired and wireless channels. In this scenario, we assume that the number of served UEs N_r equals the number of RAU antennas N, meaning that the more RAU antennas we employ, the more UEs we are able to serve but, from the other hand, the more bandwidth we need to allocate over the cable fronthaul (i.e., $N = N_r = N_s \cdot N_f$, with $N_s = 4$).

Type of SF2SF optimization	Type of UE ordering optimization	Radio SNR, $1/\sigma_w^2$ [dB]						Complexity (K) at $1/\sigma_w^2 = 25$ dB
		5	10	15	20	25	30	
optimal (exh. search)	optimal (exh. search)	0.856	1.462	2.053	2.376	2.600	2.620	518400
hill-climbing, $d_\pi = 2$	optimal (exh. search)	0.852	1.458	2.048	2.371	2.597	2.601	23760 ($N_{it} = 2.2$)
optimal (exh. search)	WF ordering	0.821	1.389	1.917	2.118	2.304	2.311	720
hill-climbing, $d_\pi = 2$	WF ordering	0.784	1.346	1.865	2.059	2.236	2.241	32 ($N_{it} = 2.15$)
no	no	0.189	0.494	0.766	0.987	1.118	1.148	-

Table 8.3.: MU-MISO rates [bps/Hz] with ordered THP, max min-rate optimal solution/ordering vs heuristics, $N = 6$ RAU antennas, $N_s = 2$ frequency bands at 300 and 500 MHz. Rates are in [bps/Hz]

As for the SU-MISO case, we first demonstrate that also in the MU-MISO scenario the performance obtained by the hill-climbing approach attain the optimal achieved by the $N!$ exhaustive search. This is shown in Table 8.2 for the *min-rate maximization* SF2SF problem with non-ordered THP precoding, and assuming to employ $N = 8$ RAU antennas forwarding to the UEs the BBU signals coming from $N_f = 2$ cable frequency bands allocated similarly as SU-MISO at 300 MHz and 500 MHz (reduced problem size due to the complexity of the optimal solution). THP makes the rates larger then Table 8.1.

A similar result is in Table 8.3, which shows the user rates obtained by *jointly* solving both the *min-rate maximization* SF2SF and the *min-rate maximization* UE ordering problems. In particular, Table. 8.3 compares *i)* the rates obtained by optimally solving *both* problems (i.e., by an exhaustive search over all the $N!$ possible SF2SF permutations $\mathbf{\Pi}_c$ combined with all the $N!$ UE ordering permutations $\mathbf{\Pi}_w$), *ii)* the rates obtained by the fully heuristic solution (i.e., hill-climbing algorithm plus WF UE ordering), and *iii)* the rates obtained by the two hybrid optimal-heuristic solutions (i.e., exhaustive search for SF2SF plus WF ordering and, vice versa, hill-climbing plus exhaustive search for UE ordering). Due to the $(N!)^2$ searches required by the optimal solution, only $N = 6$ antennas have been employed here to relay to the UEs the BBU signals carried over only $N_s = 3$ out of the 4 pairs (one pair for other services) and $N_f = 2$ cable bands allocated over the cable at 300 MHz and 500 MHz. Table 8.3 shows that the fully heuristic solution achieves a good trade-off between performance and computational complexity: the loss with respect to the optimum amounts to less then ≈ 0.4 bps/Hz, while the computational complexity is reduced by 4 orders of magnitude. It is worth noting also the nearly-optimal performance achieved by the combination of hill-climbing algorithm and optimal UE user ordering, which, however, is still prohibitive from a computational cost perspective.

The mean UE rate versus $1/\sigma_w^2$ is shown in Fig. 8.6 for linear ZF precoding (solid lines) and non-ordered THP (dashed lines), with and without *sum-rate maximization* SF2SF mapping (circle marker and cross-marker, respectively), and for $N = 24$ RAU antennas. Beside the expected superior performance of THP with respect to linear ZF, it is worth noting that, for linear ZF, even if SF2SF mul-

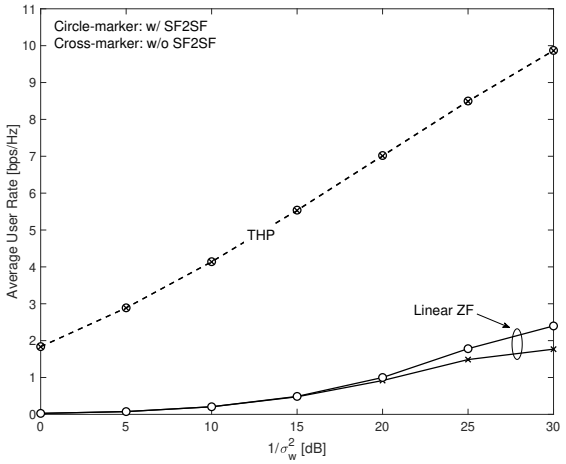

Figure 8.6.: Mean user rate vs $1\backslash\sigma_w^2$ for and $N = 24$ RAU antennas: linear ZF versus THP w/ and w/o sum-rate maximization SF2SF mapping

Technique	**Number of RAU antennas (N)**							
	4	**8**	**16**	**32**	**40**	**56**	**72**	**88**
SF2SF: optimal (exh. search)	24	40320	$\approx 10^{13}$	$\approx 10^{35}$	$\approx 10^{47}$	$\approx 10^{74}$	$\approx 10^{103}$	$\approx 10^{134}$
SF2SF: hill-climb., $d_\pi = 2$, no ordering	6 ($N_{it} = 1$)	70 ($N_{it} = 2.51$)	451 ($N_{it} = 3.76$)	$2.21 \cdot 10^3$ ($N_{it} = 4.46$)	$3 \cdot 10^3$ ($N_{it} = 3.95$)	$2.63 \cdot 10^3$ ($N_{it} = 1.71$)	$2.58 \cdot 10^3$ ($N_{it} = 1.01$)	$3.83 \cdot 10^3$ ($N_{it} = 1$)
SF2SF: hill-climb., $d_\pi = 2$, WF ordering	6 ($N_{it} = 1$)	67 ($N_{it} = 2.38$)	409 ($N_{it} = 3.41$)	$2.16 \cdot 10^3$ ($N_{it} = 4.35$)	$3.77 \cdot 10^3$ ($N_{it} = 4.84$)	$8.07 \cdot 10^3$ ($N_{it} = 5.24$)	$1.13 \cdot 10^4$ ($N_{it} = 4.41$)	$7.5 \cdot 10^3$ ($N_{it} = 1.96$)

Table 8.4.: MU-MISO for $1/\sigma_w^2 = 25$ dB: computational complexity for THP max-min rate SF2SF multiplexing w/ and w/o WF user ordering

tiplexing improves the mean user rate by almost 33%, the performance achieved for the considered scenario are very poor, i.e., slightly more then 2 bps/Hz can be achieved for $1/\sigma_w^2 = 25\,\text{dB}$ (taken as reference wireless SNR). As expected (see Appendix B.3), the impact of SF2SF on the mean user rate of THP is almost indiscernible, which is the reason why in this chapter the *min-rate maximization* criterion is preferred to the *sum-rate maximization* one. The performance of THP are shown in Fig. 8.7 with and without SF2SF multiplexing (filled and empty markers, respectively), with and without WF user ordering (solid and dashed lines, respectively), and for $N = 24$ RAU antennas. Again, the impact of both SF2SF multiplexing and WF user ordering on the mean UE rate is negligible, and all methods converge to the same rate as SNR increases. However, the minimum rate per UE around $1/\sigma_w^2 = 25\,\text{dB}$ is improved by 0.5 bps/Hz in the case of SF2SF alone (square marker) and by more then 3 bps/Hz in the case of WF-ordered THP (circle marker), while the gain with respect to conventional THP raises up to ≈ 5

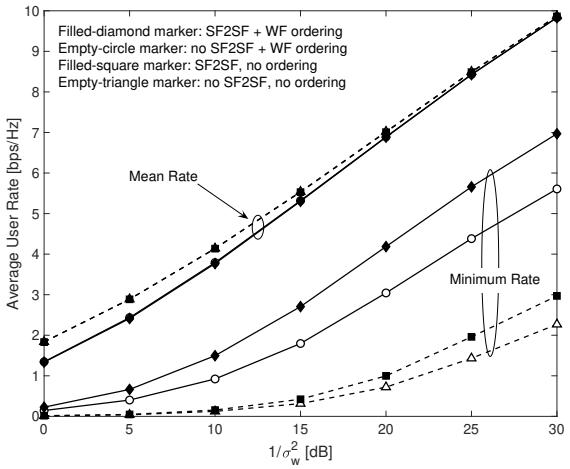

Figure 8.7.: User rate vs $1/\sigma_w^2$ for $N = 24$ RAU antennas: comparison between WF ordered and non-ordered THP w/ and w/o min-rate maximization SF2SF multiplexing

bps/Hz when the two techniques are combined together (diamond marker).

The impact of SF2SF multiplexing on the performance of THP-based techniques is shown in Fig. 8.8 for $1/\sigma_w^2 = 25$ dB by increasing the number of served users N_r, and, consequently, by increasing both the number of RAU antennas N and the allocated cable bandwidth. It follows from Fig. 8.8 that the achieved mean user rate (equal for all methods) is slightly more then 6 bps/Hz when serving all the $N_r = 88$ users. Non-ordered THP with SF2SF (dotted-lines, cross-maker) achieves exactly the same maximum rate of conventional THP (solid line) still improving the minimum. Again, the utmost gain in terms of minimum UE rate is achieved when SF2SF is combined with WF user ordering (dashed-line, circle marker), which is able to provide 7 bps/Hz up to approx. $N_r = 30$ UEs, while at least 6 bps/Hz and 4 bps/Hz are guaranteed for $N_r = 40$ and $N_r = 56$ UEs, respectively. The minimum UE rate drops down to less then 2 bps/Hz only approaching the $N_r = 70$ served UEs. The computational complexity required by the hill-climbing algorithms for the exact same settings of Fig. 8.8 is reported in Table 8.4 by showing how it scales with the number of RAU antennas.

In Fig. 8.9, it is shown the comparison between THP with WF ordering and SF2SF multiplexing, which is the best-performing among the proposed methods (filled markers), and the optimum *SVD Relay* scheme proposed by Chae *et al.* in [146] (empty markers) for multi-user AF MIMO relay systems. The *SVD Relay* is a particular meaningful benchmark for our systems since it combines THP processing at the BBU, singular-value-decomposition (SVD) processing at the RAU and UE ordering. The main difference from our proposed architecture is that in [146]

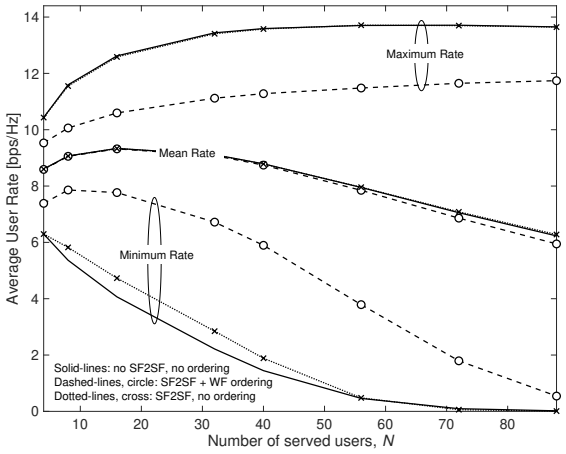

Figure 8.8.: MU-MISO for $1/\sigma_w^2 = 25$ dB: average user rates vs RAU antennas N, comparison of THP techniques w/ and w/o WF user ordering and w/ and w/o max-min rate SF2SF

the RAU (i.e., the fixed relay node) is equipped with linear processing capability and it performs MIMO precoding/equalization, while for A-MIMO-RoC all the processing is completely moved to the BBU-side leaving the all-analog RAU with the only tasks to scale and up-convert the signals to the proper frequency bands and antennas. Since the *SVD Relay* is designed following a sum-rate maximization criterion while the proposed heuristic solves a min-rate maximization problem, it is necessary to compare on the same basis also the minimum and the maximum rates achieved by the two techniques. Fig. 8.9 shows the gain achieved by the proposed technique in terms of minimum user rate with respect to the scheme in [146], which is more pronounced for a lower number of UEs (say < 40), while it reduces to few bps/Hz approaching the 88 UEs. As expected, however, there is a price to pay in terms of mean and maximum user rate for achieving such a minimum user rate and for avoiding any signal processing at the RAU: this amounts to approx. 2 bps/Hz and 4 bps/Hz (for $N_r = 88$ users) in mean and maximum user rates, respectively.

8.6. Concluding Remarks

This chapter investigated the downlink of the Analog MIMO Radio-over-Copper (A-MIMO-RoC) architecture, in which the overall channel from the BaseBand Unit (BBU) to the end-users is made by the cascade of a MIMO cable and a MIMO radio channels. The focus here is on the mapping between air- and cable-link resources, referred to as Space-Frequency to Space-Frequency (SF2SF) multiplexing.

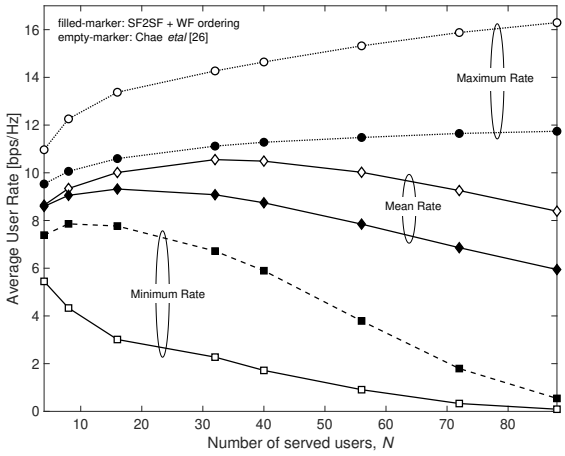

Figure 8.9.: MU-MISO for $1/\sigma_w^2 = 25$ dB: average user rates vs RAU antennas N, comparison between WF-THP + SF2SF and *SVD Relay* [146]

In particular, the chapter demonstrated that, in case of multiple-users served in the same physical resources, a joint optimization of SF2SF multiplexing, digital-precoding at the BBU and user ordering allows to cope with cable impairments providing substantial performance gains in terms of minimum rate guaranteed for all the users. Numerical results also showed that the proposed architecture fairly compares with existing amplify-and-forward design techniques achieving an interesting trade-off between performance and overall system complexity, which confirms the potential of A-MIMO-RoC as an attractive solution for 5G indoor fronthaul applications.

9. Analog MIMO RoC in Heterogeneous 5G Network

9.1. Introduction

ACCOMMODATING the heterogeneity of users' requirements is one of the main challenges that both industry and academia are facing in order to make 5G a reality [155]. In fact, next-generation wireless communication systems must be designed to provision different services, each of which with distinct constraints in terms of latency, reliability, and information rate. In particular, 5G is expected to support three different macro-categories of services, namely enhanced Mobile BroadBand (eMBB), massive Machine-Type Communications (mMTC), and Ultra-Reliable and Low-Latency Communications (URLLC) [156, 157, 158].

eMBB service is meant to provide very-high data-rate communications as compared with current (4G) networks. This can be generally achieved by using codewords that spread over a large number of time-frequency resources, given that latency is not an issue. mMTC supports low-rate bursty communication between a massive number of uncoordinated devices and the network. Finally, URLLC is designed to ensure low-rate ultra-reliable radio access for a few nodes, while guaranteeing very low-latency. As a result, URLLC transmissions need to be localized in time, and hence URLLC packets should be short [159].

The coexistence among eMBB, mMTC and URLLC traffic types can be ensured by slicing the Radio Access Network (RAN) resources into non-overlapping, or orthogonal, blocks, and by assigning distinct resources to different services. With the resulting Orthogonal Multiple Access (OMA), the target quality-of-service guarantees can be achieved by designing each service separately [160, 161]. However, when URLLC or mMTC traffic types are characterized by short and bursty transmissions at random time instants, resources allocated statically to these services are likely to be unused for most of time, and thus wasted. A more efficient utilization of radio resources can be accomplished by Non-Orthogonal Multiple Access (or NOMA), which allows multiple services to share the same physical resources.

By enabling an opportunistic shared use of the radio resources, NOMA can provide significant benefits in terms of spectrum efficiency, but it also poses the challenge of designing the system so that the heterogeneous requirements of the services are satisfied despite the mutual interference. The objective of this chapter is to

address this issue by considering a Cloud-RAN (C-RAN) architecture characterized by analog fronthaul links. Although the main focus is on the Analog MIMO Radio-over-Copper (A-MIMO-RoC) architecture object of this thesis, the analysis naturally extends to other analog fronthauling architectures, more generally referred to as Analog Radio-over-X.

9.1.1. C-RAN based on Analog Radio-over-X Fronthauling

C-RAN is widely considered as one of then enabling technologies for future 5G networks, as it allows for centralized signal processing, provides network scalability, increases spectral efficiency, and reduces costs. C-RAN architectures currently deployed in 4G networks rely on digital optical fronthaul links to connect colocated BaseBand Units (BBUs) to geographically distributed Remote Antenna Units (RAUs), also referred to as Edge Nodes (ENs). This solution, known as Digital Radio-over-Fiber (D-RoF), is based on the transmission of in-phase and quadrature baseband signals, upon digitization and packetization according to the CPRI protocol [7].

Over the last years, several alternative C-RAN architectures have been proposed that redistribute the RAN functionalities between BBU and ENs, obtaining different trade-offs in terms of bandwidth and latency requirements, advanced Cooperative Multi-Point processing capabilities, and EN cost and complexity [9]. In this context, as discussed in the previous chapters, for scenarios with stringent cost and latency constraints, a promising solution is to use analog fronthauling links between ENs and BBUs. Once again, C-RAN with analog fronthauling has the inherent advantages of avoiding any bandwidth expansion due to digitization, guaranteeing ENs synchronization, minimizing latency, reducing hardware cost, and improving energy efficiency [12, 132, 30].

Beside the A-MIMO-RoC architecture based on LAN cables, which is the focus of this thesis, other analog C-RAN architectures based on different fronthaul technologies have been proposed. Examples are C-RAN with analog fronthauling based on fiber links (i.e., A-RoF [12]) or with analog fronthauling based on high capacity radio links (i.e., A-RoR [15]). A summary of C-RAN architectures with analog fronthauling is depicted in Fig. 9.1. Each analog C-RAN architecture is better suited for a particular scenario, depending on the bandwidth, latency, and cost requirements demanded by the specific application.

In particular, A-RoF provides an effective example of analog fronthauling, due to its capability to support the transport of large bandwidths [12, 13]. However, A-RoF requires the deployment of a fiber optic infrastructure whose installation is not always feasible, e.g., in dense urban areas. In such scenarios, a possible solution is to rely on the A-RoR concept, thus employing point-to-point wireless links, mainly based on mmWave or THz bands, with several advantages in terms of flexibility, resiliency, hardware complexity and cost [15, 162]. Another application scenario where the installation of fiber links may be too expensive to provide satisfactory

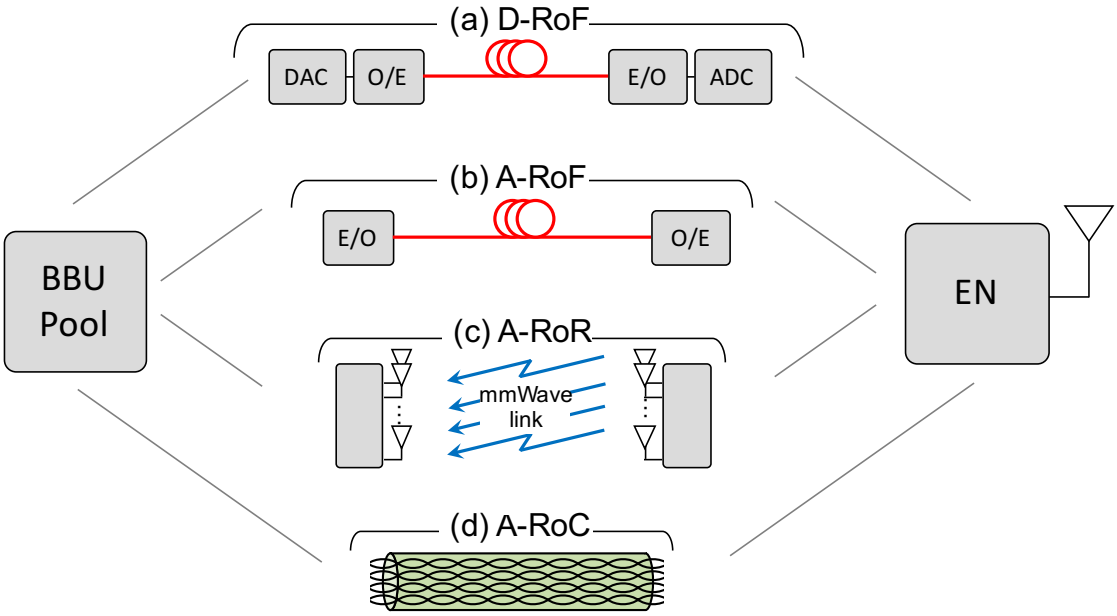

Figure 9.1.: C-RAN architecture overview for uplink direction: (a) Digital Radio-over-Fiber, (b) Analog Radio-over-Fiber, (c) Analog Radio-over-Radio, (d) Analog Radio-over-Copper.

business cases is indoor coverage. For this last case, as discussed, A-MIMO-RoC is a particularly attractive solution, since it leverages the pre-existing LAN cabling infrastructure of building and enterprises. Moreover, as shown in Chapter 6, LAN cables are equipped with four twisted-pairs with a transport capability up to 500 MHz each, or 2 GHz overall, for radio signals, thus providing enough bandwidth for analog fronthaul applications.

In this chapter, by using information theoretical tools, we study the coexistence of URLLC and eMBB services under both OMA and NOMA assuming an analog C-RAN multi-cell architecture based on the A-MIMO-RoC paradigm (see Fig. 9.1).

9.1.2. Related Works

The concept of Non-Orthogonal Multiple Access (NOMA) is well-known from the information theoretic literature [163], and its application to 5G dates back to [164], where authors demonstrated for a single-cell scenario that superimposing multiple users in the same resources achieves superior performance with respect to conventional LTE networks, provided that the resulting interference is properly

taken care of. The extension of NOMA to multi-cell networks is presented in [165], which addresses several multi-cell NOMA challenges, including coordinated scheduling, beamforming, and practical implementation issues related to successive interference cancellation.

In contrast with most of the works on NOMA, which deal with homogeneous traffic conditions (see [166] for a recent review), here the focus is on NOMA techniques in the context of heterogeneous networks, such as the forthcoming 5G wireless systems, as discussed in [167, 168]. In fact, NOMA represents an attractive solution to meet the distinct requirements of 5G services, as it improves spectral efficiency (eMBB), enables massive device connectivity (mMTC), and allows for low-transmission latency (URLLC) [169].

In [168] a communication-theoretic model was introduced to investigate the performance trade-offs for eMBB, mMTC and URLLC services in a single-cell scenario under both OMA and NOMA. This single-cell model has been later extended in [170] to the uplink of a multi-cell C-RAN architecture, in which the BBU communicates with multiple URLLC and eMBB users belonging to different cells through geographically distributed ENs. In the C-RAN system studied in [170], while the URLLC signals are locally decoded at the ENs due to latency constraints, the eMBB signals are quantized and forwarded over limited-capacity digital fronthaul links to the BBU, where centralized joint decoding is performed.

None of the aforementioned works considers the coexistence of different 5G services in a C-RAN architecture based on analog fronthaul links which is the focus of this chapter. In particular, the analysis is specialized here to the proposed A-MIMO-RoC architecture.

9.1.3. Chapter Contributions

In this chapter the coexistence between URLLC and eMBB services is investigated in the uplink of an analog C-RAN system based on A-MIMO-RoC. In the considered hybrid cloud-edge architecture, the URLLC signals are still decoded locally at the EN, while the eMBB signals are forwarded to the BBU over analog fronthaul links.

In particular, the main contributions of this chapter are three-fold:

- We extend the uplink C-RAN theoretic model proposed in [170] to the A-MIMO-RoC architecture, in which the fronthaul links are characterized by multiple, generally interfering, channels that carry the received radio signals;
- By leveraging information theoretical tools, we investigate the performance trade-offs between URLLC and eMBB services under both OMA and NOMA, by considering different interference management strategies such as puncturing, considered for the standardization of 5G New Radio [171, 172], Treating Interference as Noise (TIN), and Successive Interference Cancellation (SIC);

- The analysis demonstrates that NOMA allows for higher eMBB information rates with respect to OMA, while guaranteeing a reliable low-rate URLLC communication with minimal access latency. Moreover, differently from the case of conventional digital C-RAN architecture based on limited-capacity fronthaul links [170], in analog C-RAN, TIN always outperforms puncturing, while the best performance is still achieved by NOMA with SIC.

9.1.4. Contribution on International Conferences/Journals

Part of the material presented in this chapter has been published in:

- **A. Matera**, R. Kassab, O. Simeone, and U. Spagnolini, "Non-Orthogonal eMBB-URLLC Radio Access for Cloud Radio Access Networks with Analog Fronthauling" in *Entropy*, vol. 20, no. 9, pp. 661, 2018.

9.2. System Model

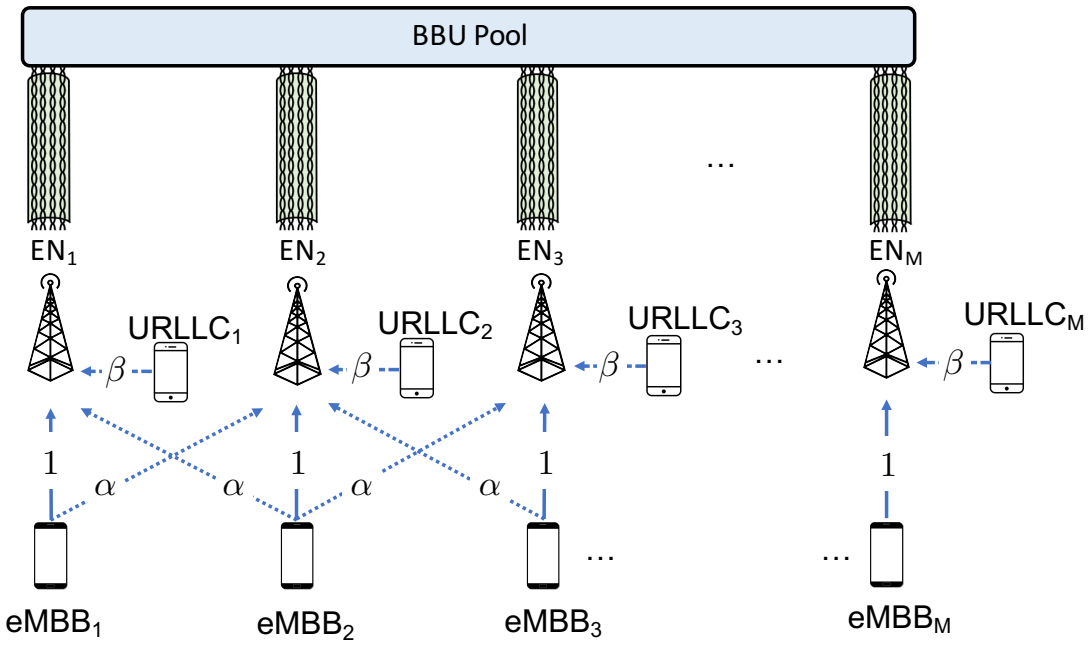

Figure 9.2.: Model of the uplink of C-RAN system based on Analog Radio-over-Copper (A-RoC) fronthauling.

The C-RAN architecture based on A-MIMO-RoC is illustrated in Fig. 9.2. In this system, the BBUs communicate with multiple User Equipments (UEs) belonging

to M cells through M single-antenna ENs. The BBUs are co-located in the so-called BBU pool so that joint processing can be performed, while the ENs are geographically distributed. In particular, we assume here that cells are arranged in a line following the conventional circulant Wyner model [173, Chapter 2], and each cell contains two single-antenna UEs with different service constraints: one eMBB user and one URLLC user.

Due to the strict latency constraints of URLLC traffic, the signal for the URLLC UEs is decoded on-site at the EN, while the eMBB signals are forwarded to the BBU through a multi-channel analog fronthaul. In this hybrid cloud-edge architecture, the mobile operator equips the EN with edge computing capabilities in order to provision the services required by the URLLC user directly from the EN. Following the A-MIMO-RoC concept, the end-to-end channel from the eMBB UEs and the BBU pool is assumed to be fully analog: the EN performs only signal amplification and frequency translation to comply with cable fronthaul capabilities and forwards the signals to the BBU, where centralized decoding is performed. In practice, as detailed later in the chapter and shown in Figs. 9.7-9.9, we assume that each EN hosts a digital module, responsible for URLLC signal decoding, and an analog module, responsible for the mapping of received radio signal over the analog fronthauling, which is identified in Figs. 9.7-9.9 as Analog-to-Analog (A/A) mapping.

While the technology used for the analog fronthauling can be either fiber-optics (A-RoF), wireless (A-RoR) or cable (A-RoC), the system model proposed in this chapter reflects mainly the last two solutions. In fact, even if the focus is on the A-MIMO-RoC architecture (see Fig. 9.2), the analysis holds also for a more general A-RoR C-RAN system.

9.2.1. RAN Model

We consider the same Wyner-type radio access model of [170], which is described in this subsection. The Wyner model is an abstraction of cellular systems that captures one of the main aspects of such settings, namely the locality of inter-cell interference. The advantage of employing such a simple model is the possibility to obtain analytical insights, which is a first mandatory step for the performance assessment under more realistic operating conditions [173]. As illustrated in Fig. 9.3, the direct channel gain from the eMBB UE and the EN belonging to the same cell is set to one, while the inter-cell eMBB channel gain is equal to $\alpha \in [0, 1]$. Furthermore, the URLLC UEs have a channel gain equal to $\beta > 0$. The URLLC user is assumed to be in the proximity of the EN, and thus it does not interfere with the neighboring cells. The eMBB user, instead, is assumed to be located at the edges of the cell in order to consider worst-case performance guarantees. As a result, each eMBB user interferes with both left and right neighboring cells, following the standard Wyner model [173]. All channel gains are assumed to be

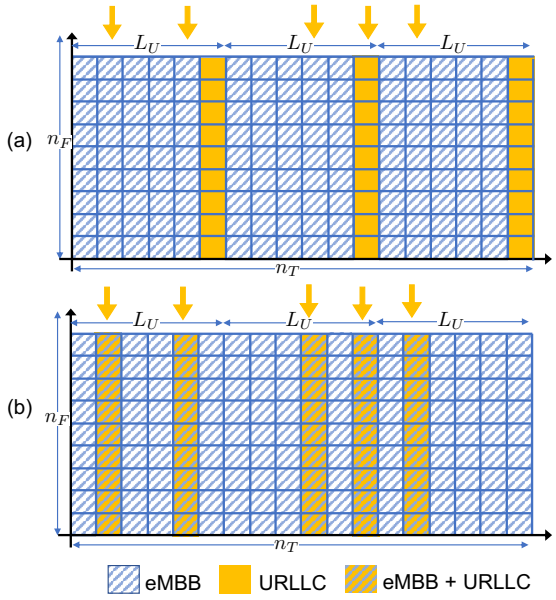

Figure 9.3.: Time-frequency resource allocation: a) Orthogonal Multiple Access (OMA) and b) Non-Orthogonal Multiple Access (NOMA). Downwards arrows denote arrival of URLLC packets.

constant over the considered radio resources shown Fig. 9.3, and known to all UEs and ENs.

As illustrated in Fig. 9.3, we assume that the time-frequency plane is divided in n_T minislots, indexed as $t \in [1, n_T]$, where each minislot is composed of n_F frequency channels, indexed as $f \in [1, n_F]$, for a total of $n_F n_T$ time-frequency radio resources. Each radio resource accommodates the transmission of a single symbol, although generalizations are straightforward. The eMBB UEs transmit over the entire $n_F \times n_T$ time-frequency frame. In contrast, due to the latency constraints of the URLLC traffic, each URLLC transmission is limited to the n_F frequency channels of a single minislot, and URLLC packets are generally small compared to the eMBB frame, which requires the condition $n_T \gg 1$. As illustrated in Fig. 9.3, each URLLC UE generates an independent packet in each minislot with probability q. This packet is transmitted at the next available transmission opportunity in a grant-free manner.

In the case of Orthogonal Multiple Access (OMA), one minislot is exclusively allocated for URLLC transmission every L_U minislots. Parameter L_U is considered here as the worst-case access latency. Accordingly, if more than one packet is generated within the L_U minislots between two transmission opportunities, only one of those packets is randomly selected for transmission and all the remaining

are discarded. The signal $Y_k^f(t)$ received at the k-th EN at the f-th frequency under OMA is

$$Y_k^f(t) = \begin{cases} \beta A_k(t) U_k^f(t) + Z_k^f(t), & \text{if } t = L_U, 2L_U, ... \\ X_k^f(t) + \alpha X_{k-1}^f(t) + \alpha X_{k+1}^f(t) + Z_k^f(t), & \text{otherwise} \end{cases} \tag{9.1}$$

where $X_k^f(t)$ and $U_k^f(t)$ are the signals transmitted at time t and subcarrier f by the k-th eMBB UE and URLLC UE, respectively; $Z_k^f(t) \sim \mathcal{CN}(0,1)$ is the unit-power zero-mean additive white Gaussian noise; and $A_k(t) \in \{0,1\}$ is a binary variable indicating whether or not the URLLC UE is transmitting at time t.

In case of Non-Orthogonal Multiple Access (NOMA), the URLLC UE transmits its packet in the same slot where it is generated by the application layer, so that the access latency is always minimal, i.e., $L_U = 1$ minislot. Under NOMA, the signal $Y_k^f(t)$ received at the k-th EN at the f-th frequency is

$$Y_k^f(t) = X_k^f(t) + \alpha X_{k-1}^f(t) + \alpha X_{k+1}^f(t) + \beta A_k(t) U_k^f(t) + Z_k^f(t). \tag{9.2}$$

According to the circulant Wyner model, in (9.1) and (9.2), we assume that $[k-1] = M$ for $k = 1$ and $[k+1] = 1$ for $k = M$, in order to guarantee symmetry.

For both OMA and NOMA, the power constraints for the k-th eMBB and URLLC users are defined within each radio resource frame respectively as

$$\frac{1}{n_F n_T} \sum_{t=1}^{n_T} \sum_{f=1}^{n_F} \mathbb{E}\left[\left| X_k^f(t) \right|^2 \right] \leq P_B, \tag{9.3}$$

and

$$\frac{1}{n_F} \sum_{f=1}^{n_F} \mathbb{E}\left[\left| U_k^f(t) \right|^2 \right] \leq P_U, \tag{9.4}$$

where the temporal average are taken over all symbols within a codeword.

Models (9.1) and (9.2) can be written in matrix form as

$$\mathbf{Y}(t) = \mathbf{X}(t)\mathbf{H} + \beta \mathbf{U}(t)\mathbf{A}(t) + \mathbf{Z}(t), \tag{9.5}$$

where matrix $\mathbf{Y}(t) = [\mathbf{y}_1(t), \mathbf{y}_2(t), ..., \mathbf{y}_M(t)] \in \mathbb{C}^{n_F \times M}$ gathers all the signals received at all the M ENs over all the n_F frequencies, and the k-th column $\mathbf{y}_k(t) \in \mathbb{C}^{n_F \times 1}$ denotes the signal received across al the radio frequencies at the k-th EN. The channel matrix $\mathbf{H} \in \mathbb{R}^{M \times M}$ is circulant with the first column given by vector $[1, \alpha, 0, ..., 0, \alpha]^T$; matrices $\mathbf{U}(t) \in \mathbb{C}^{n_F \times M}$ and $\mathbf{X}(t) \in \mathbb{C}^{n_F \times M}$ collect the signals transmitted by URLLC and eMBB UEs, respectively; and $\mathbf{Z}(t) \in \mathbb{C}^{n_F \times M}$ is the overall noise matrix. Finally, $\mathbf{A}(t)$ is a diagonal matrix whose k-th diagonal element is a Bernoulli random variable distributed as $A_k(t) \sim \mathcal{B}(q)$, $\forall k = 1, 2, ..., M$.

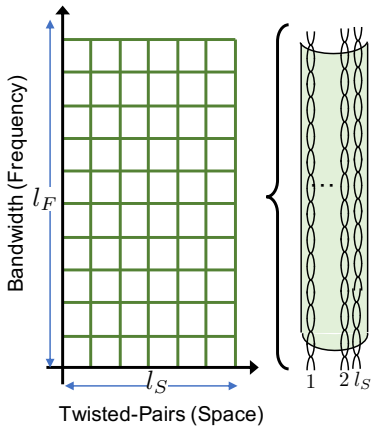

Figure 9.4.: Space-frequency cable resource allocation

9.2.2. Space-Frequency Analog Fronthaul Channel

In the considered C-RAN architecture with analog fronthauling, the k-th EN forwards the signal $\mathbf{y}_k(t)$ received by the UEs to the BBU over a wired-access link in a fully analog fashion. As depicted in Fig. 9.2, we focus our attention on the A-MIMO-RoC architecture, as it provides an important example in which the fronthaul is affected by inter-link interference. Accordingly, each of the cables (e.g., LAN cables) employed for the fronthaul contains l_S twisted-pairs, i.e., l_S space-separated channels, indexed as $c \in [1, l_S]$. Each pair carries a bandwidth equal to $l_F \leq n_F$ frequency channels of the RAN, indexed as $f' \in [1, l_F]$, so that a total of $l_S l_F$ space-frequency resource blocks are available over each cable, as shown in Fig 9.4. Furthermore, we assume that each analog fronthaul link has enough resources to accommodate the transmission of the whole radio signal at each EN, i.e., $l_S l_F \geq n_F$.

The fronthaul channel between each EN and the BBU is described by the matrix $\mathbf{H}_c \in \mathbb{R}^{l_S \times l_S}$, which accounts for direct channel gains on each cable, given by the diagonal elements $[\mathbf{H}_c]_{ii}$, and for the intra-cable crosstalk, described by the off-diagonal elements $[\mathbf{H}_c]_{ij}$, with $i \neq j$. We assume here that the channel coefficients in $\mathbf{H}_c$ do not depend on frequency f'. Furthermore, in keeping the modeling assumptions of the Wyner model, we posit that the direct channel gains for all the pairs are normalized to 1, while the crosstalk coefficients (i.e., Far-End-CrossTalk, FEXT) between any pair of twisted-pairs are given by a coupling parameter $\gamma \geq 0$. It follows that the cable fronthaul channel matrix can be written as

$$\mathbf{H}_c = \gamma \mathbf{1}_{l_S} \mathbf{1}_{l_S}^T + (1-\gamma)\mathbf{I}_{l_S}, \tag{9.6}$$

where $\mathbf{1}_n$ denotes a column vector of size n of all ones and $\mathbf{I}_n$ is the identity matrix of size n. We note that, in case of wireless fronthaul links such as in A-RoR, the

coefficient γ accounts for the mutual interference between spatially separated radio links. As a result, one typically has $\gamma > 0$ when considering sub-6 GHz frequency bands, while the condition $\gamma = 0$ may be reasonable in the mmWave or THz bands, in which communication is mainly noise-limited due to the highly directive beams [174].

For a given time t, the symbols $\mathbf{y}_k(t)$ received at EN k-th over all the n_F radio frequency channels are transported to the BBU over the $l_S l_F$ cable resource blocks, where the mapping between radio and cable resources, referred to as Space-frequency to Space-Frequency (SF2SF) multiplexing, is to be designed (see Sect. 9.3.1) and depends on the bandwidth l_F available at each twisted-pair. As SF2SF multiplexing is not the focus of this chapter, here we adopt a very simple mapping rule between radio and cable resources (see Sect. 9.3.1). In this regards, we define

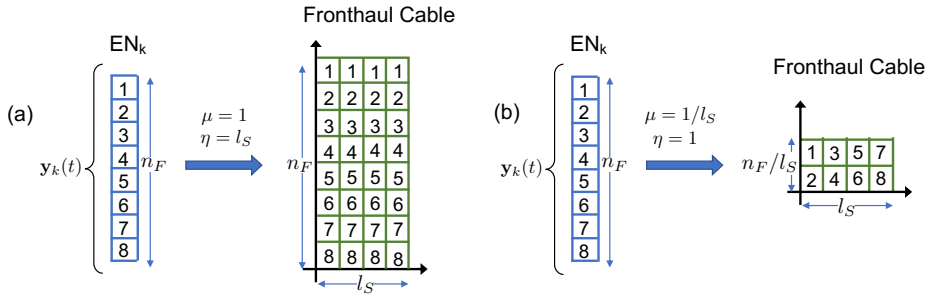

Figure 9.5.: Mapping of radio resources over cable resources: (a) maximum normalized cable bandwidth (full redundancy), $\mu = 1$, or $\eta = l_S$; (b) minimal normalized cable bandwidth (no redundancy), $\mu = 1/l_S$, or $\eta = 1$.

the fraction $\mu \in [1/l_S, 1]$ of the radio bandwidth n_F that can be carried by each pair, referred to as *normalized cable bandwidth*, as

$$\mu = \frac{l_F}{n_F}. \tag{9.7}$$

As a result, the quantity

$$\eta = \mu \cdot l_S \tag{9.8}$$

expresses the bandwidth amplification factor (or redundancy) over the cable fronthaul, as $\eta \geq 1$. To simplify, we assume here that both $1/\mu$ and η are integer numbers. The two extreme situations with $\mu = 1$, or $\eta = l_S$, and $\mu = 1/l_S$, or $\eta = 1$, are shown in Fig. 9.5 for $l_S = 4$ twisted-pairs and $n_F = 8$ subcarriers. For the first case, one replica of the whole radio signal $\mathbf{y}_k(t)$ can be transmitted over all of the l_S pairs, and the bandwidth amplification over cable is $\eta = l_S$. In the second case, disjoint fractions of the received bandwidth can be forwarded on each pair and the bandwidth amplification factor is $\eta = 1$.

We now detail the signal model for fronthaul transmission. To this end, let us define the $l_F \times l_S$ matrix $\tilde{\mathbf{Y}}_k$ containing the signal to be transmitted by the EN k-th to the BBU over the copper cable as

$$\tilde{\mathbf{Y}}_k = [\tilde{\mathbf{y}}_k^1(t), \tilde{\mathbf{y}}_k^2(t), ..., \tilde{\mathbf{y}}_k^{l_S}(t)], \tag{9.9}$$

where the k-th column $\tilde{\mathbf{y}}_k^c(t) \in \mathbb{C}^{l_F \times 1}$ denotes the signal transmitted on twisted-pair c across all the l_F cable frequency resources. The signal $\tilde{\mathbf{R}}_k \in \mathbb{C}^{l_F \times l_S}$ received at the BBU from the k-th EN across all the cable space-frequency resources is then computed as

$$\tilde{\mathbf{R}}_k(t) = \tilde{\mathbf{Y}}_k(t)\mathbf{H}_c + \tilde{\mathbf{W}}_k(t), \tag{9.10}$$

where $\tilde{\mathbf{W}}_k(t) = [\tilde{\mathbf{w}}_k^1(t), \tilde{\mathbf{w}}_k^2(t), ..., \tilde{\mathbf{w}}_k^{l_S}(t)] \in \mathbb{C}^{l_F \times l_S}$ is the additive white Gaussian cable noise uncorrelated over cable pairs and frequencies, i.e., $\tilde{\mathbf{w}}_k^c(t) \sim \mathcal{CN}(\mathbf{0}, \mathbf{I}_{l_F})$ for all pairs $c = 1, 2, ..., l_S$.

As commonly assumed in wireline communications to control cable radiations (see Chapter 2 for further details), the power of the cable symbol $[\tilde{\mathbf{y}}_k^c(t)]_{f'}$ transmitted from EN_k over twisted-pair c at frequency $f^{'}$ is constrained to P_c by the (short-term[1]) power constraint

$$\mathbb{E}\left[\left|[\tilde{\mathbf{y}}_k^c(t)]_{f'}\right|^2\right] \leq P_c \quad \forall c \in [1, l_S], f' \in [1, l_F], t \in [1, n_T]. \tag{9.11}$$

In the following, we will omit the time index t, when no confusion arises.

9.2.3. Performance Metrics

The performance metrics used to evaluate the interaction between eMBB and URLLC services in the considered C-RAN architecture based on A-MIMO-RoC are detailed in the following.

9.2.3.1. eMBB

Capacity enhancement is the main goal of the eMBB service, which is envisioned to provide very high-rate communication to all the UEs. Therefore, for eMBB UEs, we are interested in the per-UE rate defined as

$$R_B = \frac{\log_2(M_B)}{n_T n_F}, \tag{9.12}$$

where M_B is the number of codewords in the codebook of each eMBB UE.

[1]One can also consider the "long-term" power constraint $n_T^{-1} \sum_t \mathbb{E}[|[\tilde{\mathbf{y}}_k^c(t)]_{f'}|^2] \leq P_c$, $\forall c \in [1, l_S]$, $f' \in [1, l_F]$ with minor modifications to the analysis and final results.

9.2.3.2. URLLC

Differently from eMBB, URLLC service is mainly focused on low-latency and reliability aspects. Due to the short length of URLLC packets, in order to guarantee ultra reliable communications, we need to ensure that the error probability for each URLLC UE, denoted as $\Pr[E_U]$, is bounded by a predefined value ϵ_U (typically smaller than 10^{-3}) as

$$\Pr[E_U] \leq \epsilon_U. \tag{9.13}$$

Concerning latency, we define the maximum access latency L_U as the maximum number of minislots that an URLLC UE has to wait before transmitting a packet. Finally, although rate enhancement is not one of the goals of URLLC service, it is still important to evaluate the per-UE URLLC rate that can be guaranteed while satisfying the aforementioned latency and reliability constraints. Similarly to (9.12), the per-UE URLLC rate is defined as

$$R_U = \frac{\log_2(M_U)}{n_F}, \tag{9.14}$$

where M_U is the number of URLLC codewords in the codebook used by the URLLC UE for each information packet.

9.3. Analog Fronthaul Signal Processing

The analog cable fronthaul links employed in the C-RAN system under study pose several challenges in the system design, which are addressed in this section. Firstly, the radio signal received at each EN needs to be mapped over the corresponding fronthaul resources in both frequency and space dimension. Secondly, the signal at the output of each fronthaul link needs to be processed in order to maximize the Signal-to-Noise Ratio (SNR) for all UE signals. Finally, the power constraints in (9.11) must be properly enforced. All these requirements are to be addressed by all-analog processing in order to meet the low-complexity and latency constraints of the analog fronthaul. In the rest of this section, we discuss each of these problems in turn.

9.3.1. Radio Resource Mapping over Fronthaul Channels

In order to maximize the SNRs for all the signals forwarded over the fronthaul by symmetry, we need to ensure that: *i)* all the received signals are replicated η times across the cable twisted-pairs, where we recall that η is the bandwidth amplification factor defined in (9.8); and *ii)* cable cross-talk interference among different radio frequency bands is minimized. In fact, as the transmitted power at

the cable input is limited by the constraints in (9.11), a simple and effective way to cope with the impairments of the analog fronthaul links using the only analog-processing capability is by introducing redundancy in the fronthaul transmission. To this end, without loss of generality, we assume the following mapping rule between the n_F radio signals at each EN and the $l_S l_F$ cable resources.

Let us consider the radio signal $\mathbf{y}_k = \left[Y_k^1, Y_k^2, ..., Y_k^{n_F}\right]^T$ received at the k-th EN. For a given normalized cable bandwidth μ, the n_F frequency channels of the radio signal $\mathbf{y}_k$ can be split into $1/\mu$ sub-vectors of size $l_F = \mu n_F$ as

$$\mathbf{y}_k = \begin{bmatrix} \mathbf{y}_k^1 \\ \mathbf{y}_k^2 \\ \vdots \\ \mathbf{y}_k^{\frac{1}{\mu}} \end{bmatrix}, \tag{9.15}$$

where each vector $\mathbf{y}_k^j$ contains a disjoint fraction of the radio signal bandwidth n_F. Each vector $\mathbf{y}_k^j$ can be transmitted over η twisted-pairs, where we recall that η is the fronthaul redundancy factor. To this end, each signal $\mathbf{y}_k^j$ in (9.16) is transmitted over η consecutive cable twisted-pairs.

To formalize the described mapping, the first step consists in reorganizing the signal $\mathbf{y}_k$ into a $l_F \times \frac{1}{\mu}$ matrix as

$$\mathbf{Y}_k = \text{vec}^{-1}_{\frac{1}{\mu}}(\mathbf{y}_k) = \left[\mathbf{y}_k^1 \quad \mathbf{y}_k^2 \quad ... \quad \mathbf{y}_k^{\frac{1}{\mu}}\right], \tag{9.16}$$

where the operator $\text{vec}^{-1}_{\frac{1}{\mu}}(\cdot) : \mathbb{C}^{n_F} \rightarrow \mathbb{C}^{n_F \cdot \mu \times \frac{1}{\mu}}$ acts as the inverse of the vectorization operator $\text{vec}(\cdot)$, with the subindex $1/\mu$ denoting the number of columns of the resulting matrix. Then, the overall cable signal $\tilde{\mathbf{Y}}_k$ transmitted by EN k-th in (9.9) can be equivalently written as

$$\tilde{\mathbf{Y}}_k = \left[\underbrace{\mathbf{y}_k^1 \quad \mathbf{y}_k^1 \quad \dots \quad \mathbf{y}_k^1}_{\eta}, \quad \underbrace{\mathbf{y}_k^2 \quad \mathbf{y}_k^2 \quad \dots \quad \mathbf{y}_k^2}_{\eta} \quad \cdots \quad \underbrace{\mathbf{y}_k^{\frac{1}{\mu}} \quad \mathbf{y}_k^{\frac{1}{\mu}} \quad \dots \quad \mathbf{y}_k^{\frac{1}{\mu}}}_{\eta}\right], \tag{9.17}$$

or, in compact form, as

$$\tilde{\mathbf{Y}}_k = \mathbf{Y}_k \otimes \mathbf{1}_\eta^T, \tag{9.18}$$

where $\otimes$ denotes the Kronecker product (for a review of Kronecker product properties in signal processing we refer the reader to [138]). Notice that in case of full normalized cable bandwidth, i.e., $\mu = 1$ (corresponding to $\eta = l_S$), the signal $\tilde{\mathbf{Y}}_k$ transmitted over the fronthaul cable simplifies to $\tilde{\mathbf{Y}}_k = \mathbf{y}_k \otimes \mathbf{1}_{l_S}^T$, which implies that the radio signal $\mathbf{y}_k$ is replicated over all the l_S twisted-pairs. On the contrary, when the normalized cable bandwidth is minimal, i.e., $\mu = 1/l_S$ (corresponding

to $\eta = 1$), the signal $\tilde{\mathbf{Y}}_k$ does not contain any redundancy, and disjoints signals are transmitted over all pairs, so that the cable signal $\tilde{\mathbf{Y}}_k$ equals the matrix radio signal in (9.16) as $\tilde{\mathbf{Y}}_k = \mathbf{Y}_k$.

Remark 9.1. The easiest practical implementation of the proposed analog radio resource mapping at the EN is by grouping the subcarriers onto a specific frequency portion of the cable. As an example, let us assume that the EN is equipped with 5 antennas, that each antenna receives a 20-MHz radio signal, and that the analog fronthauling disposes of 4 twisted-pairs with 100 MHz bandwidth each. In this case, Chapters 6-7-8 have shown that is possible to freely map in an all-analog fashion the 5×20 MHz bands onto the overall 4×100 MHz $= 400$ MHz fronthaul bandwidth. This example corresponds to a special case of the model studied in this chapter, obtained by setting $\mu = 1$, i.e., the whole radio signal bandwidth received at the ENs is mapped/replicated over the analog fronthauling. More generally, this chapter posits the possibility to carry out the fronthaul mapping at a finer granularity, i.e., at a subcarrier level. In this case, filtering operations would in practice be mandatory in order to extract groups of subcarriers. This operation can be implemented in principle still by analog filters.

9.3.2. Signal Combining at the Fronthaul Output

As discussed, depending on the fronthaul bandwidth, a number η of noisy replicas of the radio signals received at each EN are relayed to the BBU over η different twisted-pairs. Hence, in order to maximize the SNRs for all signals, Maximum Ratio Combining (MRC) [175] is applied at the cable output as

$$\mathbf{R}_k = \tilde{\mathbf{R}}_k \mathbf{G}, \tag{9.19}$$

where $\mathbf{R}_k \in \mathbb{C}^{l_F \times \frac{1}{\mu}}$ is the signal received at BBU from the k-th EN after the combiner and $\mathbf{G} \in \mathbb{R}^{l_S \times \frac{1}{\mu}}$ is the MRC matrix. Under the assumptions here, MRC coincides with equal ratio combining and hence matrix $\mathbf{G}$ can be written as

$$\mathbf{G} = \frac{1}{\eta} \left(\mathbf{I}_{\frac{1}{\mu}} \otimes \mathbf{1}_\eta \right). \tag{9.20}$$

As an example, in the case of maximum redundancy, i.e., $\eta = l_S$, the MRC matrix $\mathbf{G} = l_S^{-1} \mathbf{1}_{l_S}$ and the MRC combines the analog signals received over all pairs, since they carry the same information signal. On the contrary, in the case of minimal normalized bandwidth $\mu = 1/l_S$ or $\eta = 1$, the matrix $\mathbf{G}$ equals the identity matrix as $\mathbf{G} = \mathbf{I}_{l_S}$, since no combining is possible.

The signal $\mathbf{r}_k \in \mathbb{C}^{n_F}$ received at the BBU from EN_k across the n_F subcarriers is thus obtained by vectorizing matrix $\mathbf{R}_k$ in (9.19) as

$$\mathbf{r}_k = \text{vec}(\mathbf{R}_k). \tag{9.21}$$

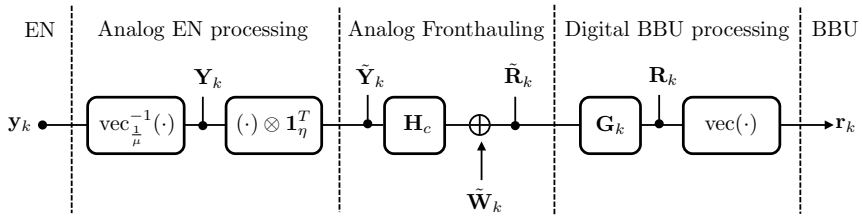

Figure 9.6.: Relationship between the signal $\mathbf{r}_k$ (9.21) obtained at the output of the combiner and the radio received signal $\mathbf{y}_k$ in (9.15).

The relationship between the signal $\mathbf{r}_k$ (9.21) obtained at the output of the combiner and the radio received signal $\mathbf{y}_k$ in (9.15) is summarized by the block-scheme in Fig. 9.6, and it is

$$\mathbf{r}_k = \mathrm{vec}\left[\left(\left(\mathrm{vec}^{-1}_{\frac{1}{\mu}}\left(\mathbf{y}_k\right)\otimes \mathbf{1}_\eta^T\right)\mathbf{H}_c + \tilde{\mathbf{W}}_k\right)\mathbf{G}_k\right]. \tag{9.22}$$

Finally, we collect the overall signal $\mathbf{R}\in\mathbb{C}^{n_F\times M}$ received at the BBU from all ENs across all frequencies in the matrix

$$\mathbf{R} = [\mathbf{r}_1, \mathbf{r}_2, ..., \mathbf{r}_M]. \tag{9.23}$$

After some algebraic manipulations, it is possible to express Eq. (9.23) in a more compact form, which is reported in the following Lemma 9.1.

Lemma 9.1. *In the given C-RAN architecture based on A-MIMO-RoC, for a given bandwidth amplification factor $\eta \geq 1$, the signal $\mathbf{R}\in\mathbb{C}^{n_F\times M}$ received at the BBU from all ENs across all radio frequencies after MRC can be written as*

$$\mathbf{R} = \left(\mathbf{H}_c^\eta \otimes \mathbf{I}_{l_F}\right)\mathbf{Y} + \mathbf{W}, \tag{9.24}$$

where

$$\mathbf{H}_c^\eta = \gamma\eta \mathbf{1}_{\frac{1}{\mu}}\mathbf{1}_{\frac{1}{\mu}}^T + (1-\gamma)\mathbf{I}_{\frac{1}{\mu}} \tag{9.25}$$

is the equivalent cable fronthaul channel matrix; $\mathbf{Y}$ is the signal received at all ENs across all frequency radio channels in (9.5)*; and $\mathbf{W} = [\mathbf{w}_1, \mathbf{w}_2, ..., \mathbf{w}_M]$ is the equivalent cable noise at the BBU after MRC, with the k-th column distributed as $\mathbf{w}_k \sim \mathcal{CN}\left(\mathbf{0}, \frac{1}{\eta}\mathbf{I}_{n_F}\right)$ for all $k = 1, 2, ..., M$.*

Proof. see Appendix C.1. □

In order to gain some insights, it is useful again to consider the two extreme cases of maximum redundancy, i.e., $\eta = l_S$, and no redundancy, i.e., $\eta = 1$. In the former case, the equivalent channel (9.25) equals the scalar $\mathbf{H}_c^\eta = 1 + \gamma(l_S - 1)$.

This demonstrates the effect of transmitting a replica of the whole radio signal over all pairs. In fact, the useful signal is received at the BBU not only through the direct path, which has unit gain, but also from the remaining $l_S - 1$ interfering paths, each with gain γ, which constructively contribute to the overall SNR after the combiner. More precisely, it can be observed that, in case of full redundancy, the SNR of the radio signal $\mathbf{Y}$ at the BBU is increased by the analog fronthaul links by a factor $(1+\gamma(l_S-1))^2/(1/\eta) = l_S(1+\gamma(l_S-1))^2$. As a result, in this case, for a coupling factor $\gamma > 0$, the SNR at the BBU increases with the cube of the number of fronthaul links l_S. In contrast, for $\mu = 1/l_S$, the equivalent fronthaul channel reflects the fact that signals forwarded over the different pairs interfere each other, and is equal to $\mathbf{H}_c^{\eta} = \mathbf{H}_c$. The beneficial effect of redundantly transmitting radio signals over different pairs is reflected also in the power of the noise after the combiner, which is reduced proportionally to the bandwidth amplification factor η.

9.3.3. Fronthaul Power Constraints

In order to enforce the cable power constraints in (9.11), it is necessary to scale the radio signal $\mathbf{Y}$ in (9.24) by a factor λ prior to the transmission over the fronthaul. This is given as

$$\lambda = \sqrt{\frac{P_c}{\delta P_B(1+2\alpha^2)+1}}, \tag{9.26}$$

where $\delta = \left(1 - L_U^{-1}\right)^{-1}$ for OMA, accounting for the fact that only $L_U - 1$ minislots are devoted to the eMBB UE, while it equals $\delta = 1$ for NOMA, since the eMBB transmission spreads over all L_U minislot. To simplify the notation, in the following we will account for the gain λ by scaling the noise over the cable after MRC in Eq. (9.25) accordingly as

$$\mathbf{w}_k(t) \sim \mathcal{CN}\left(\mathbf{0}, \frac{1}{\eta\lambda^2}\mathbf{I}\right). \tag{9.27}$$

9.4. Orthogonal Multiple Access (OMA)

As described in Sec. 9.2.1, under OMA over the radio channel, one minislot every L_U is exclusively allocated to URLLC UEs, while eMBB UEs transmit over the remaining minislots. In this way, URLLC UEs never interfere with eMBB transmissions. If more than one URLLC packet is generated at a user between two URLLC transmission opportunities, only one of such packets (randomly selected) is transmitted, while the others are discarded, causing a blockage error. Due to the latency constraints, URLLC signals are digitized and decoded locally at the ENs, while the eMB signals are first mapped over the cable fronthaul lines, and

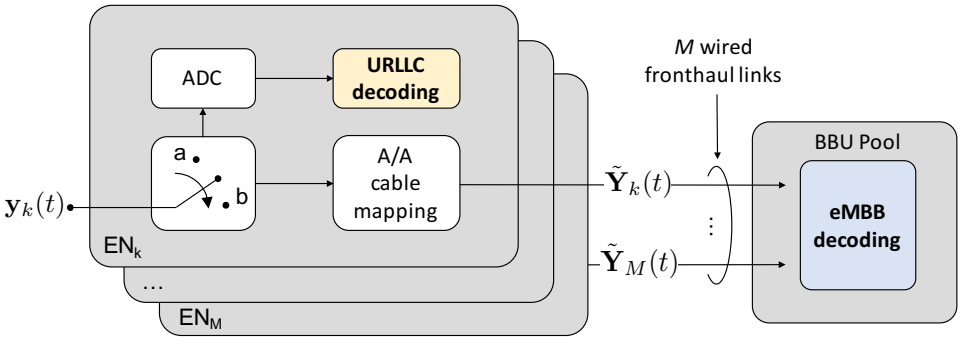

Figure 9.7.: Block diagram of the operation of the ENs and BBU for Orthogonal Multiple Access (OMA).

then analogically forwarded to the BBU, as mathematically summarized in Fig. 9.7. In this section, we derive the expressions for the eMBB and URLLC rates under OMA for a given URLLC access latency L_U and, in the case of URLLC, for a fixed URLLC target error probability ϵ_U.

9.4.1. URLLC Rate

In order to evaluate the per-UE URLLC rate under OMA and for a given URLLC target error probability ϵ_U, we follow the approach in [170], which is reviewed here. URLLC packets are generally short due to the strict latency constraints, and the maximum achievable rate can be computed by leveraging results from finite blocklength information theory. To this end, fix a given blocklength n_F and URLLC error decoding probability ϵ_U^D. Notice that this probability is different from the general URLLC target error probability ϵ_U, as detailed later in this section. According to [176], the URLLC rate can be well approximated by

$$R_U = \log_2(1+\beta^2 P_U) - \sqrt{\frac{V}{n_F}} Q^{-1}(\epsilon_U^D), \tag{9.28}$$

where

$$V = \frac{\beta^2 P_U}{1+\beta^2 P_U} \tag{9.29}$$

is the channel dispersion and $\mathcal{Q}^{-1}(\cdot)$ is the inverse Q-function.

The error probability for URLLC packets is the sum of two contributions. The first represents the probability that an URLLC packet is discarded due to blockage, given that only one URLLC packet can be transmitted within the required L_U worst-case latency; while the second is the probability that the packet is transmitted but not successfully decoded. Accordingly, the overall error probability can

be computed as

$$\Pr[E_U] = \sum_{n}^{L_U-1} p(n)\frac{n}{n+1} + \sum_{n}^{L_U-1} p(n)\frac{1}{n+1}\epsilon_U^D, \tag{9.30}$$

where $p(n) = \Pr[N_U(L_U) = n]$ is the distribution of the binomial random variable $N_U(L_U) \sim \text{Bin}(L_U - 1, q)$ representing the number of additional packets generated by the URLLC UE during the remaining minislots between two transmission opportunities. The decoding error probability ϵ_U^D in (9.28) can be obtained from the URLLC reliability constraint in (9.13), i.e., $\Pr[E_U] = \epsilon_U$.

9.4.2. eMBB Rate

The eMBB signals received at the ENs are forwarded over the analog cable fronthaul to the BBU, where centralized digital signal processing and decoding is performed. In the case of OMA, the eMBB signal is free from URLLC interference, hence signal $\mathbf{Y}$ received by all ENs over all radio channels in (9.5) can be written as

$$\mathbf{Y} = \mathbf{X}\mathbf{H} + \mathbf{Z}. \tag{9.31}$$

By substituting (9.31) in (9.24), it is possible to compute the expression for the eMBB per-UE rate under OMA, as shown in Lemma 9.2. Notice that, unlike the case of URLLC packets, the $n_F n_T$ blocklength of eMBB packets allows for the use of standard asymptotic Shannon theory in the computation of eMBB information rate.

Lemma 9.2. *In the given C-RAN architecture based on A-MIMO-RoC, for a given bandwidth amplification factor $\eta \geq 1$, the eMBB user rate under OMA is given as*

$$R_B = \mu\frac{1 - L_U^{-1}}{M} log\left(det\left(\mathbf{I} + \bar{P}_B\mathbf{R}_{z_{eq}}^{-1}\mathbf{H}_{eq}\mathbf{H}_{eq}^T\right)\right), \tag{9.32}$$

where $\bar{P}_B = P_B\left(1 - L_U^{-1}\right)^{-1}$ is the transmission power of eMBB users under OMA, $\mathbf{H}_{eq} = \mathbf{H} \otimes \mathbf{H}_c^\eta$ is the overall channel matrix comprising both the radio channel $\mathbf{H}$ and the equivalent cable channel $\mathbf{H}_c^\eta$ defined in Lemma 9.1, and $\mathbf{R}_{z_{eq}} = \mathbf{I}_M \otimes \mathbf{H}_c^\eta\mathbf{H}_c^\eta + \frac{1}{\lambda^2\eta}\mathbf{I}_{\frac{M}{\mu}}$ is the overall wireless plus cable noise at the BBU.

Proof. see Appendix. C.2. □

As a first observation, the eMBB rate (9.32) linearly scales with the normalized bandwidth μ. This shows that a potential performance degradation in terms of spectral efficiency can be incurred in the presence of fronthaul channels with bandwidth limitations, i.e., with $\mu < 1$. This loss is pronounced in the presence of

significant inter-channel interference, i.e., for large γ. In fact, a large γ increases the effective noise power as per expression of matrix $\mathbf{R}_{z_{\text{eq}}}$. It is also important to point out that in the considered C-RAN system based on the analog relaying of radio signals, the overall noise at the BBU is no longer white as it accounts both for the white cable noise and the wireless noise, where the latter is correlated when there is some bandwidth redundancy, i.e., when $\mu \geq 1/l_S$ or $\eta > 1$.

9.5. Non-Orthogonal Multiple Access (NOMA)

In NOMA, URLLC UEs transmit in the same minislot where the packet is generated, and hence the access latency is minimal and limited to $L_U = 1$ minislot. However, the URLLC signals mutually interfere with the eMBB transmission, which spans the whole time-frequency resource plane. Due to URLLC latency constraints, the eMBB signals necessarily need to be treated as noise while decoding URLLC packets at the ENs. On the contrary, several strategies can de adopted in order to deal with the interfering URLLC signal. Beside puncturing, considered for 5G NR standardization [171, 172], this chapter considers two other techniques, namely Treating Interference as Noise (TIN) and Successive Interference Cancellation (SIC), as detailed in the rest of this section.

9.5.1. URLLC Rate under NOMA

The URLLC per-UE rate for NOMA can be computed by leveraging results from finite blocklength information theory similarly to the OMA case, but accounting for the additional eMBB interference [177]. The URLLC per-UE rate under NOMA is thus well approximated by [170]

$$R_U = \log_2(1 + S_U) - \sqrt{\frac{V}{n_F}} Q^{-1}(\epsilon_U^D),$$

where

$$S_U = \frac{\beta^2 P_U}{1 + (1 + 2\alpha^2) P_B} \tag{9.33}$$

is the signal-to-interference-plus-noise ratio (SINR) for the URLLC UE, and the channel dispersion V is given as

$$V = \frac{S_U}{1 + S_U}. \tag{9.34}$$

Notice that in NOMA the incoming URLLC packet is always transmitted, and hence an URLLC error occurs only if the decoding of such packet fails, which

happens with probability ϵ_U^D. This implies that under NOMA, the probability of URLLC error is given by

$$\Pr[E_U] = \epsilon_U^D, \tag{9.35}$$

hence imposing the condition $\epsilon_U^D \leq \epsilon_U$ by the requirements (9.13).

9.5.2. eMBB Rate by Puncturing

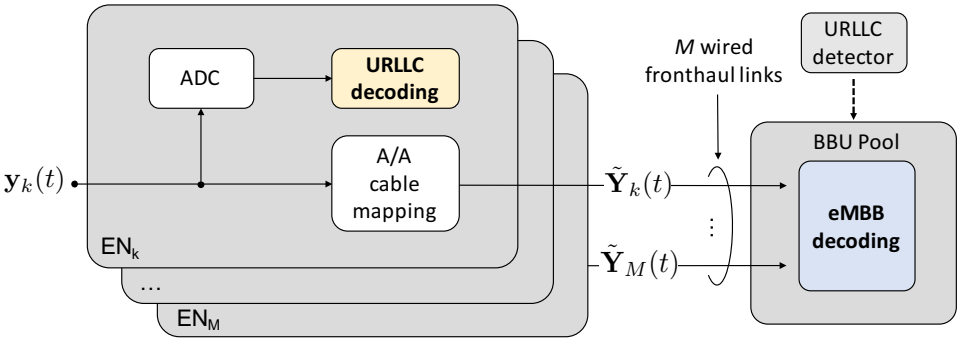

Figure 9.8.: Block diagram of the operation of the ENs and BBU for Non-Orthogonal Multiple Access (NOMA) by puncturing and treating interference as noise (TIN).

In order to carry out joint decoding at the BBU of the eMBB signals under NOMA, the standard approach is to simply discard at the eMBB decoder those signals that are interfered by URLLC. As shown in Fig. 9.8, this technique, referred to as puncturing, is based on the detection of URLLC transmissions at the BBU: if a URLLC transmission is detected in the signal received from EN$_k$, such signal is discarded. Otherwise, the interference-free eMBB signals are jointly decoded at the BBU.

Considering the aforementioned assumptions, the signal model for puncturing can be equivalently described by assuming that if the signal Y_k^f received at the EN$_k$ on frequency f is interfered by an URLLC transmission, then such signal is discarded, and the BBU receives only noise. This is mathematical described by

$$Y_k^f = B_k(X_k^f + \alpha X_{k+1}^f + \alpha X_{k-1}^f) + Z_k^f, \tag{9.36}$$

where the Bernoulli variable $B_k = 1 - A_k \sim \mathcal{B}(1-q)$ indicates the absence ($B_k = 1$) or presence ($B_k = 0$) of URLLC transmissions in the given minislot. The signal in (9.36) received across all ENs and frequencies can be written in matrix form as

$$\mathbf{Y} = \mathbf{XHB} + \mathbf{Z}, \tag{9.37}$$

with definitions given in Sect. 9.2 and with $\mathbf{B} = \text{diag}(B_1, B_2, ..., B_M)$. The rate for the eMBB UE under NOMA by puncturing is reported in Lemma 9.3 and can be derived by substituting signal (9.37) in Eq. (9.24).

Lemma 9.3. *In the given C-RAN architecture based on A-MIMO-RoC, for a given bandwidth amplification factor $\eta \geq 1$, the eMBB user rate under NOMA by puncturing yields*

$$R_B = \frac{\mu}{M}\mathbb{E}_{\mathbf{B}}\left[log\left(det\left(\mathbf{I} + P_B\mathbf{R}_{z_{eq}}^{-1}\mathbf{H}_{B,eq}\mathbf{H}_{B,eq}^T\right)\right)\right], \tag{9.38}$$

where $\mathbf{R}_{z_{eq}}$ is defined as in Lemma 9.2; $\mathbf{H}_{B,eq} = \mathbf{B}\mathbf{H}\otimes\mathbf{H}_c^{\eta}$ is the equivalent wireless plus cable channel in case of puncturing; and we have $\mathbf{B} = diag(B_1, B_2, ..., B_M)$, with B_k being i.i.d. $\mathcal{B}(1-q)$ variables .

Proof. Lemma 9.3 can be proved by following similar steps as for the proof of Lemma 2 with two minor differences: *i)* the radio channel matrix $\mathbf{H}$ is right multiplied by the random matrix $\mathbf{B}$ and *ii)* the capacity is computed by averaging over the distribution of $\mathbf{B}$. □

Differently from the rate (9.32) achieved by OMA, under NOMA, the eMBB transmission spreads over all the minislots, so that there is no scaling factor $1 - L_U^{-1}$ in front of the rate expression (9.38) to account for the resulting loss in spectral efficiency. In case of NOMA by puncturing, the noise covariance is exactly as the one in the eMBB OMA rate in Eq. (9.32), since the eMBB signal, if not discarded at the BBU, is guaranteed to be URLLC interference-free. The overall rate is computed by averaging over all the possible realizations of the random matrix $\mathbf{B}$, which left-multiplies the radio channel matrix $\mathbf{H}$ and accounts for the probability that the entire signal is discarded due to an incoming URLLC packet.

In the case of C-RAN with digital limited-capacity fronthaul links, as discussed in [170], it is advantageous to carry out the operation of detecting and, eventually, discarding the eMBB signal at the ENs. In fact, with a digital fronthaul, only the undiscarded minislots can be quantized, hence devoting the limited fronthaul resources to increase the resolution of interference-free eMBB samples.[170]. The same does not apply to the analog fronthaul considered here, as signals are directly relayed to the BBU without any digitization.

9.5.3. eMBB Rate by Treating Interference as Noise

In the case of analog fronthaul, an enhanced strategy to jointly decode the eMBB signals under NOMA at the BBU is to treat the URLLC interfering transmissions as noise at the eMBB decoder, instead of discarding the corresponding minislot as in puncturing. The block diagram is the same as for puncturing and shown in Fig. 9.8. Accordingly, based on the signals received over the fronthaul links, the BBU first detects the presence of URLLC transmission so as to properly select the

decoding metric. Then, based on this knowledge, joint decoding is performed by treating URLLC interference as noise (TIN).

Lemma 9.4. *In the given C-RAN architecture based on A-MIMO-RoC, for a given bandwidth amplification factor $\eta \geq 1$, the eMBB user rate under NOMA by treating URLLC interference as noise yields*

$$R_B = \frac{\mu}{M}\mathbb{E}_{\mathbf{A}}\left[log\left(det\left(\mathbf{I} + P_B\mathbf{R}_{A,z_{eq}}^{-1}\mathbf{H}_{eq}\mathbf{H}_{eq}^T\right)\right)\right], \tag{9.39}$$

where $\mathbf{R}_{A,z_{eq}} = \mathbf{R}_{z_{eq}} + \beta^2 P_U\left(\mathbf{A} \otimes \mathbf{H}_c^{\eta}\mathbf{H}_c^{\eta}\right)$ is the overall noise plus URLLC interference at the BBU; matrix $\mathbf{A}$ is as in (9.5); and matrices $\mathbf{R}_{z_{eq}}$ and $\mathbf{H}_{eq}$ are the same as in Lemma 9.2.

Proof. see Appendix C.3. □

Differently the two previous cases, in the case of NOMA under TIN, the noise covariance matrix $\mathbf{R}_{A,z_{\text{eq}}}$ needs to account also for the interfering URLLC transmissions, whose packet arrival probability is described by matrix $\mathbf{A}$. The achievable rate is then computed by taking the average over the random matrix $\mathbf{A}$. This average reflects the long-blocklength transmissions of the eMBB users.

9.5.4. eMBB Rate by Successive Interference Cancellation

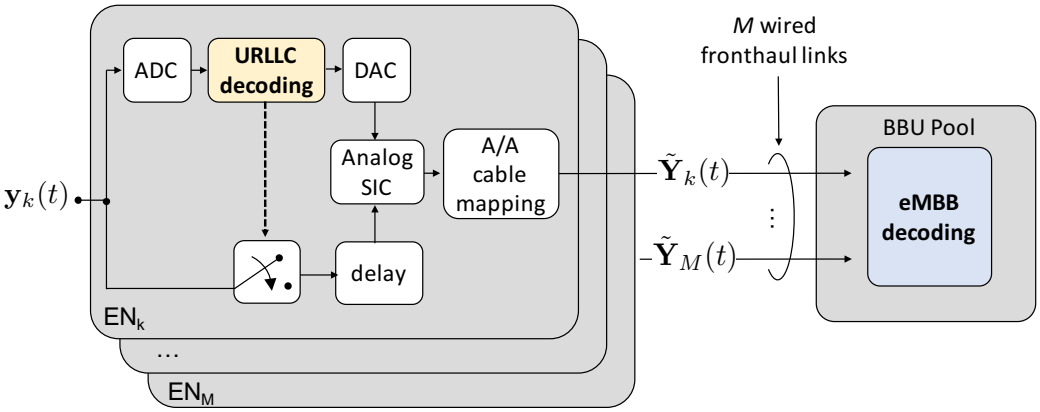

Figure 9.9.: Block diagram of the operation of the ENs and BBU for Non-Orthogonal Multiple Access (NOMA) by successive interference cancellation (SIC).

Finally, a more complex receiver architecture can be considered at the BBU, whereby interference is cancelled out from the useful signal. This technique, referred to as successive interference cancellation (SIC), is based on the idea that, if

an URLLC signal is successfully decoded at the EN_k, it can be cancelled from the overall received signal $\mathbf{y}_k$ prior to the relaying over the cable, so that an ideally interference-free eMBB signal is forwarded to the BBU. We also assume that, if the URLLC signal is not successfully decoded, signal $\mathbf{y}_k$ is discarded.

As a practical note, SIC must by performed in the analog domain, thus complicating the system design. Practical complications are not considered in the analysis here. As shown in Fig. 9.9, if the URLLC signal is successfully decoded at EN_k, this needs first be digital-to-analog converted (DAC) and then cancelled from the analog signal $\mathbf{y}_k$. Therefore, signal $\mathbf{y}_k$ needs to be suitably delayed in order to wait for the cascade of ADC, decoding, and DAC operations to be completed at the URLLC decoder. Being latency not an issue for eMBB traffic, here we assume to employ ideal ADC/DAC, so that the delay in Fig. 9.9 is assumed as ideally zero.

In order to account for imperfect SIC, the amplitude of the residual URLLC interference on eMBB signal is assumed to be proportional to a factor $\rho \in [0, 1]$. Accordingly, perfect SIC corresponds to $\rho = 0$, and no SIC to $\rho = 1$.

The signal received at the BBU from EN_k can be thus written as

$$Y_k^f = (1 - A_k E_k)(X_k^f + \alpha X_{k+1}^f + \alpha X_{k-1}^f) + \rho\beta A_k (1 - E_k) U_k^f + Z_k^f, \quad (9.40)$$

where the Bernoulli variable $E_k \sim \mathcal{B}(q\epsilon_U^D)$ indicates whether there has been an error in decoding the URLLC packet (i.e., $E_k = 1$), or it has been successfully decoded (i.e., $E_k = 0$), and A_k is the same as above. It is easy to show that the factor $(1 - A_k E_k)$ multiplying the eMBB signal indicates that the eMBB signal (9.40) is discarded only when the two following events simultaneously happen: *i)* there is a URLLC transmission (i.e., $A_k = 1$, whose probability is q), and *ii)* such URLLC transmission is not successfully decoded ($E_k = 1$, whose probability is ϵ_U^D). In turn, the factor $A_k(1 - E_k)$ multiplying the URLLC signal implies that, if there is a URLLC transmission (i.e., $A_k = 1$) and such transmission is successfully decoded at the EN_k (i.e., $E_k = 0$), then the URLLC signal is mitigated by analog SIC so that only a ρ-fraction of it is forwarded to the BBU and impairs the eMBB transmission.

The signal in (9.40) received across all ENs and frequencies in the case of NOMA by SIC can be equivalently written in matrix form as

$$\mathbf{Y} = \mathbf{X}\mathbf{H}\left(\mathbf{I} - \mathbf{A}\mathbf{E}\right) + \rho\beta\mathbf{U}\mathbf{A}\left(\mathbf{I} - \mathbf{E}\right) + \mathbf{Z}, \quad (9.41)$$

where $\mathbf{E} = \text{diag}(E_1, E_2, ..., E_M)$. The eMBB UE rate for NOMA by SIC can thus be computed by substituting signal (9.41) in (9.24) and the final result is in Lemma 9.5.

Lemma 9.5. *In the given C-RAN architecture with analog fronthaul links, for a given bandwidth amplification factor $\eta \geq 1$, the eMBB user rate under NOMA by SIC yields*

$$R_B = \frac{\mu}{M}\mathbb{E}_{\mathbf{A},\mathbf{E}}\left[log\left(det\left(\mathbf{I} + P_B \mathbf{R}_{AE,z_{eq}}^{-1}\mathbf{H}_{AE}\mathbf{H}_{AE}^T\right)\right)\right], \quad (9.42)$$

where $\mathbf{H}_{AE} = ((\mathbf{I} - \mathbf{AE})\mathbf{H}) \otimes \mathbf{H}_c^{\eta}$ *is the equivalent wireless plus cable channel in case of SIC;* $\mathbf{E} = diag(E_1, E_2, ..., E_M)$ *is a diagonal matrix whose k-th entry* $E_k \sim \mathcal{B}(q\epsilon_U^D)$ *accounts for the probability that the URLLC signal is not successfully decoded at* EN_k*; and* $\mathbf{R}_{AE,z_{eq}} = \mathbf{R}_{z_{eq}} + \rho^2\beta^2 P_U\left((\mathbf{A}(\mathbf{I} - \mathbf{E})) \otimes \mathbf{H}_c^{\eta}\mathbf{H}_c^{\eta}\right)$ *is the overall noise plus residual URLLC interference.*

Proof. Lemma 5 can be proved by following similar steps as for the proofs of the previous Lemmas. □

SIC describes a more complex ENs architecture in which the URLLC signals, if successfully decoded, are successively canceled from the eMBB signals at the EN. However, in the case of imperfect interference cancellation, i.e., $\rho > 0$, the eMBB signal is still impaired by some residual URLLC interference, which is accounted for by the overall noise covariance $\mathbf{R}_{AE,z_{\text{eq}}}$ in (9.42), similarly to TIN. The URLLC arrival probability and the probability of successful decoding of the URLLC packets are reflected by random matrices $\mathbf{A}$ and $\mathbf{E}$, respectively.

9.6. Numerical Results

Numerical results based on the previous theoretical discussion are shown in this section with the aim of providing some useful intuitions about the performance of C-RAN systems based on analog RoC in the presence of both URLLC and eMBB services. Unless otherwise stated, we consider the following settings: $M = 6$ ENs, $n_F = 60$ subcarriers[2], $P_B = 7\,\text{dB}$, $P_U = 10\,\text{dB}$, URLLC channel gain $\beta^2 = 1$, $P_C = 7\,\text{dB}$ $l_S = 4$, and, conventionally, $\epsilon_U = 10^{-3}$. In the case of OMA, the worst-case access latency for URLLC users is set to $L_U = 2$ minislots.

Fig. 9.10 shows URLLC and eMBB per-UE rates for both OMA and NOMA by varying the fronthaul crosstalk interference power γ^2 . We consider two values for the normalized bandwidth μ of each copper cable, namely $\mu = 1/l_S = 1/4$ and $\mu = 1$. Note that the first value corresponds to the minimal bandwidth, while the latter enables each twisted-pair to carry the whole signal bandwidth. For reference, the eMBB rates obtained in the case of ideal fronthaul are shown for both OMA and NOMA. The inter-cell interference power is set to $\alpha^2 = 0.2$, and the URLLC arrival probability to $q = 10^{-3}$. For NOMA, we consider here only puncturing.

The URLLC rates do not depend on cable crosstalk interference γ^2, since URLLC packets are decoded at the EN and thus never forwarded to the BBU over the fronthaul. Furthermore, with NOMA, the access latency of URLLC is minimum, i.e., $L_U = 1$, while for OMA it equals $L_U = 2$. However, Fig. 9.10 shows that

[2]This choice is motivated by the fact that, while still resembling the properties of URLLC short-packet transmissions, $n_F = 60$ is a sufficiently long packet size to ensure tight lower and upper bounds for the limited-blocklength channel capacity [159].

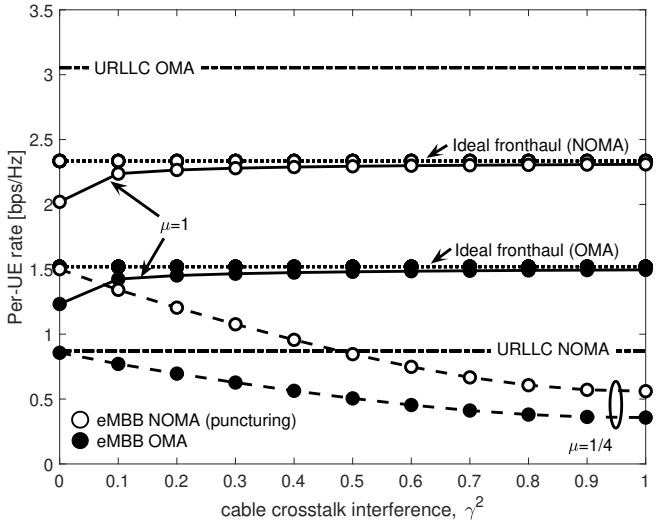

Figure 9.10.: URLLC and eMBB per-UE rates as a function of fronthaul crosstalk interference power γ^2 for OMA and NOMA with puncturing.

the price to pay for this reduced latency is in terms of transmission rate, which is lower than in the OMA case. On the contrary, in the case of eMBB, NOMA allows for a communication at higher rates than those achieved by OMA, thanks to the larger available bandwidth when q is small enough.

On the subject of eMBB rates, it is interesting to discuss the interplay between the normalized cable bandwidth μ and crosstalk power γ^2. For $\mu = 1$, the same signal is transmitted over all the $l_S = 4$ fronthaul twisted-pairs, and hence the four spatial paths sum coherently over the cable , thus turning crosstalk into a benefit. Hence, the eMBB rates under both OMA and NOMA increase with γ^2 and ultimately converge to those achieved over the ideal fronthaul.[3] For $\mu = 1/4$ instead, disjoint portions of the radio signal are transmitted over different interfering twisted-pairs, and the performance progressively decrease with γ^2. The leftmost portion of Fig. 9.10 suggests that for mild cable interference, even when the cable bandwidth is small (i.e., $\mu = 1/4$), it is still possible to provide communication with acceptable performance degradation, i.e., with a ≈ 1 bps/Hz loss from the ideal fronthaul case for NOMA, and an even smaller loss for OMA. However, when the cable crosstalk

[3] In this chapter, we consider the same interference gain g for all fronthaul links. In practice, the performance boost shown in Fig. 9.10 for increasing γ and for $\eta = 1$ would still be present, albeit to a different extent dependent on the channel realization, even if considering complex channel gain. However, this would require the use of more complex precoding techniques, such as Tomlinson-Harashima Precoding (THP, see Chapter 2 for further details), which require an estimate of the fronthaul channel. Since for wired fronthauling the channel is nearly static and time-invariant, channel state information can be easily obtained [40].

increases, the rate degradation is severe, and fair performance are achieved only if the cable bandwidth is large enough to accommodate the redundant transmission of radio signals over all pairs, i.e., $\mu = 1$.

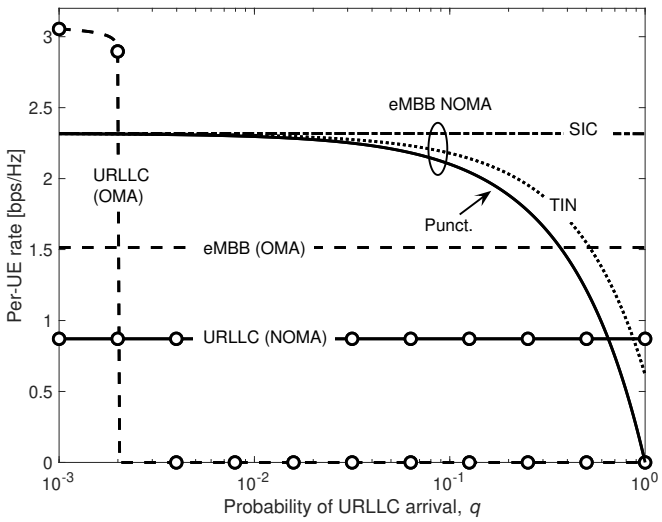

Figure 9.11.: URLLC and eMBB rates vs probability of URLLC arrival q for OMA and NOMA by puncturing, treating interference as noise (TIN), and successive interference cancellation (SIC).

Fig. 9.11 shows URLLC and eMBB rates as a function of the URLLC packet arrival probability q. eMBB rates under OMA are compared with those achieved by NOMA under puncturing, TIN and SIC. We consider here full cable bandwidth availability $\mu = 1$ and $\gamma^2 = 1$, so that, as in Fig. 9.10, the rates achieved for both OMA and NOMA for low q (say, $q < 10^{-2}$) coincide with those achieved over the ideal fronthaul. Inter-cell interference is set to $\alpha^2 = 0.2$. As noted in [170], under OMA, when q increases, the probability of an URLLC packet to be dropped due to blockage becomes very high, preventing URLLC transmission from meeting the strict reliability constraints, and results in a vanishing URLLC rate. This is unlike in NOMA, whereby the URLLC rate is not affected by q, and the access latency is minimal, i.e., $L_U = 1$. For eMBB under NOMA, TIN always outperforms puncturing. This is because TIN does not discard any received minislot, thus contributing to the overall eMBB rate. The result is in contrast with the conventional digital capacity-constrained fronthaul considered in [170]. In fact, in the latter, for sufficient low q, it is preferable not to waste fronthaul capacity resources by quantizing samples received in minislots affected by URLLC interference in order to increase the resolution of the interference-free samples. Additional gains are achieved by SIC, which takes advantages of the high reliability, and thus high probability to be cancelled, of the URLLC signal at the EN.

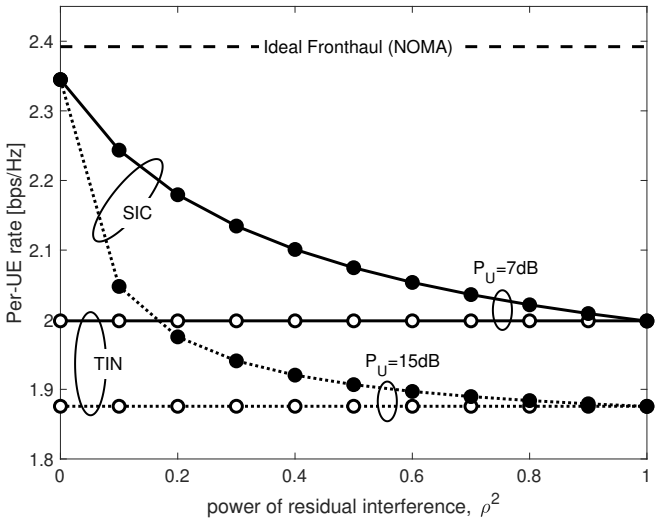

Figure 9.12.: eMBB rates for NOMA by SIC vs power of residual URLLC interference ρ^2.

Implementing SIC in a fully analog fashion is practically not trivial, and there is generally some residual URLLC interference. The effect of residual interference on the achievable eMBB rate is investigated in Fig. 9.12 for $q = 0.3$, $\alpha^2 = 0.4$, $\gamma^2 = 0.5$, $\mu = 1$ and for different power of URLLC UE P_U. Once again, in case of perfect interference cancellation, i.e., $\rho = 0$, SIC approaches the ideal fronthaul performance, while for more severe values of the residual interference power ρ, the eMBB performance progressively decreases. Nevertheless, even in the worst-case SIC scenario, i.e., $\rho = 1$, the achievable rates are never worse than those achieved by TIN irrespective of the value of P_U. This is once again due to the high reliability of URLLC transmission. It is in fact easy to prove that for $\rho = 1$ and low values of ϵ_U^D, the SIC eMBB rate in (9.42) converges to the one of TIN in (9.39).

For completeness, Fig. 9.13 shows the trade-off between eMBB and URLLC per-UE rates as a function of the access latency L_U for OMA and NOMA with puncturing, and considering $q = 10^{-3}$, $\alpha^2 = 0.2$ and $\gamma^2 = 0.5$. The behavior of the RoC-based C-RAN system versus the access latency L_U is similar to the one observed for digital capacity-constrained fronthaul [170] for both $\mu = 1$ and $\mu = 1/4$. While under OMA it is not possible to achieve a non-zero URLLC rate even at relatively low access latency such as $L_U > 3$, NOMA provides a reliable communication with constant minimal $L_U = 1$ access latency, but with lower rate. For eMBB, NOMA achieves a higher per-UE rate regardless of the value of the normalized bandwidth μ.

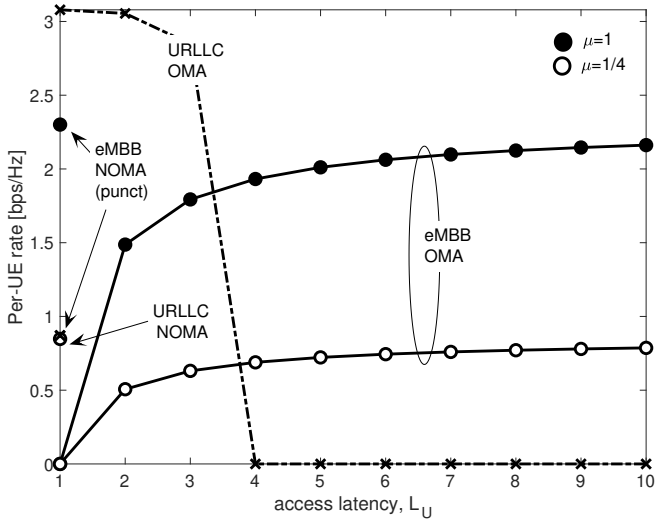

Figure 9.13.: URLLC and eMBB per-UE rates as a function of access latency L_U for OMA and NOMA with puncturing.

9.7. Concluding Remarks

This chapters considers the coexistence of eMBB and URLLC services in the uplink of an analog C-RAN architecture from an information theoretic perspective. The rate expressions for URLLC and eMBB users under orthogonal and non-orthogonal multiple access (OMA and NOMA, respectively) have been derived considering the Analog MIMO Radio-over-Copper (A-MIMO-RoC) architecture as a sample scenario, although the proposed model can be easily adapted to other analog fronthaul technologies. For eMBB signals, performance have been evaluated in terms of information rate, while for URLLC we also took into account worst-case access latency and reliability. In case of NOMA, different decoding strategies have been considered in order to mitigate the impact of URLLC transmission on eMBB information rate. In particular, the performance achieved by puncturing, considered for 5G standardization, have been compared with those achieved by Treating URLLC Interference as Noise (TIN), and by Successive URLLC Interference Cancellation (SIC).

The analysis showed that NOMA allows for higher eMBB information rates with respect to OMA, while guaranteeing a reliable low-rate URLLC communication with minimal access latency. Furthermore, numerical results demonstrated that, differently from the digital C-RAN architecture based on limited-capacity fronthaul links, for analog C-RAN, TIN always outperforms puncturing, and SIC achieves the best performance at the price of a higher decoder complexity.

As work in progress, the theoretical model can be extended to account for fading channels or geometric mmWave-link channel models.

Similarly, a frequency-dependent cable channel can be considered by making the cable crosstalk coefficient γ increase with cable frequency (e.g., as in Chapter 6-7-8). Another interesting research direction is to consider the case in which the BBU has no knowledge about the incoming signal, i.e., it is not able to detect the URLLC transmissions, so that it is impossible for the BBU to choose the proper metric for joint signal decoding [178, 179]. Finally, the overall system can be extended to the case of multiple users per-cell, where both ENs and users are equipped with multiple antennas.

10. A First Experimental Demonstration of Analog MIMO RoC

10.1. Introduction

5G will not be a further evolution of the existing 4G network, but it will rather be designed to smartly connect "anything, anywhere, any one". 5G should be highly integrative, tying together any air interface and spectrum with other 3GPP (i.e., LTE) and non-3GPP (i.e., WiFi) technologies to provide universal high-rate coverage and a seamless user experience [180]. In other words, 5G is expected to incorporate the pre-existing LTE-WiFi connectivity of all the billions of devices with multiple available interfaces in order to maintain simultaneous communication flows coming from a combination of RATs, to smooth the 5G transition, and to achieve a more efficient utilization of the available spectrum [181].

To pursue the 1000-fold rate increment foreseen by 2020, heterogeneous LTE/WiFi networks need to complement the 5G ecosystem with advanced physical layer technologies and network deployment strategies, leading to new complex interference scenarios [4]. Centralized Radio Access Network (RAN) architecture, by leveraging centralized signal processing and mutual cooperation for interference mitigation, is a very attractive solution to handle a large number of users and antennas in the same radio resources [5]. In C-RAN, multiple Remote Antenna Units (RAUs), which are geographically distributed both indoor and outdoor, are connected to colocated BaseBand Units (BBUs), where centralized processing is performed.

C-RAN based on digital fiber-optic links, namely Digital Radio-over-Fiber (D-RoF), is already deployed in current 4G mobile networks, in which BBUs and RAUs exchange over the FrontHaul (FH) link digitazed in-phase and quadrature signals [7]. However, bandwidth expansion due to digitization makes this digital fronthaul architecture hardly scalable to massive antennas RAUs and 5G-like radio signal bandwidth, thus favoring a fully analog FH link between RRUs and BBU.

Analog relaying of RF signals over the FH, which is the object of this thesis, is a promising solution for ultra-low latency applications where latency is ultimately limited to signal propagation, and also enables precise bit/carrier-frequency synchronization among multiple RAUs for MIMO joint processing [30, 31, 12, 13].

In particular, C-RAN with analog FH based on LAN cables, namely Analog Radio-over-Copper (A-RoC), is a practical solution for extending indoor coverage over the last 100-200m. As discussed in Chapter 6, LAN cables contain 4 twisted-pairs bonded together that have a transport capability that depends on cable lengths, such as 500 MHz bandwidth/pair for 200 m cable. Nevertheless, existing in-building commercial solutions based on LAN cables for the FH transmission use mainly the first few tens of MHz of LAN cable frequency bandwidth [31], for which cable attenuation and intra-cable crosstalk are mild, thus not fully exploiting the potential of copper cables. On the contrary, the A-MIMO-RoC architecture proposed here, by leveraging a smart mapping between radio and cable resources, namely Space-Frequency to Space-Frequency (SF2SF) multiplexing, pushes the frequency cable usage up to several hundreds of MHz, as shown in Chapters 7-8. The numerical analysis conducted in these previous chapters, which succeeded in showing the effectiveness of A-MIMO -RoC in terms of equivalent wireless capacity, is validated here by presenting a first experimental demonstration of A-MIMO-RoC architecture.

10.1.1. Chapter Contribution

The focus of this chapter is to demonstrate experimentally, and for the first time, the potential of A-MIMO-RoC architecture to carry multiple radio signals over the same LAN cable, thus proving A-MIMO-RoC to be an effective solution for perspective 5G indoor networks. A prototype has been developed in order to prove the feasibility of transporting, in an all-analog fashion, multiple MIMO radio signals over a single multi-pair copper cable at high cable frequency (i.e., impaired by high intra-cable crosstalk and cable attenuation, see Chapter 6) with negligible performance degradation, which enables a more efficient exploitation of LAN cables transport capabilities for indoor networks. In particular, the experiment not only confirmed that LAN cables are suitable for efficiently transporting multiple MIMO LTE radio signals, but it also demonstrated the feasibility of simultaneously carrying both MIMO LTE and MIMO Wi-Fi signals over the same cable, thus taking a first step towards the full-heterogeneity expected by 5G networks. For the purposes of this experiment, the TRIANGLE testbed [182, 183] has been employed to measure the end-to-end performance degradation introduced by the proposed A-MIMO-RoC architecture.

10.1.2. Contribution on International Conferences/Journals

Part of the material presented in this chapter has been published in:

- **A. Matera**, V. Rampa, M. Donati, A. Colamonico, A. F. Cattoni, U. Spagnolini "*Dual-RoC*: Dual Radio-over-Copper Remotization for C-RAN Architecture in 5G Deployments" presented at *2018 IEEE International Sympo-*

sium on Wireless Communication Systems Workshop (ISWCS Workshop), IEEE, 2018.

- **A. Matera**, V. Rampa, M. Donati, A. Colamonico, A. F. Cattoni, U. Spagnolini "A First Experimental Demonstration of Analog MIMO Radio-over-Copper" submitted to *IEEE Wireless Communications Letters.*
- **A. Matera**, V. Rampa, M. Donati, A. Colamonico, A. F. Cattoni and U. Spagnolini, "Analog MIMO Radio-over-Copper for Enhanced Indoor Coverage: Concepts and Validations" submitted to *IEEE Communications Magazine.*

10.2. The TRIANGLE Testbed

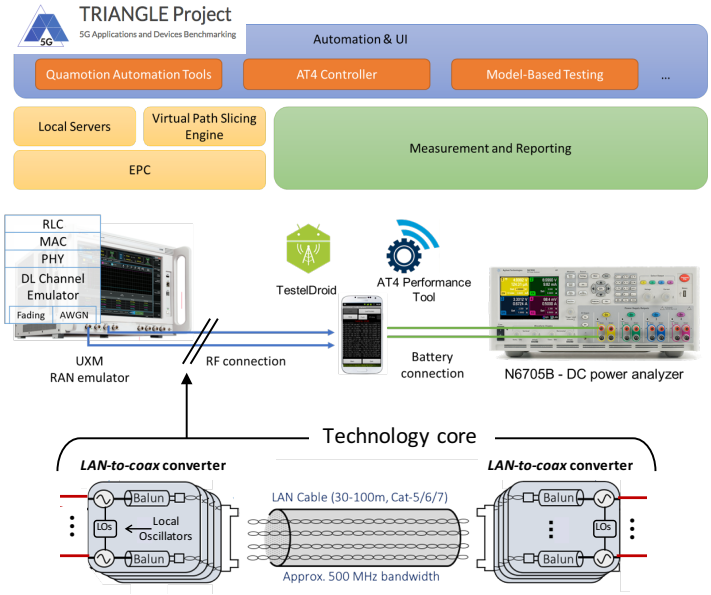

Figure 10.1.: A-MIMO-RoC integration into the TRIANGLE testbed

The TRIANGLE testbed, shown in the upper part of Fig. 10.1, is the main core of the H2020 TRIANGLE project [183], whose objective is to promote the testing and benchmarking of 5G mobile applications and User Equipments (UEs). In particular, the TRIANGLE testbed allows to run multiple tests in a controlled environment that encompasses all the elements of the telecommunication chain, from radio signal generation to the end-to-end testing of mobile applications. An extensive description of the TRIANGLE testbed is outside the scope of this chapter.

Details can be found in [182, 183], while here we review only the main elements that have been employed for the A-MIMO-RoC system.

10.2.1. Keysight UXM RAN Emulator

The UXM Wireless Test Platform device by Keysight Technologies allows to emulate multiple cellular networks in a controlled manner and supports multiple Radio Access Technologies (multi-RAT), including GSM/GPRS, UMTS and LTE-Advanced networks (i.e., 2G, 3G, 4G and 4.5G). The UXM features include intra-RAT and inter-RAT handovers, protocol debugging, IP end-to-end delay, BLock Error Rate (BLER) and throughput measurements, in addition to the possibility of performing RF conformance tests. The UXM offers great customization capabilities and a very intuitive user interface, which allow to easily evaluate the Key Performance Indicators (KPIs) of interest under any possible system setting defined by the 3GPP. Moreover, the UXM features an advanced fading engine with the main channels models defined by 3GPP [184]. In our specific case, the UXM has been employed to generate the MIMO LTE radio signal and to emulate specific propagating channel conditions, e.g., the ETSI Pedestrian at 5 Hz (EPA5) channel model, which fairly describes the indoor office scenario targeted by the A-MIMO-RoC system.

10.2.2. Mobile Device Monitoring

In order to measure the KPIs perceived by the end-device, some additional tools, detailed below, are needed on the smartphones under test (i.e., the UE), according to the scenario in Fig. 10.2.

10.2.2.1. Performance Tool

In order to guarantee high resolution reporting of the target QoS KPIs, especially in 5G scenarios, the DEKRA Performance Tool has been integrated into the TRIANGLE testbed. Beside providing accurate one-way measurements, the DEKRA Performance Tool tool includes a built-in traffic generator and enables the automation and testing of Android mobile Apps by measuring relevant Quality of Experience (QoE) KPI. In particular, the DEKRA Performance Tool was employed to perform end-to-end YouTube application testing, which allowed us to quantify the performance degradation introduced by the relaying over cable in terms of YouTube video streaming quality.

10.2.2.2. TestelDroid Mobile Monitoring App

TestelDroid is a software tool developed by the University of Malaga (UMA) [185] that enables passive monitoring of radio parameters and data traffic in Android-

based devices. Logging is implemented as an Android service that can be running in the background logging all the information while the application under test, e.g., YouTube, is being executed. This functionality enables monitoring of the traffic information generated by any application, which extends the testing to a very wide range of use cases. The logged parameters (network, neighbor cells, GPS, traffic) can be flexibly configured.

10.3. A-MIMO-RoC Experiment Setup

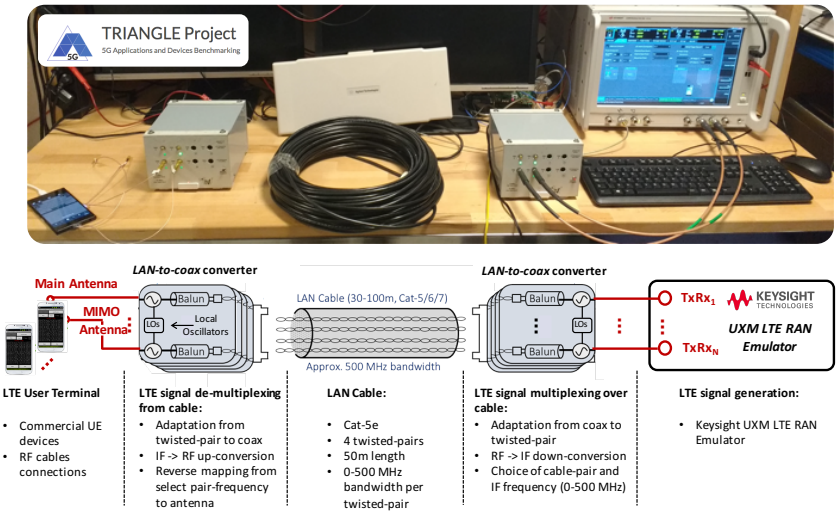

Figure 10.2.: A-MIMO-RoC experimental setup for LTE alone testing

For testing A-MIMO-RoC, the TRIANGLE testbed has been used in the typical device-testing configuration in Fig. 10.1, with the only difference that a 4-pairs RJ45 Cat-5e LAN cable has been inserted between the RF output ports of the UXM and the RF connections at the device to evaluate experimentally the performance degradation introduced by the all-analog relaying over copper. Fig. 10.1 shows the general experiment setup, while Fig. 10.2 and Fig. 10.3 detail the experiment setup used to test LTE alone and LTE-plus-WiFi, respectively. As shown in details in Figs. 10.2-10.3, the A-MIMO-RoC system is composed by two identical LAN-to-coax converters that perform impedance adaptation, cable equalization, coax-to-pairs mapping/demapping, and RF/IF conversion. Both converters include all-passive and all-analog devices along the signal path in order to perform fully bi-directional operations. For all wireless communications performed by exploiting the over A-MIMO-RoC platform, we used a 50 m long Cat-5e LAN cable (which is the cable type commonly deployed in buildings) with a cable bandwidth experimented here up to 400 MHz per twisted-pair. While the LTE signals have

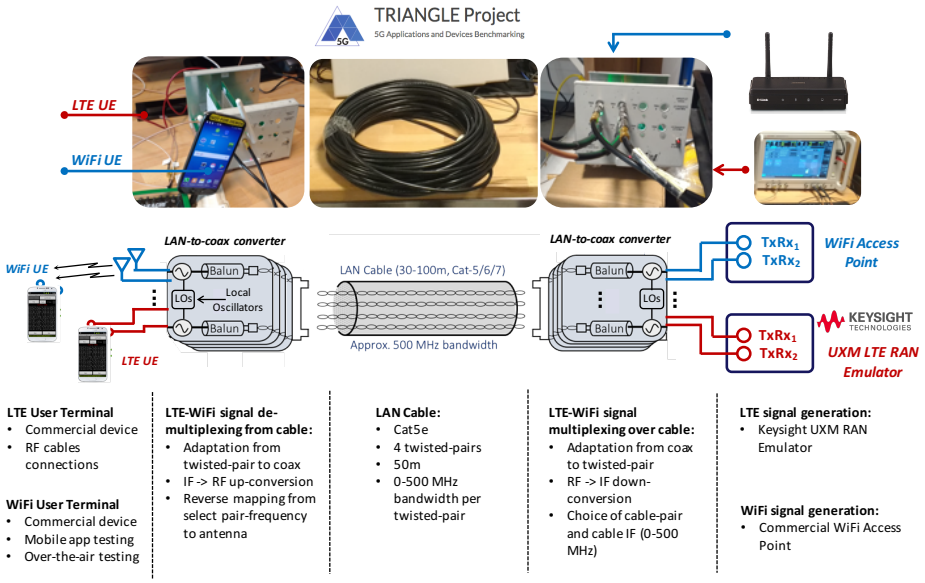

Figure 10.3.: A-MIMO-RoC experimental setup for LTE + WiFi testing

been generated by the UXM RAN emulator, for the WiFi testing, it has been employed a commercial WiFi Access Point (AP) for signal generation, and the transmission from the second LAN-to-coax converter to the device was over-the-air (see Fig. 10.3).

The experiment setup is represented in Fig. 10.2, together with a simplified block diagram detailing the role of each of the components used for the experiments (i.e., RAN Emulator, LAN-to-coax converters, LAN cables, and UE). In particular, the experiment setup is as follows (only the downlink is described, being the uplink symmetrical):

- up to 4 RF LTE (or WiFi) signals are generated by the UXM (or AP);
- RF cables are connected at each RF output of the UXM/AP;
- the signal carried on each RF cable is down-converted to Intermediate Frequency (IF) to match the bandwidth over the LAN cable (e.g., in the $10 \div 400$ MHz frequency range), possibly multiplexed in frequency over cable by the first LAN-to-coax converter;
- each IF-converted signal is conveyed by one of the 4 twisted-pairs: cable adaptation/equalization, coax-to-pairs mapping and RF/IF down-conversion between coax and twisted-pair is performed by the LAN-to-coax converter;
- at the other end of the LAN cable, RF cables (or antennas) are connected to the RF connectors of the second LAN-to-coax converter that performs cable

adaptation/equalization, pairs-to-coax de-mapping and IF/RF up-conversion to interface with the UE under test;

- DEKRA Performance Tool and TestelDroid, integrated into the TRIANGLE testbed, are used to test the UE.

10.4. Experimental Results

LTE System Settings	
Signal Generation	Keysight UXM RAN Emulator
LTE Band	B38 TDD, 2570-2620 GHz
Antenna Config.	2x2 MIMO
Transmission Mode	TM3
Channel Models	Static MIMO, EPA5 (low-, medium- and high-correlation)
Bandwidth (*BW*)	5, 10 or 20 MHz
Tx Power	-20 dBm/*BW* (Fig. 3-4), -15 dBm/*BW* (Fig. 5)

Table 10.1.: LTE system settings

WiFi System Settings	
Signal Generation	WiFi Commercial Access Point
WiFi Standard	802.11n
Bandwidth (*BW*)	20 MHz
WiFi Channel	#1, 2412 GHz
Antenna Config.	2x2 MIMO
Tx Power	0 dBm/BW

Table 10.2.: WiFi system settings

The goal of this experiment is to demonstrate the viability of remotizing RF antennas by relaying multiple LTE and WiFi signals (even simultaneously) over the same 50 m Cat-5e LAN at high cable frequency, and to evaluate the end-to-end performance degradation introduced by the copper cable. To accomplish this task, we first test A-MIMO-RoC with LTE signals alone, and then extend the experiments to the case in which both LTE and WiFi signals are carried over the same cable. The system settings parameters used for LTE and WiFi systems are reported in Table 10.1 and Table 10.2, respectively.

10.4.1. A-MIMO-RoC for LTE Testing

This section presents the experimental results related to the relaying of a 2×2 MIMO LTE signal over copper cable. The performance are evaluated here in downlink (DL) direction and in terms of throughput and Block Error Rate (BLER)

for different Modulation and Coding Schemes (MCS), ranging from 0-QPSK to 17-16QAM [186]. Two main experiments, detailed in the following, have been performed for testing the A-MIMO-RoC architecture with LTE signals.

10.4.1.1. A-MIMO-RoC versus cable IF

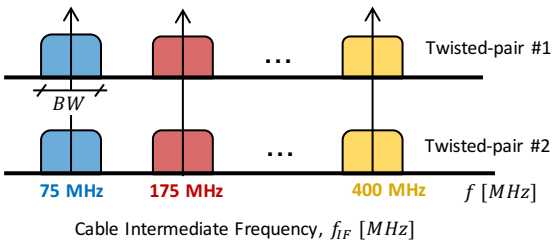

Figure 10.4.: RF signal mapping over cable: 2 LTE bands with bandwidth BW mapped over two different cable-pairs at the same cable-IF.

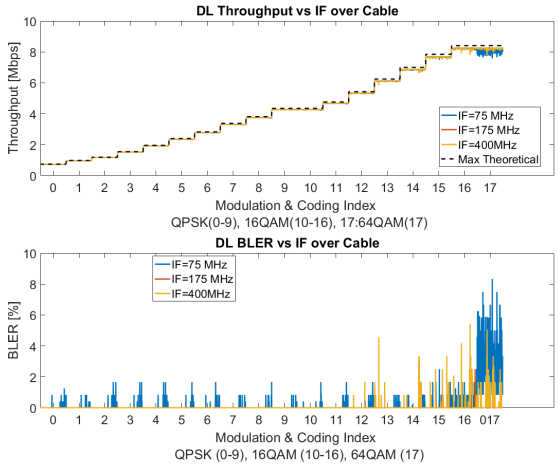

Figure 10.5.: A-MIMO-RoC performances (Throughput and BLER) vs. f_{IF} for $BW = 5$ MHz and different modulation schemes.

The goal of this experiment was two-fold: *i)* to prove the feasibility of transporting the 2 RF bands, corresponding to the 2 MIMO TX ports, over 2 different twisted-pairs of the LAN cable, but at the same cable IF frequency (f_{IF}), thus interfering each other over cable (see Fig. 10.4); and *ii)* to evaluate the performance degradation by increasing f_{IF}, i.e., by employing f_{IF} for which interference among pairs

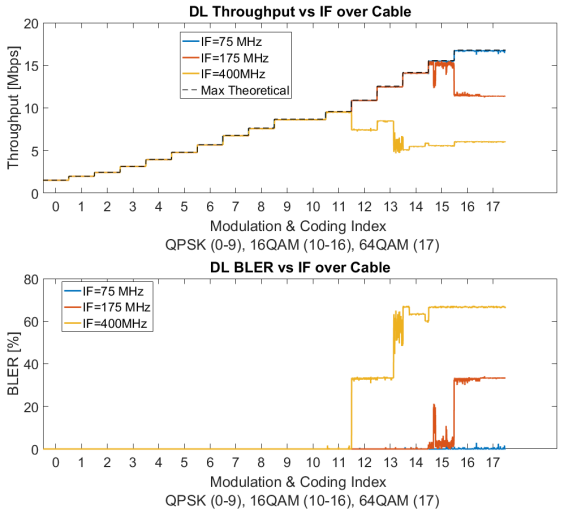

Figure 10.6.: A-MIMO-RoC performances (Throughput and BLER)vs. f_{IF} for $BW = 10$ MHz and different modulation schemes.

and attenuation are more severe (see Chapter 6 for further details).

In Fig. 10.5 and 10.6 throughput and BLER are shown considering a Static MIMO channel, -20 dBm/BW input power, and three different cable values for f_{IF}, as shown in Fig. 10.4: $f_{\text{IF}} = 75$ MHz (blue curves), $f_{\text{IF}} = 175$ MHz (red curves) and $f_{\text{IF}} = 400$ MHz (yellow curves). The maximum theoretical throughput achievable by each MCS [186] (black dashed line) over the considered channel bandwidth (BW) is shown as reference, thus quantifying the performance degradation introduced by the proposed system. In case of $BW = 5$ MHz, shown in Fig. 10.5, the loss in terms of throughput introduced by A-MIMO-RoC is almost negligible for all the considered MCS and cable f_{IF}. As expected, BLER increases for high MCS, but the degradation with respect to the maximum achievable throughput is still small. However, for $BW = 10$ MHz, shown in Fig. 10.6, the maximum throughput is achieved for all the MCS only for $f_{\text{IF}} = 75$ MHz, while for $f_{\text{IF}} = 175$ MHz and $f_{\text{IF}} = 400$ MHz the maximum MCS that can be employed with fairly low BLER are 15-16QAM and 11-16QAM, respectively. This performance degradation, which is more pronounced for higher f_{IF}, is totally expected, and it is explained by the fact that both cable crosstalk and attenuation increase with cable frequency (see Chapter 6). Moreover, the input power is the same for both settings, i.e., $BW = 5$ MHz and $BW = 10$ MHz (see Table 10.1). Hence, to smaller channel bandwidth it corresponds higher Signal-to-Noise Ratio (SNR) per subcarrier, which explains the better performance obtained in case of $BW = 5$ MHz. Notice that the LAN-to-coax converter is an all-passive device, and the relaying over cable introduces a significant attenuation (in the order of 60 dB) which forces the whole communi-

cation system to work close to the UE sensitivity [186], even by setting the input power to the maximum value allowed by the hardware devices. As a consequence, it is expected that the performance loss observed in case of $BW = 10$ MHz can be avoided by introducing some signal amplification in the system design, which is left as future works. In any case, Fig. 10.6 confirms the feasibility of relaying LTE signals over high frequency copper cable bands: even in the worst case of 2 LTE bands transported over 2 different cable twisted-pairs at the same $f_{\text{IF}} = 400$ MHz, it is still possible to achieve a throughput of approx. 10 Mbps over $BW = 10$ MHz.

10.4.1.2. A-MIMO-RoC versus Channel Models

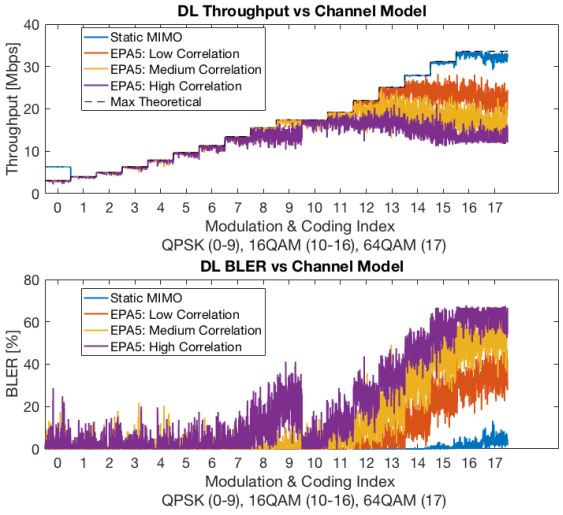

Figure 10.7.: A-MIMO-RoC vs Channel Model and MCS, $BW = 20$ MHz

The goal of this experiment was to evaluate how the A-MIMO-RoC platform performs in different MIMO channel model scenarios. In particular, we adopted the ETSI Pedestrian at 5 Hz (EPA5) channel, as it fairly describes the propagating conditions of an indoor office environment, which is the target application scenario for the A-MIMO-RoC platform. We considered a 2×2 MIMO LTE signal with $BW = 20$ MHz, where the 2 RF bands were transported over 2 different twisted-pairs at the same frequency $f_{\text{IF}} = 175$ MHz. In this experiment the input power was set to -15 dBm/BW.

Fig. 10.7 shows that, in the case of Static MIMO channel, even for $BW = 20$ MHz, the performance degradation introduced by the cable is negligible (only a small loss can be appreciated for high MCS). However, in case of EPA5 channel

model, performance get worse, especially for medium and high channel correlation. Once again, the reason for this is the all-passive circuitry implementation of our system, that simplifies the hardware design of the prototype but introduces a significant attenuation. In fact, the power fluctuations introduced by the EPA5 channel make the system oscillate around the UE sensitivity threshold for high MCS, which explains the curves behavior in the rightmost portion of the figure. Fig. 10.7 shows that, even in the worst case of high-correlated EPA5 channel, it is still possible to transmit 16QAM modulation achieving slightly less than 20 Mbps.

10.4.2. MIMO LTE-plus-WiFi-over-Copper

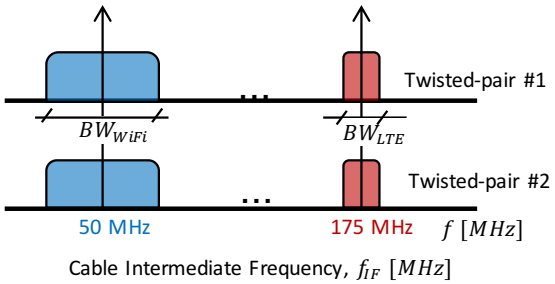

Figure 10.8.: LTE and WiFi bands mapping over cable IF

This section collects the results related to the simultaneous relaying of a MIMO LTE and a MIMO WiFi signal over the same copper cable. The aim is to experimentally prove the feasibility of transporting over the same LAN cable a 2×2 MIMO LTE signal and a 2×2 MIMO WiFi signal. In particular, our main interest was to evaluate the impact of each one of the two technologies (i.e., either LTE or WiFi) on the other, when they are simultaneously relayed over cable. As represented in Fig. 10.8, we considered a 2×2 MIMO WiFi signal with bandwidth $BW_{WiFi} = 20$ MHz and a 2×2 MIMO LTE signal with bandwidth $BW_{LTE} = 5$ MHz. Furthermore, the LAN-to-coax converters have been programmed in such a way that the 2 LTE bands have been allocated over 2 different pairs at $f_{\text{IF}} = 175$ MHz, while the 2 WiFi bands have been allocated over the same two pairs but at $f_{\text{IF}} = 40$ MHz.

Fig. 10.9 shows the performance comparison between LTE transmission alone (orange curve) and LTE transmission in coexistence with WiFi (blue curve). It can be observed that up to approx. MCS 13-16QAM the degradation on LTE performance due to WiFi is almost negligible, while it is more pronounced for higher MCS. Nevertheless, the result in Fig. 10.9 is quite encouraging: rather than a drastic performance loss (e.g., as the one shown in Fig. 10.6 for high

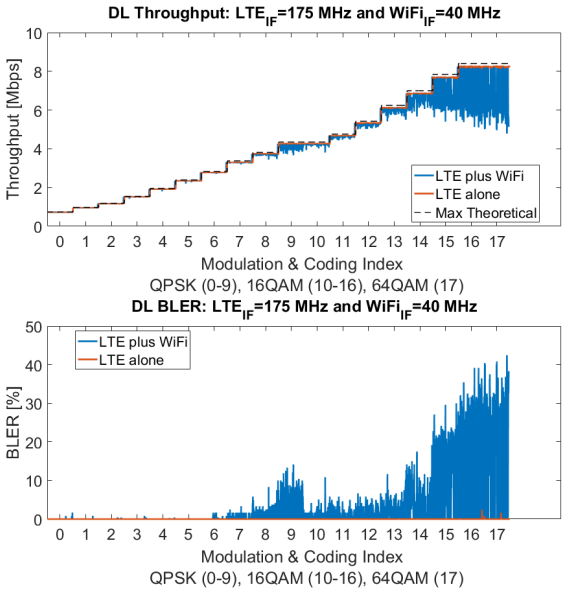

Figure 10.9.: MIMO LTE-plus-WiFi-over-Copper vs MCS

	RSSI	medium	large	hd720	hd1080
Wifi (alone)	-80 dBm	2%	1%	7%	90%
Wifi (with LTE)	-80 dBm	2%	5%	4%	89%

Figure 10.10.: MIMO LTE-plus-WiFi-over-Copper, Video Quality and RSSI

MCS), it shows that for high MCS the throughput curve (and thus the behavior of BLER) presents very quick fluctuations to/from the maximum theoretical throughput. This fluctuating effect is again due to a hardware-related issue (i.e., all-passive system implementation), and has been emphasized by the huge difference in transmitted power between WiFi and LTE signals (it was not possible to further lower the transmitted power of the commercial WiFi AP). By modifying the hardware design accordingly (i.e., by introducing some power amplification and active equalization in the circuit), we expect the performance degradation due to the simultaneous WiFi transmission to become negligible even for high MCS.

For WiFi performance testing, YouTube video streaming test has been performed. Symmetrically to the previous case, performance have been measured both for WiFi alone and in coexistence with LTE. In particular, YouTube videos have been playing on the smartphone under test for the overall duration of approx. 45 minutes. Fig, 10.10 shows the average Received Signal Strength Indicator (RSSI)

and the percentage of time during which the video has been reproduced in a specific video quality, thus confirming that YouTube streaming video quality with WiFi experiences almost no degradation due to the simultaneous LTE transmission.

10.5. Concluding Remarks

This last chapter demonstrated experimentally, and for the first time, the feasibility of an Analog MIMO Radio-over-Copper (A-MIMO-RoC) prototype to transparently relay multiple radio signals (i.e., LTE, WiFi, and LTE-plus-WiFi) over a single LAN cable in an all-analog fashion (i.e., without latency), even at high cable frequency, thus validating the numerical results presented in the previous chapters. In particular, the conclusions drawn by the experiments can be summarized as follows: *i)* LAN cables bandwidth capability can be exploited up to several hundreds of MHz for transparently transporting multiple MIMO RF signals over the last 100-200m, and this happens even when such signals are transported over different cable pairs but at the same IF, thus being affected by cable-crosstalk interference; *ii)* A-MIMO-RoC is capable of transporting, in a fully analog fashion, both MIMO LTE and MIMO WiFi signals over the same LAN cable, and this is enabled by mapping the RF signals onto purposely selected IF frequencies and twisted-pairs of the LAN cable (i.e., Space-Frequency to Space-Frequency multiplexing, SF2SF), *iii)* the performance degradation experienced for high MCS and high IF is mainly due to the low signal power received at the user device due to the attenuation introduced by the analog relay over cable; *iv)* again, due to the whole system attenuation, the prototype developed appears to be quite sensitive to signal power variations, and this reflects in some performance degradation when employing non-static MIMO channel models, e.g., ETSI Pedestrian at 5 Hz. For future developments of our technology, although the fully passive implementation considered here has substantially simplified the hardware design, the experiment results suggest that most of the issues encountered might be easily solved by introducing some active circuitry such as active equalization, amplification and power adaptations in the LAN-to-coax converters.

11. Conclusions

THIS thesis has dealt with the design of advanced interference mitigation techniques for communications systems characterized by the cascade of wireless and wired channels. The hybrid wired-wireless communication system model considered here accurately captures the physical characteristics of analog Cloud Radio Access Network (C-RAN) architecture, in which multiple, generally interfering, analog fronthaul links are used to exchange Radio-Frequency (RF) signals between the BaseBand Unit (BBU) and Remote Access Units (RAUs).

More precisely, the focus is on a particular analog C-RAN architecture, known as Analog Radio-over-Copper (A-RoC), in which twisted-pairs copper cables are employed for the fronthauling. The final goal of the thesis has been thus to propose and design a novel and more general RoC-based fronthaul architecture, denoted Analog *MIMO* RoC (A-MIMO-RoC), in which the RF signals at the multiple-antenna RAUs need to be mapped onto opportunely chosen twisted-pairs/frequency resource blocks over the cable fronthaul. This resource allocation strategy, referred to as Space-Frequency to Space-Frequency (SF2SF) multiplexing recalling the two multiplexing dimensions over wired and wireless channels, has been shown to be capable to substantially mitigate the mutually coupled wireless-plus-wired interference, thus enabling the full exploitation of the transport capabilities of the pre-exiting copper cabling infrastructure of buildings.

However, the path towards this final goal has not been so straightforward, and required some preliminary investigation steps. In order to fully understand the behavior of the hybrid wired-wireless A-MIMO-RoC architecture, which is covered in Part III of the thesis ("Interference Mitigation Techniques for Hybrid Wired-Wireless Communications Systems: *the Analog MIMO Radio-over-Copper Architecture*"), a first fundamental research stage has been entirely devoted to the deep investigation of interference mitigation techniques designed for wired and wireless channels, *separately,* covered in Part II ("Interference Mitigation Techniques for Wireless Communication Systems") and Part III ("Interference Mitigation Techniques for Wireless Communication Systems") of the thesis, respectively.

In particular, the first part of the thesis considered the problem of downstream Far-End-CrossTalk (FEXT) interference cancellation, also known as vectoring, in the next generation Digital Subscriber Line (DSL) standard, namely G.fast. Firstly, two non-linear vectoring techniques, denoted as Tomlinson-Harashima Precoding with Dynamic Ordering (THP-DO) and Lattice-Reduction Aided Zero-Forcing Precoding with Optimal Power Allocation (LR-ZF-OPA) have been proposed. The

former guarantees fair user performance by maximizing the minimum user rate, but introduces additional signal processing delay and complexity due to sequential line-by-line non-linear interference cancellation. In contrast, the latter can be implemented in parallel over all the DSL lines, but the data-rate performance are worse than those achieved by THP-DO. As a further step in this direction, in order to address the trade-off among performance, complexity and signal processing delay, a novel hybrid linear/non-linear precoding architecture has been proposed in order to parallelize conventional THP over several vectored DSL lines groups. The performance of this low-complexity/latency parallel THP architecture, referred to as Multi Vectored Group (VP) THP, attain those of centralized fully non-linear THP, but with much lower complexity and latency, which are thus spread over several VPs.

In the second part of the thesis, interference mitigation techniques for wireless communication systems have been designed focusing on multi-operator cellular systems and optical wireless communications. In particular, the proposed cooperative multi-operator interference mitigation strategy allows multiple operators, generally reluctant to exchange users' sensitive data, to cooperatively carry out joint signal transmission and precoding by exchanging only each others' interference. By leveraging tools from information theory and physical layer security, it has been shown that this precoding mechanism based on interference exchange is capable to cope with multi-operator interference while providing privacy for all the operators. As a next step, motivated by the promising results achieved for DSL systems, THP has been proposed for in-flight Visible Light Communication (VLC) systems. THP, which provides great interference cancellation capabilities while limiting the power of the transmitted signals, has been shown to be a particularly suitable precoding algorithm for VLC systems, characterized by strict power constraints on the light sources, i.e., LEDs. In particular, THP has been proved to provide higher rate performance with respect to linear precoding strategies while guaranteeing seamless user connectivity even in the challenging case of transmitter-receiver misalignment caused by user devices' movements.

The third part of the thesis, which is the core of the research activity, has been devoted to the investigation and design of the proposed Analog MIMO RoC architecture. First, the transport capabilities of copper cables (i.e., LAN cables), already deployed in buildings and enterprises, have been analyzed, showing that up to 60 RAU antennas each carrying a 20 MHz LTE signals can be carried over a single LAN cable. Once proved the A-MIMO-RoC concept for indoor fronthaul applications, the immediate next step has been the design of the aforementioned SF2SF multiplexing technique between wireless resources at the RAU antennas and twisted-pair/frequency resources over the cable. Considering a single-user scenario, the SF2SF optimization problem has been first designed for the A-MIMO-RoC uplink, and then extended to the A-MIMO-RoC downlink channel, which is complicated by the heterogeneous power constraints over the wired and wireless channels. SF2SF has been proved to provide significant performance enhancement in both cases. Furthermore, for the multi-user case, SF2SF multiplexing has been

jointly designed with digital BBU precoding techniques in order to simultaneously deal with wireless multi-user interference and cable fronthaul impairments. The proposed combination of SF2SF with digital precoding, which ha been inspired by DSL vectoring techniques, has been shown to attain the performance of state-of-the art amplify-and-forward precoding techniques while providing substantial performance gains in terms of minimum user rates. As a further step, A-MIMO-RoC has been extended to heterogeneous 5G networks in which Ultra Reliable Low Latency Communications (URLLC) and enhanced Mobile BroadBand (eMBB) services coexist in the same physical resources. The analysis has been performed from an information theoretical perspective, and provided several useful insights on the performance trade-off between eMBB and URLLC, considering both Orthogonal and Non-Orthogonal Multiple Access techniques (OMA and NOMA, respectively) and different NOMA decoding strategies. As a final step, a first A-MIMO-RoC prototype has been developed to experimentally prove the feasibility of the analog relaying of RF signals over LAN cables. The experiment proved that a single LAN cable is not only capable to transport MIMO LTE signals at high cable frequency (tested here up to 400 MHz), but it is even capable to simultaneously carry both MIMO LTE and MIMO WiFi signals with minor performance degradations.

Concluding, starting from the native idea of A-RoC, this thesis proposed A-MIMO-RoC: an analog C-RAN architecture characterized by the cascade of wired and wireless channels. Advanced precoding techniques and resource allocation strategies have been proposed to deal with the mutually coupled wireless and wired A-MIMO-RoC interferences considering different communications scenarios: uplink and downlink channels, single and multi-user scenarios, but also heterogeneous 5G networks. The overall theoretical discussion has been finally supported by experimental results which make A-MIMO-RoC not only an interesting research topic providing numerous theoretical insights, but mainly a practical solution capable to cope with real-world problems that engineers and researchers are facing today in deploying next generation 5G networks. The fact is that RF signals hardly penetrate into larger buildings from the outside network and, in this direction, A-MIMO-RoC represents an important step towards the design of dedicated indoor wireless systems for the billions of buildings which nowadays still suffer from indoor coverage issues.

A. Appendix for Chapter 7

A.1. Statistical Interference Covariance Model

The interference coming from the neighboring cells is available only in terms of spatial covariance matrix $\mathbf{R}_I$ for the beamforming design at the BBU. The computation of the statistical interference covariance matrix $\mathbf{R}_I$ is detailed here for the scenario depicted in Fig. A.1. The covariance matrix for a set of M_I interferers, characterized by powers $\{\beta_k^2\}_{k=1}^{M_I}$ received at the antenna array and DoAs $\{\theta_k\}_{k=1}^{M_I}$, is known only in its expected value as

$$\mathbf{R}_I = \mathrm{E}\left[\sum_{k=1}^{M_I} \beta_k^2 \mathbf{a}(\theta_k)\mathbf{a}(\theta_k)^H\right], \tag{A.1}$$

where the expectation is taken with respect to the random variables $\{\beta_k^2\}_{k=1}^{M_I}$ and $\{\theta_k\}_{k=1}^{M_I}$ used to describe each interferer. The received power $\beta_k^2 = 1/d_k^2$ accounts for the path loss as in (7.22). To obtain the expected value in (A.1), the first step is to derive the joint probability density function (pdf) $f(\beta^2, \theta)$ of the received power β^2 and DoA θ for a generic interferer uniformly distributed over the service area (see Fig. A.1).

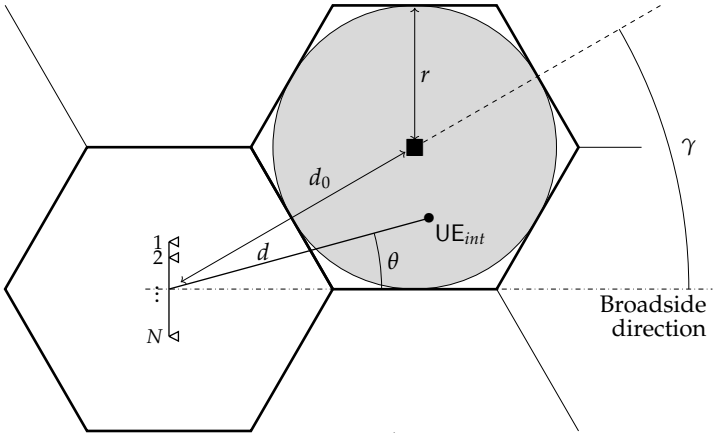

Figure A.1.: Geometric model for the statistical description of inter-cell interference

Let us consider randomly and uniformly distributed users within the cells. Hence, the pdf of the position of a user inside the cell is $f(x,y) = 1/\pi r^2$ for (x,y) inside the cell. From the geometry, the pdf of the DoA is

$$f(\theta) \propto c(\theta), \tag{A.2}$$

where $c(\theta)$ is the chord defined as

$$c(\theta) = 2r\sqrt{1 - \frac{d_0^2}{r^2}\sin^2(\gamma - \theta)}. \tag{A.3}$$

In order to have $\int_\Theta f(\theta)d\theta = 1$, a proportionality factor K is introduced:

$$K = \frac{1}{\int_\Theta c(\theta)d\theta}, \tag{A.4}$$

where Θ is the set of possible DoAs for the interferers. Hence, $\Theta = [\theta_{min}, \theta_{max}]$, where $\theta_{min}, \theta_{max} = \gamma \pm \arcsin(r/d_0)$. The conditional probability density function for the distance between the interferer and the array is

$$f(\rho|\theta) = \frac{1}{c(\theta)}, \tag{A.5}$$

Overall, the joint pdf for the distance and angular position is

$$f(\rho,\theta) = f(\rho|\theta)f(\theta) = K = \frac{1}{\int_\Theta c(\theta)d\theta}. \tag{A.6}$$

To obtain the joint pdf for received power and DoA, a change of variable is needed. Let us set $\beta^2 = g(\rho) = 1/\rho^2$. Therefore, since the transformation $g(\rho)$ is monotonic, the pdf is

$$f(\beta^2,\theta) = \left|\frac{\partial g^{-1}(\beta^2)}{\partial \beta^2}\right| f(g^{-1}(\beta^2),\theta) = \frac{1}{2\int_\Theta c(\theta)d\theta}\beta^{-3} = Z\cdot\beta^{-3}, \tag{A.7}$$

where

$$Z = \frac{1}{2\int_\Theta c(\theta)d\theta} \tag{A.8}$$

is a scaling factor. The covariance matrix for M_I interferers is then

$$[\mathbf{R}_I]_{m,n} = \mathrm{E}\left[\sum_{k=1}^{M_I}\beta_k^2 a_n(\theta_k)a_m^*(\theta_k)\right] \tag{A.9}$$

Under the assumption of $\lambda/2$-spaced uniform linear array, the expected value in (A.9) is:

$$[\mathbf{R}_I]_{m,n} = M_I\int_\Theta\int_{\beta^2_{min}(\theta)}^{\beta^2_{max}(\theta)} e^{j\pi(n-m)\sin(\theta)}Z\beta^{-1}d(\beta^2)d\theta \tag{A.10}$$

The first integral, in $d(\beta^2)$, is performed analytically, while the second, in $d\theta$, is solved numerically to obtain

$$[\mathbf{R}_I]_{n,m} = \\ 2M \cdot Z \cdot \int_{\Theta} e^{j\pi(n-m)\sin(\theta)} \left[\frac{d_{max}^2(\theta) - d_{min}^2(\theta)}{d_{min}(\theta) d_{max}(\theta)} \right] d\theta \tag{A.11}$$

where $\Theta = [\theta_{min}, \theta_{max}]$ is the support for the DoAs of the interferers, $d_{min}(\theta)$ and $d_{max}(\theta)$ are the minimum and maximum distances associated with a specific DoA, and Z is the normalization factor in (A.8).

A.2. Cardinality of the Neighboring Permutations Set

Let us first recall some important definitions.

Definition A.1. Given an arbitrary permutation matrix $\mathbf{\Pi} \in \{0,1\}^N$, univocally defined by a vector $\boldsymbol{\pi} = [\pi_1, \pi_2, ..., \pi_N]^T$, the *neighboring permutations set* at an integer distance d_π is defined as the set of all vectors obtained by permuting in any way all subsets of $d \leq d_\pi$ elements in $\boldsymbol{\pi}$.

Definition A.2. Given a vector $\boldsymbol{\pi} = [\pi_1, \pi_2, ..., \pi_N]^T$, a *derangement* is defined as a permutation of the elements of the vector $\boldsymbol{\pi}$ such that no elements appears in its initial position. The *derangement number* or *de Montmort number* $!N$ is the total number of derangements of a vector of size N and is defined as

$$!N = N! \sum_{i=0}^{N} \frac{(-1)^i}{i!}. \tag{A.12}$$

In order to compute the cardinality the neighboring permutations set at distance d_π, we need to consider that for any integer $d \leq d_\pi$, and for each of the $\binom{N}{d}$ subsets of d elements of $\boldsymbol{\pi} = [\pi_1, \pi_2, ..., \pi_N]^T$, the number of neighboring vectors $\{\boldsymbol{\pi}_{\text{near}}\}$ obtained by permuting such d elements of $\boldsymbol{\pi}$ is $d! - 1$, thus the cardinality yields

$$\tilde{K}_{d_\pi} = \sum_{d=2}^{d_\pi} \binom{N}{d} \cdot (d! - 1). \tag{A.13}$$

However, a key observation is that two different subsets of d elements in $\boldsymbol{\pi}$ generate two non-disjoint sets of permutations, meaning that the set cardinality $\tilde{K}_{d_\pi}$ in (A.13) contains multiple duplicates of the same basic vectors.

Example A.1. Let us consider the vector $\mathbf{a} = [1, 2, 3, 4]^T$ and two of the possible subsets of $d = 3$ elements of vector $\mathbf{a}$ such as $a_1 = \{1, 2, 4\}$ and $a_2 = \{1, 2, 3\}$. By permuting the elements of $\mathbf{a}$ corresponding only to the first two elements of

subsets a_1 and a_2, we obtain two duplicates of the same *neighboring* vector $\mathbf{a}_{\text{near}} = [2, 1, 3, 4]$ from two different subsets. On the contrary, it is easy to show that, if we permute all the $d = 3$ elements of both subsets in such a way that none of the 3 elements maintain its initial position, we always obtain different neighboring vectors.

The previous example shows that in order to avoid to count multiple duplicates of the same basic vectors when computing the set cardinality, for each of the $\binom{N}{d}$ subsets of d elements in $\boldsymbol{\pi}$, we need to consider only those permutations in which none of the d elements maintains its initial position, thus exploiting the concept of *derangement number* $!d$ instead of the factorial $(d! - 1)$ in (A.13), which directly leads to (8.35).

B. Appendix for Chapter 8

B.1. THP Power Considerations

The value of the scaling factor β is proportional to the power penalty to be paid by performing a complete channel inversion at the BBU side. In general, linear ZF precoding may lead to $\beta_{\text{ZF}} \gg 1$ to contrast the amplitude peaks of the encoded symbols due to the hard-channel inversion which severely degrades the transmission rates for all the UEs. In THP the problem is inherently solved by the modulo operation which limits the power of the symbols sequentially encoded: this is mathematically reflected in the fact that

$$\beta_{\text{THP}} \leq 1, \tag{B.1}$$

meaning that in THP the PLPC power constraints are always fulfilled and β_{THP} acts as an AGC in order to fully exploit the available power.

To prove (B.1), let us consider the precoded symbols $\tilde{\mathbf{x}}_c = \tilde{\mathbf{F}}_b^{-1}\mathbf{s}$ at the output of the feedback block: in case of M-ary square QAM input symbols $\mathbf{s}$, the encoded symbols $\tilde{\mathbf{x}}_c$ are approximately uncorrelated with only a slight power increment with respect to the input symbols [41] as $\sigma_{\tilde{x}}^2 = \frac{M}{M-1}\sigma_s^2$, which becomes negligible for high modulation formats used in wireline communications (e.g. in G.fast this loss is maximum 1.25 dB [28]). Therefore, it can be assumed that

$$\text{E}[\tilde{\mathbf{x}}_c\tilde{\mathbf{x}}_c^H] \approx \mathbf{I}\sigma_{\tilde{x}}^2 \approx \mathbf{I} \tag{B.2}$$

under the assumption of unit power input symbols (i.e., $\sigma_s^2 = 1$). Let us now consider the k-th precoded symbol

$$x_{c,k} = \frac{1}{\beta_{\text{THP}}}\left[\tilde{\mathbf{F}}_f\tilde{\mathbf{x}}_c\right]_k = \frac{1}{\beta_{\text{THP}}}\left[\mathbf{Q}_1\tilde{\mathbf{x}}_c\right]_k = \frac{1}{\beta_{\text{THP}}}\mathbf{q}_{1,k}^T\tilde{\mathbf{x}}_c, \tag{B.3}$$

whose power is constrained by

$$\text{E}\left[|x_{c,k}|^2\right] = \frac{1}{\beta_{\text{THP}}^2}\left\|\mathbf{q}_{1,k}^T\right\|_2^2 \leq 1 \quad , \tag{B.4}$$

with $[\mathbf{a}]_k$ denoting the k-th element of vector $\mathbf{a}$ and $\mathbf{q}_{1,k}^T \in \mathbb{C}^{1\times N_r}$ the k-th row of matrix $\mathbf{Q}_1$. From (B.4), it follows that the available power is fully exploited when

$$\beta_{\text{THP}}^2 = \max_k \left\|\mathbf{q}_{1,k}^T\right\|_2^2. \tag{B.5}$$

The key observation is that $\mathbf{q}_{1,k}^T \in \mathbb{C}^{1\times N_r}$ contains only the first N_r entries of the k-th unit-length row $\mathbf{q}_k^T$ of the original unitary matrix $\mathbf{Q}$ coming from (5.31), hence,

$$\beta_{\text{THP}}^2 = \max_k \left\|\mathbf{q}_{1,k}^T\right\|_2^2 \leq \left\|\mathbf{q}_k^T\right\|_2^2 = 1, \tag{B.6}$$

which proves (B.1). The equality holds when the number of antennas at the RAU equals the number of single-antenna users, i.e., $N = N_r$, since $\tilde{\mathbf{F}}_f = \mathbf{Q}_1 = \mathbf{Q}$.

B.2. Proof of NP-hardness of the SF2SF Problem with THP

For $N = N_r$ considered in this paper, the power scaling factors β_{THP} and γ_{THP} used in THP simplify to

$$\beta_{\text{THP}} = 1, \tag{B.7}$$

and

$$\begin{aligned}\gamma_{\text{THP}} &= \sqrt{\frac{N}{\text{tr}(\mathbf{H}_{SF}\mathbf{F}\mathbf{F}^H\mathbf{H}_{SF}^H + \sigma_c^2\mathbf{I})}} \\ &\overset{(a)}{\approx} \sqrt{\frac{N}{\text{tr}(\mathbf{H}_{SF}\tilde{\mathbf{F}}_f\tilde{\mathbf{F}}_f^H\mathbf{H}_{SF}^H + \sigma_c^2\mathbf{I})}} \\ &\overset{(b)}{=} \sqrt{\frac{N}{\text{tr}(\mathbf{H}_c\mathbf{H}_c^H + \sigma_c^2\mathbf{I})}},\end{aligned} \tag{B.8}$$

where (B.7) has been proved in (B.6), $\overset{(a)}{\approx}$ follows from the fact that the symbols $\tilde{\mathbf{x}}_c = \tilde{\mathbf{F}}_b^{-1}\mathbf{s}$ at the output of the feedback block are approximately uncorrelated as in (B.2), and $\overset{(b)}{=}$ is due to the unitary feed-forward matrix $\tilde{\mathbf{F}}_f = \mathbf{Q}$ and to the linearity and invariance under cyclic permutations of the $\text{tr}(\cdot)$ operator. The decision variable for the k-th UE yields

$$y_k = \gamma_{\text{THP}}\mathbf{h}_{w,k}^H\mathbf{H}_{SF}\mathbf{Q}\tilde{\mathbf{x}}_c + \gamma_{\text{THP}}\mathbf{h}_{w,k}^H\mathbf{n}_c + n_{k,w},$$

and the corresponding UE rate is

$$r_k = \log_2\left(1 + \frac{\Gamma_k(\mathbf{\Pi}_c)}{\left\|\mathbf{h}_{w,k}\right\|_2^2\sigma_c^2 + \sigma_k^2/\gamma_{\text{THP}}^2}\right),$$

where $\Gamma_k(\mathbf{\Pi}_c) = \text{tr}\left(\mathbf{\Pi}_c^T\mathbf{H}_c\mathbf{H}_c^H\mathbf{\Pi}_c\mathbf{h}_{w,k}\mathbf{h}_{w,k}^H\right)$ is the signal power at the decision variable. Since both the SF2SF sum-rate maximization problem (8.33) and the SF2SF min-rate maximization problem (8.34) involve the maximization of $\Gamma_k(\mathbf{\Pi}_c)$, similarly to the SU-MISO case discussed in Sect. 8.4.1.1, we confirm the NP-hardness of both SF2SF problems under THP precoder design.

B.3. Impact of SF2SF and UE Ordering on the A-MIMO-RoC Sum-Rate

From (5.26) and (9.16), the sum-rate of the system can be computed as

$$\begin{aligned} R =& \sum_{k=1}^{N_r} \log_2 \left(1 + \frac{|h_{e,k}|^2}{\sigma_c^2 \left\| \mathbf{h}_{w,k} \right\|_2^2 + \sigma_w^2/\gamma^2} \right) \\ =& \log_2 \left(\left| \mathbf{I} + \mathbf{R}_n^{-1} \mathbf{H}_e \mathbf{H}_e^H \right| \right) \\ \approx& \log_2 \left(\left| \mathbf{R}_n^{-1} \mathbf{H}_e \mathbf{H}_e^H \right| \right), \end{aligned} \tag{B.9}$$

where $\mathbf{R}_n = \sigma_c^2 \cdot \text{diag}\left(\left\| \mathbf{h}_{w,1} \right\|_2^2, \left\| \mathbf{h}_{w,2} \right\|_2^2, ..., \left\| \mathbf{h}_{w,N_r} \right\|_2^2 \right) + \mathbf{I} \frac{\sigma_w^2}{\gamma^2}$ is a diagonal matrix containing the equivalent noise variances at all the N_r UEs and $\mathbf{H}_e = \mathbf{H}_\pi \mathbf{F}$ is the equivalent channel matrix defined in (5.23) with $\mathbf{H}_\pi = \mathbf{H}_w \mathbf{\Pi}_c^T \mathbf{H}_c \mathbf{\Pi}_c$ and $\mathbf{F} = \beta^{-1} \left(\mathbf{\Pi}_w \mathbf{H}_\pi \right)^{-1}$ denoting the (permuted) wired-plus-wireless channel and the THP precoding matrix (see Sect. 5.4.2), respectively. The approximation in (B.9) follows from the high-SNR working regime of the systems.

Under the assumption of equal number of UEs and RAU antennas (i.e., $N_r = N$), the equivalent channel matrix simplifies to $\mathbf{H}_e = \beta^{-1} \mathbf{H}_w \mathbf{\Pi}_c^T \mathbf{H}_c \mathbf{\Pi}_c \mathbf{H}_\pi^{-1} \mathbf{\Pi}_w^T$. Finally, considering the determinant property $\left| \prod_k \mathbf{A}_k \right| = \prod_k \left| \mathbf{A}_k \right|$ and reminding that the determinant of unitary matrices such as permutations is 1, i.e.,

$$\left| \mathbf{\Pi}_w \right| = \left| \mathbf{\Pi}_c \right| = 1, \tag{B.10}$$

it is easy to prove that the impact of both the SF2SF multiplexing operator $\mathbf{\Pi}_c$ and the UE ordering matrix $\mathbf{\Pi}_w$ is almost null on the sum-rate in (B.9), thus confirming the numerical results presented in Sect. 9.6.

C. Appendix for Chapter 9

C.1. Proof of Lemma 1

The proof of Lemma 9.1 is structured in two main steps detailed in the following: *i)* MRC at the cable output, *ii)* cable signal vectorization.

C.1.1. Maximum Ratio Combining at the Cable Output

The signal $\mathbf{R}_k \in \mathbb{C}^{l_F \times \frac{1}{\mu}}$ after the MRC at the cable output is

$$\begin{aligned}\mathbf{R}_k &= \tilde{\mathbf{R}}_k \mathbf{G} \\ &= \left(\tilde{\mathbf{Y}}_k \mathbf{H}_c + \tilde{\mathbf{W}}_k\right) \mathbf{G},\end{aligned} \tag{C.1}$$

where the definitions of $\tilde{\mathbf{R}}_k$, $\mathbf{G}$, $\tilde{\mathbf{Y}}_k$ and $\mathbf{H}_c$ follow from and (9.10), (9.20), (9.18) and (9.6), respectively. Thus, Eq. (C.1) can be rewritten as

$$\begin{aligned}\mathbf{R}_k &= \left(\mathbf{Y}_k \otimes \mathbf{1}_\eta^T\right)\left(\gamma \mathbf{1}_{l_S} \mathbf{1}_{l_S}^T + (1-\gamma)\mathbf{I}_{l_S}\right)\mathbf{G} + \tilde{\mathbf{W}}_k \mathbf{G} \\ &= \underbrace{\gamma \left(\mathbf{Y}_k \otimes \mathbf{1}_\eta^T\right) \mathbf{1}_{l_S} \mathbf{1}_{l_S}^T \mathbf{G}}_{\mathbf{R}_k'} + \underbrace{(1-\gamma)\left(\mathbf{Y}_k \otimes \mathbf{1}_\eta^T\right)\mathbf{G}}_{\mathbf{R}_k''} + \underbrace{\tilde{\mathbf{W}}_k \mathbf{G}}_{\mathbf{W}_k},\end{aligned} \tag{C.2}$$

where $\mathbf{W}_k = \tilde{\mathbf{W}}_k \mathbf{G}$ is the noise post MRC. The first term in (C.2) can be rewritten as

$$\begin{aligned}\mathbf{R}_k' &= \frac{\gamma}{\eta}\left(\mathbf{Y}_k \otimes \mathbf{1}_\eta^T\right)\mathbf{1}_{l_S}\mathbf{1}_{l_S}^T\left(\mathbf{I}_{\frac{1}{\mu}} \otimes \mathbf{1}_\eta\right) \\ &\overset{(a)}{=} \gamma\left(\mathbf{Y}_k \otimes \mathbf{1}_\eta^T\right)\mathbf{1}_{l_S}\mathbf{1}_{\frac{1}{\mu}}^T \\ &\overset{(b)}{=} \gamma\eta \mathbf{Y}_k \mathbf{1}_{\frac{1}{\mu}} \mathbf{1}_{\frac{1}{\mu}}^T,\end{aligned} \tag{C.3}$$

where $\overset{(a)}{=}$ comes from the fact that $\mathbf{1}_{l_S}^T\left(\mathbf{I}_{\frac{1}{\mu}} \otimes \mathbf{1}_\eta\right) = \left(\mathbf{1}_{\frac{1}{\mu}}^T \otimes \mathbf{1}_\eta^T\right)\left(\mathbf{I}_{\frac{1}{\mu}} \otimes \mathbf{1}_\eta\right) = \eta \mathbf{1}_{\frac{1}{\mu}}^T$ due to the mixed-product property of Kronecker product operator $(\mathbf{A} \otimes \mathbf{B})(\mathbf{C} \otimes \mathbf{D}) = \mathbf{AC} \otimes \mathbf{BD}$ (see [138], Chapter 2), and, similarly, $\overset{(b)}{=}$ is obtained by $\left(\mathbf{Y}_k \otimes \mathbf{1}_\eta^T\right)\mathbf{1}_{l_S}\mathbf{1}_{\frac{1}{\mu}}^T =$

$\left(\mathbf{Y}_k \otimes \mathbf{1}_\eta^T\right)\left(\mathbf{1}_{\frac{1}{\mu}}\mathbf{1}_{\frac{1}{\mu}}^T \otimes \mathbf{1}_\eta\right) = \eta\mathbf{Y}_k\mathbf{1}_{\frac{1}{\mu}}\mathbf{1}_{\frac{1}{\mu}}^T$. Using similar arguments, the second term in (C.2) simplifies to

$$\begin{aligned}\mathbf{R}_k^{''} &= \frac{1-\gamma}{\eta}\left(\mathbf{Y}_k \otimes \mathbf{1}_\eta^T\right)\left(\mathbf{I}_{\frac{1}{\mu}} \otimes \mathbf{1}_\eta\right) \\ &= (1-\gamma)\mathbf{Y}_k.\end{aligned} \tag{C.4}$$

Finally, substituting (C.3) and (C.4) in (C.2) we obtain

$$\mathbf{R}_k = \mathbf{Y}_k\mathbf{H}_c^\eta + \mathbf{W}_k, \tag{C.5}$$

where

$$\mathbf{H}_c^\eta = \gamma\eta\mathbf{1}_{\frac{1}{\mu}}\mathbf{1}_{\frac{1}{\mu}}^T + (1-\gamma)\mathbf{I}_{\frac{1}{\mu}} \tag{C.6}$$

is the equivalent cable channel matrix accounting for the bandwidth amplification factor over cable η, and $\mathbf{Y}_k$ is the radio signal reorganized in matrix form as in (9.16).

C.1.2. Cable Signal Vectorization

The vector signal $\mathbf{r}_k \in \mathbb{C}^{n_F \times 1}$ received at the BBU from the k-th EN over all the radio frequency channels can be obtained by vectorizing matrix $\mathbf{R}_k$ in (C.5) as

$$\begin{aligned}\mathbf{r}_k &= \mathrm{vec}(\mathbf{Y}_k\mathbf{H}_c^\eta + \mathbf{W}_k) \\ &= (\mathbf{H}_c^\eta \otimes \mathbf{I}_{l_F})\,\mathrm{vec}(\mathbf{Y}_k) + \mathrm{vec}(\mathbf{W}_k) \\ &= (\mathbf{H}_c^\eta \otimes \mathbf{I}_{l_F})\,\mathbf{y}_k + \mathbf{w}_k,\end{aligned} \tag{C.7}$$

where $\mathbf{y}_k$ is the radio signal received at EN k-th. The overall cable noise vector $\mathbf{w}_k$ can be rewritten as

$$\begin{aligned}\mathbf{w}_k &= \mathrm{vec}(\mathbf{W}_k) \\ &= \mathrm{vec}(\tilde{\mathbf{W}}_k\mathbf{G}) \\ &= \left(\mathbf{G}^T \otimes \mathbf{I}_{l_F}\right)\mathrm{vec}(\tilde{\mathbf{W}}_k) \\ &= \frac{1}{\eta}\left(\mathbf{I}_{\frac{1}{\mu}} \otimes \mathbf{1}_\eta^T \otimes \mathbf{I}_{l_F}\right)\tilde{\mathbf{w}}_k.\end{aligned} \tag{C.8}$$

It is important to notice that since the cable noise $\tilde{\mathbf{W}}_k$ is white Gaussian and uncorrelated over cable pairs (see (9.10)), $\tilde{\mathbf{w}}_k = \mathrm{vec}(\tilde{\mathbf{W}}_k)$ is also white Gaussian distributed as $\tilde{\mathbf{w}}_k \sim \mathcal{CN}(\mathbf{0}, \mathbf{I}_{l_S l_F})$. Hence, the covariance $\mathbf{R}_w$ of the overall cable

noise vector $\mathbf{w}_k$ yields

$$\begin{aligned}\mathbf{R}_w &= \mathbb{E}\left[\mathbf{w}_k \mathbf{w}_k^H\right] \\ &= \frac{1}{\eta^2}\left(\mathbf{I}_{\frac{1}{\mu}} \otimes \mathbf{1}_\eta^T \otimes \mathbf{I}_{l_F}\right)\left(\mathbf{I}_{\frac{1}{\mu}} \otimes \mathbf{1}_\eta^T \otimes \mathbf{I}_{l_F}\right)^T \\ &\overset{(a)}{=} \frac{1}{\eta}\left(\mathbf{I}_{\frac{1}{\mu}} \otimes \mathbf{I}_{l_F}\right) \\ &= \frac{1}{\eta}\mathbf{I}_{n_F},\end{aligned} \tag{C.9}$$

where the equality $^{(a)}$ comes again from the mixed-product property of Kronecker product. Eq. (C.9) shows that the MRC allows to take advantages from the signal redundancy over the cable, which results in a reduction of the cable noise power by a factor η.

The proof is completed by gathering the signals $\mathbf{r}_k$ (C.7) received at the BBU from all ENs as

$$\begin{aligned}\mathbf{R} &= [\mathbf{r}_1, \mathbf{r}_2, ..., \mathbf{r}_M] \\ &= \left(\mathbf{H}_c^\eta \otimes \mathbf{I}_{l_F}\right)[\mathbf{y}_1, \mathbf{y}_2, ..., \mathbf{y}_M] + [\mathbf{w}_1, \mathbf{w}_2, ..., \mathbf{w}_M] \\ &= \left(\mathbf{H}_c^\eta \otimes \mathbf{I}_{l_F}\right)\mathbf{Y} + \mathbf{W},\end{aligned} \tag{C.10}$$

where $\mathbf{Y}$ is the signal received by all ENs over all radio channels in (9.5).

C.2. Proof of Lemma 2

By substituting signal $\mathbf{Y}$ in (9.31) received by all ENs over all radio channels in case of OMA in Eq. (9.24), we obtain

$$\mathbf{R} = \left(\mathbf{H}_c^\eta \otimes \mathbf{I}_{l_F}\right)\mathbf{X}\mathbf{H} + \left(\mathbf{H}_c^\eta \otimes \mathbf{I}_{l_F}\right)\mathbf{Z} + \mathbf{W}. \tag{C.11}$$

In order to compute the per-UE eMBB rate, a further vectorization is needed, leading to

$$\begin{aligned}\mathbf{r} &= \mathrm{vec}(\mathbf{R}) \\ &= \mathrm{vec}\left(\left(\mathbf{H}_c^\eta \otimes \mathbf{I}_{l_F}\right)\mathbf{X}\mathbf{H}\right) + \mathrm{vec}\left(\left(\mathbf{H}_c^\eta \otimes \mathbf{I}_{l_F}\right)\mathbf{Z}\right) + \mathrm{vec}(\mathbf{W}) \\ &= \left(\mathbf{H}^T \otimes \mathbf{H}_c^\eta \otimes \mathbf{I}_{l_F}\right)\mathbf{x} + \left(\mathbf{I}_M \otimes \mathbf{H}_c^\eta \otimes \mathbf{I}_{l_F}\right)\mathbf{z} + \mathbf{w} \\ &= \bar{\mathbf{H}}_{\mathrm{eq}}\mathbf{x} + \bar{\mathbf{z}}_{\mathrm{eq}},\end{aligned} \tag{C.12}$$

where $\bar{\mathbf{H}}_{\mathrm{eq}} = \mathbf{H}^T \otimes \mathbf{H}_c^\eta \otimes \mathbf{I}_{l_F}$ is the overall equivalent channel comprising both cable and radio channels over all ENs, and $\bar{\mathbf{z}}_{\mathrm{eq}} = \left(\mathbf{I}_M \otimes \mathbf{H}_c^\eta \otimes \mathbf{I}_{l_F}\right)\mathbf{z} + \mathbf{w}$ is the overall noise vector comprising both the vectorized radio noise $\mathbf{z} = \mathrm{vec}(\mathbf{Z}) \sim \mathcal{CN}(\mathbf{0}, \mathbf{I}_{n_F M})$ and the vectorized cable noise $\mathbf{w} = \mathrm{vec}(\mathbf{W}) \sim \mathcal{CN}(\mathbf{0}, \frac{1}{\lambda^2 \eta}\mathbf{I}_{n_F M})$, where we recall

that the scaling λ is due to the cable power constraints. Hence, the covariance of the equivalent noise $\bar{\mathbf{z}}_{\text{eq}}$ yields

$$\begin{aligned}\bar{\mathbf{R}}_{z_{\text{eq}}} &= \mathbb{E}\left[\bar{\mathbf{z}}_{\text{eq}}\bar{\mathbf{z}}_{\text{eq}}^{H}\right] \\ &= \left(\mathbf{I}_M \otimes \mathbf{H}_c^{\eta} \otimes \mathbf{I}_{l_F}\right)\left(\mathbf{I}_M \otimes \mathbf{H}_c^{\eta} \otimes \mathbf{I}_{l_F}\right)^{H} + \frac{1}{\lambda^2\eta}\mathbf{I}_{n_F M} \\ &= \mathbf{I}_M \otimes \mathbf{H}_c^{\eta}\mathbf{H}_c^{\eta} \otimes \mathbf{I}_{l_F} + \frac{1}{\lambda^2\eta}\mathbf{I}_{n_F M}.\end{aligned} \tag{C.13}$$

The eMBB per-UE rate under OMA is computed by

$$\begin{aligned}R_B &= \frac{(1-L_U^{-1})}{n_F M} I(\mathbf{r},\mathbf{x}) \\ &= \frac{(1-L_U^{-1})}{n_F M}\log\left(\det\left(\mathbf{I} + \bar{P}_B \bar{\mathbf{R}}_{\bar{z}_{\text{eq}}}^{-1}\bar{\mathbf{H}}_{\text{eq}}\bar{\mathbf{H}}_{\text{eq}}^{T}\right)\right),\end{aligned} \tag{C.14}$$

where $\bar{\mathbf{H}}_{\text{eq}}\bar{\mathbf{H}}_{\text{eq}}^{T} = \mathbf{H}\mathbf{H} \otimes \mathbf{H}_c^{\eta}\mathbf{H}_c^{\eta} \otimes \mathbf{I}_{l_F}$. Finally, using the determinant property of the Kronecker product $|\mathbf{A} \otimes \mathbf{B}| = |\mathbf{A}|^m |\mathbf{B}|^n$, Eq. (C.14) simplifies to

$$\begin{aligned}R_B &= \frac{l_F(1-L_U^{-1})}{n_F M}\log\left(\det\left(\mathbf{I} + \bar{P}_B \mathbf{R}_{\bar{z}_{\text{eq}}}^{-1}\mathbf{H}_{\text{eq}}\mathbf{H}_{\text{eq}}^{T}\right)\right) \\ &= \mu\frac{1-L_U^{-1}}{M}\log\left(\det\left(\mathbf{I} + \bar{P}_B \mathbf{R}_{z_{\text{eq}}}^{-1}\mathbf{H}_{\text{eq}}\mathbf{H}_{\text{eq}}^{T}\right)\right),\end{aligned} \tag{C.15}$$

where $\mathbf{H}_{\text{eq}} = \mathbf{H} \otimes \mathbf{H}_c^{\eta}$ and $\mathbf{R}_{z_{\text{eq}}} = \mathbf{I}_M \otimes \mathbf{H}_c^{\eta}\mathbf{H}_c^{\eta} + \frac{1}{\lambda^2\eta}\mathbf{I}_{\frac{M}{\mu}}$, thus concluding the proof.

C.3. Proof of Lemma 4

By substituting the signal (9.5) received at the k-th EN under NOMA into (C.10) and by following similar steps as for the proof of Lemma 9.2, the overall vector signal received at the BBU comprising both cable and radio channels over all ENs under NOMA by treating interference as noise yields

$$\mathbf{r} = \bar{\mathbf{H}}_{\text{eq}}\mathbf{x} + \beta\bar{\mathbf{A}}_{\text{eq}}\mathbf{u} + \bar{\mathbf{z}}_{\text{eq}}, \tag{C.16}$$

where the definitions of $\bar{\mathbf{H}}_{\text{eq}}$ and $\bar{\mathbf{z}}_{\text{eq}}$ are the same as in (C.12), $\bar{\mathbf{A}}_{\text{eq}} = \mathbf{A} \otimes \mathbf{H}_c^{\eta} \otimes \mathbf{I}_{l_F}$ accounts for the relay of URLLC signal over the cable, and $\mathbf{u}$ is the vectorization of the URLLC signal matrix $\mathbf{U}$ in (9.5). Similarly to the proof of Lemma 9.2, the eMBB per-UE rate under NOMA by treating URLLC interference as noise can be computed by

$$\begin{aligned}R_B &= \frac{1}{n_F M} I\left(\mathbf{r},\mathbf{x}\,|\mathbf{A}\right) \\ &= \frac{\mu}{M}\mathbb{E}_{\mathbf{A}}\left[\log\left(\det\left(\mathbf{I} + P_B \mathbf{R}_{A,z_{\text{eq}}}^{-1}\mathbf{H}_{\text{eq}}\mathbf{H}_{\text{eq}}^{T}\right)\right)\right]\end{aligned} \tag{C.17}$$

where the average is taken over all the possible values of matrix $\mathbf{A}$, P_B is the power of the eMBB user under NOMA and $\mathbf{H}_{\text{eq}}$ is defined as in (C.15). Finally, the covariance $\mathbf{R}_{A,z_{\text{eq}}}$ of the noise plus URLLC interference yields

$$\mathbf{R}_{A,z_{\text{eq}}} = \beta^2 P_U \quad \mathbf{A}_{\text{eq}}\mathbf{A}_{\text{eq}}^T + \mathbf{R}_{z_{\text{eq}}},$$

where $\mathbf{A}_{\text{eq}} = \mathbf{A} \otimes \mathbf{H}_c^\eta$ and $\mathbf{R}_{z_{\text{eq}}}$ is the same as in (C.15). The proof is completed by noticing that $\mathbf{A}_{\text{eq}}\mathbf{A}_{\text{eq}}^T = (\mathbf{A} \otimes \mathbf{H}_c^\eta)(\mathbf{A} \otimes \mathbf{H}_c^\eta)^H = \mathbf{A} \otimes \mathbf{H}_c^\eta\mathbf{H}_c^\eta$, since matrix $\mathbf{A}$ is idempotent and $\mathbf{H}_c^\eta$ symmetric.

Bibliography

[1] "5G-Thriving Indoors, Cisco White Paper." Available online: https://www.cisco.com/c/dam/en/us/solutions/collateral/service-provider/ultra-services-platform/5g-ran-indoor.pdf.

[2] MarketsAndMarkets, "Distributed antenna system (das) market by offering (components and services), coverage (indoor and outdoor), ownership (carrier, neutral-host, and enterprise), user facility, vertical (commercial, public safety), and geography," *Report - Global Forecast to 2023*, 2018.

[3] CommScope, "Wireless in buildings: What building professionals think," *Report*, 2016.

[4] F. Boccardi, R. W. Heath, A. Lozano, T. L. Marzetta, and P. Popovski, "Five disruptive technology directions for 5G," *IEEE Communications Magazine*, vol. 52, no. 2, pp. 74–80, 2014.

[5] A. Checko *et al.*, "Cloud RAN for Mobile Networks: A Technology Overview," *Commun. Surveys Tuts*, vol. 17, no. 1, pp. 405–426, 2015.

[6] C. Mobile, "C-RAN: The Road Towards Green RAN," *White Paper*, 2011.

[7] "CPRI Specifications V.6.1 (2014-07-01)," September 2014.

[8] S. Nanba and A. Agata, "A New IQ Data Compression Scheme for Fronthaul Link in Centralized RAN," in *IEEE PIMRC*, Sept. 2013.

[9] J. Bartelt, P. Rost, D. Wubben, J. Lessmann, B. Melis, and G. Fettweis, "Fronthaul and backhaul requirements of flexibly centralized radio access networks," *IEEE Wireless Communications*, vol. 22, no. 5, pp. 105–111, 2015.

[10] 3GPP TSG RAN, "TR 38.801 v14.0.0, Study on new radio access technology: Radio access architecture and interfaces (Release 14)," 2017.

[11] 3GPP TSG RAN, "TR 38.913 V14.3.0, Study on Scenarios and Requirements for Next Generation Access Technologies (Release 14)," 2017.

[12] D. Wake, A. Nkansah, and N. J. Gomes, "Radio over fiber link design for next generation wireless systems," *Journal of Lightwave Technology*, vol. 28, no. 16, pp. 2456–2464, 2010.

[13] L. Combi, A. Gatto, M. Martinelli, P. Parolari, and U. Spagnolini, "Pulse-Width optical modulation for CRAN front-hauling," in *Globecom Workshops (GC Wkshps), 2015 IEEE*, pp. 1–5, IEEE, 2015.

[14] A. Ng'oma, *Radio-over-fibre technology for broadband wireless communication systems*. Technische Universiteit Eindhoven, 2005.

[15] J. Bartelt and G. Fettweis, "Radio-over-radio: I/q-stream backhauling for cloud-based networks via millimeter wave links," in *Globecom Workshops (GC Wkshps), 2013 IEEE*, pp. 772–777, IEEE, 2013.

[16] B. Skubic, M. Fiorani, S. Tombaz, A. Furuskar, J. Martensson, and P. Monti, "Optical transport solutions for 5g fixed wireless access [invited]," *IEEE/OSA Journal of Optical Communications and Networking*, vol. 9, pp. D10–D18, Sept 2017.

[17] "eCPRI Press Release, Aug. 2017, http://www.cpri.info/press.html."

[18] 3GPP TSG RAN WG3, "Transport requirement for CU and DU functional splits options," 2016.

[19] 3GPP TSG RAN WG3, "The peak bitrate requirement for different split options," 2016.

[20] D. Wubben *et al.*, "Benefits and impact of cloud computing on 5G signal processing: Flexible centralization through cloud-RAN," *IEEE Signal Processing Magazine*, vol. 31, pp. 35–44, Nov 2014.

[21] T. Starr, J. M. Cioffi, and P. J. Silverman, *Understanding digital subscriber line technology*. Prentice Hall PTR, 1999.

[22] J. Maes and C. Nuzman, "The past, present, and future of copper access," *Bell Labs Technical Journal*, vol. 20, pp. 1–10, Mar 2015.

[23] Telecommunication Standartization Sector of ITU, "Fast access to subrscriber terminals (G.fast) – Power spectral density specification," in *Recommendation ITU-T G.9700*, (Geneva, Switzerland), April 2014.

[24] W. Coomans, R. B. Moraes, K. Hooghe, A. Duque, J. Galaro, M. Timmers, A. J. van Wijngaarden, M. Guenach, and J. Maes, "Xg-fast: Towards 10 gb/s copper access," in *2014 IEEE Globecom Workshops (GC Wkshps)*, pp. 630–635, Dec 2014.

[25] R. Cendrillon, M. Moonen, J. Verlinden, T. Bostoen, and G. Ginis, "Improved linear crosstalk precompensation for DSL," in *Acoustics, Speech, and Signal Processing, 2004. Proceedings. (ICASSP '04). IEEE International Conference on*, vol. 4, pp. iv–1053–6, May 2004.

[26] G. Ginis and J. Cioffi, "Vectored transmission for digital subscriber line systems," *Selected Areas in Communications, IEEE Journal on*, vol. 20, pp. 1085–1104, Jun 2002.

[27] M. Guenach, C. Nuzman, P. Tsiaflakis, and J. Maes, "Power optimization in vectored and non-vectored g.fast transmission," in *Global Communications Conference (GLOBECOM), IEEE*, pp. 2229–2233, Dec 2014.

[28] W. Lanneer, P. Tsiaflakis, J. Maes, and M. Moonen, "Low-complexity non-linear zero-forcing precoding under per-line power constraints for improved downstream g.fast active-user peak-rates," *IEEE Transactions on Communications*, pp. 1–1, 2018.

[29] W. Lanneer, P. Tsiaflakis, J. Maes, and M. Moonen, "Linear and nonlinear precoding based dynamic spectrum management for downstream vectored g.fast transmission," *IEEE Transactions on Communications*, vol. 65, pp. 1247–1259, March 2017.

[30] J. Gambini and U. Spagnolini, "Wireless over cable for femtocell systems," *IEEE Commun. Mag.*, vol. 51, pp. 178–185, May 2013.

[31] C. Lu *et al.*, "Connecting the dots: small cells shape up for high-performance indoor radio," *Ericsson Rev.*, vol. 91, pp. 38–45, Dec. 2014.

[32] Y. Huang, E. Medeiros, N. Fonseca, S. Host, T. Magesacher, P.-E. Eriksson, C. Lu, P. Odling, and P. O. Borjesson, "Lte over copper-potential and limitations," in *Personal, Indoor, and Mobile Radio Communications (PIMRC), 2015 IEEE 26th Annual International Symposium on*, pp. 1339–1343, IEEE, 2015.

[33] E.Medeiros *et al.*, "Crosstalk Mitigation for LTE-Over-Copper in Downlink Direction," *IEEE Comm. Lett.*, vol. 20, pp. 1425–1428, July 2016.

[34] M. Timmers, M. Guenach, C. Nuzman, and J. Maes, "G.fast: Evolving the copper access network," *Communications Magazine, IEEE*, vol. 51, pp. 74–79, August 2013.

[35] Telecommunication Standartization Sector of ITU, "Fast access to subrscriber terminals (G.fast) – Physical layer specification," in *Recommendation ITU-T G.9701*, (Geneva, Switzerland), December 2014.

[36] S. Huberman, C. Leung, and T. Le-Ngoc, "Dynamic spectrum management (DSM) algorithms for multi-user xDSL," *Communications Surveys Tutorials, IEEE*, vol. 14, pp. 109–130, First 2012.

[37] F. Müller, C. Lu, P.-E. Eriksson, S. Host, and A. Klautau, "Optimizing power normalization for G.fast linear precoder by linear programming," in *Communications (ICC), 2014 IEEE International Conference on*, pp. 4160–4165, June 2014.

[38] G. Ginis and J. Cioffi, "A multi-user precoding scheme achieving crosstalk cancellation with application to DSL systems," in *Signals, Systems and Computers, 2000. Conference Record of the Thirty-Fourth Asilomar Conference on*, vol. 2, pp. 1627–1631, Oct 2000.

[39] D. Wübben, D. Seethaler, J. Jalden, and G. Matz, "Lattice reduction," *Signal Processing Magazine, IEEE*, vol. 28, pp. 70–91, May 2011.

[40] S. Zafaruddin, I. Bergel, and A. Leshem, "Signal processing for gigabit-rate wireline communications: An overview of the state of the art and research challenges," *IEEE Signal Processing Magazine*, vol. 34, no. 5, pp. 141–164, 2017.

[41] R. F. Fischer, C. Windpassinger, A. Lampe, and J. B. Huber, "Space-Time Transmission using Tomlinson-Harashima Precoding," in *Proceedings of 4. International ITG Conference on Systems, Communications and Coding(SCC)*, (Berlin, Germany), pp. 139–147, January 2002.

[42] M. Joham, J. Brehmer, and W. Utschick, "MMSE approaches to multiuser spatio-temporal Tomlinson-Harashima precoding," in *in Proc. ITG SCC'04*, pp. 387–394, January 2004.

[43] P. Wolniansky, G. Foschini, G. Golden, and R. Valenzuela, "V-BLAST: An architecture for realizing very high data rates over the rich-scattering wireless channel," in *Signals, Systems, and Electronics, 1998. ISSSE 98. 1998 URSI International Symposium on*, pp. 295–300, Sep 1998.

[44] D. Wubben, R. Bohnke, J. Rinas, V. Kuhn, and K.-D. Kammeyer, "Efficient algorithm for decoding layered space-time codes," *Electronics letters*, vol. 37, no. 22, pp. 1348–1350, 2001.

[45] K. Kerpez and G. Ginis, "Software-defined access network (SDAN)," in *Information Sciences and Systems (CISS), 2014 48th Annual Conference on*, pp. 1–6, March 2014.

[46] K. Zu, R. de Lamare, and M. Haardt, "Multi-branch Tomlinson-Harashima precoding design for MU-MIMO systems: Theory and algorithms," *Communications, IEEE Transactions on*, vol. 62, pp. 939–951, March 2014.

[47] C. D. Meyer, *Matrix analysis and applied linear algebra*. SIAM, 2000.

[48] M. Huang, S. Zhou, and J. Wang, "Analysis of Tomlinson-Harashima precoding in multiuser MIMO systems with imperfect channel state information," *Vehicular Technology, IEEE Transactions on*, vol. 57, pp. 2856–2867, Sept 2008.

[49] R. Fischer and C. Windpassinger, "Improved MIMO precoding for decentralized receivers resembling concepts from lattice reduction," in *Global Telecommunications Conference, 2003. GLOBECOM '03. IEEE*, vol. 4, pp. 1852–1856, Dec 2003.

[50] Ad-hoc Convenor, "G.fast: Ad-hoc report on vectoring simulation conditions," in *ITU-T 2012-11-4A-082*, (Geneva, Switzerland), January 2012.

[51] R. Habendorf and G. Fettweis, "Vector precoding with bounded complexity," in *Signal Processing Advances in Wireless Communications, 2007. SPAWC 2007. IEEE 8th Workshop on*, pp. 1–5, June 2007.

[52] F. Liu, L. Jiang, and C. He, "Low complexity lattice reduction aided MMSE precoding design for MIMO systems," in *Communications and Networking in China (CHINACOM). Second International Conference on*, pp. 498–502, Aug 2007.

[53] W. Lanneer, M. Moonen, P. Tsiaflakis, and J. Maes, "Linear and nonlinear precoding based dynamic spectrum management for downstream vectored G.fast transmission," in *2015 IEEE Global Communications Conference (GLOBECOM)*, pp. 1–6, Dec 2015.

[54] M. Chiang, "Geometric programming for communication systems," *Foundations and Trends in Communications and Information Theory*, vol. 2, no. 1-2, pp. 1–154, 2005.

[55] S. Boyd, S.-J. Kim, L. Vandenberghe, and A. Hassibi, "A tutorial on geometric programming," *Optimization and Engineering*, vol. 8, no. 1, pp. 67–127, 2007.

[56] G. Xu, "Global optimization of signomial geometric programming problems," *European Journal of Operational Research*, vol. 233, no. 3, pp. 500–510, 2014.

[57] X.-P. Hou, P.-P. Shen, and Y.-Q. Chen, "A global optimization algorithm for signomial geometric programming problem," *Abstract and Applied Analysis*, vol. 2014, p. 12, 2014.

[58] G. Alirezaei, O. Taghizadeh, and R. Mathar, "Optimum power allocation in sensor networks for active radar applications," *Wireless Communications, IEEE Transactions on*, vol. 14, pp. 2854–2867, May 2015.

[59] C. He, Y. Li, F. Zheng, and X. You, "Power allocation criteria for distributed antenna systems," *Vehicular Technology, IEEE Transactions on*, vol. PP, no. 99, pp. 1–8, 2014.

[60] M. Taherzadeh, A. Mobasher, and A. Khandani, "Communication over MIMO broadcast channels using lattice-basis reduction," *Information Theory, IEEE Transactions on*, vol. 53, pp. 4567–4582, Dec 2007.

[61] R. Zamir, *Lattice Coding for Signals and Networks*. Cambridge University Press, 2014.

[62] R. F. H. Fischer, *Precoding and Signal Shaping for Digital Transmission*. 2002.

[63] S. Boyd and L. Vandenberghe, *Convex Optimization*. New York, NY, USA: Cambridge University Press.

[64] R. Cendrillon, W. Yu, M. Moonen, J. Verlinden, and T. Bostoen, "Optimal multiuser spectrum balancing for digital subscriber lines," *IEEE Transactions on Communications*, vol. 54, no. 5, pp. 922–933, 2006.

[65] A. R. Forouzan, M. Moonen, J. Maes, and M. Guenach, "Joint level 2 and 3 dynamic spectrum management for upstream vdsl," *IEEE Transactions on Communications*, vol. 59, no. 10, pp. 2851–2861, 2011.

[66] R. Zidane, S. Huberman, C. Leung, and T. Le-Ngoc, "Vectored dsl: benefits and challenges for service providers," *IEEE Communications Magazine*, vol. 51, no. 2, pp. 152–157, 2013.

[67] Q. H. Spencer, A. L. Swindlehurst, and M. Haardt, "Zero-forcing methods for downlink spatial multiplexing in multiuser mimo channels," *IEEE transactions on signal processing*, vol. 52, no. 2, pp. 461–471, 2004.

[68] A. H. Fazlollahi, X. Wang, and Y. Zeng, "Fext exploitation in next generation dsl systems," in *Global Communications Conference (GLOBECOM), 2016 IEEE*, pp. 1–6, IEEE, 2016.

[69] V. Stankovic and M. Haardt, "Generalized design of multi-user mimo precoding matrices," *IEEE Transactions on Wireless Communications*, vol. 7, no. 3, pp. 953–961, 2008.

[70] S. H. R. Naqvi and U. Spagnolini, "Interference-cooperation in multi-user/multi-operator receivers," *arXiv preprint arXiv:1507.07698*, 2015.

[71] Swisscom, "Additional loop sets for simulation purposes," in *ITU-T Q4/SG15 2013-01-Q4-044R1*, (Geneva, Switzerland).

[72] BT, "Release of BT cable measurements for use in simulations," in *ITU-T Q4a/SG15 2012-11-4A-034*, (Chengdu, China).

[73] Ad Hoc Convener, "G.fast: Ad-hoc report on vectoring simulation conditions," in *ITU-T Q4a/15 Contribution 2012-11-4A-082*, (Chengdu, China), November 2012.

[74] D. Gesbert, S. Hanly, H. Huang, S. Shamai Shitz, O. Simeone, and W. Yu, "Multi-cell MIMO cooperative networks: A new look at interference," *Selected Areas in Communications, IEEE Journal on*, vol. 28, pp. 1380–1408, December 2010.

[75] G. Zheng, I. Krikidis, C. Masouros, S. Timotheou, D.-A. Toumpakaris, and Z. Ding, "Rethinking the role of interference in wireless networks," *Communications Magazine, IEEE*, vol. 52, no. 11, pp. 152–158, 2014.

[76] D. Lee, H. Seo, B. Clerckx, E. Hardouin, D. Mazzarese, S. Nagata, and K. Sayana, "Coordinated multipoint transmission and reception in LTE-advanced: Deployment scenarios and operational challenges," *Communications Magazine, IEEE*, vol. 50, no. 2, pp. 148–155, 2012.

[77] E. Jorswieck, L. Badia, T. Fahldieck, E. Karipidis, and J. Luo, "Spectrum sharing improves the network efficiency for cellular operators," *Communications Magazine, IEEE*, vol. 52, pp. 129–136, March 2014.

[78] B. Hochwald, C. Peel, and A. Swindlehurst, "A vector-perturbation technique for near-capacity multiantenna multiuser communication-part II: perturbation," *Communications, IEEE Transactions on*, vol. 53, pp. 537–544, March 2005.

[79] Y.-T. Lin, H. Tembine, and K.-C. Chen, "Inter-operator spectrum sharing in future cellular systems," in *Global Communications Conference (GLOBECOM), 2012 IEEE*, pp. 2597–2602, Dec 2012.

[80] C.-B. Chae, I. Hwang, R. Heath, and V. Tarokh, "Interference aware-coordinated beamforming in a multi-cell system," *Wireless Communications, IEEE Transactions on*, vol. 11, pp. 3692–3703, October 2012.

[81] Y.-F. Liu, Y.-H. Dai, and Z.-Q. Luo, "Coordinated beamforming for MISO interference channel: Complexity analysis and efficient algorithms," *Signal Processing, IEEE Transactions on*, vol. 59, no. 3, pp. 1142–1157, 2011.

[82] M. Bloch, J. Barros, M. Rodrigues, and S. McLaughlin, "Wireless information-theoretic security," *Information Theory, IEEE Transactions on*, vol. 54, pp. 2515–2534, June 2008.

[83] Y. Liang, H. V. Poor, and S. Shamai (Shitz), *Foundations and Trends in Communications and Information Theory: Information Theoretic Security*. Now Publisher, 2009.

[84] A. D. Wyner, "The wire-tap channel," *The Bell System Technical Journal*, vol. 54, pp. 1355–1387, Oct 1975.

[85] I. Csiszar and J. Korner, "Broadcast channels with confidential messages," *IEEE Transactions on Information Theory*, vol. 24, pp. 339–348, May 1978.

[86] A. Khisti and G. W. Wornell, "Secure transmission with multiple antennas i: The MISOME wiretap channel," *IEEE Transactions on Information Theory*, vol. 56, pp. 3088–3104, July 2010.

[87] T. Liu and S. Shamai, "A note on the secrecy capacity of the multiple-antenna wiretap channel," *IEEE Transactions on Information Theory*, vol. 55, pp. 2547–2553, June 2009.

[88] F. Oggier and B. Hassibi, "The secrecy capacity of the MIMO wiretap channel," *IEEE Transactions on Information Theory*, vol. 57, pp. 4961–4972, Aug 2011.

[89] R. Liu, I. Maric, P. Spasojevic, and R. D. Yates, "Discrete memoryless interference and broadcast channels with confidential messages: Secrecy rate regions," *IEEE Transactions on Information Theory*, vol. 54, pp. 2493–2507, June 2008.

[90] O. O. Koyluoglu, H. E. Gamal, L. Lai, and H. V. Poor, "Interference alignment for secrecy," *IEEE Transactions on Information Theory*, vol. 57, pp. 3323–3332, June 2011.

[91] R. Liu and H. V. Poor, "Secrecy capacity region of a multiple-antenna gaussian broadcast channel with confidential messages," *IEEE Transactions on Information Theory*, vol. 55, pp. 1235–1249, March 2009.

[92] E. Ekrem and S. Ulukus, "Secrecy in cooperative relay broadcast channels," *IEEE Transactions on Information Theory*, vol. 57, pp. 137–155, Jan 2011.

[93] E. Ekrem and S. Ulukus, "Effects of cooperation on the secrecy of multiple access channels with generalized feedback," in *Information Sciences and Systems, 2008. CISS 2008. 42nd Annual Conference on*, pp. 791–796, March 2008.

[94] R. D. Yates, D. Tse, and Z. Li, "Secret communication on interference channels," in *2008 IEEE International Symposium on Information Theory*, pp. 374–378, July 2008.

[95] E. Perron, S. Diggavi, and E. Telatar, "On cooperative wireless network secrecy," in *INFOCOM 2009, IEEE*, pp. 1935–1943, April 2009.

[96] P. Mohapatra and C. R. Murthy, "Secrecy in the 2-user symmetric deterministic interference channel with transmitter cooperation," in *2013 IEEE 14th Workshop on Signal Processing Advances in Wireless Communications (SPAWC)*, pp. 270–274, June 2013.

[97] A. S. Avestimehr, S. N. Diggavi, and D. N. C. Tse, "Wireless network information flow: A deterministic approach," *IEEE Transactions on Information Theory*, vol. 57, pp. 1872–1905, April 2011.

[98] S. Goel and R. Negi, "Guaranteeing secrecy using artificial noise," *IEEE Transactions on Wireless Communications*, vol. 7, pp. 2180–2189, June 2008.

[99] G. Geraci, M. Egan, J. Yuan, A. Razi, and I. B. Collings, "Secrecy sum-rates for multi-user MIMO regularized channel inversion precoding," *IEEE Transactions on Communications*, vol. 60, pp. 3472–3482, November 2012.

[100] Y. Liang, G. Kramer, H. V. Poor, and S. Shamai, "Compound wiretap channels," *EURASIP J. Wirel. Commun. Netw.*, vol. 2009, pp. 5:1–5:12, Mar. 2009.

[101] A. Carleial, "Interference channels," *IEEE Transactions on Information Theory*, vol. 24, pp. 60–70, Jan 1978.

[102] T. Komine and M. Nakagawa, "Fundamental analysis for visible-light communication system using LED lights," *IEEE Trans. Consum. Electron*, vol. 50, 2004.

[103] GoGo, ""GoGo 2ku: High performance inflight connectivity"," 2017.

[104] V. Degardin, P. Laly, M. Lienard, and P. Degauque, "Investigation on power line communication in aircrafts," *IET Communications*, vol. 8, pp. 1868–1874, July 2014.

[105] E. Chan, "Wireless optical links for airplane applications," in *2012 IEEE Photonics Society Summer Topical Meeting Series*, pp. 76–77, July 2012.

[106] D. Krichene, M. Sliti, W. Abdallah, and N. Boudriga, "An aeronautical visible light communication system to enable in-flight connectivity," in *2015 17th International Conference on Transparent Optical Networks (ICTON)*, pp. 1–6, July 2015.

[107] I. H. Park, Y. H. Kim, and J. Y. Kim, "Interference mitigation scheme of visible light communication systems for aircraft wireless applications," in *2012 IEEE International Conference on Consumer Electronics (ICCE)*, pp. 355–356, Jan 2012.

[108] C. Quintana, V. Guerra, J. Rufo, J. Rabadan, and R. Perez-Jimenez, "Reading lamp-based visible light communication system for in-flight entertainment," *IEEE Transactions on Consumer Electronics*, vol. 59, pp. 31–37, February 2013.

[109] D. Tagliaferri and C. Capsoni, "SNIR predictions for on-aircraft VLC systems," in *2016 International Conference on Broadband Communications for Next Generation Networks and Multimedia Applications (CoBCom)*, pp. 1–7, Sept 2016.

[110] P. H. Pathak, X. Feng, P. Hu, and P. Mohapatra, "Visible Light Communication, Networking, and Sensing: A Survey, Potential and Challenges," *IEEE Communications Surveys Tutorials*, vol. 17, pp. 2047–2077, Fourthquarter 2015.

[111] J. M. Luna-Rivera, R. Perez-Jimenez, J. A. Rabadan-Borjes, J. F. Rufo-Torres, V. Guerra, and C. Suarez-Rodriguez, "Multiuser scheme for indoor visible light communications using RGB LEDs," in *3rd IEEE International Work-Conference on Bioinspired Intelligence*, pp. 119–123, July 2014.

[112] K. Zhou, C. Gong, Q. Gao, and Z. Xu, "Inter-cell interference coordination for multi-color visible light communication networks," in *2016 IEEE Global Conference on Signal and Information Processing (GlobalSIP)*, pp. 6–10, Dec 2016.

[113] T. Fath and H. Haas, "Performance Comparison of MIMO Techniques for Optical Wireless Communications in Indoor Environments," *IEEE Transactions on Communications*, vol. 61, pp. 733–742, February 2013.

[114] C. W. Hsu, C. W. Chow, I. C. Lu, Y. L. Liu, C. H. Yeh, and Y. Liu, "High Speed Imaging 3 x 3 MIMO Phosphor White-Light LED Based Visible Light Communication System," *IEEE Photonics Journal*, vol. 8, pp. 1–6, Dec 2016.

[115] B. Li, J. Wang, R. Zhang, H. Shen, C. Zhao, and L. Hanzo, "Multiuser MISO transceiver design for indoor downlink visible light communication under per-led optical power constraints," *IEEE Photonics Journal*, vol. 7, pp. 1–15, Aug 2015.

[116] H. Ma, L. Lampe, and S. Hranilovic, "Coordinated broadcasting for multiuser indoor visible light communication systems," *IEEE Transactions on Communications*, vol. 63, pp. 3313–3324, Sept 2015.

[117] Z. Yu, R. J. Baxley, and G. T. Zhou, "Multi-user MISO broadcasting for indoor visible light communication," in *2013 IEEE International Conference on Acoustics, Speech and Signal Processing*, pp. 4849–4853, May 2013.

[118] T. V. Pham, H. Le-Minh, and A. T. Pham, "Multi-user visible light communication broadcast channels with zero-forcing precoding," *IEEE Transactions on Communications*, vol. 65, pp. 2509–2521, June 2017.

[119] C. A. Gueymard, "Parameterized transmittance model for direct beam and circumsolar spectral irradiance," *Solar Energy*, vol. 71, no. 5, pp. 325 – 346, 2001.

[120] R. E. Bird and C. J. Riordan, "Simple simple solar spectral model for direct and diffuse irradiance on horizontal and tilted planes at the earth's surface for cloudless atmospheres," *Journal of Climate and Applied Meteorology*, vol. 25(1), pp. 87–97, Jan. 1986.

[121] S. P. Rodríguez, R. P. Jiménez, B. R. Mendoza, F. J. L. Hernández, and A. J. A. Alfonso, "Simulation of impulse response for indoor visible light communications using 3d cad models," *EURASIP Journal on Wireless Communications and Networking*, vol. 2013, p. 7, Jan 2013.

[122] J. M. Kahn and J. R. Barry, "Wireless infrared communications," *Proceedings of the IEEE*, vol. 85, pp. 265–298, Feb 1997.

[123] A. Lapidoth, S. M. Moser, and M. A. Wigger, "On the capacity of free-space optical intensity channels," *IEEE Transactions on Information Theory*, vol. 55, pp. 4449–4461, Oct 2009.

[124] Cree, ""cree plcc2 1 in 1 smd led clm1c-wkw"," 2017.

[125] Q. Wang, Z. Wang, and L. Dai, "Multiuser mimo-ofdm for visible light communications," *IEEE Photonics Journal*, vol. 7, pp. 1–11, Dec 2015.

[126] Boeing, ""737 airplane characteristics for airport planning"," 2013.

[127] U. T. C. Aerospace, ""LED wash lights 1005-x1x-001"," 2016.

[128] U. T. C. Aerospace, ""LED wash lights retrofit 2la45665y-xx"," 2017.

[129] U. T. C. Aerospace, ""LED reading lights"," 2015.

[130] 3rd G. P. P., *3GPP TS 38.211 V15.0.0 (2017-12)*, 2017 (accessed January 15, 2018).

[131] Boeing, ""777-200/300 airplane characteristics for airport planning"," 2013.

[132] J. Gambini and U. Spagnolini, "Radio over telephone lines in femtocell systems," in *IEEE PIMRC*, Sept. 2010.

[133] H. S. Chung *et al.*, "Design of RoF based Mobile Fronthaul Link with Multi-IF Carrier for LTE/LTE-A Signal Transmission," in *IEEE APMP*, 2014.

[134] F. Tonini, M. Fiorani, M. Furdek, C. Raffaelli, L. Wosinska, and P. Monti, "Radio and Transport Planning of Centralized Radio Architectures in 5G Indoor Scenarios," *IEEE Journal on Selected Areas in Communications*, vol. 35, no. 8, pp. 1837–1848, 2017.

[135] J. Wannstrom, "LTE-advanced," *Third Generation Partnership Project (3GPP)*, 2012.

[136] F. Effenberger, "Future Broadband Access Networks," *Proceedings of the IEEE*, vol. 104, pp. 2078–2081, November 2016.

[137] H. L. Van Trees, *Detection, estimation, and modulation theory, optimum array processing*. John Wiley & Sons, 2004.

[138] U. Spagnolini, *Statistical Signal Processing in Engineering*. John Wiley & Sons, 2018.

[139] S. J. Russell *et al.*, *Artificial intelligence: a modern approach*, vol. 2. Prentice hall Upper Saddle River, 2003.

[140] I. Gurobi Optimization, "Gurobi optimizer reference manual," 2016.

[141] M. Samimi *et al.*, "28 GHz millimeter-wave ultrawideband small-scale fading models in wireless channels," in *Vehicular Technology Conference (VTC Spring), 2016 IEEE 83rd*, pp. 1–6, IEEE, 2016.

[142] S. H. R. Naqvi, *Multi-user processing for next generation wired and wireless systems*. PhD thesis, Politecnico di Milano, 2016.

[143] X. Tang and Y. Hua, "Optimal design of non-regenerative MIMO wireless relays," *IEEE Transactions on Wireless Communications*, vol. 6, no. 4, 2007.

[144] O. Munoz-Medina, J. Vidal, and A. Agustin, "Linear transceiver design in nonregenerative relays with channel state information," *IEEE Transactions on Signal Processing*, vol. 55, pp. 2593–2604, June 2007.

[145] L. Sanguinetti, A. A. D'Amico, and Y. Rong, "A tutorial on the optimization of amplify-and-forward MIMO relay systems," *IEEE Journal on Selected Areas in Communications*, vol. 30, no. 8, pp. 1331–1346, 2012.

[146] C.-B. Chae, T. Tang, R. W. Heath Jr, and S. Cho, "MIMO relaying with linear processing for multiuser transmission in fixed relay networks," *IEEE Transactions on Signal Processing*, vol. 56, no. 2, pp. 727–738, 2008.

[147] O. El Ayach, S. Rajagopal, S. Abu-Surra, Z. Pi, and R. W. Heath, "Spatially sparse precoding in millimeter wave MIMO systems," *IEEE Transactions on Wireless Communications*, vol. 13, no. 3, pp. 1499–1513, 2014.

[148] M. Joham and W. Utschick, "Ordered spatial tomlinson-harashima precoding," *Smart antennas state-of-the-art*, vol. 3, 2006.

[149] Burkard *et al.*, "The quadratic assignment problem," in *Handbook of combinatorial optimization*, pp. 1713–1809, Springer, 1998.

[150] S. Sahni and T. Gonzalez, "P-complete approximation problems," *Journal of the ACM (JACM)*, vol. 23, no. 3, pp. 555–565, 1976.

[151] E. L. Lawler, "The quadratic assignment problem," *Management science*, vol. 9, no. 4, pp. 586–599, 1963.

[152] "IEEE 802.3 Ethernet Working Group, http://www.ieee802.org/3."

[153] G. R. Maccartney, T. S. Rappaport, S. Sun, and S. Deng, "Indoor office wideband millimeter-wave propagation measurements and channel models at 28 and 73 ghz for ultra-dense 5g wireless networks," *IEEE Access*, vol. 3, pp. 2388–2424, 2015.

[154] B. Ai, K. Guan, R. He, J. Li, G. Li, D. He, Z. Zhong, and K. M. S. Huq, "On indoor millimeter wave massive mimo channels: Measurement and simulation," *IEEE Journal on Selected Areas in Communications*, vol. 35, pp. 1678–1690, July 2017.

[155] M. Shafi, A. F. Molisch, P. J. Smith, T. Haustein, P. Zhu, P. D. Silva, F. Tufvesson, A. Benjebbour, and G. Wunder, "5g: A tutorial overview of standards, trials, challenges, deployment, and practice," *IEEE Journal on Selected Areas in Communications*, vol. 35, pp. 1201–1221, June 2017.

[156] 5G PPP Architecture Working Group, "View on 5G architecture," *White Paper, July*, 2016.

[157] ITU-R, "ITU-R M. - Minimum Requirements related to technical performance for IMT-2020 radio interface(s)," Report ITU-R M.2410-0, Nov. 2017.

[158] 3GPP, "Study on new radio (NR) access technology physical layer aspects," TR 38.802, Mar. 2017.

[159] G. Durisi, T. Koch, and P. Popovski, "Toward massive, ultrareliable, and low-latency wireless communication with short packets," *Proceedings of the IEEE*, vol. 104, pp. 1711–1726, Sept 2016.

[160] H. Zhang, N. Liu, X. Chu, K. Long, A. H. Aghvami, and V. C. M. Leung, "Network slicing based 5g and future mobile networks: Mobility, resource management, and challenges," *IEEE Communications Magazine*, vol. 55, no. 8, pp. 138–145, 2017.

[161] P. Popovski, J. J. Nielsen, C. Stefanovic, E. d. Carvalho, E. Strom, K. F. Trillingsgaard, A. S. Bana, D. M. Kim, R. Kotaba, J. Park, and R. B. Sorensen, "Wireless access for ultra-reliable low-latency communication: Principles and building blocks," *IEEE Network*, vol. 32, pp. 16–23, March 2018.

[162] P. T. Dat, A. Kanno, N. Yamamoto, and T. Kawanishi, "5g transport networks: the need for new technologies and standards," *IEEE Communications Magazine*, vol. 54, no. 9, pp. 18–26, 2016.

[163] T. M. Cover and J. A. Thomas, *Elements of information theory*. John Wiley & Sons, 2012.

[164] Y. Saito, Y. Kishiyama, A. Benjebbour, T. Nakamura, A. Li, and K. Higuchi, "Non-orthogonal multiple access (noma) for cellular future radio access," in *2013 IEEE 77th Vehicular Technology Conference (VTC Spring)*, pp. 1–5, June 2013.

[165] W. Shin, M. Vaezi, B. Lee, D. J. Love, J. Lee, and H. V. Poor, "Non-orthogonal multiple access in multi-cell networks: Theory, performance, and practical challenges," *IEEE Communications Magazine*, vol. 55, no. 10, pp. 176–183, 2017.

[166] Z. Ding, X. Lei, G. K. Karagiannidis, R. Schober, J. Yuan, and V. K. Bhargava, "A survey on non-orthogonal multiple access for 5g networks: Research challenges and future trends," *IEEE Journal on Selected Areas in Communications*, vol. 35, pp. 2181–2195, Oct 2017.

[167] A. Anand, G. de Veciana, and S. Shakkottai, "Joint scheduling of urllc and embb traffic in 5g wireless networks," *arXiv preprint arXiv:1712.05344*, 2017.

[168] P. Popovski, K. F. Trillingsgaard, O. Simeone, and G. Durisi, "5g wireless network slicing for embb, urllc, and mmtc: A communication-theoretic view," *arXiv preprint arXiv:1804.05057*, 2018.

[169] L. Dai, B. Wang, Y. Yuan, S. Han, C. l. I, and Z. Wang, "Non-orthogonal multiple access for 5g: solutions, challenges, opportunities, and future research trends," *IEEE Communications Magazine*, vol. 53, pp. 74–81, September 2015.

[170] R. Kassab, O. Simeone, and P. Popovski, "Coexistence of URLLC and embb services in the C-RAN uplink: An information-theoretic study," *CoRR*, vol. abs/1804.06593, 2018.

[171] Qualcomm, "Making 5G NR a reality," *White Paper, December*, 2016.

[172] 3GPP, "Final Report of 3GPP TSG RAN WG1 n.88bis v1.0.0," Spokane, USA, 3-7 April 2017.

[173] O. Simeone, N. Levy, A. Sanderovich, O. Somekh, B. M. Zaidel, H. V. Poor, S. Shamai, *et al.*, "Cooperative wireless cellular systems: An information-theoretic view," *Foundations and Trends® in Communications and Information Theory*, vol. 8, no. 1-2, pp. 1–177, 2012.

[174] T. S. Rappaport, S. Sun, R. Mayzus, H. Zhao, Y. Azar, K. Wang, G. N. Wong, J. K. Schulz, M. Samimi, and F. Gutierrez Jr, "Millimeter wave mobile communications for 5G cellular: It will work!," *IEEE access*, vol. 1, no. 1, pp. 335–349, 2013.

[175] W. C. Jakes and D. C. Cox, *Microwave mobile communications*. Wiley-IEEE Press, 1994.

[176] Y. Polyanskiy, H. Poor, and S. Verdu, "Channel coding rate in the finite blocklength regime," *IEEE Transactions on Information Theory*, vol. 56, pp. 2307 –2359, may 2010.

[177] J. Scarlett, V. Y. Tan, and G. Durisi, "The dispersion of nearest-neighbor decoding for additive non-gaussian channels," *IEEE Transactions on Information Theory*, vol. 63, no. 1, pp. 81–92, 2017.

[178] W. Zhang, "A general framework for transmission with transceiver distortion and some applications," *IEEE Transactions on Communications*, vol. 60, no. 2, pp. 384–399, 2012.

[179] N. Merhav, G. Kaplan, A. Lapidoth, and S. S. Shitz, "On information rates for mismatched decoders," *IEEE Transactions on Information Theory*, vol. 40, no. 6, pp. 1953–1967, 1994.

[180] J. G. Andrews, S. Buzzi, W. Choi, S. V. Hanly, A. Lozano, A. C. K. Soong, and J. C. Zhang, "What will 5g be?," *IEEE Journal on Selected Areas in Communications*, vol. 32, pp. 1065–1082, June 2014.

[181] N. Alliance, "5g white paper," *Next generation mobile networks, white paper*, 2015.

[182] A. F. Cattoni, G. C. Madueño, M. Dieudonne, P. Merino, A. D. Zayas, A. Salmeron, F. Carlier, B. Saint Germain, D. Morris, R. Figueiredo, *et al.*, "An end-to-end testing ecosystem for 5g," in *Networks and Communications (EuCNC), 2016 European Conference on*, pp. 307–312, IEEE, 2016.

[183] "Triangle project official website, www.triangle-project.eu."

[184] 3GPP TS 36.101 Group Radio Access Network; Evolved Universal Terrestrial Radio Access (E-UTRA), "User Equipment (UE) Radio Transmission and Reception."

[185] A. Alvarez, A. Díaz, P. Merino, and F. J. Rivas, "Field measurements of mobile services with android smartphones," in *Consumer Communications and Networking Conference (CCNC), 2012 IEEE*, pp. 105–109, IEEE, 2012.

[186] 3GPP TS 36.213 Group Radio Access Network; Evolved Universal Terrestrial Radio Access (E-UTRA), "Physical Layer Procedure."

Nomenclature

3GPP	3rd Generation Partnership Project
A-MIMO-RoC	Analog Multiple-Input Multiple Output Radio-over-Copper
A-RoC	Analog Radio-over-Copper
A-RoF	Analog Radio-over-Fiber
A-RoR	Analog Radio-over-Radio
A/A	Analog-to-Analog
ADC	Analog-to-Digital Conversion
AF	Amplify-and-Forward
AN	Artificial Noise
AoD	Angle of Departure
AP	Access Point
ATP	Aggregate Transmit Power
AWGN	Additive White Gaussian Noise
BBU	BaseBand Unit
BC	Broadcast Channel
BD	Block Diagonalization
BER	Bit Error Rate
BLER	BLock Error Rate
BS	Base Station
C-RAN	Centralized (or Cloud) Radio Access Network
CDM	Colour Division Multiplexing

CIR	Channel Impulse Response
CO	Central Office
CoMP	Cooperative MultiPoint
CP	Cyclic Prefix
CPE	Costumer Promises Equipment
CPRI	Common Public Radio Interface
CSI	Channel State Information
D-RoC	Digital Radio-over-Copper
D-RoF	Digital Radio-over-Fiber
DAC	Digital-to-Analog Conversion
DAS	Distributed Antenna System
DC	Direct Current
DD	Direct Detection
DL	DownLink
DMT	Discrete Multi-Tone
DO	Dynamic Ordering
DoA	Direction of Arrival
DP	Diagonal Precoding
DPC	Dirty Paper Coding
DS	DownStream
DSL	Digital Subscriber Line
DSLAM	DSL Access Multiplexer
DSM	Dynamic Spectrum Management
eCPRI	enhanced Common Public Radio Interface
eMBB	enhanced Mobile BroadBand

EMI	Electro-Magnetic Interference
EN	Edge Node
EPA5	ETSI Pedestrian at 5 Hz
ER-THP	Equal-Rate THP
FDD	Frequency Division Duplexing
FDM	Frequency Division Multiplexing
FEC	Forward Error Correction
FEXT	Far-End-CrossTalk
FFT	Fast Fourier Transform
FH	FrontHaul
FNS	Frobenius Norm Scaling
FOV	Field-Of-View
FTTdp	Fiber-To-The-distribution-point
GBC	Gaussian Broadcast Channel
GIC	Gaussian Interference Channel
GIC-LIET	Gaussian Interference Channel with Limited Information Exchange at the Transmitters
GP	Geometric Program
GS	Gram-Schmidt
HARQ	Hybrid Automatic Repeat reQuest
I/Q	In-phase and Quadrature
IC	Interference Channel
ID	In-Domain
IF	Intermediate Frequency
iFFT	inverse Fast Fourier Transform
IFoF	IF-over-Fiber

IL	Insertion Loss
ILP	Integer Linear Programming
IM-DD	Intensity-Modulation
IR	InfraRed
ITU	International Telecommunication Union
IVB	Inverse V-BLAST\{}\{}
JR	Joint Reception
JT	Joint Transmission
KPI	Key Performance Indicator
LAN	Local Area Network
LED	Light Emitting Diode
LLL	Lenstra–Lenstra–Lovász
LOS	Line-Of-Sight
LR	Lattice Reduction
LR-ZF-OPA	Lattice-Reduction Aided Zero-Forcing Precoding with Optimal Power Allocation
LTE	Long-Term Evolution
MAC	Medium Access Control
MCS	Modulation and Coding Scheme
MIMO	Multiple-Input Multiple-Output
MISO	Multiple-Input Single-Output
MLI	Multi Light Interference
MMC	Modified MonteCarlo
MMSE	Minimum Mean Square Error
mMTC	massive Machine-Type Communications
MRC	Maximum Ratio Combining

MSE	Mean Square Error
MU	Multi-User
MVDR	Minimum Variance Distortionless Response
NEXT	Near-End-Crosstalk
NOMA	Non-Orthogonal Multiple Access techniques
NOSS	Non-Orthogonal Spectrum Sharing
NR	New Radio
OBSAI	Open Base Station Architecture Initiative
OD	Out-of-Domain
OFDM	Orthogonal Frequency Division Multiplexing
OFDMA	Orthogonal Frequency Division Multiple Access
OMA	Orthogonal Multiple Access
OPA	Optimized Power Allocation
OSB	Optimal Spectrum Balancing
OSS	Orthogonal Spectrum Sharing
OWC	Optical Wireless Communication
PD	PhotoDiode
PDCP	Packet Data Convergence Protocol
PHY	PHysical Layer
PLPC	Per-Line Per-Carrier
PoE	Power over Ethernet
PON	Passive Optical Network
PSD	Power Spectral Density
QAM	Quadrature Amplitude Modulation
QoE	Quality of Experience

QoS	Quality of Service
QPSK	Quadrature Phase Shift Keying
RAT	Radio Access Technology
RAU	Remote Antenna Unit
RBD	Regularized Block Diagonalization
RE	Resource Element
RF	Radio-Frequency
RFoF	RF-over-Fiber
RLC	Radio Link Control
RNS	Row Norm Scaling
RoC	Radio-over-Copper
RRC	Radio Resource Control
RSSI	Received Signal Strength Indicator
RTT	Round Trip Time
RX	Receiver
SDM	Space Division Multiplexing
SF	Space-Frequency
SF2F	Space-Frequency to Frequency
SF2SF	Space-Frequency to Space-Frequency
SIC	Successive Interference Cancellation
SINR	Signal-to-Interference-plus-Noise Ratio
SIR	Signal-to-Interference Ratio
SMF	Single Mode Fiber
SNR	Signal-to-Noise Ratio
SP	Signomial Program

SU	Single-User
SVD	Singular Value Decomposition
SVP	Single Vector Processor
TDD	Time Division Duplexing
TDM	Time Division Multiplexing
THP	Tomlinson-Harashima Precoding
THP-DO	Tomlinson-Harashima Precoding with Dynamic Ordering
TIA	TransImpedance Amplifier
TIN	Treating Interference as Noise
TP	Transmitter Precoding
TX	Transmitter
UE	User Equipment
UL	UpLink
ULA	Uniform Linear Array
UPA	Uniform Planar Array
URLLC	Ultra Reliable Low Latency Communications
US	UpStream
UTP	Unshielded Twisted Pair
VB	V-BLAST
VDSL	Very-high-bit-rate DSL
VLC	Visible Light Communications
VP	Vector Processor
WF	Worst-First
ZF	Zero-Forcing